

**Conformal Parametrization of Surfaces of Genus Zero and 3D Reconstruction of
Nuclear Fusion Hotspots**

By

Ka Wai Wong

DISSERTATION

Submitted in partial satisfaction of the requirements for the degree of

DOCTOR OF PHILOSOPHY

in

APPLIED MATHEMATICS

in the

OFFICE OF GRADUATE STUDIES

of the

UNIVERSITY OF CALIFORNIA

DAVIS

Approved:

Prof. Joel Hass, Chair

Prof. Patrice Koehl

Prof. Niels Grønbech-Jensen

Committee in Charge

2020

© Ka Wai Wong, 2020. All rights reserved.

To my beloved mother and sister,
your love is the biggest reason for me to wake up every day and to fight hard for a better future

Contents

Abstract	iv
Acknowledgments	v
Funding sources and disclaimer	vii
Chapter 1. Introduction	1
1.1. Overview and Background	1
1.2. Computation of conformal maps	10
1.3. Conformalized Mean Curvature Flow	16
Chapter 2. Improvement on conformalized mean curvature flow	29
2.1. Flow behaviors and limitations	29
2.2. Initialization procedure of cMCF using Tutte embedding	51
2.3. Sphericalized cMCF - using cMCF to construct homotopy of degree one maps	72
Chapter 3. 3D reconstruction of nuclear fusion hotspot x-ray emission distributions from very few two-dimensional projections	81
3.1. Introduction to Inertial Confinement Fusion at the National Ignition Facility	81
3.2. Algebraic Reconstruction Technique (ART)	86
3.3. 3D x-ray reconstruction of nuclear fusion hotspot using two or three lines of sight with synthetic and experimental data	95
3.4. 3D electron temperature measurement of nuclear fusion hotspot using 3D X-ray reconstructions	119
Appendix A. Mathematical derivation for formulas in chapter 1	135
Appendix B. Synthetic models and their 3D electron temperature measurement	141
Bibliography	149

Abstract

The first part of this thesis is to study a modified version of mean curvature flow, the “conformalized mean curvature flow” (cMCF), developed by Kazhdan, Solomon, and Ben-Chen. The cMCF is a conformal mapping algorithm but it runs into numerical issues when it is applied on meshes with protrusions. We improve the cMCF with an initialization step which first maps the initial mesh onto a sphere. This initialization step is shown to improve the performance of cMCF such that it can be applied on meshes with long protrusions. Also, we investigate a different discretization of the Laplace-Beltrami operator involved in the cMCF that can potentially enhance its performance. More importantly, we give a new algorithm named “Sphericalized cMCF” to construct a homotopy from a degree one map to a homeomorphism from a unit sphere onto a unit sphere. We provide results from numerical experiments of applying this algorithm to closed surfaces of genus zero that are embedded in \mathbb{R}^3 , on which we construct a homotopy from a degree one map to a conformal homeomorphism onto a unit sphere.

The second part of this thesis focuses on my work in the limited view computer tomography at the Lawrence Livermore National Laboratory during a one year internship. This project is related to the inertial confinement fusion (ICF) experiments performed at the National Ignition Facility (NIF). Our work is to reconstruct the 3D x-ray emission distribution of the NIF-ICF hotspot from very limited number of 2D x-ray projection images. Such 3D x-ray reconstructions can help to characterize and compare the thermophysical states of the fusion plasma such its temperature. We apply and test the algebraic reconstruction technique (ART) to reconstruct the 3D x-ray emission distribution of the ICF hotspot. Subsequently, we infer the 3D hotspot electron temperature distribution from these 3D x-ray reconstructions in different energy channels.

Acknowledgments

I would like to thank the following people:

To Patrice, thank you for guiding me and for constantly helping me exceed my expectations. I wish I was a better student to you. I did try my very best in this PhD — both the physical and mental strain I put myself through were real. Nietzsche famously said, “was mich nicht umbringt, macht mich stärker”. I guess he is right!

To Joel, I cannot be more thankful for all your support and encouragement. The past few years of my life would have been much different if I had not met you in Jerusalem. Baruch HaShem that I did meet you though! It has always been my dream to come to the US and you helped me realize this dream. Your wisdom and kindness have made me a better person. So thank you!

To my academic brother Yanwen, thank you for being a friend and a teacher. I would not be able to finish this thesis without your help. I wish all your aspirations in mathematics to eventually come true. Have a happy life!

To my friend Bruno, thank you for caring so deeply about me. Your stellar student has become my very best friend whereas your other student dragged my name through the mud. How can our friendship be more dramatic! Thank you for standing alongside me in the darkest hours. You are truly a great person and I will always look up to you.

To my dearest friend Jake, your friendship is such a blessing to me and we had so much fun together. Thank you for always being there for me. I learned from my time in Salamanca (I was really young, oh boy!) a saying that “el que ríe último, ríe mejor”. I hope that we can laugh together longer than the others and all the way until the end!

To Jim, thank you for your wisdom and kindness throughout my PhD. I wish I had heeded your advice sooner. If I could start it all over again, I would choose a different path. Thank you for showing me the beauty of numerical analysis. I sincerely wish you a successful career ahead!

To my mentor Ben at LLNL, thank you for giving me an opportunity to work with you on the ICF hotspot reconstruction at NIF. You are an excellent mentor. The time of working in the lab was the very best and most rewarding time during my entire PhD studies. I enjoyed every single moment of it. Thank you for all your guidance and help.

Finally, to my host mother Cherie, thank you for letting me become part of your family. Thank you for sharing all my laughters and tears. My stay at your house was supposed to be three months

when I first arrived in Davis. With me overstraining your hospitality, the initial three months have turned into more than four years. Thank you for offering me a shelter in which I recuperated and strived again after each defeat. You might not understand a single mathematical equation in my thesis, but you are a far better and kinder person than many people whom I've come across throughout my PhD. Kindness reciprocates but intelligence does not. Thank you for everything and thank you!

There are two blessings “Shehecheyanu” and “Hashkiveinu” which I learned during the two years I lived in Israel. Whenever I am in doubt, in despair, or in distress, reciting these prayers always help me regain strength and remind me of how lucky I am to be alive and healthy. Humming these prayers in Hebrew while I was finishing writing this dissertation, I recalled a quote from my favorite German-born Jewish American philosopher Hannah Arendt:

“This is the precept by which I have lived: Prepare for the worst; expect the best; and take what comes.”

I look forward to what comes next!

Funding sources and disclaimer

The work presented in chapters 1 and 2 was funded by the Graduate Group of Applied Mathematics in the Department of Mathematics at UC Davis and partly supported by the NSF grant (NSF DMS 1719582).

The work presented in chapter 3 was funded by the High Energy Density Science Center at Lawrence Livermore National Laboratory (LLNL). This work was performed under the auspices of the U.S. Department of Energy by Lawrence Livermore National Laboratory under Contract DE-AC52-07NA27344.

It is released as LLNL-TH-XXXXXX.

This document was prepared as an account of work sponsored by an agency of the United States government. Neither the United States government nor Lawrence Livermore National Security, LLC, nor any of their employees makes any warranty, expressed or implied, or assumes any legal liability or responsibility for the accuracy, completeness, or usefulness of any information, apparatus, product, or process disclosed, or represents that its use would not infringe privately owned rights. Reference herein to any specific commercial product, process, or service by trade name, trademark, manufacturer, or otherwise does not necessarily constitute or imply its endorsement, recommendation, or favoring by the United States government or Lawrence Livermore National Security, LLC. The views and opinions of authors expressed herein do not necessarily state or reflect those of the United States government or Lawrence Livermore National Security, LLC, and shall not be used for advertising or product endorsement purposes.

CHAPTER 1

Introduction

This dissertation consists of results from two different projects that the author has completed. The two projects are independent from each other. The first two chapters focus on conformal parametrizations for surfaces of genus zero using the conformalized mean curvature flow (cMCF). The third chapter is on computer tomography to reconstruct a three-dimensional distribution using very limited two-dimensional projections.

Chapter 1 provides an overview on the related works in surface parametrizations and their applications. Then we study the mathematical foundations of the cMCF and its limitations in practice. In Chapter 2, we introduce an initialization step to improve the cMCF performance and present meshes that can be processed by our enhanced version of cMCF.

Chapter 3 describes our works on the 3D reconstruction of thermonuclear plasma in nuclear fusion hotspot. We give a brief introduction to the inertial confinement fusion experiment at the National Ignition Facility. Then we explain the motivation, our algorithm, the underlying mathematical theory, and the main results of our project.

1.1. Overview and Background

Parametrization of discrete surfaces is an important and widely studied topic in computational mathematics and computer graphics. It has many important applications in medical imaging, morphology, computer graphics and visions, and related fields. Conformal parametrization of a triangle mesh is to compute a correspondence between a triangulated surface patch and a domain in a canonical space through conformal mappings. Since closed manifold genus-zero meshes are topologically equivalent to a sphere, a sphere becomes a natural choice as the canonical space for our conformal maps.

1.1.1. Background. To give the background, we would like to elaborate on the statement above mathematically and describe the motivation behind our works. To do so, we need to state a few fundamental results from topology and differential geometry, which can then lead us to give

a precise definition of a conformal map between smooth surfaces. Here we define a surface S to be a 2-dimensional smooth manifold. S can be described by using a collection of coordinate charts $\{(U_i, \phi)\}$ called *atlas*, where each U_i is an open subset on S and their union covers the entire S . Each corresponding map ϕ_i is differentiable taking U_i into some open subset in \mathbb{R}^2 . A *transition map* $\phi_{ij} := \phi_j \circ \phi_i^{-1}$ takes point between overlapping charts. We will come back to use these concepts to define conformal maps.

The *genus* g of a connected, orientable surface can be defined as the maximum number of nonintersecting simple closed curves that can be on S and do not collectively disconnect S . Equivalently, the genus can also be defined as the number of handles on it. Roughly speaking, genus is the number of “holes” a surface has, for example a sphere has genus zero, a torus has genus one, a torus with n holes (a n -torus) has genus n . Genus of a closed surface S is related to its *Euler characteristic* $\chi(S)$ via

$$\chi(S_g) = 2 - 2g$$

This follows that a sphere has Euler characteristics two, a torus zero, and a n -torus $2 - 2n$. We assume our surface S to be connected, orientable, and closed, i.e. compact and without no boundary. We state the classification theorem for this kind of surfaces.

THEOREM 1.1.1. *Every connect, orientable, closed surface S is homeomorphic to either a sphere or g -torus for some $g \geq 1$.*

We look at the geometry of surfaces in \mathbb{R}^3 . So an immersion of surface S into \mathbb{R}^3 can give a Riemannian metric \mathbf{g} induced on S from the flat metric in \mathbb{R}^3 . The Riemannian metric \mathbf{g} at a point p on S is a positive-definite inner product defined on the tangent space $T_p S$. We can now define with \mathbf{g} concepts such as length of curves lying on S , angles between tangent vectors in $T_p S$, and curvature at points on S . Although many other Riemannian metrics can be defined on S , depending on our choice of the inner product, we use here the Riemannian metric induced from the flat metric in \mathbb{R}^3 .

The celebrated *Gauss-Bonnet* theorem connects the topology and the geometry of surfaces. We state this theorem for the case of closed orientable surfaces.

THEOREM 1.1.2. *Let K be the Gaussian curvature of a closed orientable surface S and dA the area measure of S ,*

$$\int \int_S K dA = 2\pi\chi(S)$$

The curvature on the left hand side is geometrical whereas the Euler characteristic on the right hand side is topological. The above theorem implies that the total curvature of S remains constant regardless of any distortion or change of curvature on S .

1.1.2. Conformal maps between surfaces. Now we are ready to define the notions of conformal mapping and the related concepts on smooth surfaces. Recall that a function $f: U \rightarrow \mathbb{C}$ with $(x, y) \rightarrow (u, v)$ is *holomorphic* if it satisfies the Cauchy-Riemann equation:

$$\frac{\partial u}{\partial x} = \frac{\partial v}{\partial y}, \quad \frac{\partial u}{\partial y} = -\frac{\partial v}{\partial x}$$

f is *biholomorphic* if f is holomorphic, one-to-one, and onto, and its inverse is also holomorphic. A *Riemann surface* is a 1-dimensional complex manifold with complex holomorphic transition functions. Indeed all orientable surfaces are Riemann surfaces. Suppose S and \tilde{S} are two Riemann surfaces, these two surfaces S and \tilde{S} are *conformal equivalent* if there exists a biholomorphic map f that maps from S to \tilde{S} .

We denote a Riemann surface S equipped with a Riemannian metric \mathbf{g} by (S, \mathbf{g}) . Suppose there is another Riemannian metric $\tilde{\mathbf{g}}$ on the same surface S . The two metrics \mathbf{g} and $\tilde{\mathbf{g}}$ are conformal if there exists a positive smooth function $\rho \in C^\infty(S)$ such that $\tilde{\mathbf{g}} = \rho \mathbf{g}$. ρ is called the *conformal factor*. Analogously, given two Riemann surfaces (S, \mathbf{g}) and $(\tilde{S}, \tilde{\mathbf{g}})$ and a map $f: S \rightarrow \tilde{S}$. f is a *conformal map* if there exists a positive smooth function $\rho \in C^\infty(S)$ such that the pullback metric $f^*(\tilde{\mathbf{g}}) = \rho \mathbf{g}$. An intuitive way of picturing the conformal map f is that its pushforward $f_*: T_p(S) \rightarrow T_p(\tilde{S})$ is an *angle-preserving* map, i.e. for any two tangent vectors $v_1, v_2 \in T_p(S)$, the angle between v_1, v_2 on $T_p(S)$ is the same as the angle between the pushforward vectors $f_*(v_1), f_*(v_2)$ on $T_p(\tilde{S})$. And the function ρ in the definitions above describes a uniform scaling of the tangent plane $T_p(S)$.

One basic but fundamental result of conformal maps is the Riemann mapping theorem from complex analysis.

THEOREM 1.1.3. *Let U be a non-empty simply connected, proper open subset in \mathbb{C} , then there exists a biholomorphic map f from U onto the open unit disk.*

The celebrated *Uniformization Theorem* by Poincaré, Klein, and Koebe generalizes the Riemann mapping theorem and classifies simply connected Riemann surfaces using conformal equivalence.

THEOREM 1.1.4. *A simply connected Riemann surface is conformally equivalent to one of the following Riemann surfaces:*

- the unit open disk \mathbb{D}
- the complex plane \mathbb{C}
- the Riemann sphere $\hat{\mathbb{C}} = \mathbb{C} \cup \{\infty\}$

In terms of conformal equivalence of metrics, the Uniformation Theorem can be restated as follows.

THEOREM 1.1.5. *Let S be a compact smooth two dimensional Riemann surface with Riemannian metric \mathfrak{g} . The metric \mathfrak{g} is conformally equivalent to a metric $\tilde{\mathfrak{g}}$ with constant Gaussian curvature, either 1, 0 or -1, depending on the topology of S . The sign of the constant curvature of $\tilde{\mathfrak{g}}$ is equal to the sign of the Euler characteristics $\chi(S)$ of the surface. Furthermore, $\tilde{\mathfrak{g}}$ is unique if $\chi(S)$ is negative.*

One important consequence of the Uniformation Theorem is that the two surfaces share the same conformal structure (surface with conformal transition functions) if they can be conformally mapped. Also, this theorem suggests a *canonical* domain, i.e. with constant curvature everywhere, for the conformal map depending on the topology of a given surface. For example, given closed surfaces of genus-zero and genus-one, we would like to construct conformal maps from them to a 2-sphere and a torus respectively. But the conformal maps constructed in these two cases are not necessarily unique as their Euler characteristics are 2 and 0 respectively. For our works in chapter 2, we will focus on the implication of the Uniformization Theorem in case of genus-zero surfaces, that is, [Ber72]

THEOREM 1.1.6. *Given any smooth genus zero surface S , there is always a conformal diffeomorphism from S to \mathbb{S}^2 , a unit 2-sphere in \mathbb{R}^3 .*

Given a genus-zero surface immersed in \mathbb{R}^3 , we would like to compute a conformal map onto a round 2-sphere.

On a side note, in the space of smooth mappings between surfaces (not necessarily of genus-zero), although the set of conformal maps form a larger subset and hence more flexible than the

set of isometric maps (such as translation and rotation), conformal maps are still restrictive since two random metrics with nontrivial topologies are rarely conformal to each other. In this case, given an arbitrary diffeomorphism f between two surfaces, one idea is to define an energy of f which is minimized when f is conformal. If not minimized, we then use this energy as a measure to quantify the deviation of f from being conformal. This lead to the following defintions. A map $f: (S_1, \mathfrak{g}_1) \rightarrow (S_2, \mathfrak{g}_2)$ is a *harmonic map* if it is a critical point of its *Dirichlet energy*, which describes the global distortion of f , defined by

$$E_D(f) = \frac{1}{2} \int_{S_1} \langle df, df \rangle dA$$

where the differential df can be seen as a section to the bundle $T^*S_1 \otimes TS_2$. For example, in a simple case where D is a open disk and $f = (f_1, f_2, \dots, f_m): D \subset \mathbb{R}^n \rightarrow \mathbb{R}^m$,

$$E_D(f) = \frac{1}{2} \int_D |df|^2 dA = \frac{1}{2} \sum_{i=1}^m \int_D |\nabla f_i|^2 dA.$$

In this case, by calculus of variation, it can be easily shown that the minimizer of Dirichlet energy satisfies the Laplace equation inside D , i.e. $\Delta f = 0$. Moreover,

PROPOSITION 1.1.1. *For any conformal map $\varphi: S_1 \rightarrow S_1$, $E_D(\varphi \circ f) = E_D(f)$, i.e. the Dirichlet energy E_D is conformally invariant.*

PROOF. φ is conformal on S_1 implies that there exists a $\lambda \in C^\infty(S_1)$ such that $\mathfrak{g}_1 \mapsto \lambda \mathfrak{g}_1$. Therefore

$$E_D(f) = \frac{1}{2} \int_{S_1} \langle d(\varphi \circ f), d(\varphi \circ f) \rangle dA = \sum_{i,j} \int_{S_1} \frac{1}{\lambda} \mathfrak{g}_1^{ij} \partial_{x^i} f \partial_{x^j} f \sqrt{|\lambda \mathfrak{g}_1|} dx^i dx^j$$

Since surface S_1 is two dimensional, $\sqrt{|\lambda \mathfrak{g}_1|} = \sqrt{\lambda^2 |\mathfrak{g}_1|} = \lambda \sqrt{|\mathfrak{g}_1|}$, the conformal factor λ and its reciprocal cancel out in above expression. Hence, $E_D(\varphi \circ f) = E_D(f)$. \square

In the case of mappings between general surfaces, a natural question is the existence and uniqueness of a harmonic map. A overview on these results can found be in [EL95]. Moreover, *harmonic maps are equivalent to conformal maps for closed genus-zero surfaces*. [SY97] Therefore, our project is equivalent to the computation of harmonic maps on closed genus-zero surfaces.

Here we state a fundamental result, the *Radó–Kneser–Choquet theorem*, concerning harmonic mappings of a unit disk onto convex regions on a plane [Dur04].

THEOREM 1.1.7. *Let $\Omega \subset \mathbb{C}$ be a bounded convex region whose boundary is a Jordan curve Γ , i.e. a plane simple closed curve. Let φ be a homeomorphism of a unit circle $\{|z| = 1\}$ onto Γ . Then the harmonic extension of φ , defined by the Poisson integral formula,*

$$f(z) = \frac{1}{2\pi} \int_0^{2\pi} \frac{1 - |z|^2}{|e^{it} - z|^2} \varphi(e^{it}) dt$$

is one-to-one in the unit disk $D := \{|z| < 1\}$ and defines a harmonic map of the unit disk onto Ω .

In general, each homeomorphism φ of the unit circle ∂D onto Γ has a unique harmonic extension to the unit disk D , defined by the Poisson integral formula. So the above theorem states a remarkable fact that if Ω is *convex*, then this harmonic extension is always *one-to-one* and it maps the unit disk D harmonically onto a convex region bounded by Γ . So we can summarize the above theorem as follows

THEOREM 1.1.8. *Suppose $\varphi: D \rightarrow \mathbb{R}^2$ is a harmonic mapping which maps the boundary ∂D homeomorphically into the boundary $\partial\Omega$ of some convex region $\Omega \subset \mathbb{R}^2$. Then φ is one-to-one.*

This theorem is closely related to the computation of *discrete harmonic maps* on triangulated surfaces via *Tutte embedding*, which will be stated and elaborated in subsequent sections.

1.1.3. Motivations for conformal parameterizations of genus-zero surfaces. A closely related question that motivates the conformal parametrizations of genus-zero surfaces is the shape comparison of such surfaces. Complex shapes arise everywhere in nature. The human brain, proteins, bones, and leaves all exhibit non-trivial geometric structures that might explain their biological functions. Therefore it is of great value to quantify the geometric differences between two complex shapes. One possible way of doing so is introduced by Hass and Koehl, in which they search for a conformal map f from one surface (S_1, \mathbf{g}_1) to the other (S_2, \mathbf{g}_2) that minimizes a *symmetric distortion energy* defined by

$$E_{sd}(f) = \sqrt{\int_{S_1} (1 - \lambda_f)^2 dA_1}$$

where λ_f is the conformal factor associated to the conformal map f , i.e. $f^*(\mathbf{g}_2) = \lambda_f \mathbf{g}_1$. Abstractly speaking, $E_{sd}(f)$ measures the deviation of the map f from being an isometry between S_1, S_2 . In addition, in the space of shapes of genus zero surfaces \mathcal{S} , they defined a distance function

$d_{sd}: \mathcal{S} \times \mathcal{S} \rightarrow \mathbb{R}^+$ using the minimal symmetric distortion energy, i.e.

$$d_{sd}(S_1, S_2) = \inf\{E_{sd}(f) | f: (S_1, \mathfrak{g}_1) \rightarrow (S_2, \mathfrak{g}_2) \text{ is a conformal diffeomorphism}\}$$

and showed that d_{sd} defines a metric on \mathcal{S} [HK17].

In implementation as shown in figure (1.1), they first construct two conformal maps c_1, c_2 warping surfaces $S_1, S_2 \subset \mathbb{R}^3$ onto the unit 2-sphere \mathbb{S}^2 respectively. The Uniformization Theorem guarantees the existence of these maps. Then a *globally optimal* conformal map $m: \mathbb{S}^2 \rightarrow \mathbb{S}^2$ is chosen such that the conformal map $f := c_2^{-1} \circ m \circ c_1^{-1}$ has the minimal associated energy $E_{sd}(f)$. Note that m belongs to the space of conformal diffeomorphisms from \mathbb{S}^2 to itself, which forms the *projective special linear group* $PSL(2, \mathbb{C})$ sometimes called the *Möbius group* and is a six real-dimensional space. Hence this framework reduces the shape comparison problem into an energy minimization problem over a six dimensional space. Hass and Koehl applied this framework to analyze roundness of proteins, brain surface mapping, comparison of animal bones, etc [KH14], [HK14], [HK15].

However, one key challenge in the implementation of the above framework is to have an *established* and *robust* discrete conformal mapping algorithm that maps the vertices of the given discrete surfaces $S_1, S_2 \subset \mathbb{R}^3$ onto \mathbb{S}^2 . An algorithm is *established* in a sense that it is applicable on a wide range of shapes, and *robust* in the sense that any moderate distortions in the input mesh does not much affect the algorithm's efficiency. The standard approach of constructing such a map is to use a geometric flow which can be *intrinsic* or *extrinsic*. While an intrinsic geometric flow is an evolution of a Riemannian metric (e.g. Ricci flow), an extrinsic geometric flow is an evolution of an immersion of a manifold into Euclidean space (e.g. mean curvature flow). Hass and Koehl used in their implementation the method proposed by Springborn et al. [SSP08] and adopted the notion of *discrete conformal equivalence* proposed by Springborn et al. [BPS15]. This notion mimics the definition of conformal equivalence for smooth surfaces. Using this notion, the problem of “flattening” a given mesh discretely conformally can be solved by minimizing a convex energy functional describing the conformality of the given mesh. We refer the reader to these papers for a full description and the drawback of this approach will be discussed in the subsequent section.

One possible generalization of the method by Hass and Koehl to higher genus surface has been done using quasi-conformal maps [Luo19].

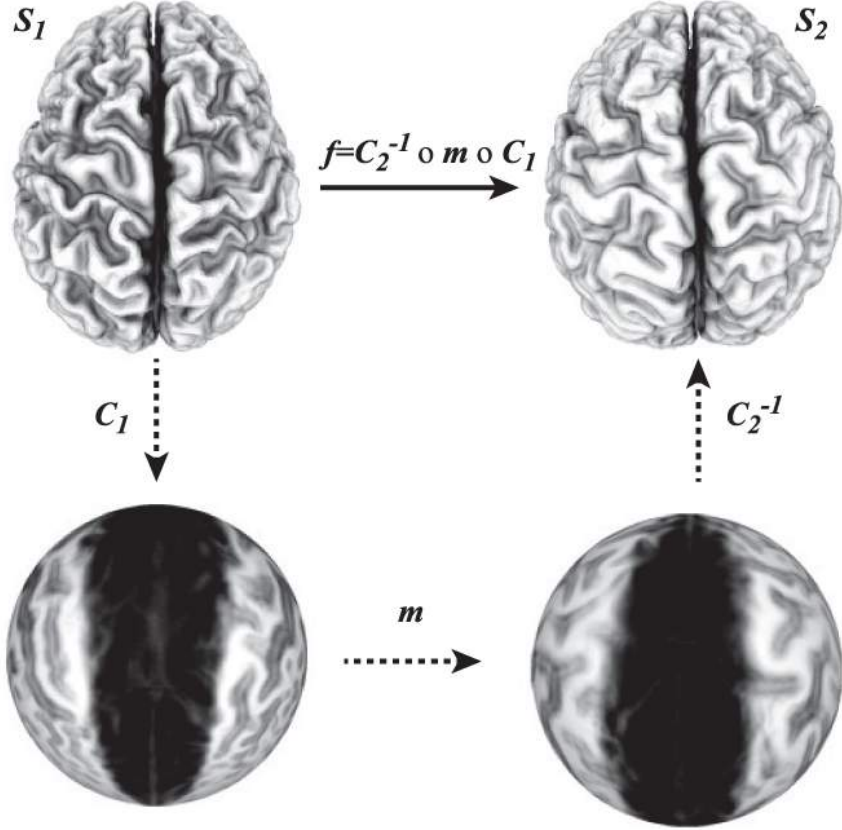


FIGURE 1.1. Globally optimal conformal mapping, source [HK14]

1.1.4. Shape space. A key idea mentioned in the previous section is to apply certain *geometric flow* on a surface to obtain its conformal parametrization. A geometric flow is defined using parabolic partial differential equations and it can be understood as a gradient flow of functionals defined in a Riemannian manifold. The conformalized mean curvature flow, introduced in subsequent sections, is used for evolving a shape to a sphere to attain its conformal parametrization on a sphere. In a continuous case, this evolution process can be seen as a path connecting the initial shape to a sphere in the space of shapes, whose direction (derivative of the path) is given by the equation of the geometric flow. We would like to give a rigorous mathematical definition for the shape spaces and state that it has a differentiable structure such that taking derivative is well-justified.

Let S be a 2-dimensional manifold without boundary. We use $C^\infty(S, \mathbb{R}^3)$ to denote the set of all smooth functions from S into \mathbb{R}^3 . An *immersion* of S into \mathbb{R}^3 refers to a function $\iota \in C^\infty(S, \mathbb{R}^3)$ such that the differential $d\iota$ from the tangent space $T_p S$ to $T_{\iota(p)} \mathbb{R}^3$ is injective for all $p \in S$ and a *embedding* of S into \mathbb{R}^3 is an immersion ι that is a homeomorphism onto its image. Our framework

can be defined using the following spaces of functions:

$$Emb(S, \mathbb{R}^3) \subset Imm(S, \mathbb{R}^3) \subset C^\infty(S, \mathbb{R}^3)$$

where $Emb(S, \mathbb{R}^3)$, $Imm(S, \mathbb{R}^3)$ denote the set of all possible embeddings and immersions of S into \mathbb{R}^3 respectively.

THEOREM 1.1.9. [KM97] *The spaces $Imm(S, \mathbb{R}^3)$ and $Emb(S, \mathbb{R}^3)$ are Fréchet manifolds.*

Parametrized surfaces refer to immersions and embeddings of S into \mathbb{R}^3 . The diffeomorphism group $Diff(S)$, which represents *reparametrizations*, acts upon $Imm(S, \mathbb{R}^3)$ from the right via

$$Imm(S, \mathbb{R}^3) \times Diff(S) \ni (\iota, \varphi) \mapsto \iota \circ \varphi \in Imm(S, \mathbb{R}^3)$$

Note that a change in parametrization of the same surface results in a different object and we want a definition for the shape of a surface which is independent of its parametrizations. So, a *shape* is a submanifold of \mathbb{R}^3 that is diffeomorphic to S . We denote by $B_i(S, \mathbb{R}^3)$ and $B_e(S, \mathbb{R}^3)$ the spaces of all immersed and embedded submanifolds. Since the immersions ι and $\iota \circ \varphi$ have the same image in \mathbb{R}^3 , we can define the *shape space*, $B_i(S, \mathbb{R}^3)$ and $B_e(S, \mathbb{R}^3)$, with quotients

$$B_i(S, \mathbb{R}^3) \cong Imm(S, \mathbb{R}^3)/Diff(S), \quad B_e(S, \mathbb{R}^3) \cong Emb(S, \mathbb{R}^3)/Diff(S)$$

The following theorems show that the shape space $B_e(S, \mathbb{R}^3)$ has a differentiable structure:

THEOREM 1.1.10. [CMM91] *The quotient space $B_e(S, \mathbb{R}^3)$ is a smooth Hausdorff manifold and the projection*

$$\pi: Emb(S, \mathbb{R}^3) \rightarrow B_e(S, \mathbb{R}^3)$$

is a smooth principal fibration with $Diff(S)$ as a structure group.

Furthermore, for $\iota \in Emb(S, \mathbb{R}^3)$, we can define a chart around $\pi(\iota) \in B_e(S, \mathbb{R}^3)$ by

$$\pi \circ \psi_\iota: C^\infty(S, (-\epsilon, \epsilon)) \rightarrow B_e(S, \mathbb{R}^3)$$

with ϵ sufficiently small, where $\psi_\iota: C^\infty(S, (-\epsilon, \epsilon)) \rightarrow Emb(S, \mathbb{R}^3)$ is defined by $\psi_\iota(a) = \iota + an_\iota$ and n_ι is the unit-length normal vector to ι .

For a complete description of shape spaces and its geometry, we refer our reader to [BBM14] for a detailed discussion.

1.2. Computation of conformal maps

Our goal is to apply extrinsic geometric flows to obtain a robust conformal mapping algorithm from surfaces of genus zero onto a unit sphere. For the sake of computation, surfaces are represented and visualized by discrete meshes in real-world applications. We want to construct an algorithm that is both robust and applicable on a wide range of meshes.

The study of geometry of surfaces is very well-established and can be traced back to the last century. Recent advances in the field of discrete differential geometry aim to develop a coherent theory of discrete surfaces and search for discrete notions of metric, curvature, harmonic and conformal maps from the smooth surface setting. These efforts are to construct discretization methods and computation algorithms that are not only robust, but preserve the geometric properties inherited in these concepts from the continuous setting [CW17].

1.2.1. Data structure for discrete surfaces. In practice, we need to have a representation of surfaces in order to process surfaces and compute conformal maps on them. A common way to approximate (and hence represent) smooth surfaces is by *triangulation* defined by $T := (V, E, F)$, where V, E, F are the sets of vertices, edges, and triangular faces, respectively. From the point of topology, a triangulation of a surface can be seen as a simplicial complex together with a homeomorphism, which maps the simplicial complex to the surface. It is obvious that a surface can have many different triangulations. Moreover, the Euler formula can compute the genus of a given mesh using (V, E, F) .

$$|V| - |E| + |F| = \chi(S) = 2 - 2g$$

In terms of data structure, a surface immersed in \mathbb{R}^3 gives vertices in V with (x, y, z) coordinates. Sets E and F contain the combinatorial information of vertices incident to each edge and triangular face respectively. An ideal triangulated mesh, representing a smooth closed, orientable surface, should satisfy that each face should contain three edges only and each edge is a shared boundary of two distinct faces. This implies $2E = 3F$. Also, it should not contain any self-intersecting or self-overlapping faces for the ease and consistency in computation. Generation of triangulated meshes satisfying these criteria to approximate surfaces has been a research field on its own [CDS12].

1.2.2. Discrete conformal maps. Here we would like to provide an overview on the recent efforts in establishing the notions of discrete conformality and discrete conformal maps. We also briefly describe algorithms constructed using these different notions. While surveying these discrete

notions and their corresponding algorithms, we can focus on the *convergences* from the viewpoints of discretization and algorithm to assess their connections to the smooth setting respectively.

- For convergence in discretization, given an algorithm to compute discrete conformal maps, does this discretized map converge to a smooth conformal map while the mesh get finer and finer through triangular subdivision? If so, it converges in what sense?
- For convergence in algorithm, we focus on the methods that are used in the algorithm. For example, if a geometric flow is used to compute a conformal map, does the algorithm compute the flow using variational method to transform it into an optimization? If the geometric flow is extrinsic and provides an embedding of the mesh along its evolution, what kind of discretization methods for the partial differential equation is used? Under what conditions does this algorithm converge?

We discuss three common approaches to compute discrete conformal maps:

- (i) **Vertex scaling** This idea was originally proposed by Luo [Luo04] and then further developed by Bobenko [BPS15], in which a conformal factor is assigned to each vertex of a triangulated surface. Two discrete metrics are *discrete conformal* if the *length-cross-ratio*, a conformally invariant notion, is preserved for each edge. (The length-cross-ratio will be defined and used as a measure for conformality in our numerical experiments in subsequent sections). Gu-Luo-Sun-Wu proved a discrete uniformization theorem, both on existence and uniqueness of the uniformization map in the discrete setting, for polyhedral surfaces based on this notion of vertex scaling [GLSW18].

For results in convergence, Gu-Luo-Wu proved the convergence of discrete conformal maps to the uniformization map if the triangulation is a “ δ triangulation” and no edge flip is required [GLW19]. Bücking showed the convergence of discrete conformal mapping to the smooth Riemann mapping through subdivision [Bü16], [Bü17].

For algorithms to compute discrete conformal maps, Springborn proposed one which transform the problem of finding a discretely conformally equivalent triangulation into a problem of minimizing a convex energy functional [SSP08]. However, if the input mesh has a region full of “flat” triangles, i.e. triangles with one angle close to π , the triangle inequality might fail during the energy minimization, then the output set of edge lengths cannot be embedded in \mathbb{R}^3 . Edge flipping or subdivision of triangles can be used to fix

this problem. Later, Gu-Luo-Sun-Wu gave a more complete algorithm using edge flip and Yamabe flow [SWGL14].

- (ii) **Circle packing** This idea was originally proposed by William Thurston as a tool to study the hyperbolic structure of 3-manifolds. See his lecture notes titled “Geometry and topology of three-manifolds”. A *circle packing metric* on a triangulated surface is to assign a circle to each vertex of the triangulation and these circle radii form a metric. Two circle packing metrics are discrete conformal if and only if they have the same triangulation. Thurston gave a proof for a discrete version of the Uniformization Theorem using circle packing metric. This idea is further generalized to the *inversive distance circle packing* which includes all possible discrete metric on surfaces.

For results in convergence, Rodin and Sullivan proved that a discrete conformal map on the disk constructed by circle packing converges to the smooth Riemann mapping under subdivision of hexagon triangulation [RS87]. Improvement on results by Rodin and Sullivan and more convergence results on discrete conformal map were done by He and Schramm in a series of papers [HS93], [HS96], [HS98].

For algorithms to compute circle packing, Collins and Stephenson gave the first complete algorithm [CS03]. Later, based on the idea of circle packing, Jin-Kim-Lu-Guo gave algorithms to unify discrete Ricci flow on surfaces of arbitrary topologies, including spherical (genus zero), euclidean (genus one), and hyperbolic (genus higher than one) [JKLG08]. More precisely, their work is to arbitrarily distribute the total curvature given by the Gauss-Bonnet theorem through assignment of discrete conformal factors on vertices. These factors are obtained through minimizing a convex energy functional derived from the Ricci flow which was given by Chow and Luo [CL03]. A detailed survey on the application of the discrete Ricci flow to computation of discrete conformal maps can be found in [ZZG⁺15].

- (iii) **Circle pattern** This idea associates a circle with each triangle face in the original mesh and results in patterns of non-intersecting circles on a triangulated surface. This construction aims to incorporate the intrinsic geometry of the mesh, in which each edge is assigned an angle between 0 and π which corresponds to the intersection angle of the two incident face circles. Bobenko and Springborn proved that such circle patterns can be

characterized as a unique minimizer of a convex energy functional expressed in terms of logarithmic radius variables and the given edge angles [BS04]. Their result generalized the previous work done by Rivin [Riv94] and Leibon [Lei02].

For results in convergence, Bücking showed that sequences of circle patterns can be employed to approximate a smooth conformal map and its first derivative. In some special cases, the convergence result can be strengthened to a uniform convergence on compact subsets [Bü08].

For algorithm to apply circle patterns in computing conformal maps, Kharevych, Springborn, and Schröder computed conformal parametrizations of genus-zero surfaces by minimizing the convex energy functional described above. They also applied their algorithm to surfaces of higher genus with the use of cone singularities [KSS06].

In terms of algorithms, all methods above compute a discrete conformal mapping through minimization of certain convex energy functionals. Most of these functional can be derived from intrinsic geometric flows such as discrete Ricci flow. In the continuous setting, Ricci flow is conformal and guaranteed to evolve a genus-zero surface to a sphere. However, Ricci flow only provides a metric of the surface but not its embedding. Therefore, in the discrete setting, the triangle inequality is not guaranteed to hold in the resulting mesh after the minimization process. Most of these algorithms also require the triangulation of the input mesh to be Delaunay.

1.2.3. Discrete harmonic map. As stated earlier, harmonic maps are equivalent to conformal maps for closed genus-zero surfaces. Therefore, It is worth mentioning that the recent advances on computation of discrete harmonic maps and its application. One natural approach of computing discrete harmonic map is to use *Tutte's embedding theorem* [Tut63]. This theorem to provide a discrete analogy to the mean value property of the harmonic map, i.e. the value at one point of this map is equal to the average of its neighboring values. Tutte's embedding theorem establishes a canonical way of straight-line embedding of a planar graph with convex prescribed boundary, which is topologically equivalent to a disk. We will state the Tutte's embedding theorem and describe its algorithm in details in the following chapter.

A method introduced by Aigerman and Lipman is to generalize Tutte's embedding to a map from a given surface onto an Euclidean orbifold with spherical topology by solving a sparse linear

system [AL15]. Their main contribution is to provide a globally bijective parametrization of a given surface without creating any landmarks artificially to cut the surface into disks. Their subsequent work extended this bijective parametrization onto spherical and hyperbolic orbifolds by minimizing a discrete Dirichlet energy [AL16, AKL17].

For results in convergence, Dym, Slutsky, and Lipman proved a linear variational principle for a sequence of piecewise linear maps obtained by Tutte's embedding converging to a smooth harmonic map under subdivision of triangulation [DSL19].

In addition, Floater used a discrete version of maximal principle to prove a discrete version of the Radó–Kneser–Choquet theorem for discrete harmonic maps and is closely related to Tutte's theorem on barycentric mappings of planar graphs [Flo03b]. Also, Gotsman, Gu, and Sheffer suggested another approach to generalize Tutte's embedding on spherical geometry by solving a non-linear system of equation. The proof for the correctness of their algorithm established a connection to spectral graph theory [GGS03].

1.2.4. Application of geometric flows in computational geometry. Geometric flows are used to evolve surface geometry and discretization of these flows is used in computing conformal maps, like the discrete Ricci flow mentioned in the previous section. Many of them have been applied to mesh processing, surface smoothing, and noise removal on meshes. We mention here some widely-used applications of geometric flows, including *mean curvature flow* and *Willmore flow*, in computational geometry in order to motivate our investigation in a modified version of the mean curvature flow.

Let Φ be an immersion of a compact region $M \subset \mathbb{R}^2$ into \mathbb{R}^3 . We can define the *surface area* functional, or sometimes stated as the *membrane energy*, E_A of Φ .

$$E_A(\Phi) := \int_M dA$$

Minimizing E_A via gradient descent gives the mean curvature flow. We use Δ to denote the Laplace–Beltrami operator induced by f .

$$\frac{\partial \Phi}{\partial t} = \frac{1}{2} \Delta \Phi$$

Note that this flow is a nonlinear parabolic PDE since the Laplace Beltrami operator Δ is a function of Φ . This flow can also be seen as minimizing the gradient of the surface embedding since

$\Delta\Phi = 2H\vec{N}$ where H is the scalar mean curvature (hence the name of the flow) and $\vec{N} \in \mathbb{R}^3$ is the surface normal. This implies that the flow can be used to smooth an embedded surface embedding.

Different algorithms for surface fairing uses different strategies to discretize the flow in space and in time. One of the earliest works on applying the discretized mean curvature flow to surfaces was done by Brakke [Bra92]. His surface evolver used the forward Euler method to discretize the mean curvature flow. It minimizes the surface area functional and can be used to produce discrete minimal surfaces. Since the flow is inherently nonlinear, Desbrun, Meyer, Schröder, and Barr proposed an implicit integration of the flow to enhance stability with large time-steps. Their implicit fairing method can rapidly remove rough features from irregularly triangulated data by applying a discretized mean curvature flow via backward Euler method [DMSB99]. Later, Clarenz, Diewald, and Rumpf mean curvature flow with discretization using finite elements method in space and a semi implicit backward Euler scheme in time. Their technique can successively smooth noisy initial surface while simultaneously enhance edges and corners on the surface [CDR00].

However, *mean curvature flow of an embedded surface can develop sharp singularities within finite time even in the continuous setting*. The *conformalized mean curvature flow (cMCF)*, originally introduced by Kazhdan, Solomon, and Ben-Chen [KSBC12], is an attempt to modify the flow in order to compute conformal map by removing the numerical instability and avoiding degeneracy in the discrete setting. We will discuss their work and our contribution in great details in the following section and chapter 2 respectively.

A closely related concept is the *Willmore energy* functional E_w of Φ defined to be the squared L^2 -norm of the mean curvature.

$$E_w(\Phi) := \int_M H^2 dA$$

E_w is invariant under the group of Möbius transformation in \mathbb{R}^3 and hence conformally invariant [Whi73]. Minimizing E_A via gradient descent gives the nonlinear Willmore flow

$$\frac{\partial \Phi}{\partial t} = -\nabla E_w(\Phi)$$

In the continuous setting, it has been showed that the solutions of the Willmore flow exist globally and converge exponentially fast to a sphere, provide that the initial shape is close to a sphere [Sim01]. However, in contrast to the mean curvature flow, it remains open whether the Willmore flow of an embedded surface can develop singularities within finite time, and counter-examples

exist for immersed surfaces [Bla09]. Moreover, This flow requires higher order surface derivatives (fourth-order), which makes it more difficult to discretize compared to the mean curvature flow. Since E_w can be rewritten using integration by parts

$$E_w(\Phi) = \frac{1}{4} \langle \Delta\Phi, \Delta\Phi \rangle = -\frac{1}{4} \langle \Delta^2\Phi, \Phi \rangle$$

one possible way to approximate the Willmore flow by the following flow using the bilaplacian operator

$$\frac{\partial\Phi}{\partial t} = \frac{1}{2}\Delta^2\Phi$$

More ideas on approximating the Willmore flow and their applications are discussed in the works of Schenider and Kobbett [SK00a], [SK00b].

Yoshizawa and Belyaev used the cotangent formula to directly discretize the energy gradient $-\nabla E_w(\Phi)$ and introduced an additional tangential force to improve the quality of the evolving. But this approach might distort the mesh texture and the flow is also unstable as the curvature flow itself [YB02]. Clarenz et al. discretized the variational formulation of the Willmore energy in linear Lagrange elements and the corresponding L2-flow can be solved by a coupled system of second order differential equations. This approach is valuable for geometric modelling since it allows tangent constraints at the boundary [CDD⁺04].

Bobenko and Schröder presented a discrete version of the Willmore energy E_w preserving its conformal invariance property. They also derived the corresponding expressions for the gradient $-\nabla E_w(\Phi)$ in the discrete setting. Later, Wardetzky et al. investigated the discrete Willmore flow by using a semi-implicit quasi-Newton scheme to cope with the nonlinearity of the flow [WBH⁺07]. Finally, a conformal Willmore flow has been suggested which is guaranteed to keep the metric conformal to the original surface. It can be used to smooth the mesh until it converges to a sphere [CPS11], [CPS13].

1.3. Conformalized Mean Curvature Flow

Here we are interested in the conformalized mean curvature flow (cMCF), originally introduced by Kazhdan, Solomon, and Ben-Chen [KSBC12]. In this section, we describe their algorithm, show the mathematical derivations, and explain the motivation behind. Then we briefly describe our own implementation of this algorithm. In the next chapter (2), we highlight some limitations of this algorithm and discuss in great details our improvement on the algorithm.

1.3.1. Mean Curvature Flow. To begin with, we start with the mean curvature flow (MCF) on a surface M . We assume M to be a compact surface of genus zero. While the MCF can be applied on non-compact surface, this assumption helps to focus on our goal of computing a conformal map from closed genus-zero surfaces.

Let $\Phi_t: M \rightarrow \mathbb{R}^3$ be a smooth family of immersions with time $t \geq 0$ and the induced metric g_t at time t . MCF is defined as

$$(1.1) \quad \frac{\partial \Phi_t}{\partial t} = \Delta_{g_t} \Phi_t$$

where Δ_{g_t} is the Laplace-Beltrami operator defined w.r.t. g_t .

$$\Delta_{g_t} := -\frac{1}{\sqrt{\det(g_t)}} \frac{\partial}{\partial x^\alpha} \left(\sqrt{\det(g_t)} g_t^{\alpha\beta} \frac{\partial}{\partial x^\beta} \right), \quad \text{where } g^{\alpha\beta} \text{ denotes the inverse of metric } g_{\alpha\beta}$$

We sometimes use Δ_t to denote Δ_{g_t} .

Since $\Delta_{g_t} \Phi_t = 2H_t \hat{N}_t$ where $H_t(p)$ is the scalar mean curvature and $\hat{N}_t(p)$ is the unit surface normal at point $p \in M$. Since g_t is the induced metric, the MCF can be rewritten as

$$\frac{\partial \Phi_t}{\partial t} = -2H_t \hat{N}_t$$

This reformulation implies that, when $\Phi_t(M)$ evolved under the mean curvature flow, Φ_t evolves points on M along its normal direction with the scalar mean curvature as speed.

The MCF (1.1) is a second order nonlinear parabolic PDE since the metric g_t depends on the immersion Φ_t at every t . So unlike the conventional heat diffusion equation which is a linear parabolic and does not develop singularities, MCF may develop singularities. Moreover, an immersion (local embedding) of a surface suffices since the mean curvature at point p can be calculated in a neighborhood alone. A global embedding of M is not required here.

In one dimension, when MCF is applied to a curve γ , Φ_t is a family of immersions of a closed curve in \mathbb{R}^2 instead of a surface in \mathbb{R}^3 , the flow becomes

$$\frac{\partial \Phi_t}{\partial t} = -2K_t \hat{N}_t$$

where $K_t(p)$ is the scalar curvature at point p . This is equivalent to the *curve shortening flow*. Gage showed [Gag83], [Gag84] that under the 1D MCF, if $\Phi_0(\gamma)$ is convex, $\Phi_t(\gamma)$ eventually converges to a circle for some $t > 0$ and then later a point in finite time where singularity occurs.

Furthermore, Gage and Hamilton later proved that all smooth convex curves eventually contract to a point (singularity) without forming any other singularities under the 1D MCF [GH86]. Finally, Grayson showed that any non-convex curves become convex in finite time, then stay remain convex under the 1D MCF [Gra87] and a simpler proof for Grayson’s result was later given [AB11].

In two dimension when MCF (1.1) is applied to surfaces, there are analogous results as in one dimension. First, a sphere remains spherical but get smaller and eventually contracts to a point under MCF. To show this, due to the rotational symmetry of the sphere, the immersion Φ_t of a sphere \mathbb{S} can be written as

$$\Phi_t(p) = r(t) \cdot \vec{N}(p), \quad \text{where } r(t) \text{ is the radius function and the inward normal vector } \vec{N}(p) = p$$

Also, the mean curvature of all points on a sphere of radius r is $H_t = 2/r$. Therefore,

$$\frac{\partial \Phi_t}{\partial t} = -2H_t \hat{N}_t = -\frac{2\vec{N}}{r}$$

Therefore, it reduces to an ODE of $r(t)$

$$r'(t) = -\frac{2}{r(t)} \quad \Rightarrow \quad r(t) = \sqrt{1 - 4t}$$

This implies that the sphere radius always goes to zero in finite time (the sphere contracts to a point). Analogous to the global result of Gage and Hamilton in one dimension, Huisken showed that closed embedded surfaces flow to sphere in \mathbb{R}^3 . Huisken’s result is indeed much more general and valid for any closed convex hypersurface in \mathbb{R}^{n+1} for $n > 1$. His result states that under MCF these hypersurfaces remains convex and eventually become extinct in a “round point” [Hui84]. The implication of Huisken’s result is that *any convex surface can flow to a round sphere by keeping the surface area constant through rescaling in every time step*.

Here we present our simulation of evolving an ellipsoid (which is convex) to a round sphere through the MCF. We discretize the flow using finite element methods which are described and analyzed in the subsequent section. We generate a discrete mesh for an ellipsoid with one unit in two of its three semi-axes and two units in the remaining semi-axis. Below are the views of looking at the ellipsoid from the side and from the tip.

This mesh has around 34k vertices and all of them have either valence of 5 or 6. Almost all triangles are close to equilateral and have similar areas. We refer readers to a detailed analysis

of our meshes in the next chapter. We run 200 iterations with step size of 0.01 until the MCF converges while keeping the surface area constant, i.e. equal to 4π of a unit sphere in this case.

This simulation shows that the mesh stays convex and eventually converges to a sphere. Their values of sphericity are $s = 0.92, 0.97, 0.99, 0.997, 0.998$ at the 0th, 50th, 100th, 150th, 200th step of iteration.



FIGURE 1.2. Side view
of ellipsoid

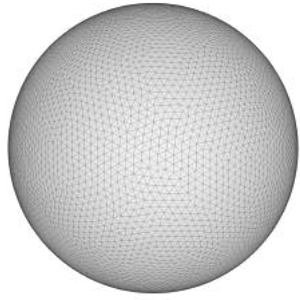


FIGURE 1.3. Front view
of ellipsoid



FIGURE 1.4. 50th step

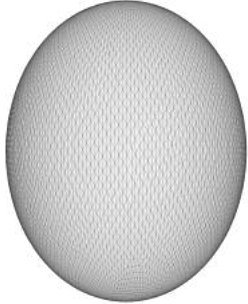


FIGURE 1.5. 100th step

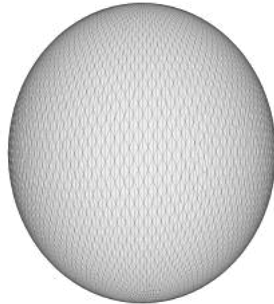


FIGURE 1.6. 150th step

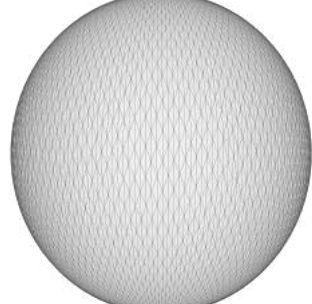


FIGURE 1.7. 200th step

However, although MCF can provide a spherical parametrization for the ellipsoid in this case, this parametrization is not conformal. Moreover, non-convex surfaces are known to develop singularities under MCF. Grayson showed analytically that a neck-pinch forms in the dumbbell shape, which consists of two spheres and a sufficiently long and narrow barbell handle [Gra89]. The handle becomes narrower and thinner under MCF and eventually develops singularity. The figures below are taken from [CMP15]:

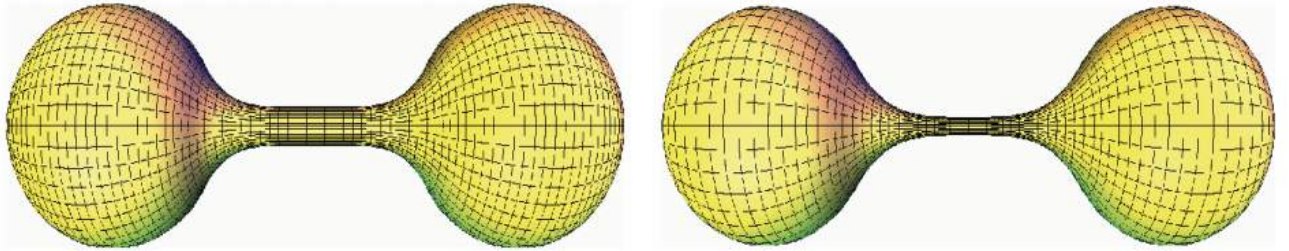


FIGURE 1.8. initial shape and the handle becomes thinner under MCF

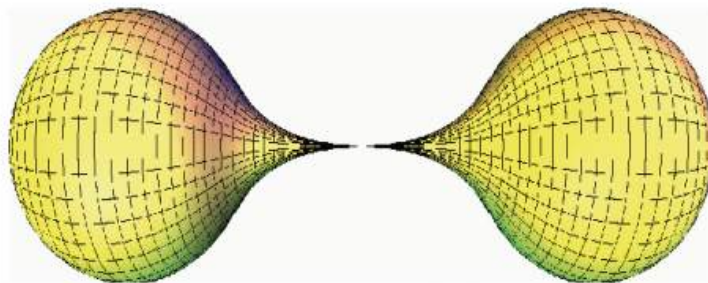


FIGURE 1.9. formation of neck-pinch

We illustrate the development of singularities under MCF with the mesh “spot” shown below. It has around 3k vertices and all of them have either valence of 5 or 6. We use a step size of $\tau = 0.05$ while keeping the surface area constant. The spot’s head evolves into a spike where singularity forms within the first few steps of iterations. Iterations stop with the emergence of singularities.

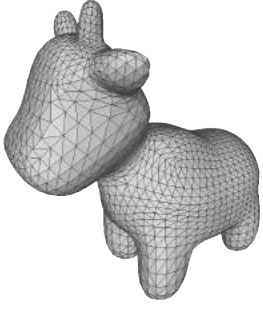


FIGURE
1.10. Initial
mesh “spot”

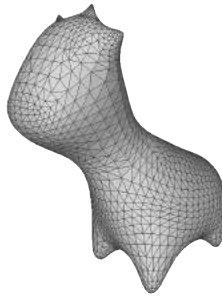


FIGURE 1.11. 5th step

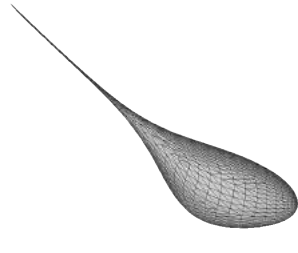


FIGURE 1.12. 10th step

1.3.2. Finite element method and numerical analysis of mean curvature flow. In this section, we present the discretization of the MCF using finite element method. Then we can explain the formation of singularities emerged in the MCF, which we demonstrated in the previous section, by identifying the corresponding numerical instabilities that arise in the discretized MCF. The following analysis we present here is the work of Kazhdan, Solomon, and Ben-Chen [**KSBC12**]. We present their work here in our words and with more detailed mathematical derivations.

In order to discretize the MCF equation (1.1), we use the *Galerkin method* from finite element methods, which is to use a set of basis functions to convert a partial differential equation with a continuous operator (the Laplace-Beltrami operator) into a discrete problem.

Suppose the embedding map of the MCF, Φ_t , is defined on a closed surface of genus zero M and we have a set of N function basis $\{B_1, \dots, B_N\} : M \rightarrow \mathbb{R}$. We can *approximate*¹ the map Φ_t by coefficient vectors $\{x_1(t), x_2(t), \dots, x_N(t)\} \subset \mathbb{R}^3$, where these coefficient vectors are independent of surface M :

$$(1.2) \quad \Phi_t(p) = \sum_{i=1}^N x_i(t) B_i(p) \quad \forall p \in M$$

We substitute the (1.2) into the MCF (1.1) and use the weak formulation, i.e. multiply both sides with a basis function B_j where $1 \leq j \leq N$ and integrate over M with respect to the area measure dA ²:

$$\int_M \sum_i \left(\frac{\partial x_i}{\partial t} \cdot B_i \right) \cdot B_j dA_t = \int_M \sum_i \left(\frac{\partial x_i}{\partial t} \cdot \Delta_{g_t} B_i \right) \cdot B_j dA_t$$

¹This approximation is in the least-square sense. Suppose that the initial embedding $\Phi_0(M) \notin \text{span}\{B_1, \dots, B_N\}$, we find the closest embedding $\tilde{\Phi}_0(M) \in \text{span}\{B_1, \dots, B_N\}$ such that $\|\Phi_0 - \tilde{\Phi}_0\|_2$ is minimized.

² dA_t denotes the surface area induced by the metric g_t

Integration by parts³ gives

$$\sum_i \int_M \frac{\partial x_i}{\partial t} (B_i \cdot B_j) dA_t = \sum_i x_i(t) \int_M g_t(\nabla_t B_i, \nabla_t B_j) dA_t$$

where ∇_t is to compute the gradient vector with respect to the induced metric g_t .

Using backward Euler method to approximate the time derivative, we obtain

$$\sum_i \left(\frac{x_i(t + \tau) - x_i(t)}{\tau} \right) \int_M (B_i \cdot B_j) dA_t = \sum_i x_i(t + \tau) \int_M g_t(\nabla_t B_i, \nabla_t B_j) dA_t$$

We can rewrite this using matrix formulation by defining a matrix $\vec{x}(t) := \{x_1(t), x_2(t), \dots, x_N(t)\}^T$, the **mass matrix** D^t , and the **stiffness matrix** L^t

$$(1.3) \quad D_{ij}^t := \int_M B_i B_j dA_t, \quad L_{ij}^t := \int_M g_t(\nabla_t B_i, \nabla_t B_j) dA_t,$$

Then we have

$$D^t (\vec{x}(t + \tau) - \vec{x}(t)) = \tau L^t \vec{x}(t + \tau)$$

At time t where $\vec{x}(t)$ is known, we compute $\vec{x}(t + \tau)$ at the next time step $t + \tau$:

$$(1.4) \quad \Rightarrow \quad (D^t - \tau L^t) \vec{x}(t + \tau) = D^t \vec{x}(t)$$

Note that $\vec{x}(t)$ is matrix of dimension $N \times 3$ since each coefficient vector $x_i(t) \in \mathbb{R}$, whereas D and L are of dimension $N \times N$. Therefore, we are solving for coefficient vectors $x_i(t)$ in the x, y, z -directions in each time step. The equation (1.4) is the discrete version of the continuous MCF equation (1.1).

³

$$\begin{aligned} \int_M (\Delta_t B_i \cdot B_j) dA_t &= - \int_M \frac{1}{\sqrt{\det(g_t)}} \frac{\partial}{\partial x^\alpha} \left(\sqrt{\det(g_t)} g_t^{\alpha\beta} \frac{\partial B_i}{\partial x^\beta} \right) B_j \sqrt{\det(g_t \cdot g_0^{-1})} dA_0 \\ &= \int_M \left(\sqrt{\det(g_t)} g_t^{\alpha\beta} \frac{\partial B_i}{\partial x^\beta} \right) \frac{\partial B_j}{\partial x^\alpha} \sqrt{\det(g_0^{-1})} dA_0 \\ &= \int_M g_{t\nu\mu} g_t^{\mu\beta} \frac{\partial B_i}{\partial x^\beta} g_t^{\nu\alpha} \frac{\partial B_j}{\partial x^\alpha} \sqrt{\det(g_t \cdot g_0^{-1})} dA_0 \\ &= \int_M g_t(\nabla_t B_i, \nabla_t B_j) dA_t \end{aligned}$$

where divergence theorem is applied in the second equality.

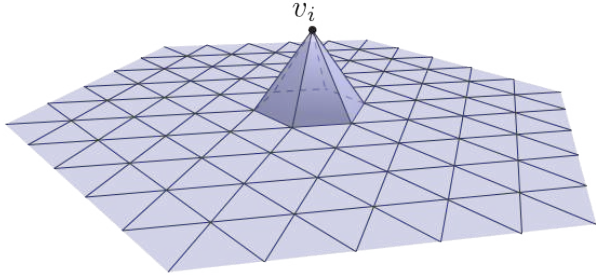


FIGURE 1.13. Hat basis I
source: discrete differential geometry by Keenan Crane

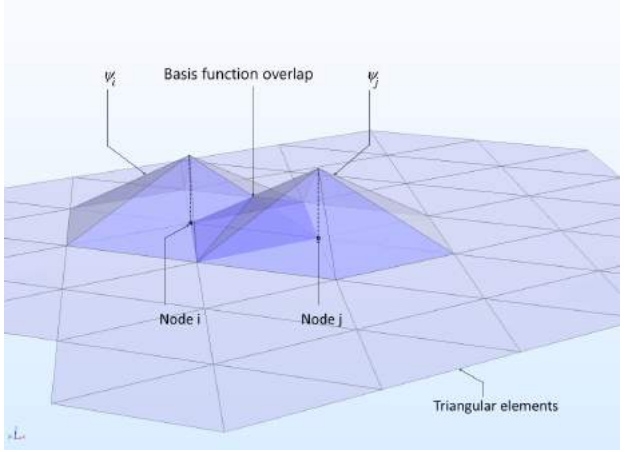


FIGURE 1.14. Hat basis II
source: discrete differential geometry by Keenan Crane

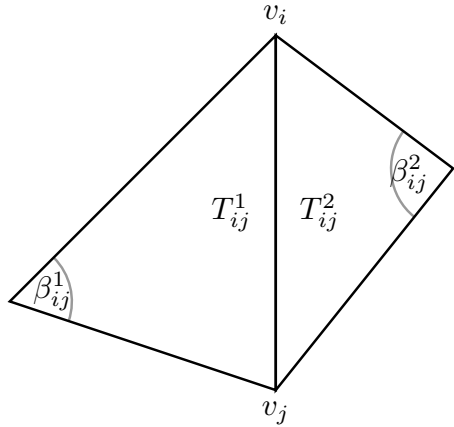


FIGURE 1.15. T_{ij}^1, T_{ij}^2 share an edge $e_{ij} = (v_i, v_j)$

Now we define our basis function: given a triangulated surface approximating M , defined by $(\mathcal{V}, \mathcal{E}, \mathcal{T})$, the *hat basis* $B_i: \mathcal{V} \rightarrow \mathbb{R}$, see figures (1.13) and (1.14), is defined by

$$(1.5) \quad B_i(v_j) = \begin{cases} 1 & i = j \\ 0 & i \neq j \end{cases} \quad \forall v_j \in V$$

One immediate consequence of using the hat basis is that *the coefficient vector $x_j(t)$ now describes the trajectory of the vertex v_j since*

$$\Phi_t(v_j) = \sum_i x_i(t) B_i(v_j) = \sum_i x_i(t) \delta_{ij} = x_j(t)$$

Furthermore, we can give explicit formulas to compute the mass matrix D and the stiffness matrix L on a discrete surface $(\mathcal{V}, \mathcal{E}, \mathcal{T})$, which is a discrete equivalence to the continuous formulation (1.3). Given $T_{ij}^1, T_{ij}^2 \in \mathcal{T}$ such that $T_{ij}^1 \cap T_{ij}^2 = e_{ij} \in \mathcal{E}$ and $\beta_{ij}^1, \beta_{ij}^2$ are the two angles opposite edge e_{ij} , see figure (1.15).

(1.6)

$$D_{ij} = \begin{cases} \frac{1}{12} (\text{Area } (T_{ij}^1) + \text{Area } (T_{ij}^2)) = \frac{1}{12} (\text{Area of two adjacent triangles to edge } e_{ij}) & i \sim j \\ \sum_{k \in N(i)} D_{ik} = \frac{1}{\text{valence of } v_i} (\text{Area of all triangles adjacent to vertex } v_i) & i = j \\ 0 & \text{otherwise} \end{cases}$$

(1.7)

$$L_{ij} = \begin{cases} -\frac{1}{2} (\cot \beta_{ij}^1 + \cot \beta_{ij}^2) & i \sim j \\ -\sum_{k \in N(i)} L_{ik} & i = j \\ 0 & \text{otherwise} \end{cases}$$

where $i \sim j$ implies that vertex v_i is adjacent to v_j .

The derivation of the formulas (1.6) and (1.7) are in the Appendix (A).

Next, we go back to the MCF in the continuous setting and look into the operator in the flow.

Recall that the embedding map of surface M is $\Phi_t(M)$ at time t over the map. Suppose the parametrization of the embedded surface $\Phi_t(M)$ is given by the map $X^t: U \subset \mathbb{R}^2 \mapsto \mathbb{R}^3$ defined by $X^t(x_1, x_2) := \Phi(p)$, where (x^1, x^2) is the local coordinate chart and $p \in M$. The measure of the surface area at $t = t_0$ and $t = t_1$ are given respectively by

$$dA_0 = \sqrt{\det(g_0)} dx^1 \wedge dx^2, \quad dA_1 = \sqrt{\det(g_1)} dx^1 \wedge dx^2$$

Hence,

$$dA_0 = \frac{\sqrt{\det(g_0)}}{\sqrt{\det(g_1)}} \sqrt{\det(g_1)} dx^1 \wedge dx^2 = \sqrt{\det(g_0 \cdot g_1^{-1})} dA_1 \Rightarrow dA_1 = \sqrt{\det(g_1 \cdot g_0^{-1})} dA_0$$

The operator $g_1 \cdot g_0^{-1}$ is an endomorphism of the tangent space to itself. *It characterizes how the geometry of the embedded surface $\Phi_t(M)$ is stretched over the course of the flow from time t_0*

to t_1 . Its eigenvectors, $v_1(t)$ and $v_2(t)$, define the principal directions of stretch (orthogonal with respect to both g_0 and g_1) and its eigenvalues $\lambda_1^2(t), \lambda_2^2(t)$ define the magnitudes of stretch along these directions [KSBC12].

We define a linear map $\Lambda: T\Phi_0(p) \mapsto T\Phi_1(p)$ between tangent planes of Φ_0 and Φ_1 at point $p \in M$. Λ maps orthogonal vectors $\partial_{v_1}, \partial_{v_2} \in T\Phi_0(p)$ with $\partial_{v_1} \perp \partial_{v_2}$ to the two orthogonal vectors, $\partial_{w_1}, \partial_{w_2} \in T\Phi_1(p)$ with $\partial_{w_1} \perp \partial_{w_2}$ such that

$$\Lambda := d\Phi_1 \circ d\Phi_0^{-1} \quad \Rightarrow \quad \Lambda \partial_{v_i} = \lambda_i \partial_{w_i}, \quad i = 1, 2$$

where $d\Phi_0$ and $d\Phi_1$ are the pushforwards of maps Φ_0 and Φ_1 . Also, the eigenvectors ∂_{w_i} and the eigenvalues (stretch factors) λ_i are time dependent.

More importantly, the existence of the map Λ can be proved by Intermediate Value Theorem. We provide the proof in the appendix (A).

We let $|\Lambda|$ denote the determinant of Λ . So we have $|\Lambda| = \lambda_1 \lambda_2$. Furthermore, using the relation between the embedding map and its induced metric $g_t = d\Phi_t^T d\Phi_t$, we can compute the determinant of the map $g_1 \cdot g_0^{-1}$:

$$\det(g_1 \cdot g_0^{-1}) = |g_1| |g_0|^{-1} = |d\Phi_1^T d\Phi_1| |d\Phi_0^T d\Phi_0|^{-1} = |d\Phi_1^T d\Phi_0|^{-1} = |\Lambda|^2 = (\lambda_1 \lambda_2)^2$$

Therefore,

$$(1.8) \quad dA_1 = (\lambda_1 \lambda_2) dA_0$$

We can apply equation (1.8) on the mass and stiffness matrices D^t and L^t in formula (1.3)

$$D_{ij}^t = \int_M B_i \cdot B_j dA_t = \int_M B_i \cdot B_j (\lambda_1(t) \lambda_2(t)) dA_0$$

Since the area of the embedded surface is decreasing under the MCF, $\lambda_1(t) \lambda_2(t)$ tend to get smaller over the course of the flow, so the computation of D_{ij}^t is numerically stable.

$$L_{ij}^t = \int_M g_t(\nabla_t B_i, \nabla_t B_j) dA_t$$

Since

$$g_t(\nabla_t B_i, \nabla_t B_j) = \underbrace{g_{\mu\nu} g^{\nu\alpha}}_{=\delta_{\mu\alpha}} \partial_\alpha B_i g^{\mu\beta} \partial_\beta B_j = g^{\alpha\beta} \partial_\alpha B_i \partial_\beta B_j,$$

we have

$$L_{ij}^t = \int_M \begin{pmatrix} \frac{\partial B_i}{\partial w_1} & \frac{\partial B_i}{\partial w_2} \end{pmatrix} \begin{pmatrix} g_0(v_1, v_1) & 0 \\ 0 & g_0(v_2, v_2) \end{pmatrix}^{-1} \begin{pmatrix} \frac{\partial B_j}{\partial w_1} \\ \frac{\partial B_j}{\partial w_2} \end{pmatrix} dA_t.$$

Using $\partial_{w_i} = \frac{1}{\lambda_i} \partial_{v_i}$, we can rewrite

$$L_{ij}^t = \int_M \begin{pmatrix} \frac{1}{\lambda_1} \frac{\partial B_i}{\partial v_1} & \frac{1}{\lambda_2} \frac{\partial B_i}{\partial v_2} \end{pmatrix} \begin{pmatrix} g_0(v_1, v_1) & 0 \\ 0 & g_0(v_2, v_2) \end{pmatrix}^{-1} \begin{pmatrix} \frac{1}{\lambda_1} \frac{\partial B_j}{\partial v_1} \\ \frac{1}{\lambda_2} \frac{\partial B_j}{\partial v_2} \end{pmatrix} (\lambda_1 \lambda_2 dA_0).$$

Therefore,

$$\begin{aligned} L_{ij}^t &= \int_M \left(\frac{1}{g_0(v_1, v_1)} \cdot \frac{1}{\lambda_1^2} \frac{\partial B_i}{\partial v_1} \frac{\partial B_j}{\partial v_1} + \frac{1}{g_0(v_2, v_2)} \cdot \frac{1}{\lambda_2^2} \frac{\partial B_i}{\partial v_2} \frac{\partial B_j}{\partial v_2} \right) \lambda_1 \lambda_2 dA_0 \\ &= \int_M \left(\frac{1}{g_0(v_1, v_1)} \cdot \frac{\lambda_2}{\lambda_1} \frac{\partial B_i}{\partial v_1} \frac{\partial B_j}{\partial v_1} + \frac{1}{g_0(v_2, v_2)} \cdot \frac{\lambda_1}{\lambda_2} \frac{\partial B_i}{\partial v_2} \frac{\partial B_j}{\partial v_2} \right) dA_0 \end{aligned}$$

On one hand, the terms $\frac{1}{g_0(v_1, v_1)} \frac{\partial B_i}{\partial v_1} \frac{\partial B_j}{\partial v_1}$ and $\frac{1}{g_0(v_2, v_2)} \frac{\partial B_i}{\partial v_2} \frac{\partial B_j}{\partial v_2}$ only depend on the values of the partial derivatives of the basis function B_i along directions that are unit-length under the initial metric g_0 , so their values remain stable during the flow. On the other hand, the stretch ratios $\frac{\lambda_1 \lambda_2}{\lambda_1 \lambda_1}$ and $\frac{\lambda_1 \lambda_2}{\lambda_2 \lambda_2}$ can tend to infinity when the embedding map Φ_t becomes less and less conformal with respect to the initial metric g_0 .

1.3.3. Conformalized Mean Curvature Flow. The idea for the formulation of the conformalized Mean Curvature Flow is to replace the metric g_t with a metric \tilde{g}_t that is conformal to the initial metric g_0 , i.e. a *conformalized metric*

$$\tilde{g}_t := \sqrt{|g_0^{-1} \cdot g_t|} g_0$$

The corresponding linear map $\Lambda: T\Phi_0(p) \mapsto T\Phi_1(p)$ between tangent planes of Φ_0 and Φ_1 have two equal eigenvalues $\tilde{\lambda}_1 = \tilde{\lambda}_2$ since \tilde{g}_t is conformal to g_0 . Moreover, the conformalized metric \tilde{g}_t has the same determinant as the old metric g_t :

$$|\tilde{g}_t| = \left(\sqrt{|g_0^{-1} \cdot g_t|} \right)^2 \cdot |g_0| = |g_t|$$

This gives $\tilde{\lambda}_1 \tilde{\lambda}_2 = \lambda_1 \lambda_2$. Hence $\tilde{\lambda}_1 = \tilde{\lambda}_2 = \sqrt{\lambda_1 \lambda_2}$.

The coefficients of the mass matrix D_{ij}^t remains the same using the conformalized metric \tilde{g}_t and the coefficients of the stiffness matrix L_{ij}^t becomes independent of time t since

$$\begin{aligned}\tilde{L}_{ij}^t &= \int_M \left(\frac{1}{g_0(v_1, v_1)} \cdot \frac{\tilde{\lambda}_2}{\tilde{\lambda}_1} \frac{\partial B_i}{\partial v_1} \frac{\partial B_j}{\partial v_1} + \frac{1}{g_0(v_2, v_2)} \cdot \frac{\tilde{\lambda}_1}{\tilde{\lambda}_2} \frac{\partial B_i}{\partial v_2} \frac{\partial B_j}{\partial v_2} \right) dA_0 \\ &= \int_M \left(\frac{1}{g_0(v_1, v_1)} \cdot \frac{\partial B_i}{\partial v_1} \frac{\partial B_j}{\partial v_1} + \frac{1}{g_0(v_2, v_2)} \cdot \frac{\partial B_i}{\partial v_2} \frac{\partial B_j}{\partial v_2} \right) dA_0 = L_{ij}^0\end{aligned}$$

Replace the metric g_t with the conformalized metric \tilde{g}_t in the mean curvature flow, we get the **conformalized mean flow** (cMCF). Let $\Phi_t: M \rightarrow \mathbb{R}^3$ be a smooth family of immersions with time $t \geq 0$ and the induced metric g_t at time t . cMCF is defined as

$$(1.9) \quad \frac{\partial \Phi_t}{\partial t} = \sqrt{|g_0||g_t|^{-1}} \Delta_{g_0} \Phi_t$$

Note that if the map Φ_t is conformal with respect to the initial metric g_0 , $\Delta_{g_t} = \sqrt{|g_0||g_t|^{-1}} \Delta_{g_0}$. Then the cMCF becomes the MCF.

The corresponding discretized cMCF using the finite element method is

$$(1.10) \quad (D^t - \tau L^0) \vec{X}(t + \tau) = D^t \vec{X}(t)$$

While the mass matrix D^t is updated at every step, the initial stiffness matrix L^0 is used and remains the same during the flow.

1.3.4. Metrics to measure discrete conformality and sphericity. Here are two metrics to measure discrete conformality:

(I). Angular distortion associated to each triangle,

$$\max_{\theta=\alpha,\beta,\gamma} \left(\frac{|\theta - \theta'|}{\theta} \right)$$

where α, β, γ are the three angles in a triangle and α', β', γ' are the transformed angles. The value 0 implies no angular distortion.

We measure the angular distortion for all triangles and compute the mean value.

(II). Deviation of the *length-cross-ratio* (lcr) associated to each edge: the lcr of an edge e_{ij} is defined to be, see figure (1.16),

$$\mathfrak{c}_{ij} = \frac{\ell_{im} \cdot \ell_{jk}}{\ell_{mj} \cdot \ell_{ki}}$$

We let \mathfrak{c}_{ij} denote the lcr of the original edge and \mathfrak{c}'_{ij} denote the lcr of the transformed edge. **Two meshes are conformally equivalent if and only if $\mathfrak{c}_{ij} = \mathfrak{c}'_{ij}$ for all edges e_{ij}** [BPS15]. This is equivalent to $\frac{\mathfrak{c}'_{ij}}{\mathfrak{c}_{ij}} = 1$.

We measure the ratio of the lcr $\frac{\mathfrak{c}'_{ij}}{\mathfrak{c}_{ij}}$ associated to all edges and compute the mean value.

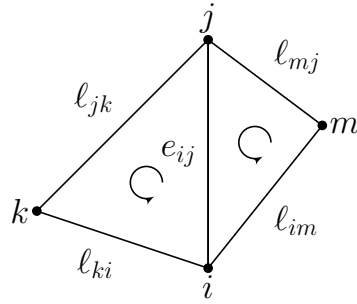


FIGURE 1.16. length-cross-ratio of edge e_{ij}

In addition, we use the dimensionless number $s = \frac{(36\pi V^2)^{\frac{1}{3}}}{A}$ to measure the sphericity, where V and A are the volume and the total surface area of the mesh respectively.

Clearly, $0 \leq s \leq 1$ and $s = 1$ implies if and only if the given surface is a sphere.

CHAPTER 2

Improvement on conformalized mean curvature flow

In this chapter, we study the behavior of the conformalized mean curvature flow (cMCF). In Section 1, we apply the flow to mesh with simple geometry such as a sphere and ellipsoids. There are strong experimental evidences demonstrating that meshes with protrusions further elongates under the flow until it converges to a unit sphere. Then, we discuss the numerical issues caused by this behavior of further elongation of meshes. In section 2, we introduce an initialization step that gives a spherical parametrization of the input mesh and demonstrate the use of cMCF to obtain a conformal spherical parametrization. This enhanced procedure can be applied to meshes that the original cMCF procedure cannot handle. We provide results from numerical experiments in which we test our algorithm on a wide variety of meshes. In section 3, we give a new algorithm named "Sphericalized cMCF" using cMCF to construct a homotopy of an arbitrary degree one map to a homeomorphism from a unit sphere to itself. We demonstrate the use of this algorithm using Gauss map applied on closed genus-zero surfaces as a degree one map. Finally, in section 4, we investigate a different discretization of the Laplace-Beltrami operator involved in the cMCF in order to stabilize the flow.

2.1. Flow behaviors and limitations

To begin with, we stated in the introduction chapter (1) that the cMCF is identical to the mean curvature flow (MCF) when it is applied on a sphere. It is because the embeddings of a sphere under the MCF is conformal, i.e. a sphere under MCF is to shrink towards its center until the sphere collapses into a point. Since we keep the surface area of the mesh constant in our cMCF implementation, a unit sphere should remain unchanged regardless of how many iterations are performed. We would like to verify it experimentally. Below are two meshes of a unit sphere with different mesh sizes.

Since the valences of most vertices are either 5 or 6, the number of edges and faces, $|E| \sim 3|V|$, $|F| \sim 2|V|$, can be computed by the Euler formula. Also, one measure for the mesh quality is to compute the statistics of distribution of maximal and minimal angles in all triangles. If sphere

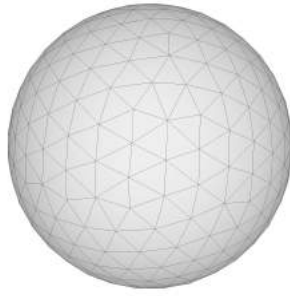


FIGURE 2.1. Sphere 1 with
 $|V| \approx 500$

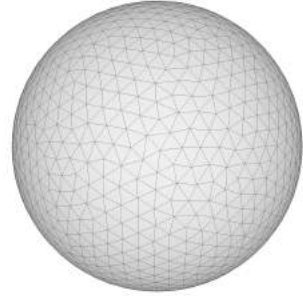


FIGURE 2.2. Sphere 2 with
 $|V| \approx 2k$

1 is uniformly triangulated by equilateral triangles, the expected area of each triangle should be $4\pi/|F| \approx 1.3e - 2$ units. The maximal and minimal area of the triangle differ only with 15% and 7%. These statistics showed that these spherical meshes have *almost all equilateral triangles* and are *uniformly triangulated*.

Sphere 1	mean μ	std σ
max. ang.	67°	5°
min. ang.	55°	3°
	max.	min
area	1.5e-02	1.2e-02

Sphere 2	mean μ	std σ
max. ang.	68°	5°
min. ang.	54°	4°
	max.	min
area	4.1e-03	3.0e-03

Moreover, we obtain two more meshes of a unit sphere by performing *barycentric subdivision* on the above spherical meshes. The number of vertices is scaled by $|V| + |F| \sim 3|V|$ from the original sphere. Our expected mean for the maximal and minimal angles are 120° and 30° respectively.

Subdivided sphere 1	mean μ	std σ
max. ang.	120°	6°
min. ang.	29°	3°

Subdivided sphere 2	mean μ	std σ
max. ang.	120°	7°
min. ang.	30°	3°

Now we apply cMCF to these spherical meshes. We run $2^6 = 64$ steps of iteration. The spherical meshes, sphere 1 and its subdivided mesh, stay spherical throughout the iterations, as indicated in the following plot of sphericity. It is the same result for sphere 2. Furthermore, it is independent of the step size chosen, i.e. any values of τ in the range from $1e - 6$ to 0.1.

As for the change in conformality, the average length-cross-ratio is constantly (almost) equal to 1 (≈ 0.999 in actual data). we also show the basic statistics for the distribution of the maximal angular distortion in all triangles. There is barely any angular change in each piece of trianlge.

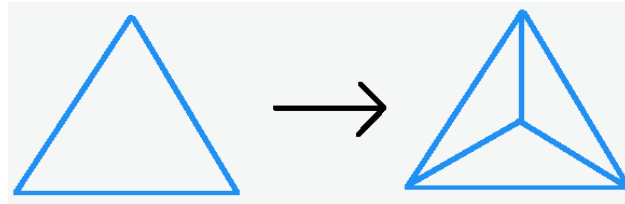


FIGURE 2.3. Barycentric subdivision

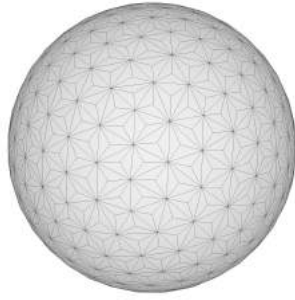


FIGURE 2.4. Subdivided sphere 1 with $|V| \approx 1.5k$

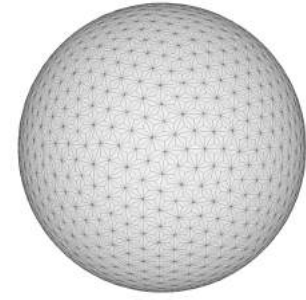
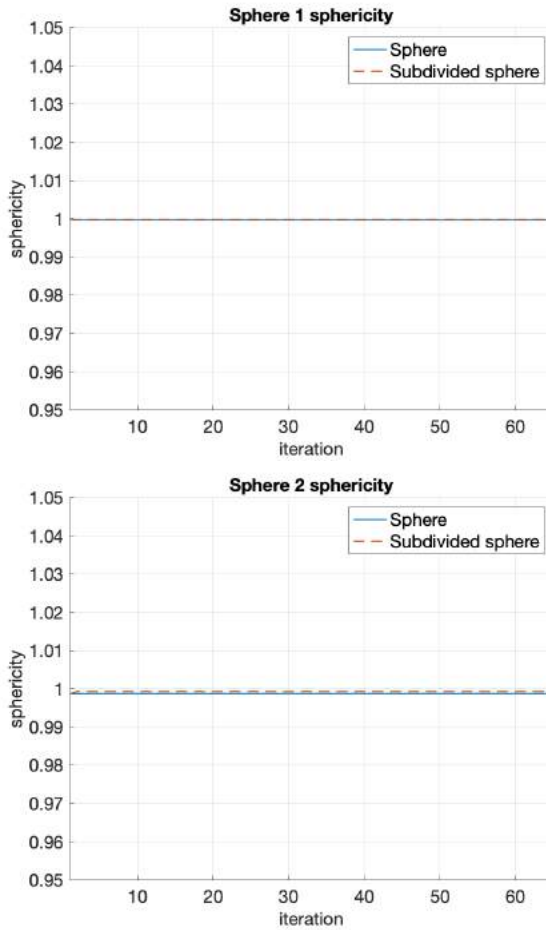


FIGURE 2.5. Subdivided sphere 2 with $|V| \approx 5.5k$



	mean μ	std σ
Sphere 1	1.4e-4	1.1e-8
Subdivided sphere 1	2.0e-4	1.2e-8
Sphere 2	4.2e-4	1.2e-7
Subdivided sphere 2	6.9e-4	1.3e-7

TABLE 2.3. Maximal ratio of angular distortion

These data show that *a spherical mesh remains unchanged under the cMCF, independent of its mesh sizes and mesh quality.* This confirms the derivation of the cMCF in the continuous case.

2.1.1. Ellipsoids and numerical issues. Next, we look at a set of ellipsoids with different radii. Ellipsoid has simple geometry but can shed light on the behavior of meshes under the cMCF. We keep two of the three semi-axes in the ellipsoid constant, say 1 unit, and we vary the value of the remaining semi-axis, denoted by r .

Again, these statistics on the maximal and minimal angles and the area of triangles show that these ellipsoidal meshes have *almost all equilateral triangles* and are *uniformly triangulated*. Also, We apply the same subdivision procedure to these ellipsoids as in the case of spheres.

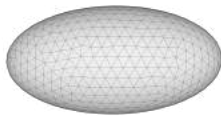


FIGURE 2.6. $r = 2$
with $|V| = 780$



FIGURE 2.7. $r = 4$
with $|V| \approx 1.4k$



FIGURE 2.8. $r = 8$
with $|V| \approx 2.6k$



FIGURE 2.9. $r = 16$ with $|V| \approx 5.2k$



FIGURE 2.10. $r = 24$ with $|V| \approx 7.6k$



FIGURE 2.11. $r = 32$ with $|V| \approx 10k$

ellipsoids	mean μ	std σ
$r = 2$	67°	5°
$r = 4$	67°	5°
$r = 8$	66°	4°
$r = 16$	66°	4°
$r = 24$	65°	3°
$r = 32$	65°	3°

(A) Maximal angle

ellipsoids	mean μ	std σ
$r = 2$	54°	3°
$r = 4$	54°	3°
$r = 8$	55°	3°
$r = 16$	55°	3°
$r = 24$	56°	3°
$r = 32$	56°	3°

(B) Minimal angle

ellipsoids	max. area μ	min. area
$r = 2$	1.5e-02	1.2e-02
$r = 4$	1.7e-02	1.2e-02
$r = 8$	1.8e-02	1.1e-02
$r = 16$	1.8e-02	1.1e-02
$r = 24$	1.8e-02	1.1e-02
$r = 32$	1.8e-02	1.2e-02

TABLE 2.5. Area of triangles

subdivided ellipsoids	mean μ	std σ
$r = 2$	120°	6°
$r = 4$	120°	6°
$r = 8$	120°	5°
$r = 16$	120°	5°
$r = 24$	120°	4°
$r = 32$	120°	6°

(A) Maximal angle

subdivided ellipsoids	mean μ	std σ
$r = 2$	29°	3°
$r = 4$	29°	3°
$r = 8$	29°	3°
$r = 16$	29°	3°
$r = 24$	29°	2°
$r = 32$	29°	2°

(B) Minimal angle

subdivided ellipsoids	max. area μ	min. area
$r = 2$	5.1e-3	3.9e-3
$r = 4$	5.6e-3	3.8e-3
$r = 8$	5.9e-3	3.8e-3
$r = 16$	6e-3	3.8e-3
$r = 24$	5.9e-3	3.8e-3
$r = 32$	5.9e-3	4.1e-3

TABLE 2.7. Area of triangles

We apply cMCF to these ellipsoid meshes. We run $2^9 = 512$ steps with a fixed step size $\tau = 0.01$.

The sphericity first tends to worsen, then slowly increases again and eventually converges to one. That suggests that *an ellipsoid is first deformed into an even less spherical object and then converges back to a sphere*. Also, the sphericity evolution of the ellipsoids and their counterparts of worse mesh quality through barycentric subdivisions are identical (the solid lines and the dashed lines overlap on top of each other). Therefore, *the behavior of ellipsoids under cMCF observed here is attributed to its geometry and this behavior is independent of the mesh quality*.

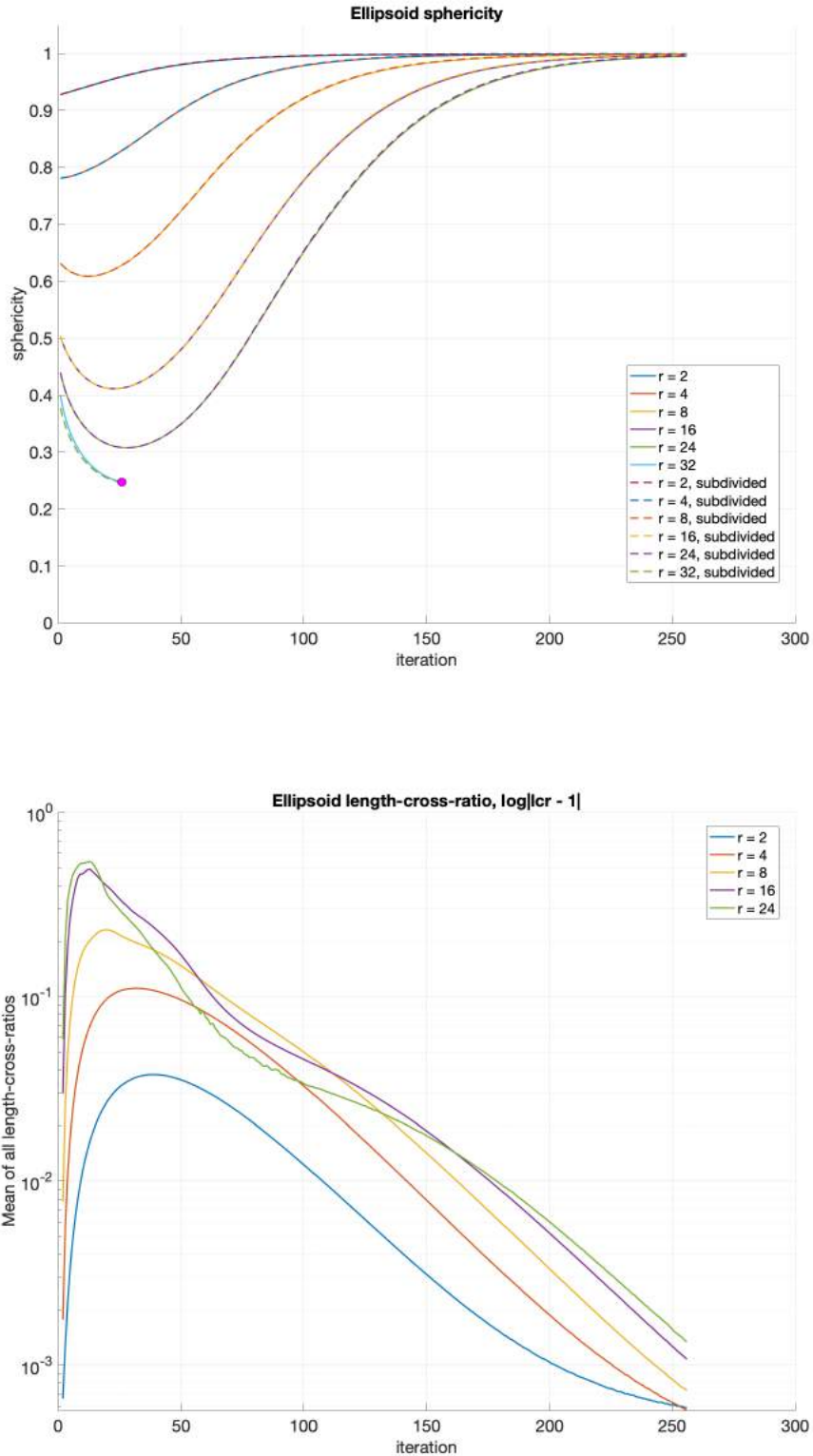
In terms of the discrete conformality, the length-cross-ratios of the ellipsoids and their counterparts of worse mesh quality have similar behavior despite their difference in magnitude. While the sphericity decreases, the mean of all length-cross-ratio deviates largely from one. This implies that the intermediate shapes under the cMCF are not discrete conformal to the original ellipsoids. As the cMCF converges, the mean of the length-cross-ratio converges to one. Both the mean of the length-cross-ratio and that of the angular distortion ratio confirm that the resulting sphere is discrete conformal to the ellipsoids.

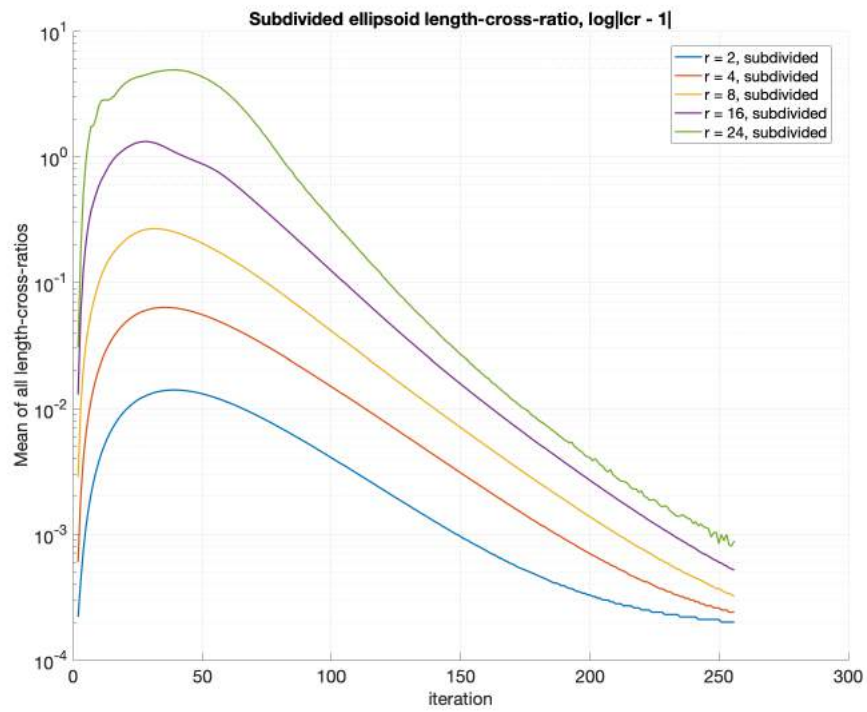
Ellipsoids	mean μ	std σ	subdivided ellipsoids	mean μ	std σ
$r = 2$	4.0e-2	1.9e-4	$r = 2$	4.2e-2	2.6e-4
$r = 4$	7.2e-2	4.7e-4	$r = 4$	7.5e-2	6.8e-4
$r = 8$	9.0e-2	6.3e-4	$r = 8$	9.6e-2	1.1e-3
$r = 16$	0.10	1e-3	$r = 16$	0.10	2e-3
$r = 24$	0.10	1e-3	$r = 24$	0.11	2e-3

TABLE 2.8. Maximal ratio of angular distortion

Numerical issue For the ellipsoid of $r = 32$, we stopped the cMCF flow of the ellipsoid after the first 30 iterations due to numerical problems. There are degenerate triangles forming in the mesh, in which triangles are collapse into a point. The calculations of their edge length and area are no longer possible due to precision limit. *The cMCF cannot be applied into this extreme case*

without running into numerical errors. We will describe our strategy to enhance the performance of cMCF in such case in the following section.





Here are front views (looking at the tip) of the ellipsoid of $r = 8$ and its deformation at 12th step.

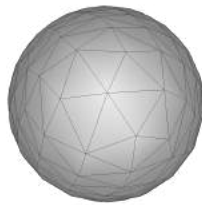


FIGURE 2.12. Initial $r = 8$

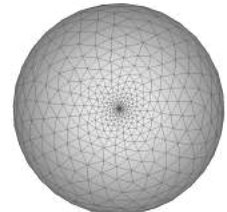


FIGURE 2.13. $r = 8$ after 12 iterations

Here are side views of the ellipsoid of $r = 16$ and its deformation at 20th step and close-ups.



FIGURE 2.14. Initial $r = 16$



FIGURE 2.15. $r = 16$ after 20 iterations

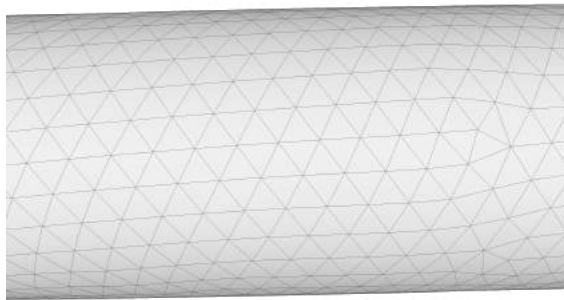


FIGURE 2.16. Initial $r = 16$



FIGURE 2.17. $r = 16$ after 20 iterations

From the different views of the ellipsoids during the cMCF shown above, we observe that the triangles at the tip of ellipsoid are squeezed into very tiny triangles whereas the triangles in the long body of the ellipsoids are being stretched into thin and long triangles. These can be explained by the fact that the initial ellipsoid tip has the highest curvature and hence the conformal factor of mapping this region onto a sphere is the largest. *The ellipsoids are being further elongated before it converges to a sphere that is discrete conformal to the initial shape.* The further elongation results in the thin and long triangles in the ellipsoid during the evolution. The front view and the side view of the resulting sphere from the cMCF (ellipsoid of $r = 4$ shown) also confirm this observation.

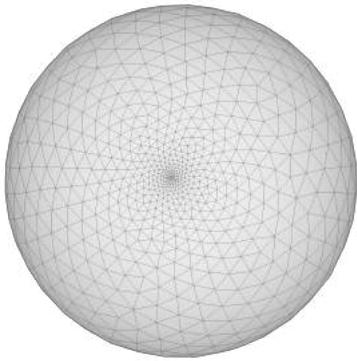


FIGURE 2.18. Front view of resulting sphere

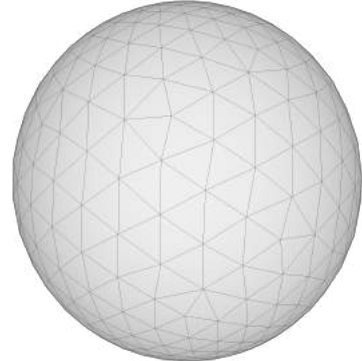


FIGURE 2.19. Side view of resulting sphere

2.1.2. Elongation of meshes under cMCF. In the previous section, the experimental data that the ellipsoid meshes first elongate further before converging to a unit sphere which is discretely conformal to the original mesh. We want to verify that such behavior is not limited to ellipsoids but to any long cylindrical meshes or meshes that have protrusions. Here are some examples.

The mesh of the Gyroscope's axle consists of a octagonal cylinder with octagonal pyramids on both ends. The mesh of the Rod consists of a cylinder with semi-spheres on both ends. The mesh of the Rod with grooves consists of a rectangular bar with semi-circular ridges distributed in a evenly spaced fashion on the top. *All these meshes are topologically equivalent to a sphere* since $|V| - |E| + |F| = 2$ which implies that the meshes have genus zero.

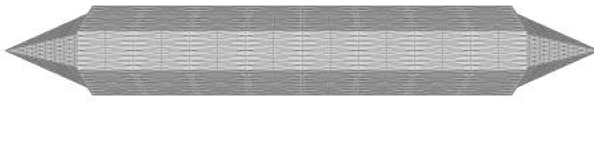


FIGURE 2.20. Gyroscope's axle,
 $|V| \approx 3.5k$



FIGURE 2.21. Semi-cylinder, $|V| \approx 6k$



FIGURE 2.22. Rod, $|V| \approx 20k$

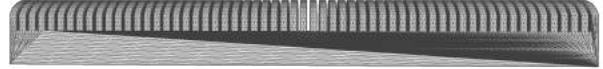


FIGURE 2.23. Rod with grooves,
 $|V| \approx 54k$

We run $2^9 = 512$ steps with fixed step size $\tau = 0.01$. Regardless of how the step size is chosen between $[0.1, 1e - 4]$, the behavior of the sphericity and the mean length-cross-ratio of the meshes are similar.

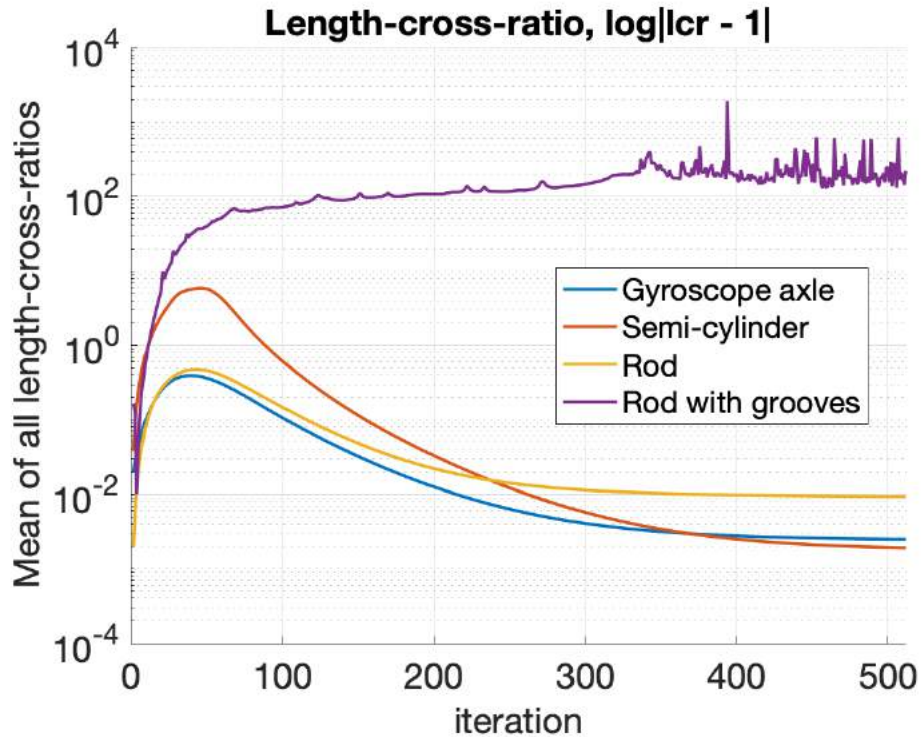
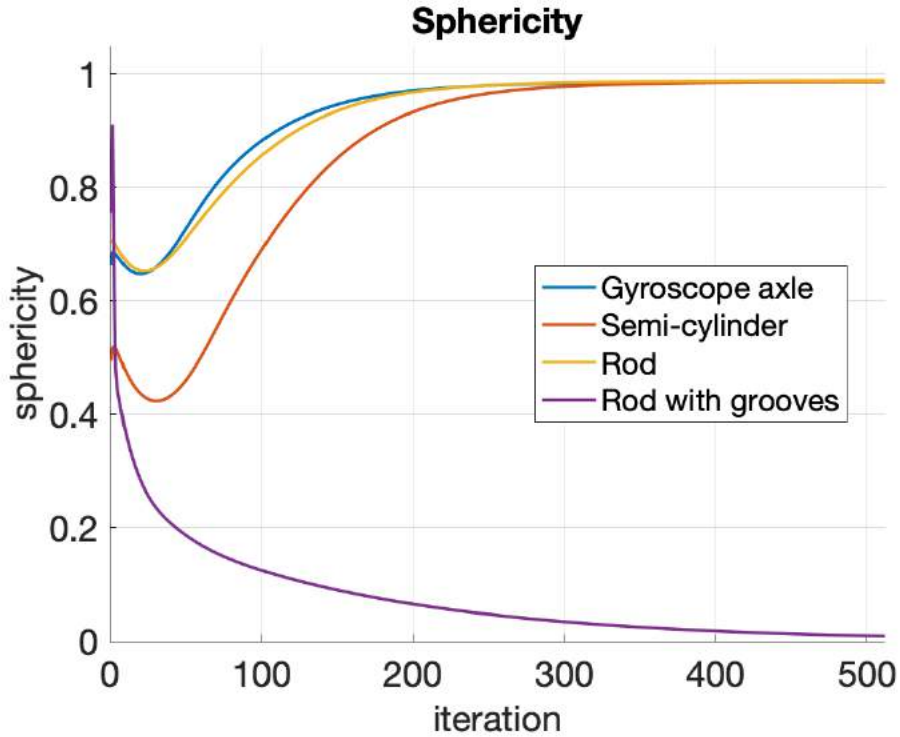
The Gyroscope's axle, semi-cylinder, and Rod all first further stretch along the direction of their protrusion, then get rounder and eventually converge to a unit sphere. The length-cross-ratio shows that the discrete conformality improves steadily while the meshes converging to a unit sphere. The Rod with grooves fails to converge under the cMCF. The mesh got stretched infinitely into a thin line. We show here the evolution of the mesh after 10 and 20 iterations.



FIGURE 2.24. Rod with grooves,
10th step



FIGURE 2.25. Rod with grooves,
20th step



2.1.3. Robustness. Despite the limitations and drawbacks described in previous section, the cMCF is relatively robust when applied on meshes with no significant protrusions. In this case,

robustness means that the further elongation of meshes are not noticeable. Here we present a set of meshes with a wide variety of geometries:

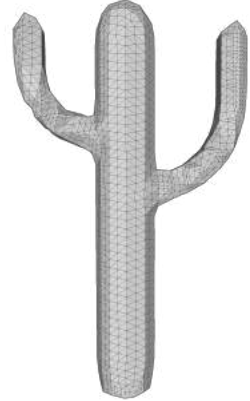


FIGURE 2.26. cactus, $|V| \approx 2.4k, |F| \approx 5k$

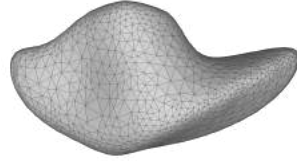


FIGURE 2.27. blobby, $|V| \approx 2k, |F| \approx 4k$

cactus	mean μ	std σ
max. ang.	83°	10°
min. ang.	41°	8°
	max.	min
area	5.9e-3	6.1e-4

blobby	mean μ	std σ
max. ang.	77°	13°
min. ang.	47°	9°
	max.	min
area	2e-2	1.6e-4

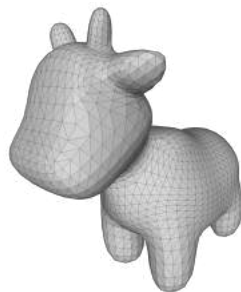


FIGURE 2.28. spot, $|V| \approx 3k, |F| \approx 6k$

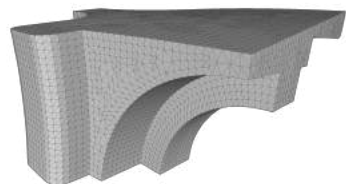


FIGURE 2.29. fandisk, $|V| \approx 6k, |F| \approx 12k$

spot	mean μ	std σ
max. ang.	84°	9°
min. ang.	38°	9°
	max.	min
area	8.8e-3	5.4e-5

fandisk	mean μ	std σ
max. ang.	86°	7°
min. ang.	44°	4°
	max.	min
area	5.3e-3	1.1e-4

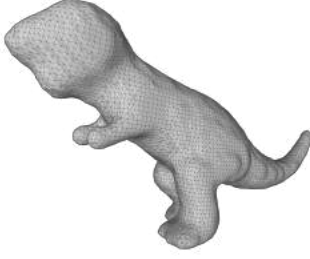


FIGURE 2.30. dinosaur, $|V| \approx 10k, |F| \approx 20k$



FIGURE 2.31. human, $|V| \approx 9k, |F| \approx 18k$

dinosaur	mean μ	std σ
max. ang.	84°	14°
min. ang.	42°	9°
	max.	min
area	1.3e-3	9.3e-5

human	mean μ	std σ
max. ang.	83°	13°
min. ang.	43°	8°
	max.	min
area	1.4e-3	5.4e-5

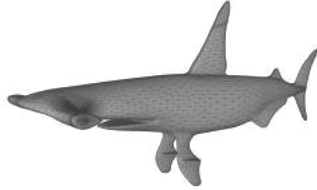


FIGURE 2.32. shark, $|V| \approx 10k, |F| \approx 20k$

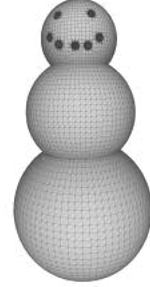


FIGURE 2.33. snowman, $|V| \approx 15k, |F| \approx 31k$

shark	mean μ	std σ
max. ang.	98°	18°
min. ang.	22°	13°
	max.	min
area	4.6e-3	5.4e-7

snowman	mean μ	std σ
max. ang.	91°	9°
min. ang.	33°	13°
	max.	min
area	3.6e-2	1.7e-8

We keep the surface area of all meshes to be 4π for the sake of comparison. The statistics on the maximal and minimal angles show that the meshes are not triangulated with equilateral triangles. The triangles tend to be obtuse at the sharp corners, like the fandisk or the fins of the shark, or at a tip with *large discrete curvature*, like the tips of the cactus or the ear of spot or the tip of the dinosaur's tail or the tip of the human's limbs.

Moreover, the size of the triangles can differ greatly. Except in the mesh of blobby where the maximal and minimal triangle areas are comparable, they can differ by a factor of 10 as in cactus up to 1e4 in shark or 1e6 in snowman. The triangles in the head of shark are much smaller than those in its body. The triangles are large on the bottom part of the snowman while the triangles on the snowman's face are very small.

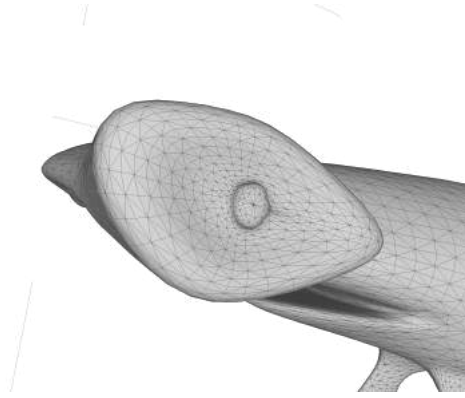


FIGURE 2.34. shark's head

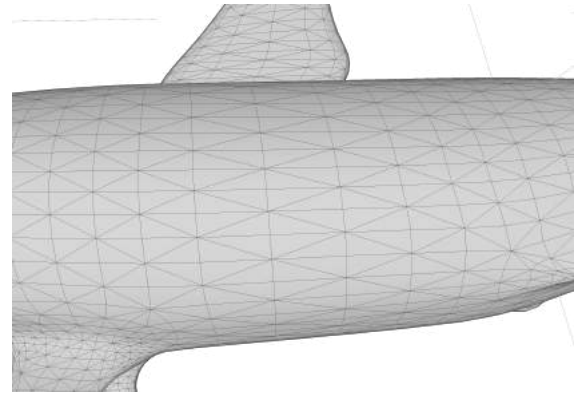


FIGURE 2.35. shark's body



FIGURE 2.36. Bottom part of snowman

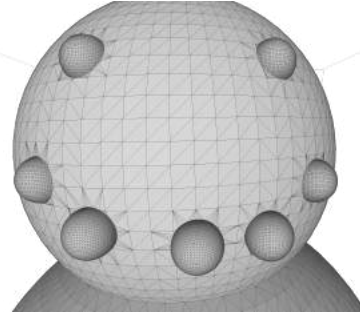


FIGURE 2.37. snowman's face

We run $2^8 = 256$ steps with fixed step size $\tau = 0.01$. Regardless of how the step size is chosen between $[0.1, 1e-4]$, the behaviors of the sphericity and the mean length-cross-ratio of the meshes are similar.

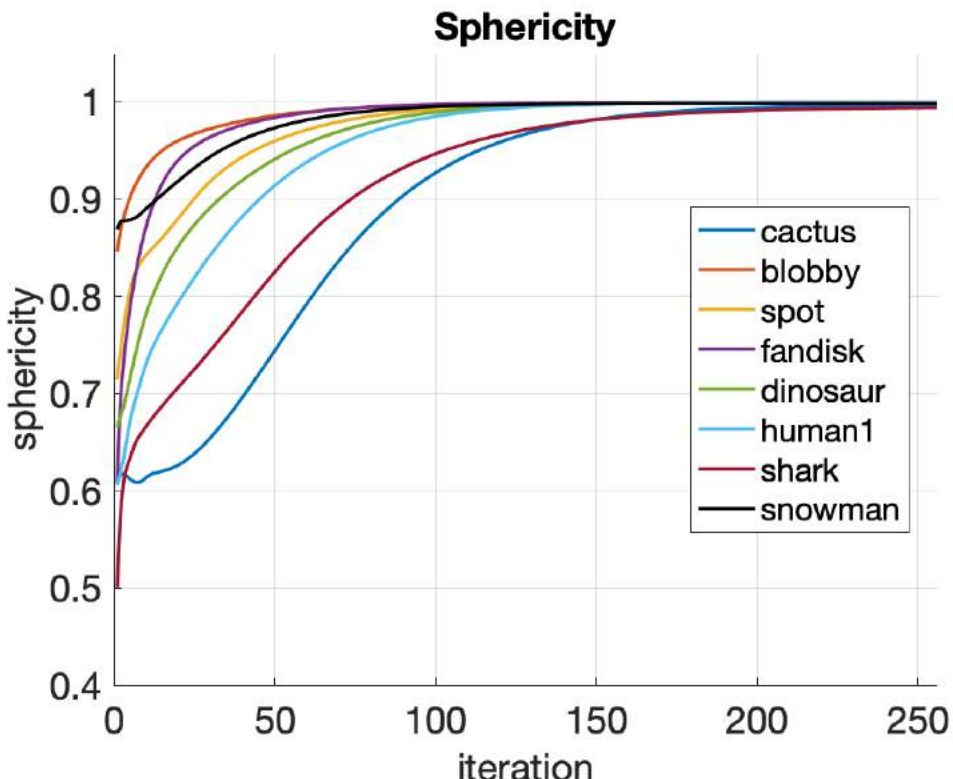
The sphericity of all the meshes increase monotonically. No unidirectional elongation of the mesh is observed. The gradients of all meshes except the snowman at the first few steps indicate a fast convergence to a sphere. The mean of the length-cross-ratio converges to one and the rates of

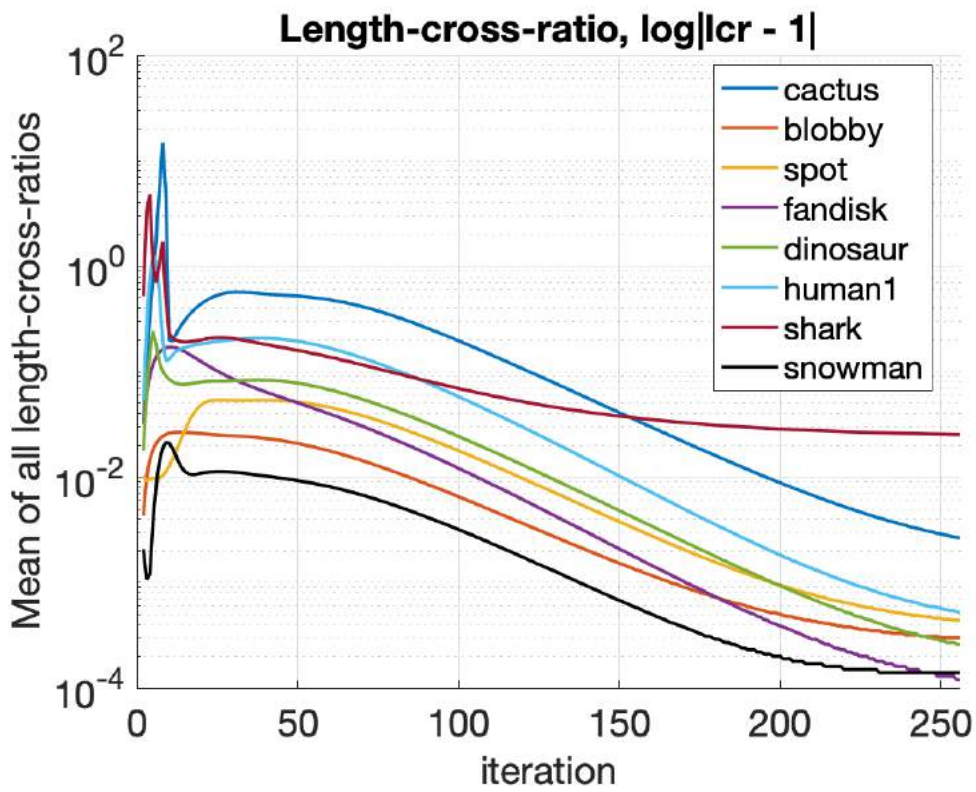
convergence are similar across all meshes. This fast convergence to a discrete unit sphere suggests the strong robustness of the cMCF when it is applied across a wide variety of meshes, except the long cylindrical meshes shown in the previous chapter.

Despite the large discrepancy in the maximal and minimal size of the triangles on the mesh as well as the discrepancy between the maximal and minimal angles in these triangles, the maximal ratios of angular distortion are less than 10% except cactus and shark. That can be explained by the large curvatures at the end of the branches of cactus and the same for the tips of the shark fins.

	mean μ	std σ
cactus	1.6e-1	6.4e-3
blobby	3.6e-2	5.7e-4
spot	8.5e-2	6.3e-3
fandisk	3.7e-2	1.2e-3
dinosaur	6.1e-2	1.9e-3
human	8.8e-2	4.8e-3
shark	1.9e-1	5.0e-2
snowman	3.3e-2	4.1e-4

TABLE 2.13. Maximal ratio of angular distortion





Note the regions with high conformal factors in the original mesh can still be recognized on the resulting sphere since they clearly show a high concentration of small triangle clusters:

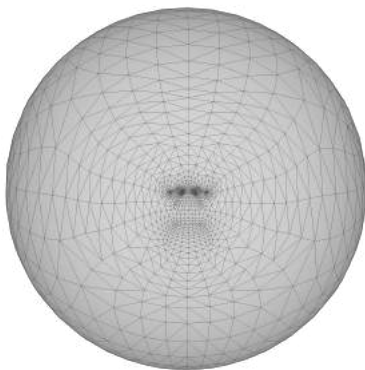


FIGURE 2.38. Front view of resulting sphere of spot

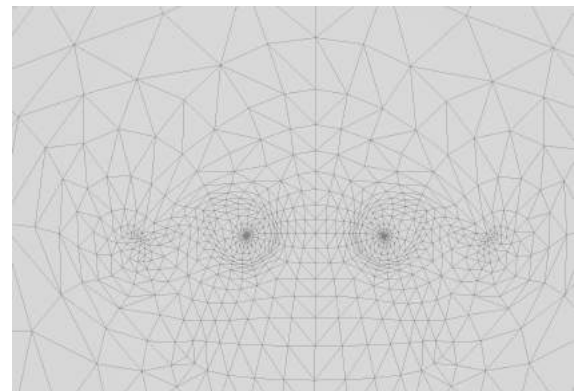


FIGURE 2.39. Ears and horns of spot on resulting sphere

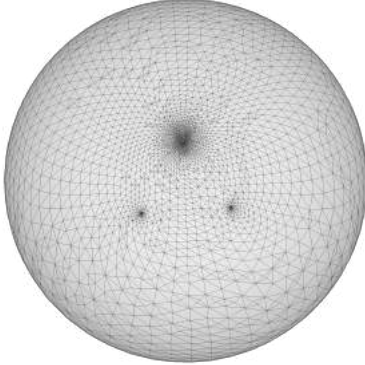


FIGURE 2.40. Front view of resulting sphere of dinosaur

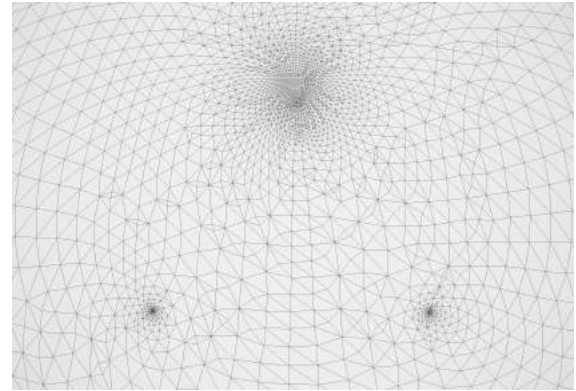


FIGURE 2.41. Head and hands of dinosaur on resulting sphere

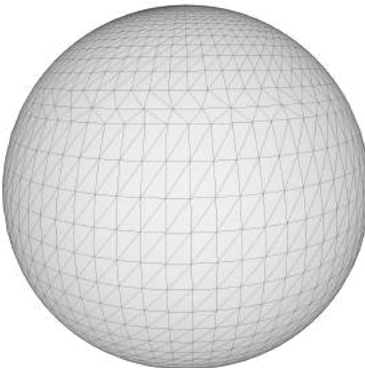


FIGURE 2.42. Front view of resulting sphere of snowman

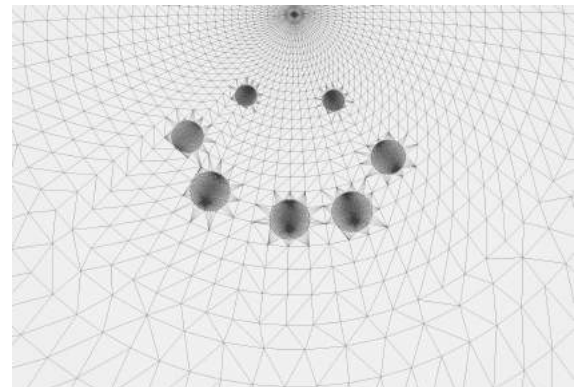


FIGURE 2.43. Eyes and mouth of snowman on resulting sphere

Another noticeable drawback of the cMCF is, namely that, if there is a flat area covered with triangles with large area on the original mesh, that part will remain relatively flat and noticeable on the surface of the converging sphere. This can be improved by performing triangulation subdivision specifically on that area. That enhances the sphericity of the resulting sphere.

We use the *midpoint subdivision* as it preserve the mesh quality by not creating even larger and smaller angles than in the existing meshes.



FIGURE 2.44. Midpoint subdivision



FIGURE 2.45. Original bot-
tom of snowman

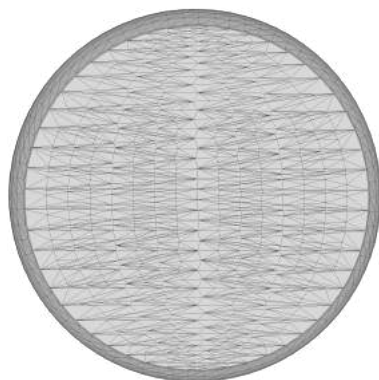


FIGURE 2.46. After mid-
point subdivision

	sphericity
snowman	0.99826
snowman with subdivision on the bottom	0.99946

TABLE 2.14. Improvement on sphericity of resulting sphere

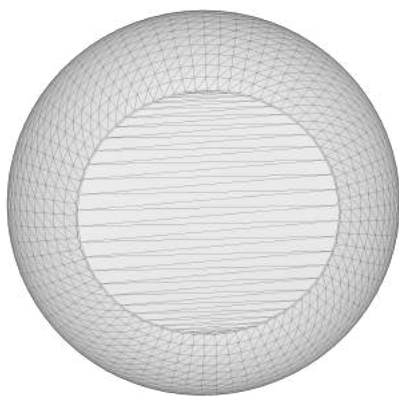


FIGURE 2.47. Bottom part
of resulting sphere of snow-
man.png

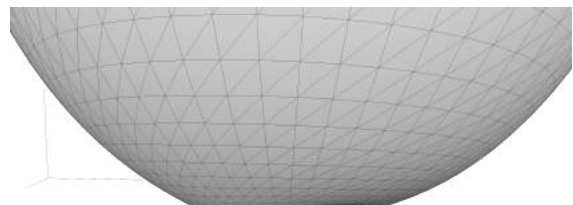


FIGURE 2.48. Side view

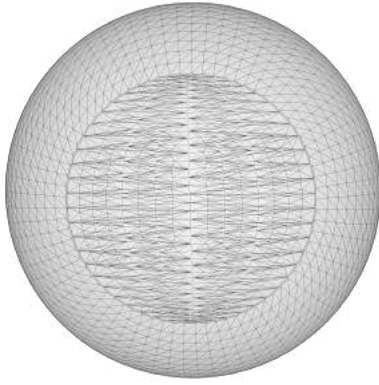


FIGURE 2.49. Bottom part
of resulting sphere of snow-
man.png

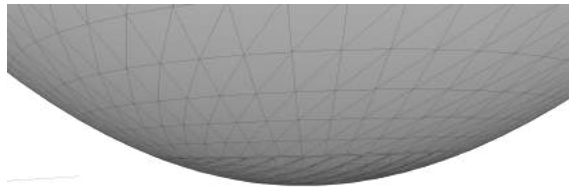
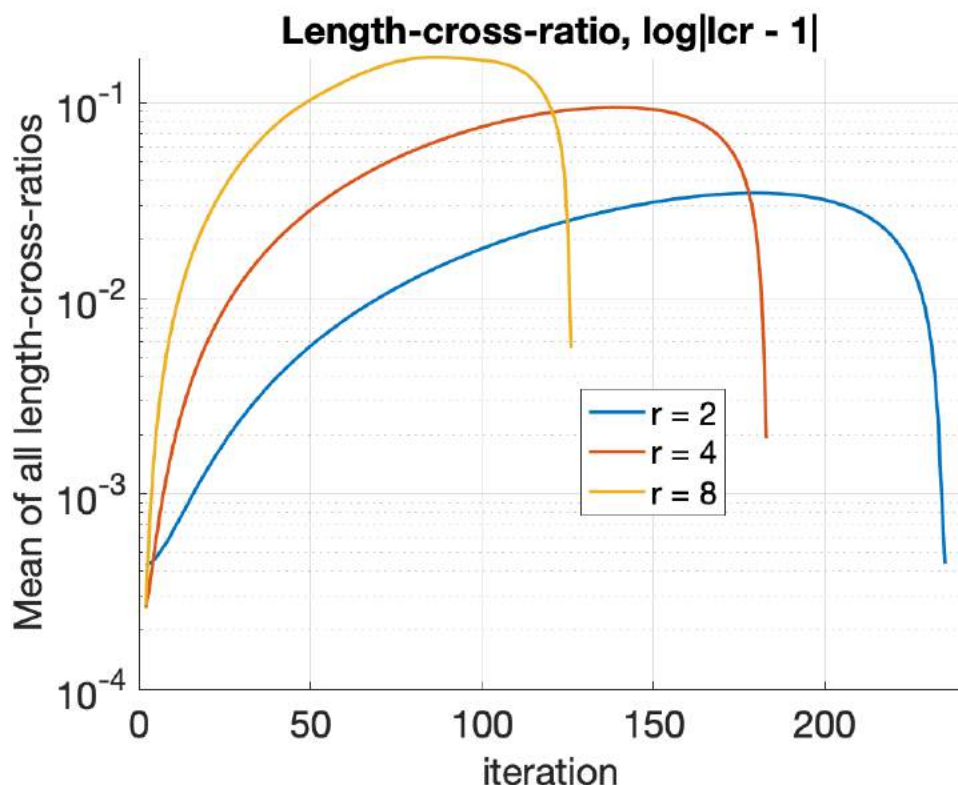
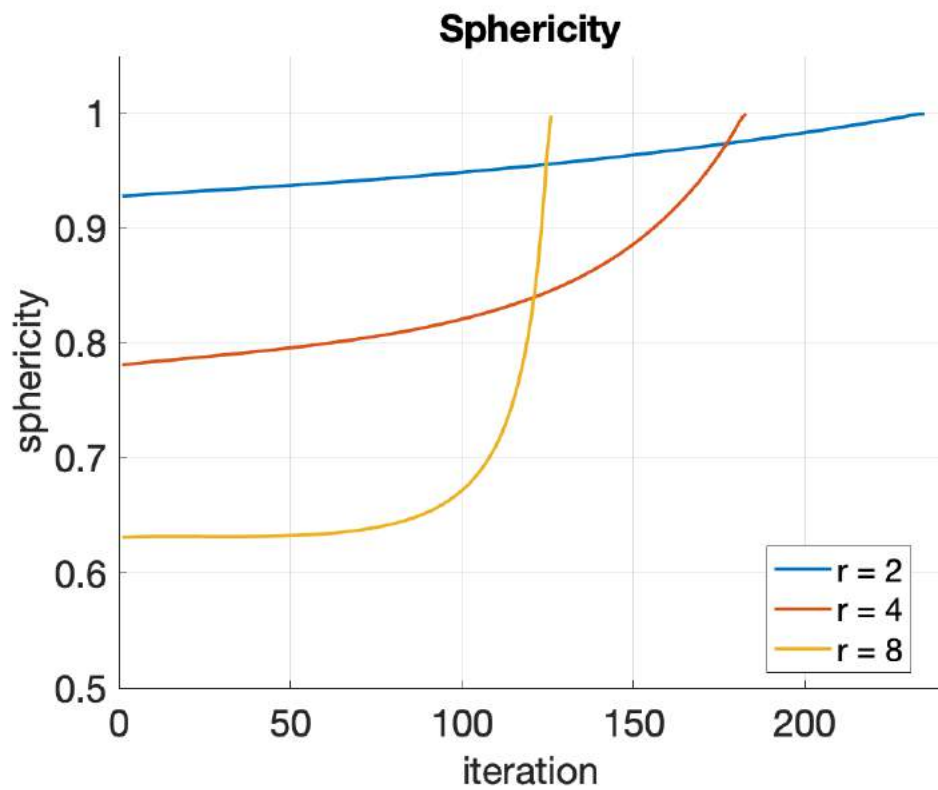


FIGURE 2.50. Side view

2.1.4. cMCF without area rescaling. As stated in the mathematical derivations in chapter 1, Kazhdan, Solomon, and Ben-Chen showed that the cMCF is a gradient flow guided by an energy functional consisting of a surface area functional and a conformality energy functional. Here we demonstrate with experimental evidence that *the surface area energy term is very dominant at the beginning of the flow leading to a steady decrease in surface area, but once the surface area gets small enough, the conformality energy term becomes dominant and minimizing the overall energy functional leads to a rapid convergence to a discrete conformal sphere.*

Without area rescaling, we apply cMCF on the ellipsoid meshes with $r = 2, 4, 8$ from the previous section with a time stepsize $\tau = 0.001$. We stop the run until the area of the mesh decreases beyond our precision limit. In such case, coordinates of vertices are so close to each other and cannot be recorded accurately. The area of some triangles become negative since the length of edges is not longer accurate due to precision errors.

Below are the plots for sphericity, conformality, and area of the meshes under cMCF. The evolutions of the sphericity and the mean of the length-cross-ratio shown are totally different than that under the cMCF with area rescaling. As the meshes contract to a point, the meshes become more spherical. *Once the area is small enough (as the meshes are shrinking to a point with accelerating rate), the conformality improves drastically within a few iterations before running into numerical issues.*



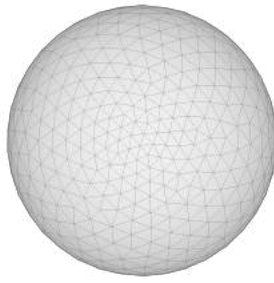
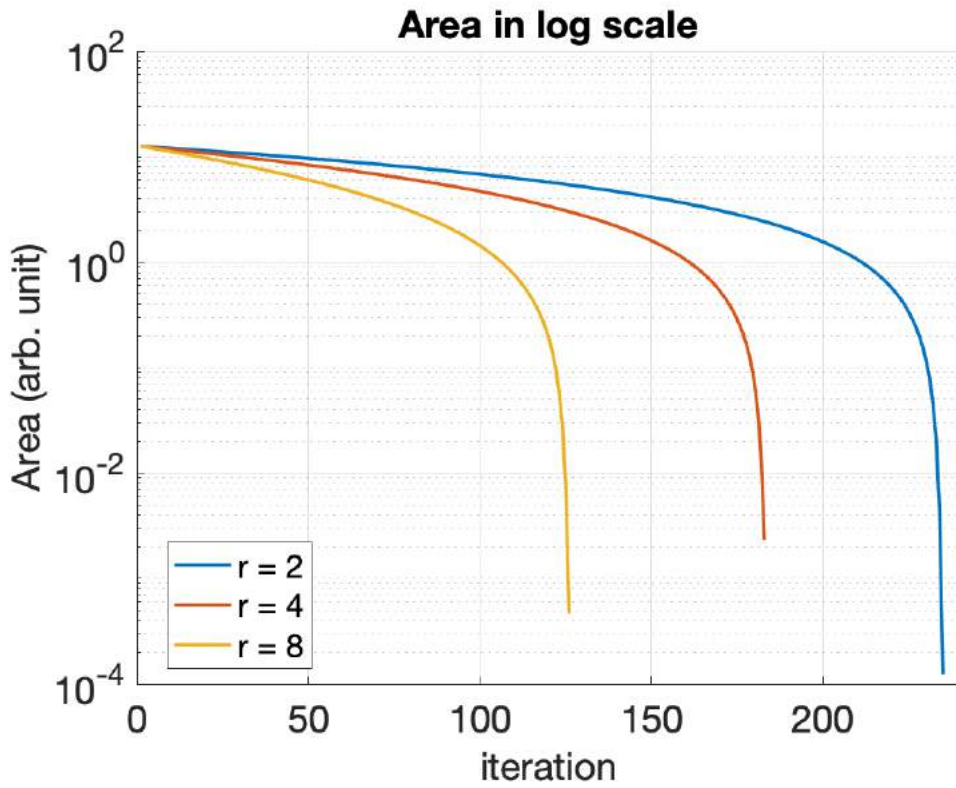


FIGURE
2.51. 234th
step of ellipsoid
 $r = 2$

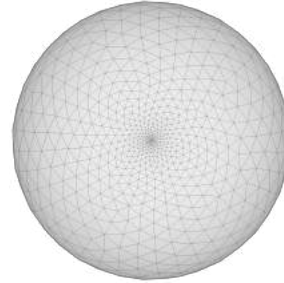


FIGURE
2.52. 182th
step of ellipsoid
 $r = 4$

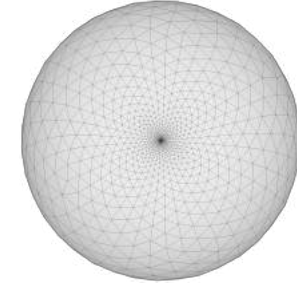


FIGURE
2.53. 125th
step of ellipsoid
 $r = 8$

Also, the conformality measures, both the mean of the length-cross-ratio and the maximal ratio of angular distortion, indicate a comparable level of discrete conformality to the original meshes as in the case of cMCF with area rescaling (after converging to a unit sphere).

Although the sphericity of the ellipsoid meshes does not first decrease and then increase as described in the previous section, cMCF without area rescaling is not a *practical* method to compute a discrete conformal map from a given mesh on to a sphere. It is in general very hard to control

ellipsoids	mean lcr after 512 steps
$r = 2$	1.000
$r = 4$	1.002
$r = 8$	1.006

(A) Mean of lcr without area rescaling

ellipsoids	mean lcr in the final step
$r = 2$	1.000
$r = 4$	1.000
$r = 8$	1.000

(B) Mean of lcr with area rescaling

ellipsoids	mean μ	std σ
$r = 2$	3.8e-2	2.9e-4
$r = 4$	8.3e-2	1.7e-4
$r = 8$	1.1e-1	2.0e-3

(A) Angular distortion without area rescaling

ellipsoids	mean μ	std σ
$r = 2$	4.0e-2	1.9e-4
$r = 4$	7.2e-2	4.7e-4
$r = 8$	9.0e-2	6.3e-4

(B) Angular distortion with area rescaling

the evolution of the mesh once its surface area decreases drastically and the flow does not converge afterwards. So we need to abruptly terminate the flow for each mesh on a case-by-case basis which makes this implementation impractical.

However, during the course of our investigation of cMCF, this observation from cMCF without area rescaling suggested the following idea (see figure 2.54): *in the discrete setting, suppose we first construct a function that maps the initial mesh onto a sphere and that function is not a discrete conformal map. Then we start the cMCF on the spherical mesh with respect to the metric of the original mesh (with area rescaling to keep surface area constant), will the spherical mesh continue to stay spherical while converging to a discrete conformal sphere?* If so, this modified procedure of cMCF would be a much more robust method to compute the desired discrete conformal map. A more important question is then *if this procedure is applicable to meshes in which the cMCF failed before.*

Our answers to both of these questions are affirmative. In summary, we apply an initialization consisting of Tutte embedding and an inverse stereographic projection to compute a function that maps an initial mesh onto a sphere, then we apply the cMCF on the spherical mesh using the discrete metric of the initial mesh with area rescaling.

2.2. Initialization procedure of cMCF using Tutte embedding

In this section, we introduce an initialization procedure to improve the performance of cMCF. Here we focus on the cMCF implementation applied to discrete surfaces rather than the PDE theory of cMCF applied on manifolds.

We are going to construct a function to map any genus-zero meshes onto a unit sphere and use cMCF as a tool to make the sphere discretely conformal to the original mesh. Given a mesh

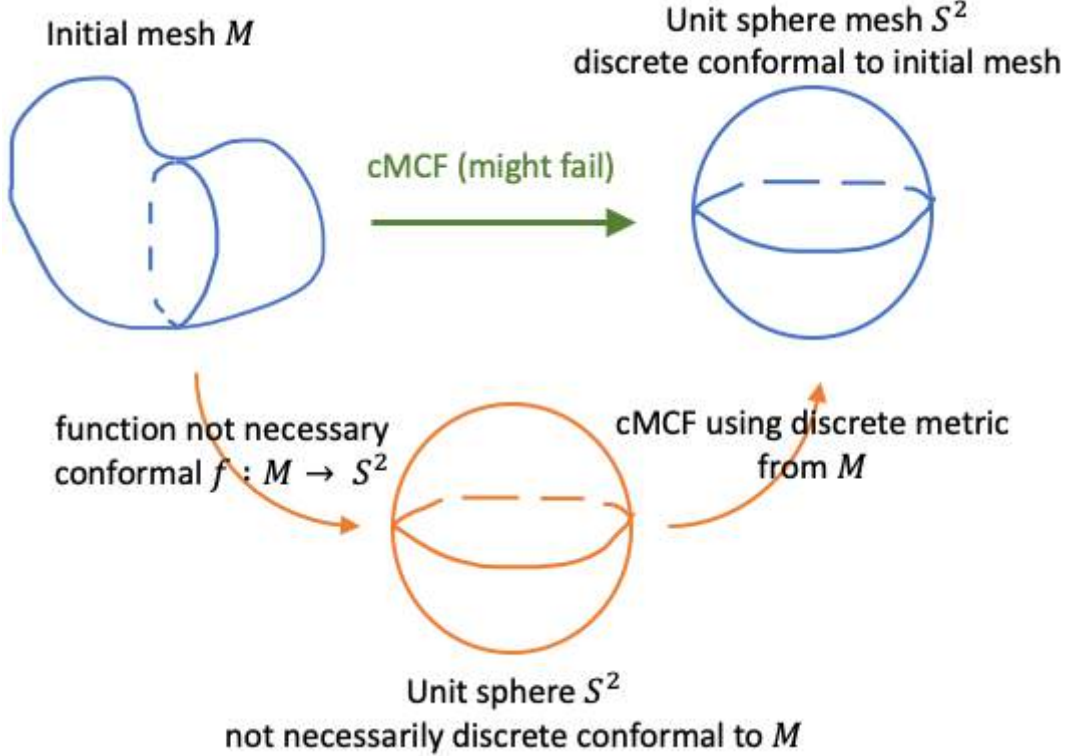


FIGURE 2.54. cMCF versus Modified procedure cMCF

approximating a closed surface of genus zero in \mathbb{R}^3 , we first transform it into a topological disk by removing one of its vertices and its associated 1-ring region. Then we apply Tutte embedding to “flatten” it into a convex polygonal region while maintaining the combinatorial information of the original mesh. Next, we map it onto a unit sphere via the inverse stereographic projection and add back the vertex removed earlier so that the mesh is again equivalent to a sphere topologically. Subsequently we apply a Möbius transformation on this spherical mesh such that its vertices spread evenly on the surface and position its center of mass to the origin. Finally, we initialize the cMCF using the original stiffness matrix (with cotangent weights) and a new mass matrix calculated from the triangulated sphere.

2.2.1. Tutte embedding. We begin with Tutte’s embedding theorem and then describe our exact implementation of the algorithm. Tutte’s theorem is a discrete version of the mean value property of continuous harmonic maps, i.e. the value at one point of this map is equal to the average of its neighboring values. Given a triangulation $T = (V, E, F)$ of a disk where the vertices and edges of T can be seen as a planar graph. Tutte [Tut63] proved that a 3-connected planar graph has a “nice” embedding in the plane in the sense that it can be drawn so that the boundary

of every face is a convex polygon and every edge is a straight line segment. To be concrete, Tutte's embedding requires specification of coordinates of the boundary vertices of T as the convex prescribed boundary and then finds the coordinates of the remaining vertices by solving a linear system of equations. We state the Tutte theorem using the formulation given by Floater [Flo03b]

THEOREM 2.2.1. *Suppose $T = (V, E, F)$ is a triangulation of a convex polygon and that $\varphi: D_T \rightarrow \mathbb{R}^2$ is a convex combination mapping which maps the the cyclically ordered boundary vertices v_1, \dots, v_n of T to the cyclically ordered vertices $\varphi(v_1), \dots, \varphi(v_n)$ of an n -sided convex polygon. Then φ is one-to-one.*

2.2.2. Implementation and algorithm. First, we remove one vertex from the initial mesh. There are many different choices we can make to select this vertex. A common way is remove the vertex with the largest curvature. Over many numerical experiments we have done, the choice of vertex does not affect the robustness of our mapping onto the sphere. Also, the numbering of vertices and the associated combinatorial information in our data structure (using OpenMesh) would change if any but the last vertex is removed. Therefore, we remove the last vertex in a given mesh, as listed in its .off, .stl, .obj, or .ply file depending on its mesh file format.

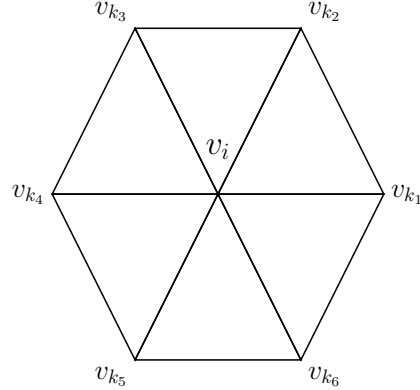


FIGURE 2.55. 1-ring region of vertex v_i includes vertex v_i and all edges and faces adjacent to it

Given that our initial input mesh $T = (V, E, F)$ represents a closed surface S of genus zero, i.e. $|V| - |E| + |F| = \chi(S) = 2$. Suppose that a vertex of valence k and its associated 1-ring region are removed, the resulting mesh has a “hole” and is topologically equivalent to a disk. One way of verifying this is by the Euler formula:

$$(|V| - 1) - (|E| - k) + (|F| - k) = |V| - |E| + |F| - 1 = 1$$

which matches with the Euler characteristic of a disk. Furthermore, the library *OpenMesh* provides a command `.is_trimesh` to effectively verify that the resulting mesh is still a proper triangulation.

Then we apply Tutte embedding to map the resulting mesh onto a convex polygon. The boundary vertices of the polygon are exactly those adjacent to the one vertex we removed, i.e. vertices v_{k_j} for $j = 1, 2, \dots, 6$ as shown in the above figure. Our algorithm proceeds as follows:

- (1) To each (directed) interior edge $e = (i, j) \in E$ from vertex i to vertex j , assign a *positive* weight w_{ij} such that

$$\sum_{j \in N(i)} w_{ij} = 1$$

where $N(i)$ is the list of vertices neighboring the i -th vertex. Note that a symmetry condition $w_{ij} = w_{ji}$ is not required.

- (2) To all other entries (i, j) , assign $w_{ij} = 0$
- (3) Embed the boundary vertices in the plane such that they form a closed convex polygon.

We position the boundary vertices uniformly on a unit circle in the xy -plane and set their coordinates to be the root of unity, depending on the valence of the vertex removed.

- (4) Solve the two linear systems for the x and y coordinates of the n interior vertices:

$$(I - W)x = b^x, \quad (I - W)y = b^y$$

where W is a $n \times n$ matrix containing w_{ij} , and b^x and b^y vectors with non-zero entries corresponding to vertices adjacent to the boundary.

We rewrite the above linear system in the following way,

$$\sum_{j \in N(i)} w_{ij} x_j = x_i, \quad i = 1, \dots, V - B,$$

$$\sum_{j \in N(i)} w_{ij} y_j = y_i, \quad i = 1, \dots, V - B,$$

$$x_i = b_i^x, \quad i = V - B + 1, \dots, V,$$

$$y_i = b_i^y, \quad i = V - B + 1, \dots, V,$$

where B is the set of vertices in the boundary of the convex polygon.

The solution to this linear system are the coordinates for all interior vertices in \mathbb{R}^2 while the vertices are connected based on the combinatorics of the original triangulation T . Tutte theorem

showed that this map is one-to-one. Also, the x and y coordinates of each interior vertex is a convex combination of the x and y of its adjacent vertices respectively. Moreover, the coefficient matrix of the above linear system is *diagonally dominant* due to the normalization imposed on the row sum of w_{ij} . That guarantees the *existence and uniqueness of the solution*. But the coefficient matrix might not be symmetric depending on our choice of w_{ij} .

2.2.3. Different choices of weight used in Tutte embedding. Here we compare two commonly used weights for Tutte embedding: cotangent weights and graph Laplacian.

For the cotangent weights, we need to normalize them to have unit row sums, i.e.

$$\tilde{w}_{ij} := \frac{\cot(\alpha_{ij}) + \cot(\beta_{ij})}{\ell^2} \Rightarrow w_{ij} = \frac{\tilde{w}_{ij}}{\sum_{j \in N(i)} \tilde{w}_{ij}}$$

Note that the cotangent weights makes the coefficient matrix symmetric and these weights are only positive if the triangulation of the mesh $T = (V, E, F)$ is *Delaunay*, i.e. no vertex in V is inside the circumcircle of any triangle in F . More importantly, these weights can be derived by computing the discrete Dirichlet energy of a piecewise linear map. These weights are used in computing discrete harmonic maps [PP93]. Since harmonic maps on the closed genus-zero surface are equivalent to conformal maps in both continuous and discrete settings, *so the resulting convex polygonal mesh from Tutte embedding using cotangent weights should be conformal to the input mesh*.

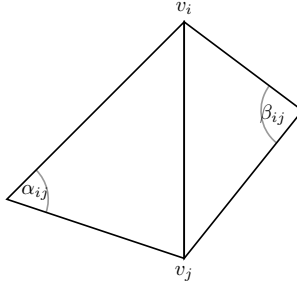


FIGURE 2.56. The two angles α and β associated to the weight w_{ij} of edge (i, j)

For the graph Laplacian, the weights are defined as

$$\tilde{w}_{ij} = \frac{1}{\text{valence of vertex } v_i}$$

The definition automatically implies the condition of unit row sum $\sum_{j \in N(i)} w_{ij} = 1$. Although these weights can be computed much more directly than the cotangent weights, they do not guarantee that the coefficient matrix is symmetric. And more importantly, *using the graph Laplacian weights*

does not produce a conformal mesh from Tutte embedding. To demonstrate these properties, we first apply Tutte embedding onto the three simple meshes:



FIGURE
2.57. Trian-
gulated cube



FIGURE
2.58. Icosa-
hedron



FIGURE
2.59. Icosa-
hedron after
subdivision

	V	E	F	sphericity
cube	8	12	6	0.81
icosahedron	12	30	20	0.93
Subdivided icosahedron	42	120	80	0.98

TABLE 2.17. Cube, icosahedron, and subdivided icosahedron

The subdivided icosahedron is produced by performing midpoint subdivision on the icosahedron. So it has four times as many faces as the icosahedron and it has total number of vertices $12 + 30 = 42$. Then each newly added vertex is projected on the surface of the sphere circumscribing the icosahedron. As a consequence, the subdivided icosahedron has sphericity closer to one than the icosahedron.

We remove one vertex from each mesh and apply Tutte embedding using cotangent weights and graph Laplacian weights respectively:

At the first glance, the resulting meshes of icosahedron and its subdivision looks identical under Tutte embedding using cotangent and graph Laplacian weights respectively. But we can show easily that the two linear systems involving the interior vertices are the same. (The boundary vertices are fixed in both cases.)

For the graph Laplacian weights, the valence of all vertices in icosahedron is 5. Hence $w_{ij} = 1/5 = 0.2$ for all i, j . So the resulting matrix solving for x, y -coordinates of the interior vertices has diagonal of one and five of the non-zero entries equal to -0.2 in each row.

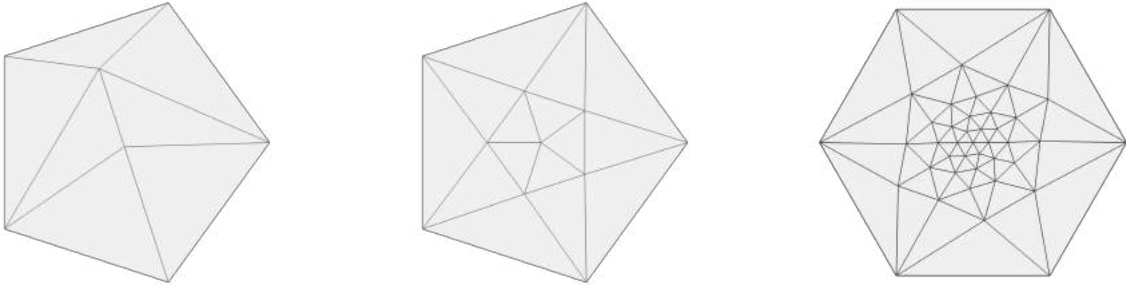


FIGURE 2.60. Tutte embedding using cotangent weights

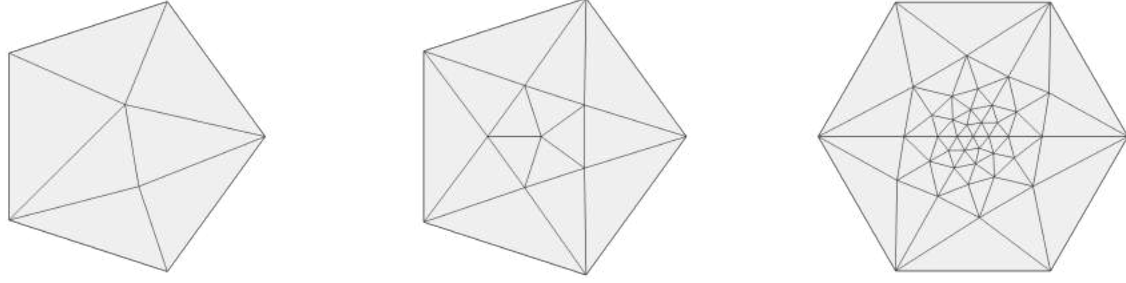


FIGURE 2.61. Tutte embedding using graph Laplacian weights

For the cotangent weights, since all triangles in an icosahedron are equilateral. Hence $w_{ij} = 2\cot(\pi/3) = 2/\sqrt{3}$. The row sum is $5 \times 2/\sqrt{3}$. After the normalization, the resulting matrix has diagonal of one and five of the non-zero entries equal to $-\frac{2/\sqrt{3}}{10/\sqrt{3}} = -0.2$ in each row. Indeed, by the same token, *a mesh that is uniformly triangulated by equilateral triangles and has the same valence for all its vertices, its Tutte embedding is the same using cotangent or graph Laplacian weights.*

We apply the Tutte embedding with different weights to meshes of larger size to observe the difference in conformality. Here we use the meshes of sphere 1, ellipsoid with $r = 2$, and spot from the previous section. We show the mean of the length-cross-ratio below. This provides the numerical evidence to confirm that *using the cotangent weights can better preserve the conformality of the input mesh except the triangles that were removed.*

	cotangent weights	graph Laplacian weights
cube	0.9	0.9
icosahedron	0.83	0.83
Subdivided icosahedron	0.96	0.96
sphere 1	1.001	1.03
ellipsoid $r = 2$	0.998	1.01
spot	1.006	1.361

TABLE 2.18. Mean of length-cross-ratio after Tutte embedding

Finally, for the sake of completeness, we list here other choices of weights which can be found in the literature such as

- (1) Edge length $\tilde{w}_{ij} = |e(i,j)| = \|v_i - v_j\|$
- (2) Mean Value weights [Flo03a]: $\tilde{w}_{ij} = \frac{\tan(\alpha_{ij}/2) + \tan(\beta_{ij}/2)}{\|v_i - v_j\|}$
- (3) Cotangent weights normalized by edge lengths: $\tilde{w}_{ij} = \frac{\cot(\alpha_{ij}) + \cot(\beta_{ij})}{\|v_i - v_j\|^2}$

2.2.4. Inverse stereographic projection. In the previous section, we obtain a convex polygonal mesh in the xy -plane via Tutte embedding. Now we project the planar mesh onto a unit sphere via *inverse stereographic projection*, i.e. for a vertex with coordinates (u, v) on the plane, its coordinates (x, y, z) on the unit sphere in \mathbb{R}^3 (except the north pole) are given by $f: \mathbb{R}^2 \rightarrow \mathbb{S}^2 \setminus \{(0, 0, 1)\}$ given by

$$f(u, v) = (f_1(u, v), f_2(u, v), f_3(u, v)) = \left(\frac{2u}{1 + u^2 + v^2}, \quad \frac{2v}{1 + u^2 + v^2}, \quad \frac{-1 + u^2 + v^2}{1 + u^2 + v^2} \right)$$

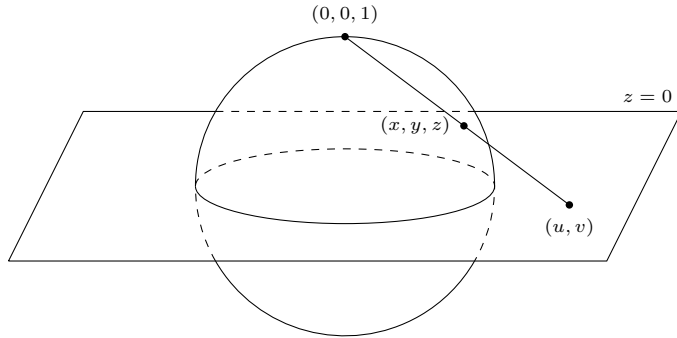


FIGURE 2.62. Inverse stereographic projection from \mathbb{R}^2 to $\mathbb{S}^2 \setminus \{(0, 0, 1)\}$

The *inverse stereographic projection* is a conformal map. We can prove this and compute the corresponding conformal factor. First, we write down the pushforward map of the tangent spaces by computing the Jacobian of f , $df: T_{(u,v)}\mathbb{R}^2 \rightarrow T_{f(u,v)}\mathbb{S}^2$,

$$df(u, v) = \begin{bmatrix} \frac{\partial f}{\partial u} & \frac{\partial f}{\partial v} \end{bmatrix} = \frac{1}{(1 + u^2 + v^2)^2} \begin{bmatrix} 2(-u^2 + v^2 + 1) & -4uv \\ -4uv & 2(u^2 - v^2 + 1) \\ 4u & 4v \end{bmatrix}$$

Given two tangent vectors $\vec{a} = (a_1, b_1), \vec{b} = (b_1, b_2) \in T_{(u,v)}\mathbb{R}^2$, their images under df are

$$df(\vec{a}) = \left[\frac{\partial f_i}{\partial u} a_1 + \frac{\partial f_i}{\partial v} a_2 \right]_{i=1,2,3}, \quad df(\vec{b}) = \left[\frac{\partial f_i}{\partial u} b_1 + \frac{\partial f_i}{\partial v} b_2 \right]_{i=1,2,3}.$$

Using the fact that

$$\left\| \frac{\partial f}{\partial u} \right\|^2 = \sum_{i=1}^3 \left(\frac{\partial f_i}{\partial u} \right)^2 = 4(1+u^2+v^2)^2, \quad \left\| \frac{\partial f}{\partial v} \right\|^2 = 4(1+u^2+v^2)^2, \quad \frac{\partial f}{\partial u} \cdot \frac{\partial f}{\partial v} = 0,$$

we can compute the inner product

$$\langle df(\vec{a}), df(\vec{b}) \rangle = \left\| \frac{\partial f}{\partial u} \right\|^2 a_1 b_1 + \left(\frac{\partial f}{\partial u} \cdot \frac{\partial f}{\partial v} \right) (a_1 b_2 + a_2 b_1) + \left\| \frac{\partial f}{\partial v} \right\|^2 a_2 b_2 = \frac{4}{(1+u^2+v^2)^2} \langle \vec{a}, \vec{b} \rangle.$$

Since df preserves the inner product on the tangent planes and hence the angle between tangent vectors, f is a conformal map with conformal factor $\rho(u, v) = \frac{4}{(1+u^2+v^2)^2}$. For (u, v) on the unit circle such that $u^2 + v^2 = 1$, the scaling factor is equal to 1. Similarly, the scaling factor is 4 for $(0, 0)$ whereas the scaling factor is close to zero as (u, v) tend to infinity.

In our implementation, since all vertices in the planar mesh have coordinates satisfying $u^2 + v^2 \leq 1$ and hence $z \leq 0$, their projection are all mapped onto the southern hemisphere. Tutte embedding clustered many vertices around the center $(0, 0)$ of the convex polygon. As a consequence, *most vertices are concentrated around $(0, 0, -1)$* . Then the vertex removed earlier is added back to the north pole of the unit sphere with coordinates $(0, 0, 1)$. It is connected back to the boundary vertices on the equator and the corresponding triangle faces are added back. So the mesh is transformed back into a topologically sphere. But note that *the triangles which are added back are no longer conformal to the original mesh before Tutte embedding*.



FIGURE 2.63. Side views of cube, icosahedron, and subdivided icosahedron from inverse stereographic projection

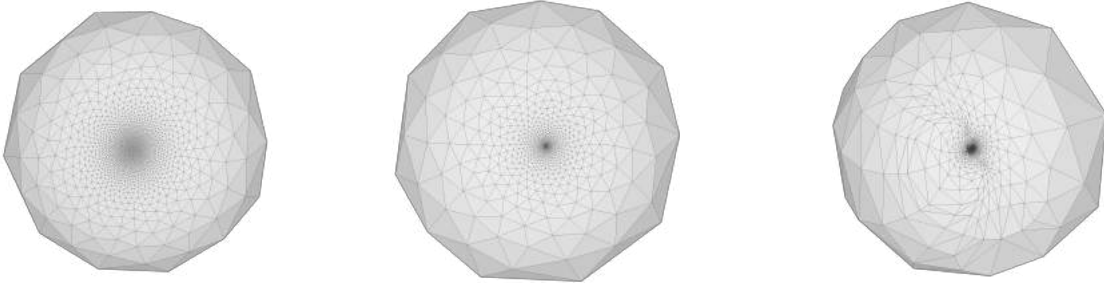


FIGURE 2.64. Bottom views of sphere 1, ellipsoid with $r = 2$, and spot from the inverse stereographic projection

2.2.5. Centering of mass. Although the meshes obtained via the inverse stereographic projection have all its vertices on the sphere, most of its vertices and hence the *center of mass* (COM) of the mesh are concentrated near the south pole. These meshes also have large area distortions in triangles that were added back and adjacent to the north pole. Since the discretization of the cMCF flow uses the finite element methods and its mass matrix depends on the triangle areas, the large area distortion often leads to instability of the flow in practice. Applying cMCF cannot effectively mitigate these large pieces of triangles around the north pole (regardless of the size of time steps).

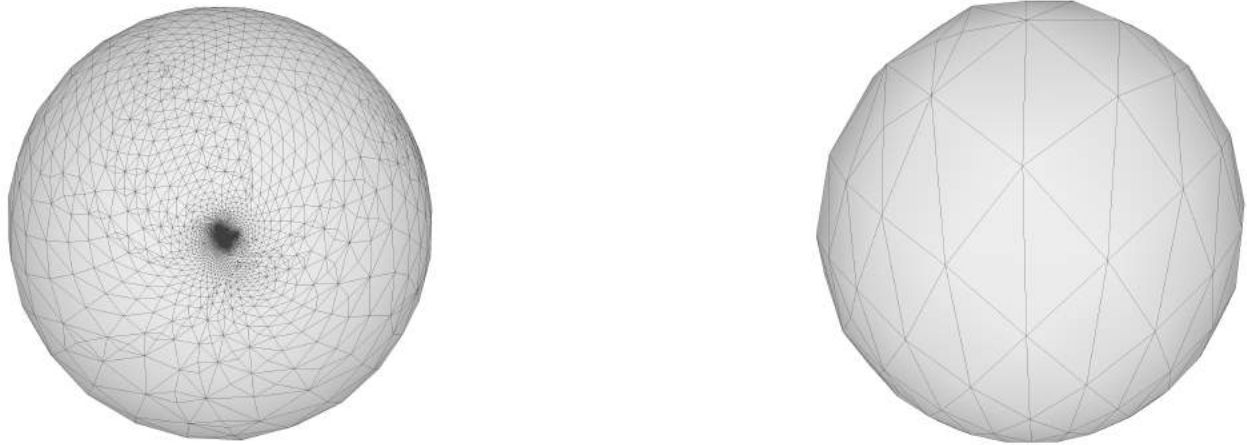


FIGURE 2.65. Dinosaur - left: bottom view, right: side view
cMCF applied on the mesh from the inverse stereographic projection after 1024 iterations with step size 0.01. All vertices are still concentrated on south pole, compared to resulting sphere of dinosaur from cMCF in section 2.1.3

It is known that Möbius transformations from a sphere to itself, such as translation, rotation, scaling, spherical inversions, and their compositions, are conformal maps. Given the meshes are

obtained from the inverse stereographic projection, our goal here is to *find a canonical way to compute a spherical conformal parametrization of our mesh using Möbius transformation such that its vertices are evenly spreaded on a unit sphere and hence its COM is positioned at the center of the unit sphere.*

With the help of Prof. Patrice Koehl, we implement the centering algorithm `MöbiusCenter` introduced by Baden, Crane, Kazhdan [BCK18]. Their idea is to seek a *spherical inversion* that moves the COM to the origin of the sphere and their algorithm is to perform Gauss-Newton method to minimize an energy functional measuring the distance between the COM of the mesh and the origin. We refer the readers to their original paper for the details of mathematical derivation and the algorithm.

Here we use the same collection of meshes from section 2.1.3. We compare the COM and the sphericity before and after the application of the `MöbiusCenter` algorithm.

	Before	After
cactus	(0.11, -0.40, -1.03)	(8e-12, -4e-11, -3e-11)
blobby	(-0.08, -0.27, -1.12)	(2e-14 8e-15, 3e-14)
spot	(0.07, 0.00, -1.12)	(-7e-15, 1e-15, 1e-14)
fandisk	(-0.20, 0.33, -1.07)	(-4e-13, 4.8e-12, -1e-12)
dinosaur	(0.06, 0.31, -1.15)	(3e-12, -2e-13, 5e-12)
human	(-0.50, 0.46, -1.04)	(2e-12, 1.5e-11, 7.5e-12)
shark	(0.29, 0.00, -1.05)	(-2e-11, 1e-12, 1e-11)
snowman	(0.09, 0.28, -1.11)	(2e-15, -6e16 7e-15)

TABLE 2.19. Center of mass before and after `MöbiusCenter`

	Original	Before	After
cactus	0.61	0.95	0.997
blobby	0.84	0.93	0.998
spot	0.71	0.95	0.998
fandisk	0.61	0.94	0.9998
dinosaur	0.67	0.90	0.9994
human	0.61	0.85	0.9993
shark	0.50	0.94	0.998
snowman	0.86	0.93	0.998

TABLE 2.20. Sphericity of the original mesh, before, and after `MöbiusCenter`

After applying the `MöbiusCenter` algorithm, the COM of all meshes are centered exactly at the origin $(0, 0, 0)$ of a unit sphere. Moreover, the sphericity of all meshes increases as their vertices

spread more evenly on the sphere surface and hence the mesh volume increases. We can clearly see on the meshes that their vertices are much more evenly distributed after `MöbiusCenter`.

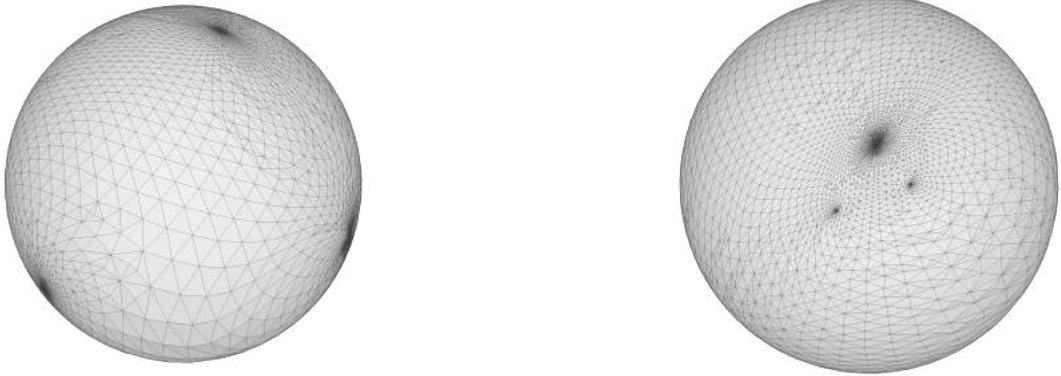


FIGURE 2.66. Dinosaur after `MöbiusCenter` - left: bottom view, right: side view

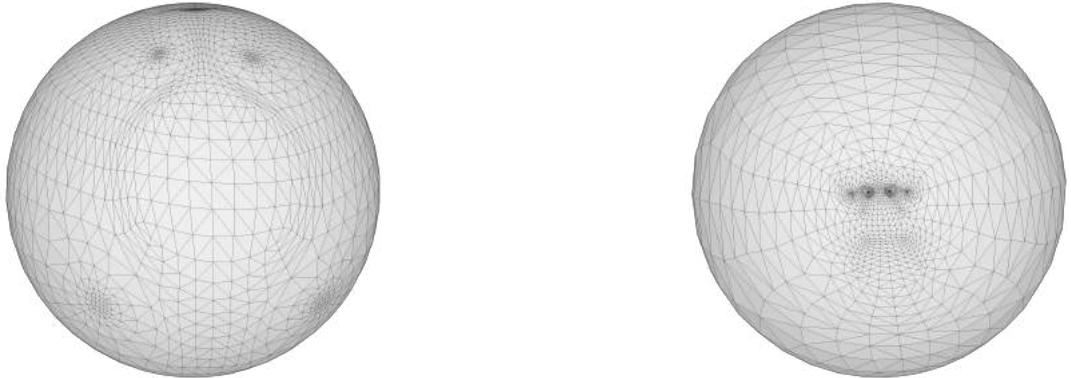


FIGURE 2.67. Spot after `MöbiusCenter` - left: bottom view, right: side view

2.2.6. Improvement on cMCF performance. Given the spherical meshes from the previous section, we start the cMCF on them with respect to the metric of the original mesh before the Tutte embedding is applied. At the same time, we apply area rescaling in each step such that the surface area of the mesh is kept constant during the evolution. In the following, we are going to demonstrate with numerical evidences that *these spherical meshes are shown to converge to a unit sphere that is discretely conformal to the original mesh under the modified procedure of cMCF*.

In this section, we present a collection of meshes on which cMCF either cannot converge or cannot produce a discrete conformal map to a unit sphere. Some examples such as a very long ellipsoid and rod with grooves as shown in the beginning of this section, we introduce here one

more mesh that resembles a bicycle's crank arm. The triangulation of this mesh consists uniformly of long and thin triangles.

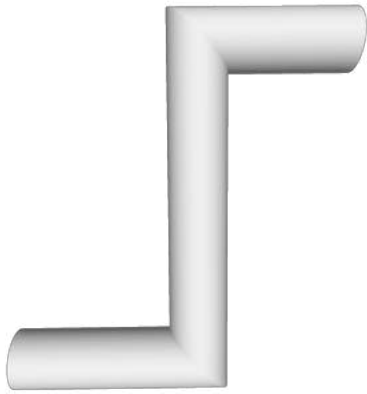


FIGURE 2.68. Bicycle's crank arm

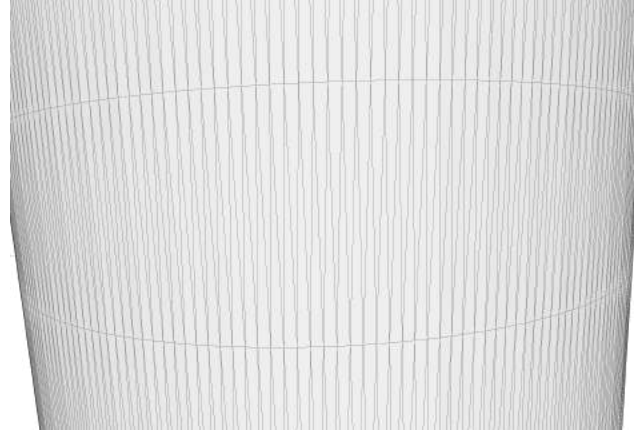


FIGURE 2.69. Zoomed-in view of crank arm's triangulation

bicycle's crank arm	mean μ	std σ
max. ang.	99°	19°
min. ang.	3.4°	2.7°
	max.	min
area	4.5e-4	1.5e-6

Rod with grooves (fig 2.23)	mean μ	std σ
max. ang.	111°	34°
min. ang.	19°	14°
	max.	min
area	3.9e-3	8.1e-6

We apply on the ellipsoid with $r = 32$, rod with grooves, and bicycle's crank arm. both cMCF and the modified cMCF procedure with an additional initialization of mapping the initial mesh onto a unit sphere via Tutte embedding (with cotangent weights) and the inverse stereographic projection. The step size chosen is $\tau = 0.01$ for $2^9 = 512$ iterations. A step size larger than that might run into risk of numerical instability, a step size in the range $[0.1, 1e - 4]$ shows similar flow behaviors, and a step size smaller than $1e - 4$ is inefficient to produce any discernible changes on the meshes over the given iterations.

Below are the plots of sphericity and the mean of the length-cross-ratio. The suffix `- tutte` indicates that the modified cMCF procedure is applied. We also show the basic statistics for the maximal ratio of angular distortion in all triangles.

For the ellipsoid with $r = 32$ and the bicycle crank arm, we can conclude that both cMCF and the modified procedure eventually converge to a unit sphere that are comparably discrete conformal to the initial mesh. But *the modified procedure clearly transforms the mesh into an almost unit*

sphere after the first step and this converges to a discretely conformal sphere much faster in contrast to the cMCF.

For the rod with grooves, we demonstrated in the previous section that the cMCF never converges in which the mesh is stretched infinitely long into a line. In the modified procedure, our initialization step of mapping the mesh onto a unit sphere does not work effectively (with a sphericity of approximately 0.7). *Not only restarting cMCF on this mesh helps it converge to a unit sphere, the resulting sphere is also discrete conformal to the initial mesh.*

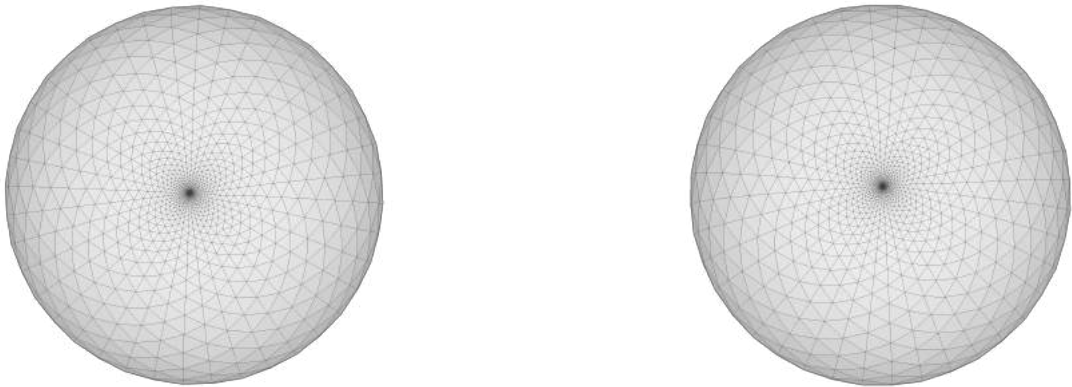


FIGURE 2.70. Front view of resulting sphere of ellipsoid with $r = 32$
left: cMCF, right: modified procedure of cMCF

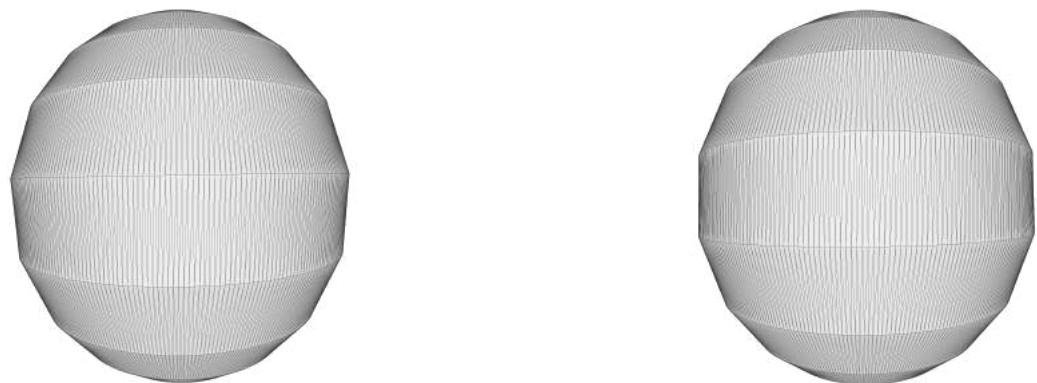


FIGURE 2.71. Front view of resulting sphere of bicycle crank arm
left: cMCF, right: modified procedure of cMCF
The long thin triangles are still visible on the sphere

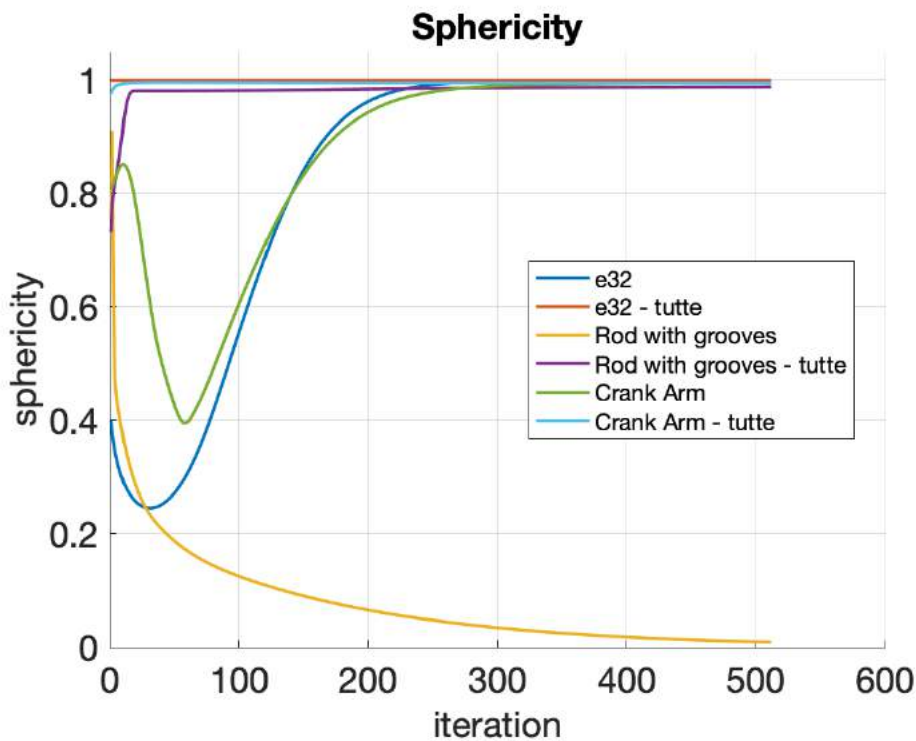
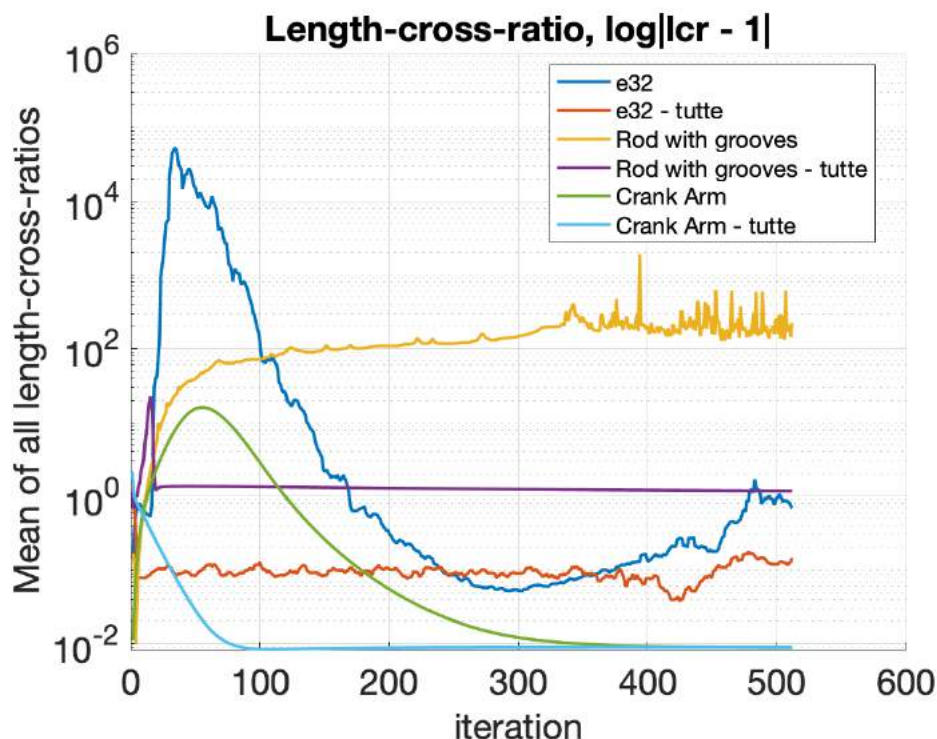


FIGURE 2.72. The curves of e32 - tutte and Crank Arm - tutte overlap each other almost completely



	Flow	mean μ	std σ
ellipsoid with $r = 32$	1	2.1e-1	1.4e-1
	2	1.5e-1	7.0e-2
Rod with grooves	1	1.7	3.85
	2	5.7e-1	5.8e-1
Bicycle's crank arm	1	1.8e-1	1.6e-2
	2	1.9e-1	6.4e-1

TABLE 2.22. 1 : cMCF, 2 : cMCF - tutte
Maximal ratio of angular distortion

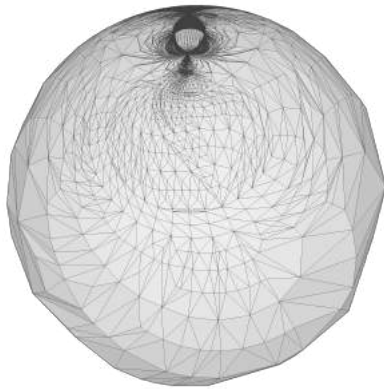


FIGURE 2.73. Spherical mesh of rod with grooves after initialization step

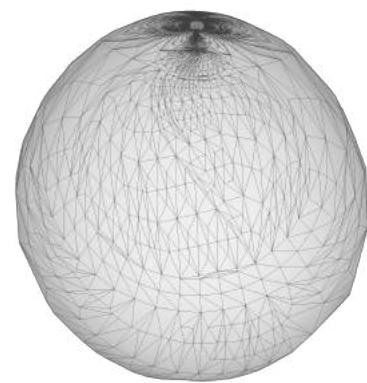


FIGURE 2.74. Resulting discrete conformal sphere of rod with grooves

Next, we apply both cMCF and the modified procedure on meshes with multiple protrusions (crystal chamber and deer) and meshes of large size (armadillo). The pictures and the statistics below show that all three meshes are not uniformly triangulated. The shape and size of the triangles vary large in different parts of the meshes. The pillars in the crystal chamber and the atlas in the deer have high conformal factors when the meshes are being mapped discrete conformally onto a unit sphere.

The step size chosen is $\tau = 0.001$ for $2^9 = 512$ iterations. A step size larger than that causes numerical instability in the flow and the flow does not converge. A step size smaller than that takes much more iterations for the flow to converge and this is inefficient. Below are the plots of sphericity and the mean of the length-cross-ratio. The suffix **- tutte** indicates that the modified cMCF procedure is applied. We also show the basic statistics for the maximal ratio of angular distortion in all triangles.

crystal chamber	mean μ	std σ	deer	mean μ	std σ	armdillo	mean μ	std σ
max. ang.	90°	11°	max. ang.	96°	20°	max. ang.	83°	10°
min. ang.	21°	13°	min. ang.	30°	12°	min. ang.	43°	7°
	max.	min		max.	min		max.	min
area	8.4e-3	6.2e-6	area	3.7e-3	3.1e-6	area	3.0e-4	2.8e-11

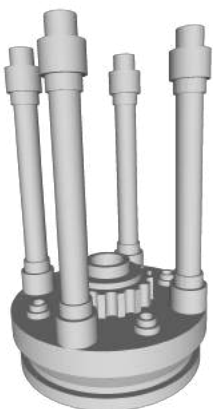


FIGURE 2.75. crystal chamber,
 $|V| \approx 24k, |F| \approx 49k$



FIGURE 2.76. deer, $|V| \approx 57k, |F| \approx 113k$

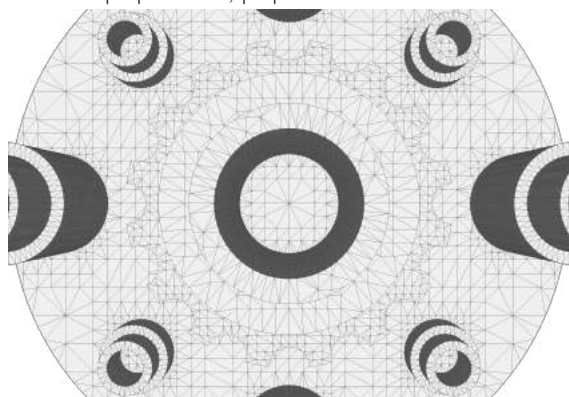


FIGURE 2.77. crystal chamber's platform

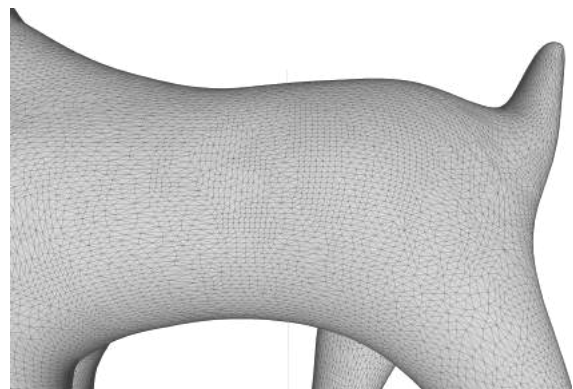


FIGURE 2.78. deer's body

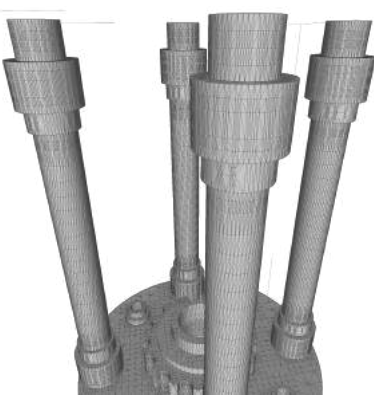


FIGURE 2.79. crystal chamber's pillar

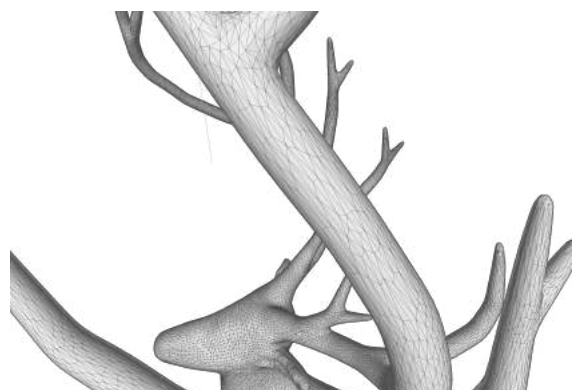


FIGURE 2.80. deer's atlas



FIGURE 2.81. arm-daillo, $|V| \approx 173k$, $|F| \approx 346k$

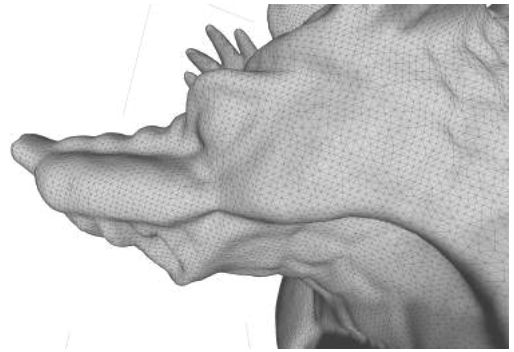


FIGURE 2.82. armadillo's face

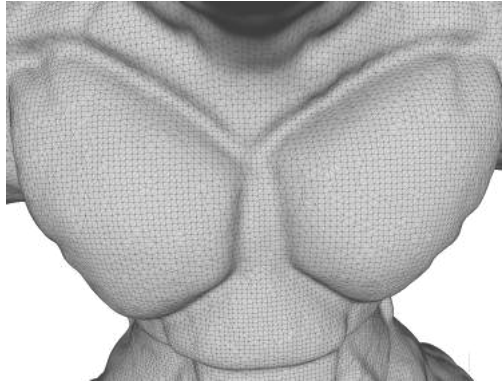


FIGURE 2.83. arm-daillo's body

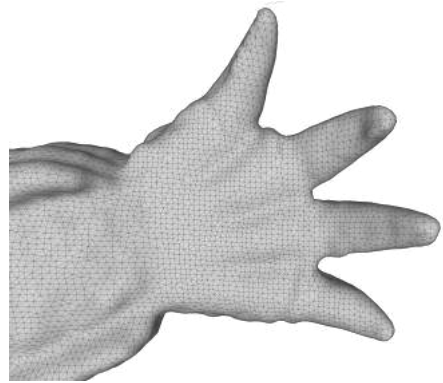


FIGURE 2.84. armadillo's hand

All three meshes under the cMCF tend to converge to a unit sphere over the course of iterations.

But the modified procedure is more effective to map all three meshes onto a unit sphere that is discrete conformal to the original meshes, both in terms of sphericity and discrete conformality.

For the crystal chamber and the armadillo, the modified procedure achieves significantly better discrete conformality than the cMCF.

Moreover, we show pictures of the spherical meshes (after applying Tutte embedding and the inverse stereographic projections) and the resulting spheres after applying the cMCF. These provides numerical evidence that these spherical meshes stay spherical under the cMCF while converging to sphere that are discretely conformal to the original mesh. In this sense, *our modified procedure has used the cMCF to improve the discrete conformality on the spherical meshes.*

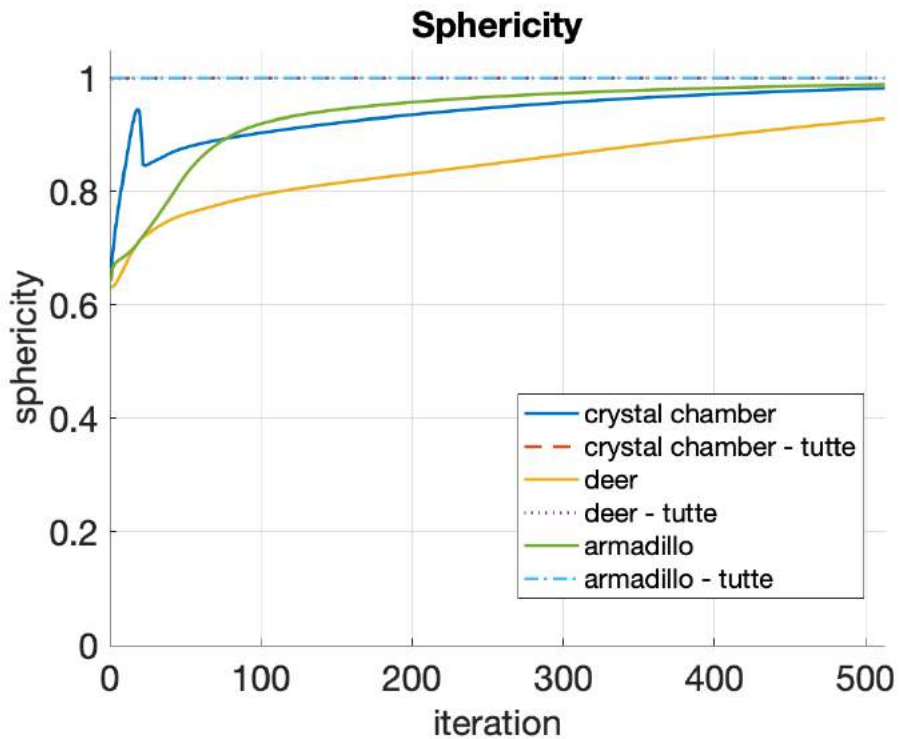
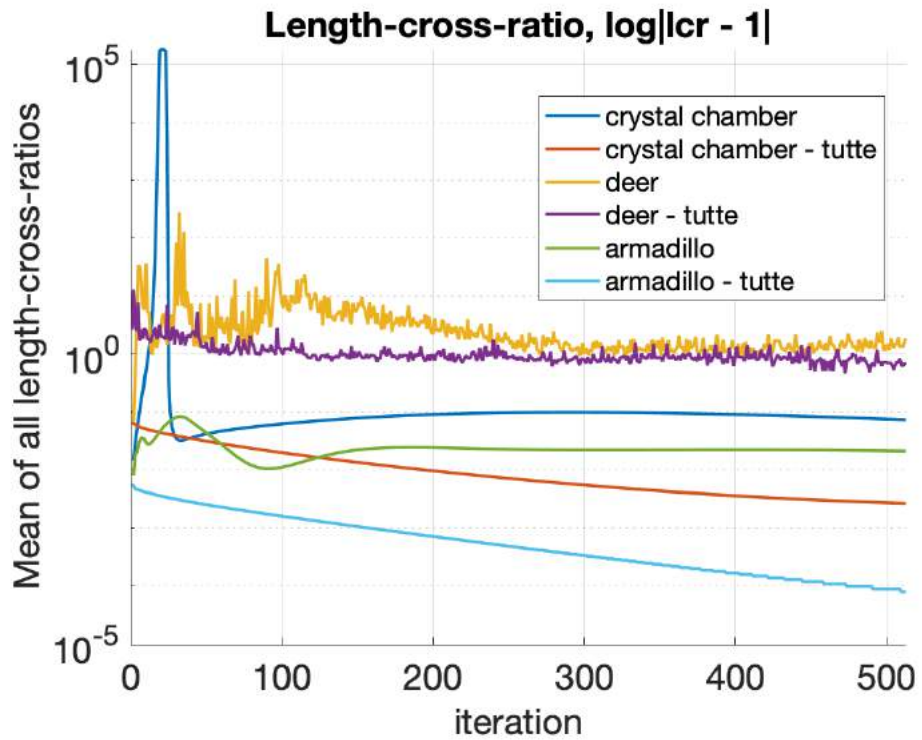


FIGURE 2.85. The curves of crystal chamber - tutte, deer - tutte, and Crank Arm - tutte are completely overlapped



	Flow	after initial step	after 512 iterations
Crystal chamber	1	0.797	0.982
	2	0.9993	0.9994
Deer	1	0.659	0.928
	2	0.9983	0.9998
Armadillo	1	0.688	0.988
	2	0.9999	0.9999

TABLE 2.24. Sphericity - 1 : cMCF, 2 : cMCF - tutte

	Flow	mean μ	std σ
Crystal chamber	1	3.0e-1	3.6e-2
	2	1.5e-1	1.9e-2
Deer	1	4.5e-1	4.5e-1
	2	3.0e-1	5.1e-1
Armadillo	1	1.3e-1	5.0e-3
	2	2.7e-2	7.2e-4

TABLE 2.25. 1 : cMCF, 2 : cMCF - tutte
Maximal ratio of angular distortion

The deer after 512 iterations under cMCF is not yet spherical and it takes in total of 2048 iterations for it to converge to a sphere (with sphericity of 0.9993), as round as under the modified procedure after 512 iterations. This advantage of computation efficiency using the modified procedure can be illustrated clearly in the case of the armadillo, which has more than 3 times of vertices and faces than the deer. *The initialization step in the modified procedure takes only around 10 seconds to produce a discretely conformal spherical mesh of armadillo. Using 512 iterations of the original cMCF to evolve the armadillo takes more than 1300 seconds (or 20 minutes) but still fails to obtain a mesh that is spherical.* These running times, in seconds, were measured on a laptop computer using an Intel i9 CPU processor running at 2.9GHZ, with 32GB of RAM.



FIGURE 2.86. Evolution of deer after 512 (left) and 2048 (right) iterations under cMCF



FIGURE 2.87. Left: Evolution of armadillo after 512 iterations under cMCF
Right: Sphericalized armadillo after the initial step of the modified procedure

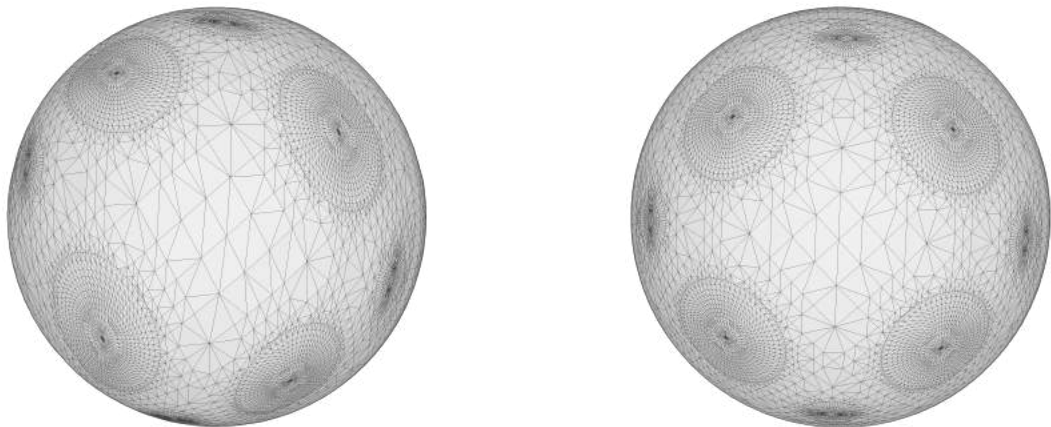


FIGURE 2.88. Left: Sphericalized crystal chamber after the initial step
Right: after 512 additional iterations under cMCF
The cMCF has improved the discrete conformality on the spherical mesh

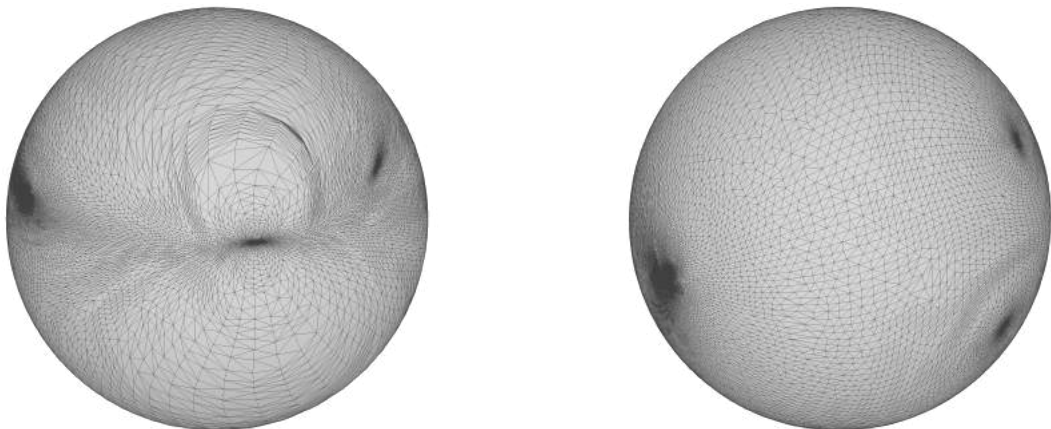


FIGURE 2.89. Left: Sphericalized deer the initial step
Right: after 512 additional iterations under cMCF
The cMCF has improved the discrete conformality on the spherical mesh

2.3. Sphericalized cMCF - using cMCF to construct homotopy of degree one maps

In this section, we give a new algorithm named “Sphericalized cMCF” using the cMCF to construct a homotopy from a *degree one map* to a *homeomorphism* mapping from a unit sphere to a unit sphere. In summary, first we obtain an embedded surface M via the parametrization map f applied on the unit sphere. Then we apply to the given degree one map g (not necessarily injective) to map M onto a unit sphere. We apply the cMCF on the unit sphere using the induced metric on M . The cMCF is performed with surface rescaling and spherical projection to ensure that the sign surface area remains constant and the image is a unit sphere throughout the flow. Given that cMCF converges, the resulting mapping from the surface M onto the unit sphere is a conformal map. In this case, the degree one map $g \circ f = H_0 \circ f$ is homotopic to the homeomorphism $\phi := H_T \circ f: \mathbb{S}^2 \rightarrow \mathbb{S}^2$. More specifically, this proposed algorithm uses the cMCF to construct a homotopy $H_t \circ f: \mathbb{S}^2 \times [0, 1] \rightarrow \mathbb{S}^2$ with $(H \circ f)(x, 0) = (g \circ f)(x)$ and $(H \circ f)(x, 0)(x, T) = \phi(x)$ for $x \in \mathbb{S}^2$. See algorithm (1) and figure (2.90).

Algorithm 1 Sphericalized conformalized Mean Curvature Flow

Input: A degree one map g , an embedded surface M (from a unit sphere \mathbb{S}^2 via parametrization map f), iteration time step τ

Output: A homeomorphism $\phi: \mathbb{S}^2 \rightarrow \mathbb{S}^2$ and a homotopy from $g \circ f$ to ϕ

```

1: procedure SPHERICALIZED cMCF( $g$ )
2:   Apply  $g$  to map  $M$  onto a unit sphere  $\mathbb{S}^2$ 
3:   Initialize cMCF on the resulting unit sphere  $\mathbb{S}^2$  using the induced metric defined on  $M$ 
4:   Set time  $t = 0$ 
5:   while the unit sphere  $\mathbb{S}^2$  is not conformal to  $M$  do
6:     An iteration of cMCF on  $\mathbb{S}^2$  with time step  $\tau$  and set  $t \leftarrow t + \tau$ 
7:     Rescale resulting surface from cMCF such that its signed surface area is equal to  $4\pi$ 
8:     Projection onto the unit sphere  $\mathbb{S}^2$  via  $p \mapsto \frac{v}{\|v\|}$  for each point on the surface
9:   Obtain a conformal map from  $M$  to  $\mathbb{S}^2$ ; its composition with parametrization map  $f$ 
   results in  $\phi$ 

```

We first lay out the theoretical framework for our algorithm in the setting of continuous surfaces and then present results in the discrete setting from our numerical experiments by using the Gauss map as a degree one map. *Gauss map is used since it can easily be implemented in contrast to other*

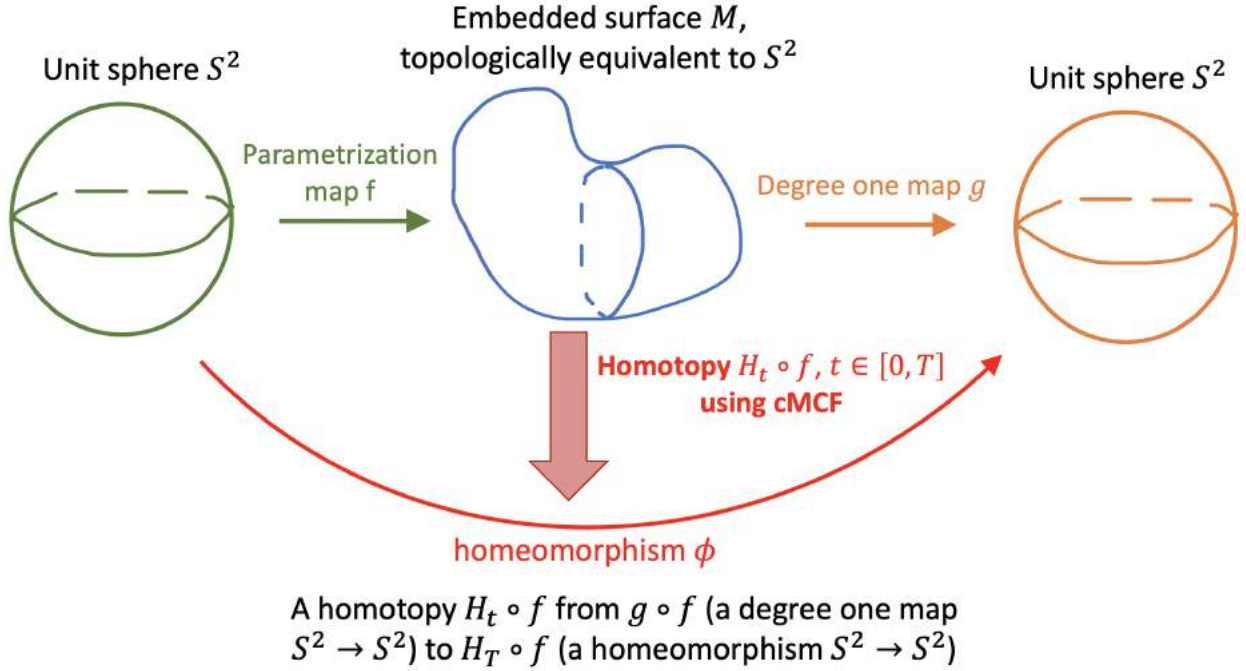


FIGURE 2.90. Sphericalized cmCF - Homotopy from a degree one map to a homeomorphism, defined from a unit sphere to a unit sphere

degree one maps. There are many variations how to compute a discrete Gauss map on a mesh. Here the Gauss map we compute is to assign to each vertex a unit normal vector as a sum of unit normal vectors of adjacent faces weighted by their areas.

2.3.1. Theoretical framework. To begin with, we recall the definitions of degree of a map between smooth surfaces, homotopy of maps, and state the Hopf theorem. We refer readers to an in-depth treatment of these concepts in the textbooks [Hat00], [Mil65].

Throughout this section, we assume M, N to be smooth oriented, compact, connected surfaces without boundary to stay relevant to our setting. We stress that the following concepts are more general and they can be defined in a broader context of manifolds of higher dimensions. First, Let $M \times [0, T]$ denote (x, t) with $x \in M$ and $0 \leq t \leq T$ (we can think it as a smooth three-dimensional manifold bounded by two “copies” of M). Two mappings $f, g: M \rightarrow N$ are called *smoothly homotopic*, abbreviated $f \sim g$, if there exists a smooth map $F: M \times [0, T] \rightarrow N$ with

$$F(x, 0) = f(x), \quad F(x, T) = g(x)$$

for all $x \in M$. This map F is called a *smooth homotopy* between f and g . Note that the relation of smooth homotopy is an equivalent relation among maps from M to N .

Second, we define the degree of a map $f: M \rightarrow N$. Let $x \in M$ be a regular point of f , meaning that $df_x: TM_x \rightarrow TN_{f(x)}$ is a linear isomorphism between the oriented vector spaces. The *sign* of df is defined to be $+1$ or -1 depending on if df preserves or reverses orientation. For any regular value $y \in N$, an integer called the local degree of f at y is defined by a summation formula

$$\deg(f; y) = \sum_{x \in f^{-1}(y)} \text{sign}(df_x)$$

One can show that the degree of the map f does not depend on the choice of the value y and depends only on the map f , i.e. $\deg(f) = \deg(f; y)$ for any $y \in N$. Furthermore, one can show that homotopic maps have the same degree, i.e. $f \sim g \Rightarrow \deg(f) = \deg(g)$. The degree is always an integer. It follows from the defintion that $\deg(f)$ is positive if f is orientation-preserving and negative if f is orientation-reversing. Intuitively, $\deg(f)$ represents the number of times that the manifold M wraps around N under the mapping f . For $\deg(f) = 1$, a *degree one map* f does not need to be injective in general. But all *orientation-preserving homeomorphisms* are degree one maps.

Lastly, we recall Hopf theorem

THEOREM 2.3.1. *If M is a connected and oriented n -dimensional manifold without boundary, then two continuous maps from M onto a n -sphere $f, g: M \rightarrow \mathbb{S}^n$ are smoothly homotopic if and only if they have the same degree.*

Note that the direction $f \sim g \Rightarrow \deg(f) = \deg(g)$ is obvious from the previous discussion on degree. Hopf theorem shows that the converse statement is also true. In our application, both M and the sphere are two-dimensional.

2.3.2. Proof of homotopy. Using the Hopf theorem, we can give a one-line proof that in our application (2.90) the degree one map $H_0 := g$ is smoothly homotopic to the conformal homeomorphism $H_T := \phi$ obtained by applying cMCF with area rescaling.

PROOF. Since $\phi: M \rightarrow \mathbb{S}^2$ is a conformal homeomorphism, it is an orientation preserving homeomorphism. Hence $\deg(\phi) = 1$. Since map g is also degree one, g and ϕ are homotopic by Hopf theorem.

2.3.3. Experimental results in homotopy construction. we present results from our numerical experiments in constructing homotopy using our sphericalized cMCF algorithm. Before

doing so, we recall the definition of *Gauss map* in the continuous setting. Given a surface X in \mathbb{R}^3 , Gauss map $G: X \rightarrow \mathbb{S}^2$ is a continuous map defined by normal vector, i.e. for each point $x \in X$, $G(x)$ is its unit normal vector which lies on a unit sphere. The Gauss map is globally defined on X if and only if X is orientable. The Gauss map applied on a closed compact orientable surface S in \mathbb{R}^3 with positive Gaussian curvature everywhere is bijective (or more precisely, a local diffeomorphism in this case). Indeed one can show that if S has a point p with negative Gauss curvature, the Gauss map defined on S is no injective, i.e. there is another point $q \in S$ with $q \neq p$ such that $G(q) = G(p)$.

We recall a fundamental result from topology, Alexander's theorem.

THEOREM 2.3.2. *Every smooth embedded 2-sphere in \mathbb{R}^3 bounds a smooth embedded 3-ball.*

The following proposition holds in both discrete and continuous settings

PROPOSITION 2.3.1. *Gauss map has degree one when it is applied on a closed orientable surface of genus zero.*

PROOF. We denote the Gauss map on M as $g_1: M \rightarrow \mathbb{S}^2$. By Alexander's theorem, we can deform M continuously to a unit sphere to obtain a homotopy from g_1 to the identity map $I: \mathbb{S}^2 \rightarrow \mathbb{S}^2$, i.e. $g_1 \sim I$. Since $\deg(I) = 1$, so is the Gauss map.

More generally, if the Gauss map is defined globally on a closed smooth orientable surface S , its degree is equal to the half of the Euler characteristic of S . See Chapter 6, theorem 1 in [Mil65].

Our algorithm is given as follows. First, given an initial mesh M of genus zero, we use Gauss map to construct a degree one map to map all vertices of M onto a unit sphere \mathbb{S}^2 . Second, we apply the cMCF on the resulting unit sphere from the Gauss map applied on M . We implement the flow using the original stiffness matrix (with cotangent weights) from M . Each iteration of the intermediate cMCF step is performed with area rescaling and spherical projection $\vec{v} \mapsto \frac{\vec{v}}{\|\vec{v}\|}$ such that the sign surface area remains 4π and all vertices remain on a unit sphere during the flow. Also, in each cMCF step, we calculate a new mass matrix from the triangulated sphere. When the flow converges, we then obtain a discrete conformal map from initial mesh M onto \mathbb{S}^2 . As a result, we have constructed a homotopy from the degree one map (Gauss map in this case) to a *discrete conformal map* between the mesh M and a unit sphere \mathbb{S}^2 . See figure (2.91).

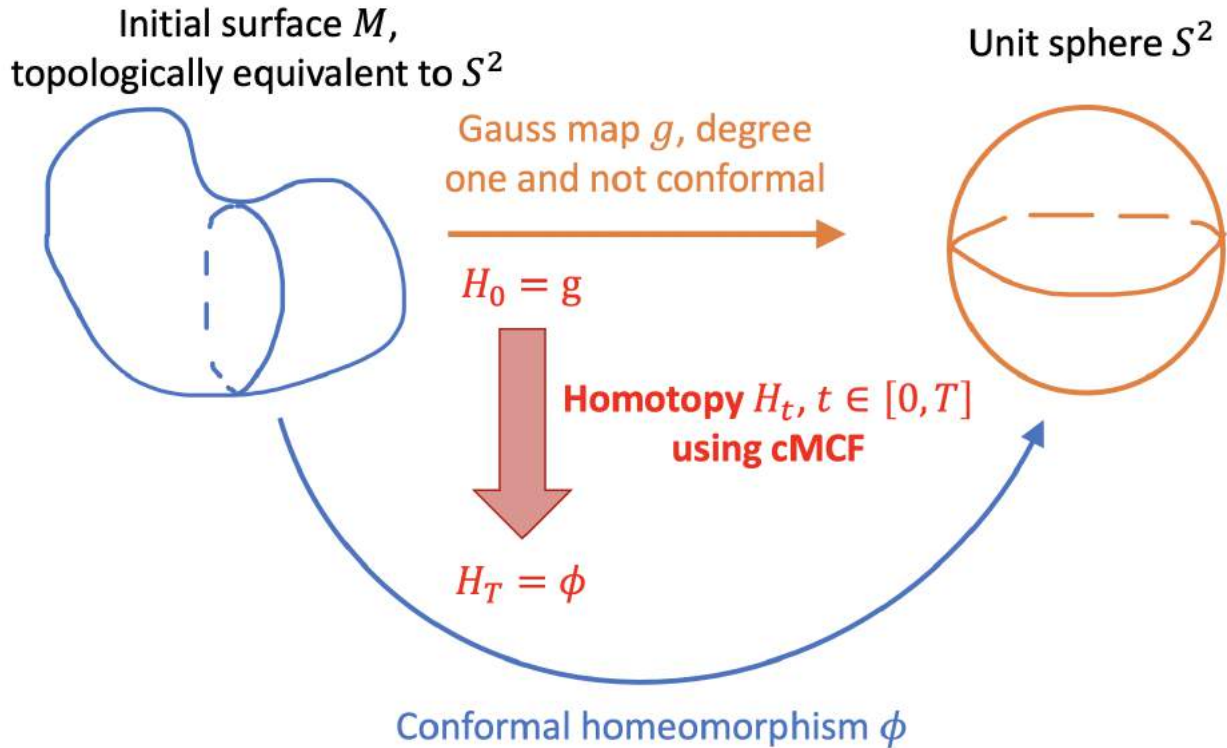


FIGURE 2.91. Numerical experiment of sphericalized cMCF - Homotopy of a degree one map to a conformal homeomorphism onto a unit sphere

Here we apply the “Sphericalized cMCF” algorithm on four meshes, i.e. blobby and spot from previous section and two new meshes, ghost and bunny, which have similar mesh size and quality as blobby and spot:

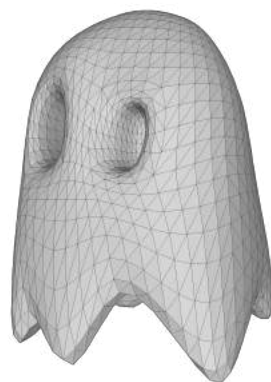


FIGURE 2.92. ghost, $|V| \approx 1.6k$, $|F| \approx 3.3k$

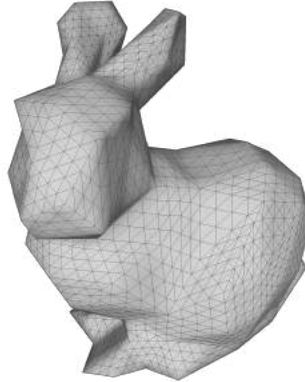


FIGURE 2.93. bunny, $|V| \approx 2.6k$, $|F| \approx 5.2k$

ghost	mean μ	std σ
max. ang.	92°	13°
min. ang.	34°	8°
	max.	min
area	1.4e-2	2.8e-4

bunny	mean μ	std σ
max. ang.	91°	22°
min. ang.	35°	12°
	max.	min
area	6.5e-3	1.3e-4

After applying Gauss map as a degree on map on these four meshes, we obtain four spherical meshes having many of their faces overlapping or intersecting with each other (colored in red).

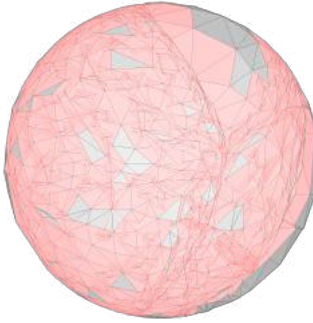


FIGURE 2.94. Gauss map on blobby



FIGURE 2.95. Gauss map on spot

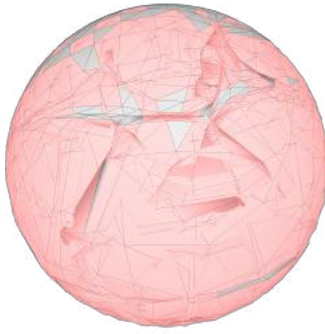


FIGURE 2.96. Gauss map on ghost



FIGURE 2.97. Gauss map on bunny

We run $2^8 = 256$ steps of cMCF with fixed step size $\tau = 0.01$ (or any step size in the range of $\tau \in [1e-4, 1e-2]$ with more iteration steps) using the original stiffness matrix from the initial mesh while keep updating mass matrix from the triangulated sphere in each iteration.

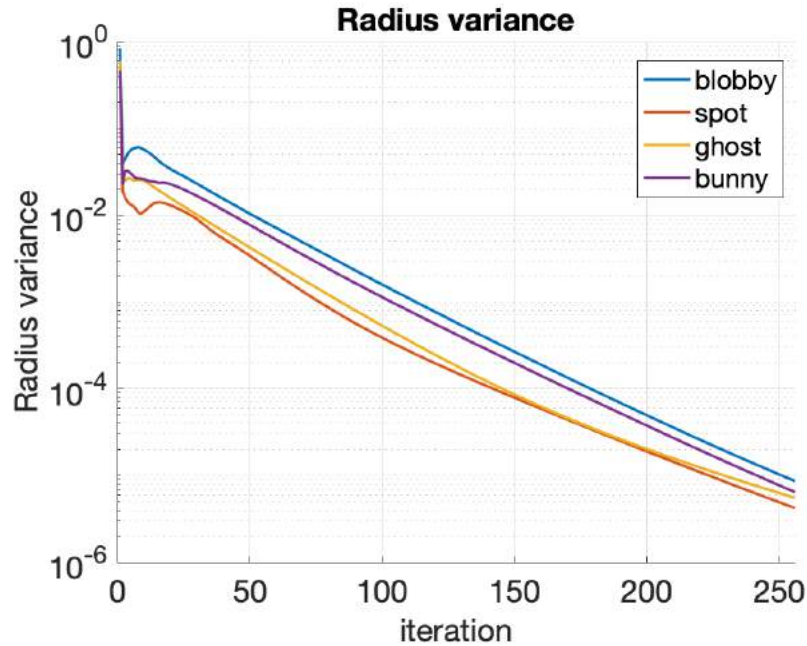
The overlapping or self-intersecting triangular faces make it more challenging to compute actual surface area and volume of the spherical meshes. So instead of computing the sphericity, we compute the radius variance as a measure for the roundness of the meshes. If all vertices of the meshes lie

on a unit sphere, the radius variance is then zero. Below are the plots for the radius variance and the mean of the length-cross-ratio.

Also, we show evolution of the meshes at the 5th, 10th, 20th, and 256th time step. These illustrate the different steps in the homotopy we constructed from the degree one map (Gauss map) to a conformal map. The red region on the meshes shown are the overlapping or self-intersecting faces while the grey and black regions are free of these faces. The number of these faces at different time step are listed in a table.

In all four meshes, the radius variance stay between $[1e - 1, 1e - 6]$ indicating that the meshes stay spherical after the Gauss map and during the homotopy via cMCF. At the same time, the mean of length-cross-ratio rapidly converges to one after the first 100 steps of iteration. This indicates a convergence to a conformal map from the initial sphere obtained by the Gauss map to a spherical mesh that is discretely conformal to the original input mesh.

More importantly, the overlapping or intersecting faces produced by the Gauss map as a degree one map indicate that the degree one map is not injective in this case. But these face “unfold” and the corresponding number of face intersection decreases steadily during the homotopy and finally the given degree one map becomes a conformal homeomorphism which is a bijective map.



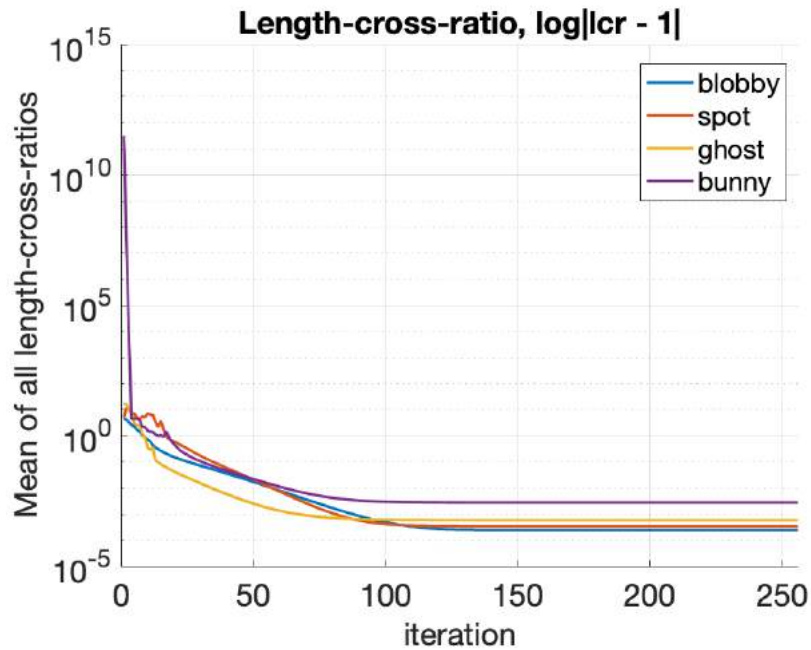


TABLE 2.27. Number of overlapping or intersecting faces

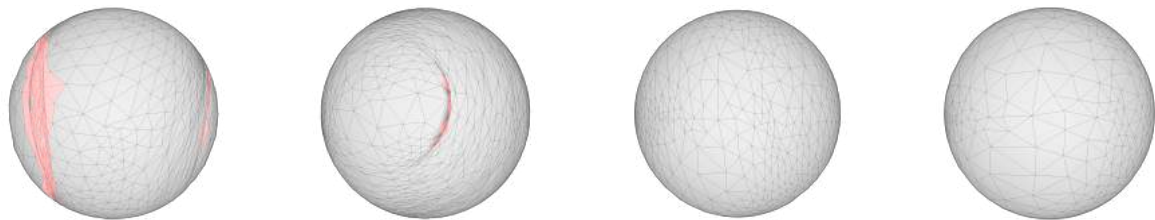


FIGURE 2.98. Blobby's evolution at 5th, 10th, 20th, and 256th step

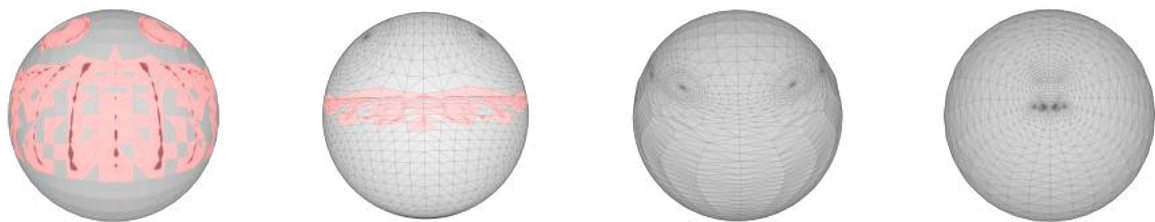


FIGURE 2.99. Spot's evolution at 5th, 10th, 20th, and 256th step

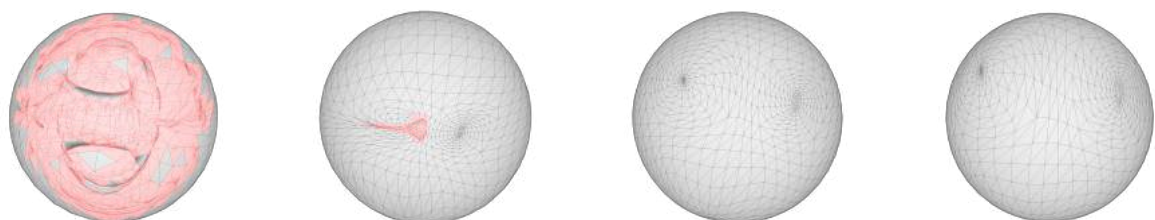


FIGURE 2.100. Ghost's evolution at 5th, 10th, 20th, and 256th step

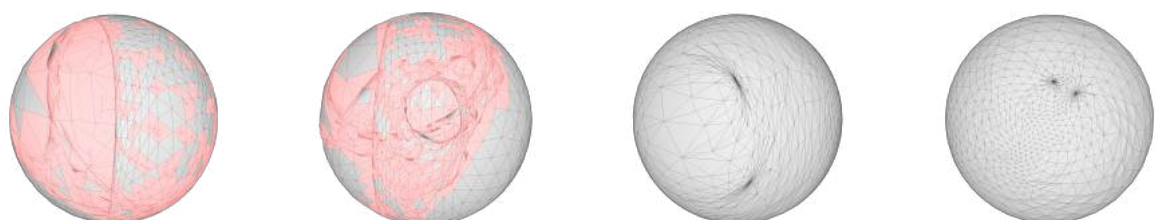


FIGURE 2.101. Bunny's evolution at 5th, 10th, 20th, and 256th step

CHAPTER 3

3D reconstruction of nuclear fusion hotspot x-ray emission distributions from very few two-dimensional projections

In this chapter, we present our work in limited view computer tomography on inertial confinement fusion experiments at the National Ignition Facility. These experiments aim to achieve thermonuclear ignition of a deuterium-tritium plasma by performing nuclear fusion. Given very few, for example two or three, 2D x-ray projection images from different directions in the experiment, we apply the Algebraic Reconstruction Technique to reconstruct the 3D x-ray emission distribution of the hotspot region in which the fusion process takes place. Moreover, we infer the 3D electron temperature distribution of the plasma using different x-ray energy channels. These 3D electron temperature measurements can help to further our understanding of the nuclear fusion physics.

First, we give an overview on the fusion experiments setup and explain briefly the underlying physics. Then we describe the mathematical theory of the Algebraic Reconstruction Technique algorithms (abbreviated as ART). Finally, we present results on 3D x-ray reconstructions and 3D electron temperature measurements in both our synthetic and experimental data studies.

3.1. Introduction to Inertial Confinement Fusion at the National Ignition Facility

Nuclear fusion is to combine atomic nuclei of low atomic number into a heavier nucleus and gain energy. The inertial confinement fusion (ICF) experiments attempt to initiate nuclear fusion using laser beams to heat and compress a mixture of deuterium-tritium (D-T) gas, which are the two heavy hydrogen isotopes and the fuel to the nuclear fusion. The products of the D-T reaction are an alpha particle (helium nucleus) and a neutron (see figure 3.1). Since the helium nucleus and the neutron have a slightly smaller total mass than the sum of the masses of the deuterium and tritium nuclei, the difference in mass is released as kinetic energy given by $E = \Delta mc^2$, where Δm and c are the change in mass and the speed of light respectively. This fusion process is conducted at the National Ignition Facility (NIF) in the Lawrence Livermore National Laboratory (LNLL). As of this writing, It has the world's most energetic laser with 192 beams which can deliver nearly

2 million joules of ultraviolet laser energy in nanosecond pulses to a gold cylindrical shell, known as *hohlraum*, in the target chamber's center. A D-T fuel pellet is located in the center of the hohlraum (See figures 3.2, 3.3, 3.4).

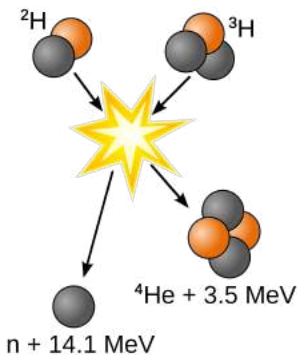


FIGURE 3.1. nuclear fusion of deuterium-tritium mixture
source: nuclear fusion on Wikipedia

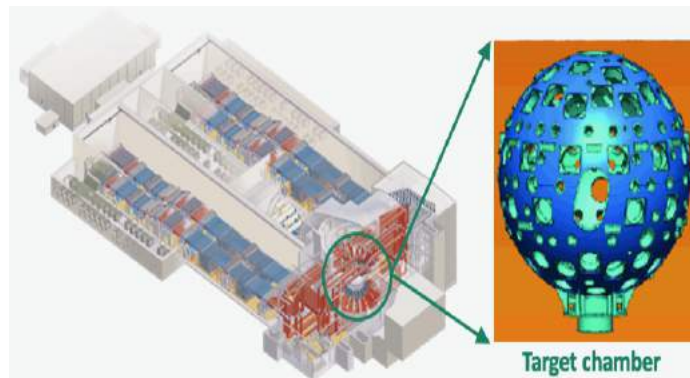


FIGURE 3.2. NIF's basic layout (size of three football fields) and the target chamber
source: National Ignition Facility on Wikipedia

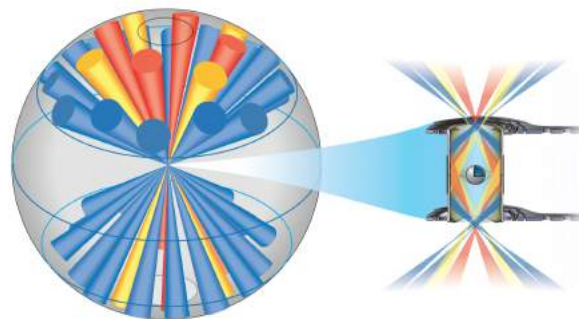


FIGURE 3.3. Laser beams of NIF shoot at hohlraum, different colors indicate that laser beams enter into the hohlraum with different incident angles
source: LLNL NIF user guide

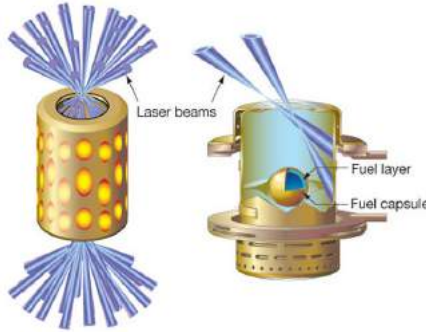


FIGURE 3.4. Illustration of target capsule inside hohlraum with laser beams, the capsule contains deuterium-tritium (D-T) mixture that fuels the ignition process
source: LLNL NIF & Photon Science

The ICF experiment at NIF uses the lasers to heat the gold inner walls of a hohlraum to create a hot plasma which radiates a uniform bath of soft x-rays. When these X-rays rapidly heat the outer surface of the fuel pellet, they cause a high-speed ablation, or a “rocket-like” blowoff, of the capsule surface materials . By Newton’s third law of motion, this ablation implodes the fuel capsule such that the D-T gas is highly compressed to extreme density and temperature, roughly at a density 100 times that of solid lead and 100 million degrees Celsius (hotter than the center of the sun). This capsule implosion forms a central *hotspot* (ideally in a symmetric fashion) in which the nuclear fusion reaction takes place (see figure 3.5). The *stagnation* point, or “bang time”, refers to the time when the capsule’s implosion reaches its maximum compression and the implosion kinetic energy is turned into the fuel thermal energy of the hotspot. Ideally, at this stage, the plasma ignites and the compressed D-T fuel burns before it can disassemble. This so-called *Ignition* occurs when the thermonuclear burn spreads through the compressed fuel. In the case of ignition, the energy gained is more than the input energy. For more details in the underlying physics of the ICF experiments, we refer our readers to [LAB⁺⁰⁴].

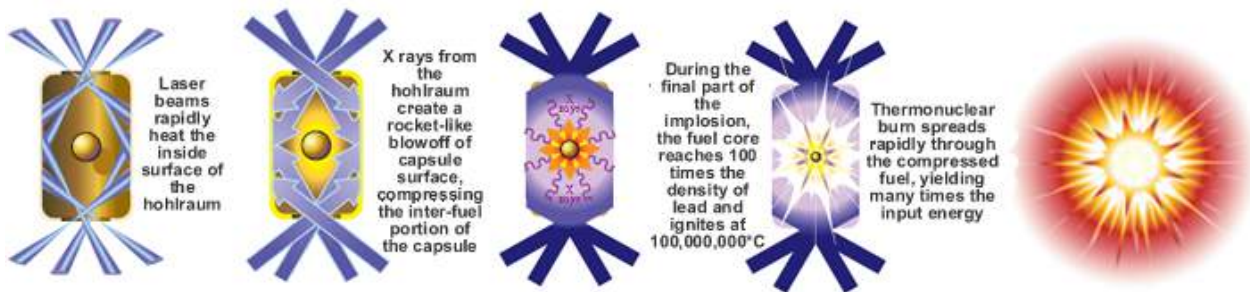


FIGURE 3.5. Explanation of the ICF experiment at NIF
source: LLNL NIF & Photon Science

So far NIF experiments have shown to have *fuel gains greater than unity*, where the energy generated through the fusion reaction in ICF plasma exceeds the amount of energy deposited into the D-T fusion fuel and the hotspot [HCC⁺14]. Latest experiments have demonstrated *alpha-particle self-heating* which is a process essential for achieving ignition, i.e. the fusion neutron yield produced due to the alpha-particle heating exceeds that produced by the work done on the fuel [HCC⁺16].

At the same time, in order to measure the extreme physical properties of the ICF hotspot, such as the implosion velocity of the fuel capsule, down-scattered neutron, and X-ray emissions, a wide range of diagnostics methods and instruments were developed and fielded at the NIF target chamber. Nearly 120 different diagnostics are available to both internal and external NIF users. A complete list of NIF diagnostics and their respective diagnostics can be found at [Laba].

In order to further our understanding of the stagnated plasma and benchmark the hydrodynamics simulations in ICF experiments, it is crucial to make 3D measurements of different physical quantities of the hotspot. These include its shape and distributions of X-ray and neutron production as well as density, and pressure. Not only can these 3D measurements help to characterize symmetry of the hotspot and quantify the significance of radiation loss, they can also provide important parameters to determine the proximity to ignition. In the context of the ICF experiments, previous work done on 3D reconstructions of neutron/x-ray source from limited number of 2D projections uses an iterative generalized expectation-maximization algorithm to find the maximum likelihood estimation of the 3D neutron/x-ray distribution [VDF⁺14], [VDM⁺15]. An alternative approach is to use spherical harmonics as basis functions to infer the 3D neutron and x-ray distributions from a few available projections in order to compare measured data with simulations [VDF⁺17]. These methods were tested using neutron images from the Neutron Imaging System at NIF [MBB⁺12] and x-ray pinhole images at the OMEGA Laser in Rochester, New York [BBC⁺97]. In addition, a different diagnostic called multi-monochromatic x-ray imager (MMI) uses a multi-layered Bragg mirror to record a collection of hotspot images across slightly different energy ranges. After post-processing, these MMI data can be used to infer the shape and volume of the hotspot and its 3D temperature and density distributions [NMF⁺12].

Our approach focuses on 3D reconstruction of the hotspot x-ray emission distribution from limited number of 2D time-integrated x-ray images at stagnation. Given images taken at different lines-of-sight (LOS), we transform the reconstruction process into solving a sparse linear algebraic

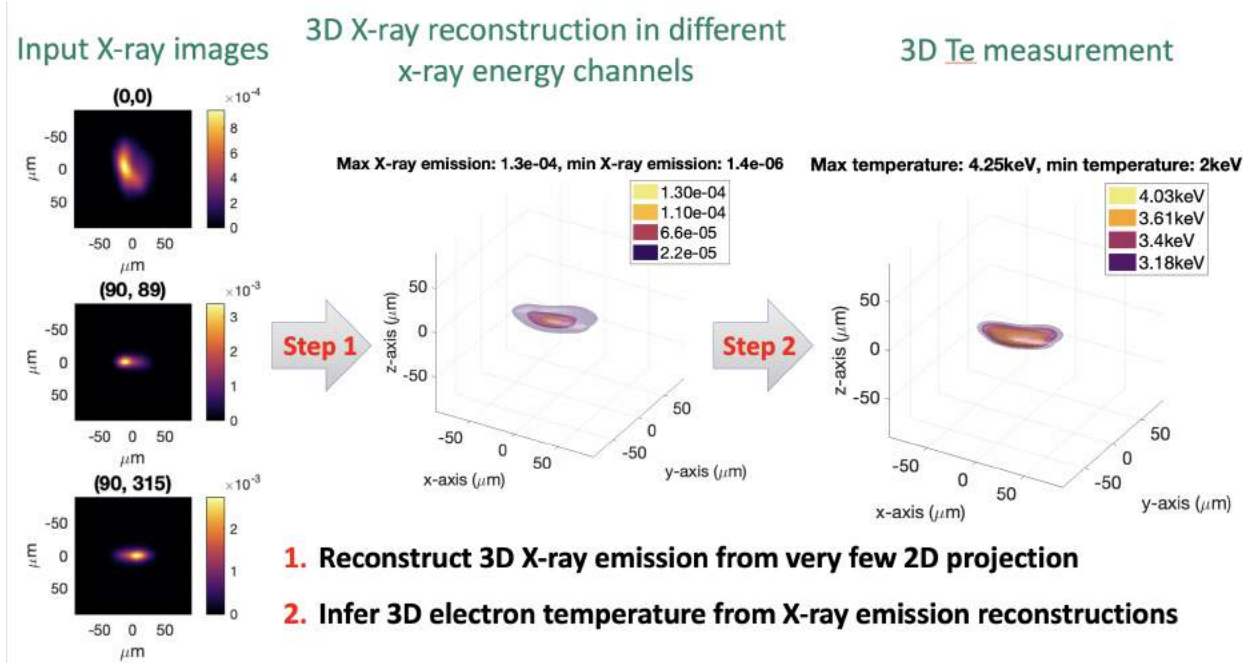


FIGURE 3.6. Our goal is to reconstruct a 3D electron temperature distribution of the plasma in the ICF hotspot using very few 2D X-ray images from different lines-of-sight.

system in which the source distribution constitutes the unknowns, see step 1 in figure (3.6). This is analogous to solving a “3D Sudoku puzzle” by accordingly filling in the unknown values based on their known projection values (sums), as shown in figure (3.7). The matrix involved is usually very large in size and highly deficient in rank. So a direct matrix inversion is not possible and the solution is in general not unique. One technique of efficiently solving such linear system with limited view tomography is the Algebraic Reconstruction Technique (ART). Naturally the more 2D projection images we have from different LOS, the more accurate our reconstruction will be. But due to the limited space inside the target number at the NIF, only limited number of diagnostics can be fielded in an experiment. Our project focuses on reconstruction using 2D projections from two or three LOS, which is generally the number of x-ray images we can use as input for 3D reconstruction.

Furthermore, by varying filtration materials in front of the image detector, we are able to take images of different x-ray energy. Then we can reconstruct x-ray distributions in different energy channels and compute their ratio to infer a 3D electron temperature (Te) measurement of the hotspot, see step 2 in figure (3.6). As input to our 3D x-ray reconstruction, we use the 2D time-integrated x-ray images from *penumbral imaging*, which have high signal-to-noise ratio and

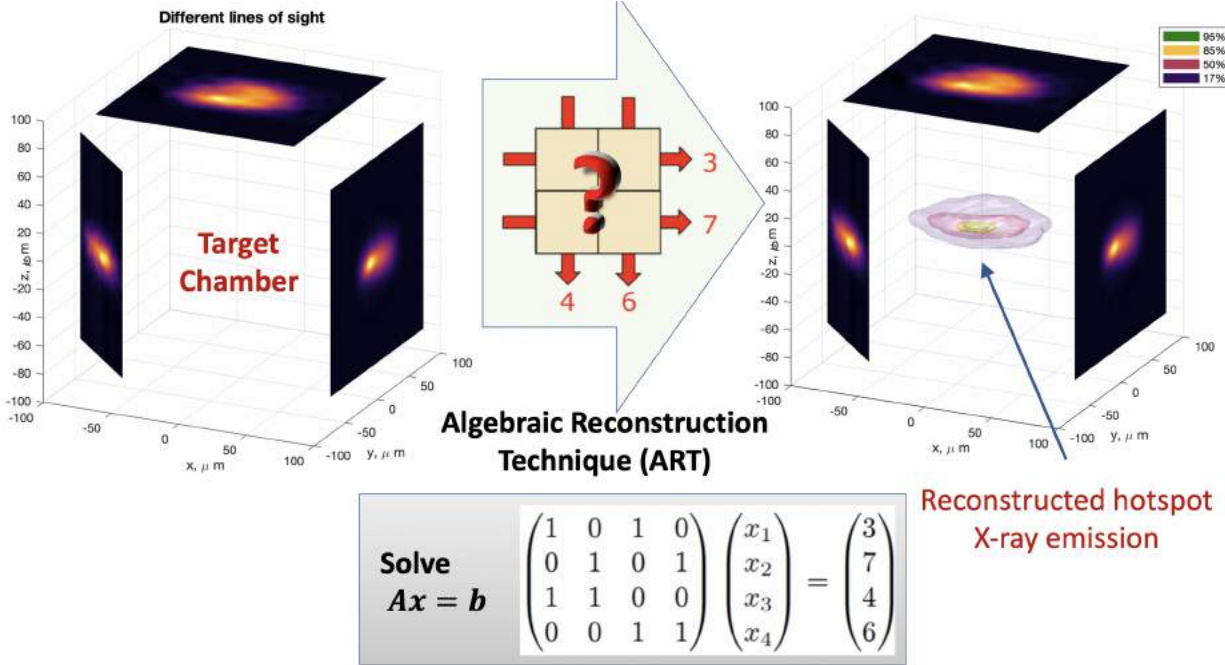


FIGURE 3.7. Reconstruction of 3D X-ray emission distribution using very few 2D X-ray projections via ART which is analogous to solving a “3D Sudoku” puzzle

resolution [BHF⁺16], [BASA⁺17]. Before we present our x-ray image data, we briefly discuss the underlying mathematical theory of the Algebraic Reconstruction Technique.

3.2. Algebraic Reconstruction Technique (ART)

3.2.1. Background. In computed tomography, an essential problem is to reconstruct a set of unknown values based on the given observation values, e.g. projection. A simple example (figure 3.8) is to solve for four unknowns, given projection values of four rays.

$$\begin{array}{|c|c|} \hline x_1 & x_3 \\ \hline x_2 & x_4 \\ \hline \end{array} \rightarrow \begin{array}{l} 3 \\ 7 \\ 4 \\ 6 \end{array}$$

$$\begin{pmatrix} 1 & 0 & 1 & 0 \\ 0 & 1 & 0 & 1 \\ 1 & 1 & 0 & 0 \\ 0 & 0 & 1 & 1 \end{pmatrix} \begin{pmatrix} x_1 \\ x_2 \\ x_3 \\ x_4 \end{pmatrix} = \begin{pmatrix} 3 \\ 7 \\ 4 \\ 6 \end{pmatrix}$$

FIGURE 3.8. A Sudoku puzzle - reconstruction of unknowns from known projections
Source: Per Christian Hansen, Technical University of Denmark

This is equivalent to solving a system of linear equation $Ax = b$ for an unknown vector x . The one entries in the i -th row of the matrix A indicate the intersections of the i -th projection ray with

the unknowns and the i -th entry of the vector b gives the corresponding projection value. In general, the matrix A can be of dimension $m \times n$ where m is the number of rays and n the number of known. In the *limited-view* computer tomography where only few projection rays are given, we can assume $m \leq n$ and the matrix A to be sparse. In our illustrative example, the matrix A is rank-deficient and hence there are *infinitely many solutions* given by $x = \begin{pmatrix} 1 & 3 & 2 & 4 \end{pmatrix}^T + k \cdot \begin{pmatrix} -1 & 1 & 1 & -1 \end{pmatrix}^T$ for any $k \in \mathbb{R}$, where the vector $\begin{pmatrix} -1 & 1 & 1 & -1 \end{pmatrix}^T$ can be replaced with an arbitrary component in the null space of A . This shows that the uniqueness of the solution can be characterized by the rank of the matrix A . From linear algebra, we know that in the case of $n = m$, the solution is uniquely determined if A is full-rank (and hence invertible, the solution is then $x = A^{-1}b$).

More importantly, a geometric interpretation in solving for n knowns with m given projections is that the i -th equation from the linear system, $r_i \cdot x = b_i$ with r_i being the i -th row vector in A and the i -th entry in vector b , defines an affine plane in \mathbb{R}^n . The solution x_* lies in the intersection of all hyperplanes, i.e.

$$x_* \in \bigcap_{i=1}^N \{x \in \mathbb{R}^N \mid r_i \cdot x = b_i\}, \quad \text{where } A := \begin{pmatrix} r_1 & r_2 & \cdots & r_N \end{pmatrix}^T \text{ and } b := \begin{pmatrix} b_1 & b_2 & \cdots & b_N \end{pmatrix}^T$$

In the case of $m = n = 2$ and $A = \begin{pmatrix} a_{11} & a_{12} \\ a_{21} & a_{22} \end{pmatrix}$, the intersection of the two straight lines in \mathbb{R}^2 is the solution (figure 3.9).

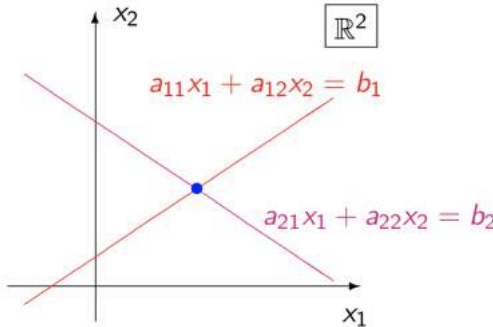


FIGURE 3.9. Geometric interpretation of $Ax = b$ in $m = n = 2$
Source: Per Christian Hansen, Technical University of Denmark

3.2.2. ART. The *Kaczmarz* algorithm is one of the most basic iterative solvers for the linear systems arising computer tomography. It is also known as the *Algebraic Reconstruction Technique* (ART). [Nat01], [Her09], [Buz08]. The original algorithm is due to Kaczmarz [Kac] and the name ART originates from the seminal paper by Gordon, Bender, and Herman [GBH70]. The

ART algorithm can be best described using the geometric interpretation above: Given some initial guess x_0 in \mathbb{R}^n in the solution space, the current iterate is projected from the previous iterate orthogonally on one of the affine hyperplane $r_i \cdot x = b_i$ (figure 3.10). The common practice is to perform the projections following *cyclically* the given row order of the matrix A of dimension $m \times n$, i.e. $i = 1, 2, \dots, m, 1, 2, \dots, m, 1, 2, \dots$.

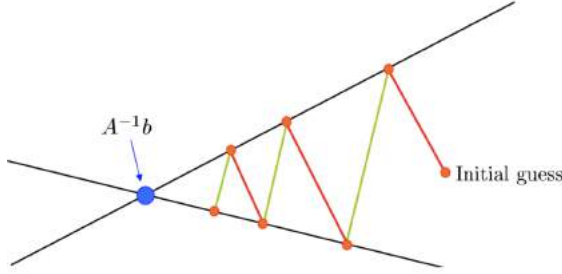


FIGURE 3.10. Successive orthogonal projection onto hyperplanes in ART
Source: Per Christian Hansen, Technical University of Denmark

Algorithm 2 Basic Kaczmarz algorithm

Input: initial vector $x^{(0)}$, matrix A , vector b , and number of iteration n

Output: $n - th$ iterated vector $x^{(n)}$

```

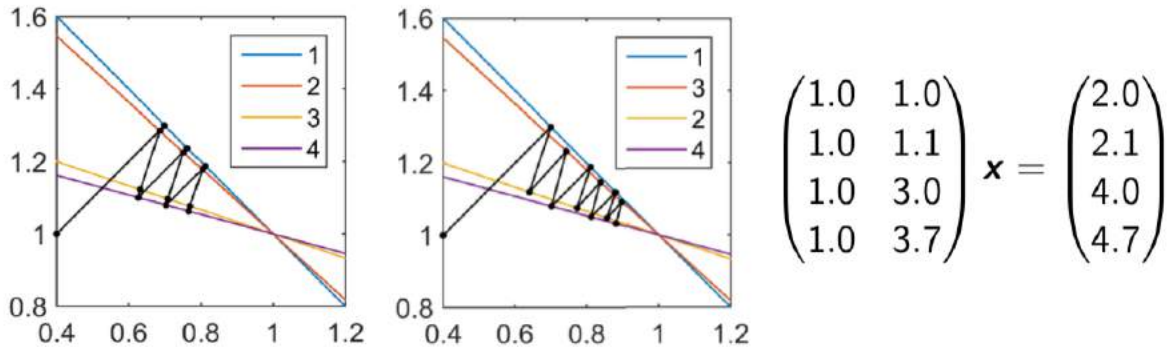
1: procedure KACZMARZ( $x^{(0)}$ , A, b n)
2:   for  $k = 1 \rightarrow n$  do
3:      $i = k \pmod m$                                       $\triangleright$  cyclic row sweep
4:     Compute perpendicular vector from  $x^{(k)}$  to hyperplane  $\{x \in \mathbb{R}^N \mid r_i \cdot x = b_i\}$ 
5:      $v_i(x^{(k)}) = \frac{b_i - r_i \cdot x^{(k)}}{\|r_i\|_2^2} r_i$ 
6:      $x^{(k+1)} \leftarrow x^{(k)} + v_i(x^{(k)})$             $\triangleright$  Compute projection vector and update

```

Note that each iteration corresponds to one projection in the algorithm. One sweep through all m rows of A consists of m iteration. Kaczmarz showed convergence in his paper, i.e. the algorithm produces monotonically improving approximations as the iteration number increases. However, since the Kaczmarz algorithm accesses rows of the matrix *sequentially* (one row per iteration), the convergence rate of this algorithm depends on the selection of the row ordering. This can be illustrated using the geometric interpretation (see figure 3.11). So in general it is difficult to quantify the associated convergence rate. Various linear convergence rates are proved [Deu85], [DH97]. But an undesirable ordering of the rows can significantly worsen the algorithm performance. Therefore,

alternative choices of sweeps through the rows of the matrix were suggested and shown in some cases to improve the rate of convergence:

- Symmetric Kacmarz [BE79]: row sweep from top through bottom and back to top, then repeat, i.e. $i = 1, 2, \dots, m-1, m, m-1, \dots, 1, 2, \dots$.
- Randomized Kacmarz [SV08]: select row i randomly, possibly with probability proportional to the row norm $\|r_i\|_2$



The ordering 1-3-2-4 is preferable: almost twice as fast.

FIGURE 3.11. ART convergence rate depends on the ordering of rows in the matrix
Source: Per Christian Hansen, Technical University of Denmark

Assume that A is invertible ($m = n$ and A has full rank) and all rows of A are scaled to unit 2-norm ($r_i \rightarrow \frac{r_i}{\|r_i\|_2}$ and hence $\|r_i\|_2^2 = 1$ for all i). By considering the Kaczmarz's method (using cyclic row sweep) as successive alternating projections onto some finite dimensional subspaces, an error bound can be shown as

$$\|x^{(k+1)} - x_*\|_2^2 \leq (1 - \det(A)^2) \|x^{(k)} - x_*\|_2^2 \quad [\text{Gal05}]$$

which shows a *linear convergence* of the cyclic Kaczmarz's algorithm.

The simplest randomized scheme to avoid the influence of row ordering is to *choose each possible row with equal probability $1/m$* . Let x_* be the solution such that $Ax_* = b$. In this case, we can derive an expected error bound for the Kaczmarz's method. First, by using Pythagorean theorem (see 3.12) on the k -th and $(k+1)$ -th iterations, we have

$$\|x^{(k+1)} - x_*\|_2^2 = \|x^{(k)} - x_*\|_2^2 - \|x^{(k+1)} - x^{(k)}\|_2^2$$

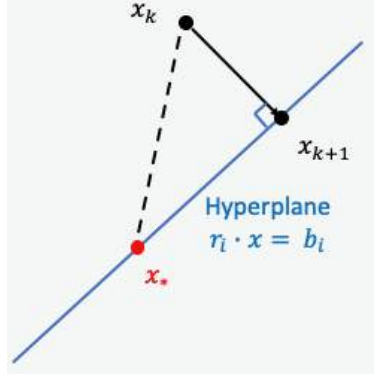


FIGURE 3.12. Projection onto a hyperplane

Second, we compute the expectation with respect to the $(k + 1)$ -th iteration

$$\begin{aligned}\mathbb{E}\|x^{(k+1)} - x_*\|_2^2 &= \|x^{(k)} - x_*\|_2^2 - \mathbb{E}\|x^{(k+1)} - x^{(k)}\|_2^2 = \|x^{(k)} - x_*\|_2^2 - \mathbb{E}\left[\left\|\frac{b_i - r_i \cdot x^{(k)}}{\|r_i\|_2^2} r_i\right\|_2^2\right] \\ &= \|x^{(k)} - x_*\|_2^2 - \mathbb{E}\left[\frac{\|b_i - r_i \cdot x^{(k)}\|_2^2}{\|r_i\|_2^4} \|r_i\|_2^2\right]\end{aligned}$$

Since $\|r_i\|_2^2 = 1$ and $b_i = (Ax_*)_i = r_i \cdot x_*$, we have

$$\begin{aligned}\mathbb{E}\|x^{(k+1)} - x_*\|_2^2 &= \|x^{(k)} - x_*\|_2^2 - \mathbb{E}\left[\|r_i \cdot x_* - r_i \cdot x^{(k)}\|_2^2\right] \\ &= \|x^{(k)} - x_*\|_2^2 - \sum_{i=1}^m \frac{1}{m} \left\|r_i \cdot (x_* - x^{(k)})\right\|_2^2 \\ &= \|x^{(k)} - x_*\|_2^2 - \sum_{i=1}^m \frac{1}{m} \left\|A(x^{(k)} - x_*)\right\|_2^2 = \left(1 - \frac{1}{m} \frac{\|A(x^{(k)} - x_*)\|_2^2}{\|x^{(k)} - x_*\|_2^2}\right) \|x^{(k)} - x_*\|_2^2\end{aligned}$$

Note that we did not assume our solution x_* is unique. Indeed the above inequality holds for any solution x_* . Furthermore, recall the definition of the 2-norm of the inverse matrix ,

$$\text{for any vector } v, \quad \frac{\|v\|_2}{\|Av\|_2} \leq \sup_{x \neq 0} \frac{\|x\|_2}{\|Ax\|_2} := \|A^{-1}\|_2 \quad \Rightarrow \quad \frac{\|A(x^{(k)} - x_*)\|_2^2}{\|x^{(k)} - x_*\|_2^2} \geq \frac{1}{\|A^{-1}\|_2^2}$$

Therefore, we arrive at a bound for the expected error

$$\mathbb{E}\|x^{(k+1)} - x_*\|_2^2 \leq \left(1 - \frac{1}{m\|A^{-1}\|_2^2}\right) \|x^{(k)} - x_*\|_2^2$$

which shows a linear convergence if the reduction factor $\rho := 1 - \frac{1}{m\|A^{-1}\|_2^2}$ is less than one.

Using $\|A\|_2 \|A^{-1}\|_2 \geq \|AA^{-1}\|_2 = \|I\| = 1$ together with the matrix inequality $\|A\|_2 \leq \|A\|_F$ where $\|A\|_F := \sqrt{\sum_{i=1}^m \sum_{j=1}^n a_{ij}^2}$, we have

$$\frac{1}{\|A^{-1}\|_2} \leq \|A\|_2 \leq \sqrt{\sum_{i=1}^m \sum_{j=1}^n a_{ij}^2} \leq \sqrt{m \cdot \max_i \|r_i\|_2^2} = \sqrt{m} \quad \Rightarrow \quad 0 \leq \frac{1}{m\|A^{-1}\|_2^2} \leq 1$$

which shows that $\rho < 1$.

An alternative randomized Kaczmarz's method suggested by Strohmer and Verhsynin is to choose each row with the probability $\frac{\|r_i\|_2^2}{\|A\|_F^2}$. They arrive at the following expected error bound:

$$\mathbb{E}\|x^{(k+1)} - x_*\|_2^2 \leq \left(1 - \frac{1}{R^2}\right) \|x^{(k)} - x_*\|_2^2 \quad [\text{SV08}]$$

where $R := \|A\|_F \|A^{-1}\|_2$ and R is closely related to the condition $\kappa(A) := \|A\|_2 \|A^{-1}\|_2$. Using the matrix inequality $\|A\|_2 \leq \|A\|_F \leq \sqrt{\text{rank}(A)} \|A\|_2$, this bound can be rewritten as

$$\mathbb{E}\|x^{(k+1)} - x_*\|_2^2 \leq \left(1 - \frac{1}{m\kappa(A)^2}\right) \|x^{(k)} - x_*\|_2^2$$

If κ is large, after $k = m$ steps, the reduction factor is approximately $(1 - \frac{1}{m\kappa^2})^m \approx 1 - \frac{1}{\kappa^2}$.

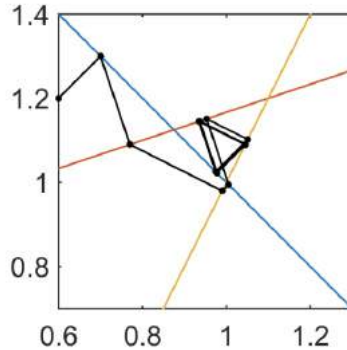


FIGURE 3.13. Cyclic convergence in ART, $m = 3, n = 2$
Source: Per Christian Hansen, Technical University of Denmark

Lastly, if the system $Ax = b$ is *inconsistent*, e.g. there is no solution due to incorrect projection values given. This is equivalent to saying that affine hyperplanes associated with the rows of A do not intersect at a single point, or the vector b is not in the range of the matrix A . This might lead to a *cyclic convergence* (see figure 3.13) where the sequence of projections on each hyperplane converges to a point [Tan71]. To avoid this, we can consider a relaxation of algorithm (2) by adding a relaxation parameter in step 6, i.e. $x^{(k+1)} \leftarrow x^{(k)} + \omega v_i(x^{(k)})$ with $0 < \omega < 2$. Choosing diminishing

parameters such as $\omega = 1/k$ or $\omega = 1/\sqrt{k}$, where k is the total number of row updates, the Kaczmarz iterates are proved to converge to a single point, instead of cyclic convergence [Ber11].

3.2.3. Cimmino algorithm. In order to avoid the potential problem of row ordering, one way is to *simultaneously*, instead of sequentially, involve all rows at a time. The *Cimmino's method* computes the next iteration vector as the average of all the projections of the previous iterated vector (see 3.14). We can formulate the Cimmino's method mathematically by using the symbols from the Kaczmarz method in algorithm (2):

$$x^{(k+1)} = x^{(k)} + \frac{1}{m} \sum_{i=1}^m v_i(x^{(k)}) = x^{(k)} + \frac{1}{m} \sum_{i=1}^m \frac{b_i - r_i \cdot x^{(k)}}{\|r_i\|_2^2} r_i$$

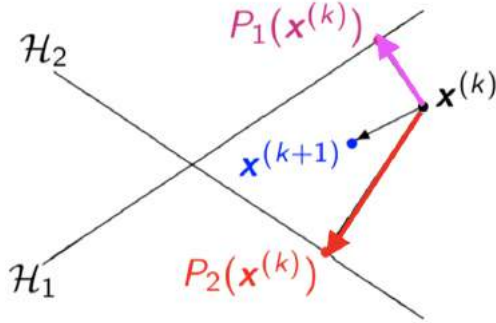


FIGURE 3.14. Geometric interpretation of Cimmino's method
Source: Per Christian Hansen, Technical University of Denmark

Naturally, since all rows are used, the Cimmino's algorithm can be re-written using matrix multiplications:

$$\begin{aligned} x^{(k+1)} &= x^{(k)} + \frac{1}{m} \left(\frac{r_1}{\|r_1\|_2^2} \cdots \frac{r_m}{\|r_m\|_2^2} \right) \begin{pmatrix} b_1 - r_1 \cdot x^{(k)} \\ \vdots \\ b_m - r_m \cdot x^{(k)} \end{pmatrix} \\ &= x^{(k)} + \frac{1}{m} (r_1 \quad \vdots \quad r_m)^T \begin{pmatrix} \|r_1\|_2^{-2} & & \\ & \ddots & \\ & & \|r_m\|_2^{-2} \end{pmatrix} (b - Ax^{(k)}) \\ &= x^{(k)} + A^T M (b - Ax^{(k)}), \quad \text{where } M = \text{diag} \left(\frac{1}{m \|r_i\|_2^2} \right) \end{aligned}$$

Algorithm 3 Basic Cimmino algorithm

Input: initial vector $x^{(0)}$, matrix A , vector b , and number of iteration n

Output: n -th iterated vector $x^{(n)}$

```

1: procedure CIMMINO( $x^{(0)}$ , A, b n)
2:   for  $k = 1 \rightarrow n$  do
3:      $M \leftarrow diag\left(\frac{1}{m\|r_i\|_2^2}\right)$ 
4:      $x^{(k+1)} \leftarrow x^{(k)} + A^T M (b - Ax^{(k)})$ 

```

Clearly, one Cimmino iteration involves all rows of matrix A whereas one Kaczmarz iteration involves only one row. Therefore, the computational cost of one Cimmino iteration is equivalent to one sweep (m iterations) in the Kaczmarz method. In terms of convergence, there are results showing the mathematical equivalence between the action of averaging projections in the Cimmino method and the row-by-row action in the Kaczmarz method [Gor18].

We can illustrate the convergence of the algorithm in some simple cases. We assume A is invertible ($m = n$ and A has full rank) and $x^{(0)} = 0$ as initial vector. We denote I as the $m \times m$ identity matrix, then

$$x^{(1)} = A^T Mb, \quad x^{(2)} = (I - A^T MA)A^T Mb + A^T Mb$$

So the $(k+1)$ -th iteration can be expressed as

$$x^{(k+1)} = \sum_{i=0}^k (I - A^T MA)^i A^T Mb$$

This is a geometric series of matrix. Since A is invertible, so is $A^T MA$. Hence,

$$\begin{aligned} x^{(k+1)} &= \sum_{i=0}^k (I - A^T MA)^i A^T Mb = \left[I - (I - A^T MA)^{k+1} \right] (A^T MA)^{-1} A^T Mb \\ &= \left[I - (I - A^T MA)^{k+1} \right] A^{-1} b \end{aligned}$$

We can show that the largest eigenvalue of the symmetric matrix $I - A^T MA$ is strictly smaller one. We denote the eigenvalues of the matrix $A^T MA$ with $\lambda_1 \geq \lambda_2 \geq \dots \geq \lambda_n$ in a decreasing order.

To see that, first, the symmetric matrix $A^T MA$ is positive definite since for any vector v , $v^T A^T M A v = (D A v)^2 > 0$ where D is a diagonal matrix with $D = diag\left(\frac{1}{\sqrt{m}\|r_i\|_2}\right)$. Hence $\lambda_1 \geq \lambda_2 \geq \dots \geq \lambda_n \geq 0$ and all of them are real. Second, $tr(A^T MA) = 1$, this implies $\sum_{j=1}^n \lambda_j = 1$.

Combing with the first observation gives $0 < \lambda_j < 1$ for all j . Therefore, all eigenvalues of $I - A^T M A$ satisfy $0 < 1 - \lambda_j < 1$ and hence have magnitude strictly smaller than one.

Therefore, the geometric series converges to the identity matrix, i.e.

$$\lim_{k \rightarrow \infty} \left[I - (I - A^T M A)^{k+1} \right] = I,$$

and the iterations converge to the solution, i.e. $\lim_{k \rightarrow \infty} x^{(k+1)} = A^{-1} b$.

Furthermore, if matrix A is both invertible and scaled such that $\|A\|_2^2 = m$, an error bound can be shown as

$$\|x^{(k+1)} - x_*\|_2^2 \leq \left(1 - \frac{2}{1 + \kappa^2}\right) \|x^{(k)} - x_*\|_2^2 \quad [\text{Nes14}]$$

This shows a *linear convergence* of the Cimmino's method. Furthermore, if κ is large, the reduction factor of one iteration in the Cimmino's method is approximately $1 - \frac{2}{\kappa^2}$, which is almost the same reduction factor for one sweep over all rows in the (randomized) Kacmarz's method.

There are other algorithms similar to the Cimmino's method, which access to all rows of matrix in one iteration. These methods form a class of technique named *Simultaneous iterative reconstruction technique* (SIRT). A general form of these methods involves update of the form

$$x^{(k+1)} \leftarrow x^{(k)} + \omega D A^T M (b - A x^{(k)})$$

where ω is a relaxation parameter and D, M are both diagonal matrices. In the case of the Cimmino's method, D is an identity matrix, $M_{ii} = \frac{1}{m\|r_i\|_2^2}$, and $0 < \omega < \frac{2}{\|A^T M A\|_2}$. In the case of both D, M being the identity matrices and $0 < \omega < \frac{2}{\|A\|_2}$, it becomes the *Landweber* algorithm, also known as the *projected gradient descent* method which is commonly used in solving convex optimization problems.

Lastly, even if the system $Ax = b$ is inconsistent, the Cimmino's method (with a fixed relaxation parameter) is *guaranteed to converge*. Indeed, the Cimmino's method corresponding to the gradient descent method in solving the following weighted least square problem

$$\arg \min_{x \in \mathbb{R}^n} \left\| M^{1/2} (Ax - b) \right\|_2^2, \quad \text{where } M_{ii}^{1/2} = \frac{1}{\sqrt{m\|r_i\|_2}}$$

Hence, in the case of an inconsistent linear system, the Cimmino's iterations still converge to the corresponding (weighted) least square solution.

In our 3D X-ray reconstruction, we apply the Cimmino's method. We use an open-source MATLAB software package *AIR Tool* (github.com/jakobsj/AIRToolsII) [HJ18]. This package is originally developed for two-dimensional computer tomography and we generalize the usage of the package and apply it to solve three-dimensional problems.

3.3. 3D x-ray reconstruction of nuclear fusion hotspot using two or three lines of sight with synthetic and experimental data

In this section, the purpose of a synthetic data study is to quantify the systematic errors in the 3D x-ray reconstruction produced in ART. Here is the procedure in our synthetic data study:

- (1) We start with a synthetic 3D electron temperature (T_e) distribution, use it to compute 3D synthetic x-ray emission distributions in different x-ray energy channels, and use these distributions to generate 2D x-ray projection images along different lines of sight (LOS).
- (2) We apply our ART algorithm on the 2D x-ray images to reconstruct the 3D x-ray emission distributions.
- (3) We use different metrics to compare our x-ray reconstruction with the original 3D synthetic x-ray emission distribution derived from our T_e distribution model in step (1).

We first present results from our synthetic data study of comparing x-ray reconstructions using two versus three lines-of-sight. That include a collection of 3D synthetic x-ray emission distributions with different geometries and their reconstructions by applying ART. Then we apply our reconstruction method on four different shots at NIF using the experimental data from N181007, N190530, N190602, and N190730.¹

3.3.1. Generation of 2D x-ray projections. To begin with, in order to obtain our synthetic 3D x-ray emission distributions, we present two models of 3D T_e distributions which resemble the experimental data. Both models are oblate in shape. We show their 3D contour plot of 95%, 85%, 75%, and 50% respectively, with respect to the maximal x-ray emission. We also plot their central lineouts in the x,y,z-directions (figures 3.15, 3.16). The T_e in both models ranges from 2keV to 5 keV.

¹The nomenclature uses YYMMDD to indicate the exact date of an ICF experiment at NIF, where Y, M, and D indicate the year, month, and date respectively.

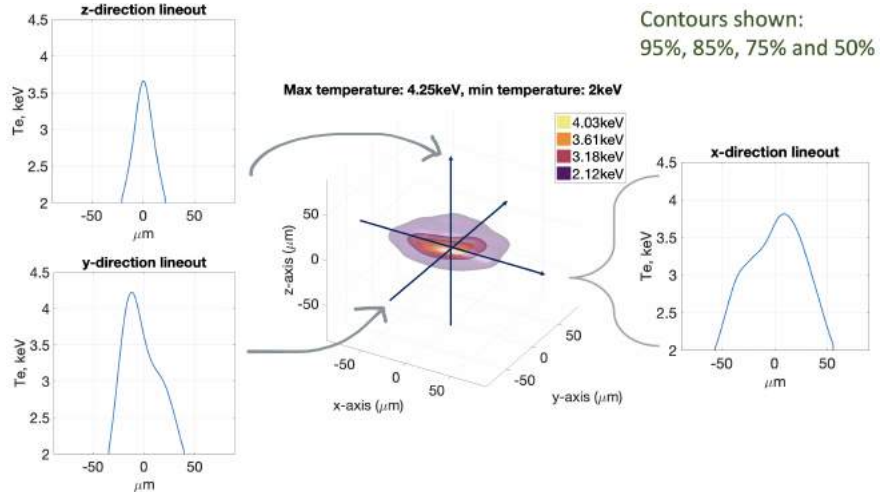


FIGURE 3.15. T_e distribution model A with central lineouts, $T_e \in [2\text{keV}, 5\text{keV}]$

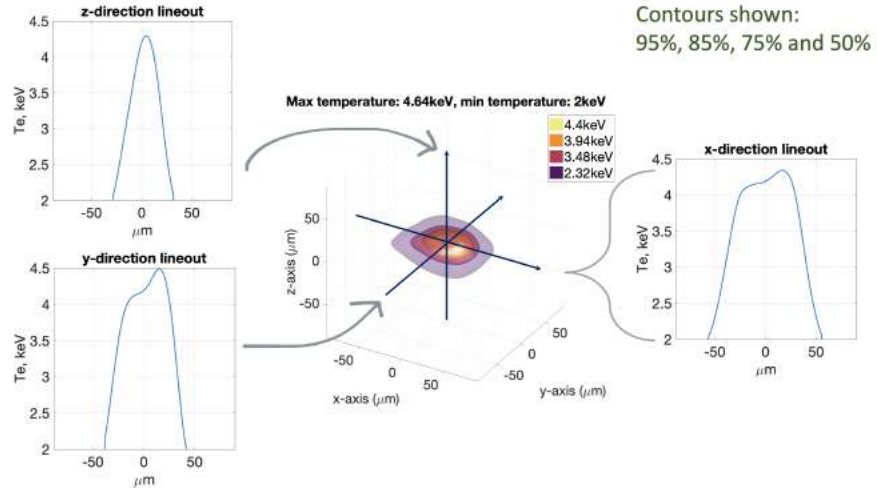


FIGURE 3.16. T_e distribution model B with central lineouts, $T_e \in [2\text{keV}, 5\text{keV}]$

At a given temperature T_e , the x-ray from free-free emission (*bremsstrahlung radiance* ϵ) of a deuterium-tritium nuclear fusion reaction can be expressed as a function of energy $h\nu$ [JBM⁺18],

$$(3.1) \quad \epsilon(h\nu) \propto \frac{\exp(-h\nu/T_e)}{(h\nu)^{0.39}} \frac{\exp(-\tau_\nu)}{T_e^{0.15}}$$

where τ is the optical depth accounting for the attenuation of the x-ray emission by the fuel and remaining ablator at stagnation. This equation implies that the lower T_e is, the faster the exponential decay of the emission over $h\nu$, see figure (3.17) in which the y-axis is in a logarithmic scale.

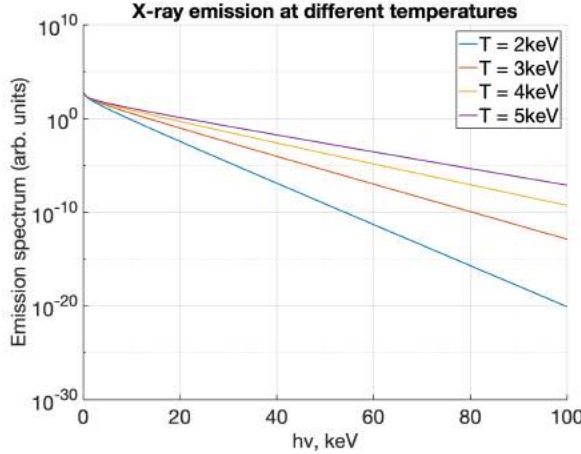


FIGURE 3.17. X-ray emission at different T_e

Moreover, we use two different x-ray energy channels which are typically fielded in the diagnostic setup at NIF. We list the exact filtration materials of the two energy channels, see table in figure (3.18). They differ only by the amount of titanium. Channel 1 is a “softer” channel compared to channel 2 since it contain less titanium and hence allows more x-ray energy to pass through and be absorbed by an image plate inside an x-ray image detector. The *system response* of these channels are obtained by multiplying the filter’s response with the response of the image plate in the image detector. Here we choose an optical depth $\tau(11\text{keV}) = 1$, evaluated at a photon energy of 11 keV. Figure (3.19) show the plot of system responses of the two x-ray energy channels on the left and the detected x-ray emissions at $T_e = 4\text{keV}$ on the right, which are the product of the x-ray emission $\epsilon(4\text{keV})$ and the corresponding system responses of channels 1 and 2.

Filtration materials	Channel 1	Channel 2
Polycarbonate	$2000\mu\text{m}$	$2000\mu\text{m}$
Kapton (polyimide)	$456\mu\text{m}$	$456\mu\text{m}$
Diamond	$120\mu\text{m}$	$120\mu\text{m}$
Gold	$2.25\mu\text{m}$	$2.25\mu\text{m}$
Titanium	$108.5\mu\text{m}$	$217\mu\text{m}$

FIGURE 3.18. Filtration materials of the two x-ray energy channels

In each voxel in the synthetic 3D T_e model, knowing the T_e in it, we can compute the x-ray emission using the equation (3.1), multiply it with the system response curve of channel 1 (or 2), and then integrate it over the energy spectrum $h\nu$ to obtain a detected x-ray emission value $\tilde{\epsilon}$. Let ϵ denote the bremsstrahlung radiation calculated using equation (3.1), which is a function of both

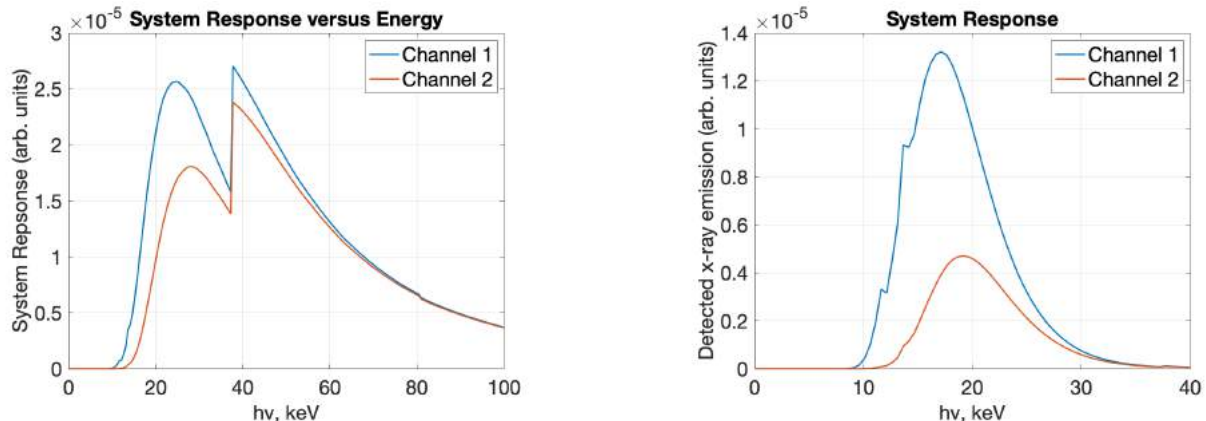


FIGURE 3.19. System response (left) and detected x-ray emission at $T_e = 4\text{keV}$ (right)

T_e and $h\nu$. Also let s denote the system response of an energy channel which is a function of $h\nu$. The mathematical expression to compute $\tilde{\epsilon}$ at a given temperature T_e is

$$(3.2) \quad \tilde{\epsilon}(T_e) = \int \epsilon(T_e, h\nu) \cdot s(h\nu) d(h\nu)$$

Using this formula, we can obtain synthetic 3D x-ray emission distributions in channels 1 and 2 for both T_e models A and B. We show here the 3D contour plots of 95%, 85%, 50%, and 17% (with respect to the maximum x-ray emission) of the x-ray distribution emissions in channel 1 for both T_e models. The x-ray distribution emissions in channel 2 are similar. We also show their central lineouts of x-ray emission and the original T_e , see figures (3.20) and (3.21). Note that *the x-ray emission distributions appear to decay much more smoothly to zero towards their periphery because of the smoothing effect due to the exponential decay term in equation (3.1) together with the integration over the energy spectrum, in contrast to the sharp falloffs in the T_e resulted from the restriction on the T_e range.*² This observation also justifies the lower bound of $T_e = 2\text{keV}$ we imposed on synthetic T_e models A and B since x-ray emission from hotspot regions below 2keV can hardly be detected.

We can now generate 2D x-ray projection images by summing the x-ray emission values along different LOS. We denote the direction of our LOS inside the target chamber using the spherical coordinate (θ, ϕ) on a unit sphere where $0 \leq \theta \leq \pi$ is the polar angle and $0 \leq \phi \leq 2\pi$ is the

²In channel 1, the detected x-ray emission at $T_e = 2\text{keV}$ has order of magnitude $1\text{e-}6$ (arb. units) while the detected x-ray emission at $T_e = 0\text{keV}$ should be 0. This difference is not noticeable in the lineouts in figures (3.20) and (3.21), where the y-axis shown in the order of magnitude $1\text{e-}4$.

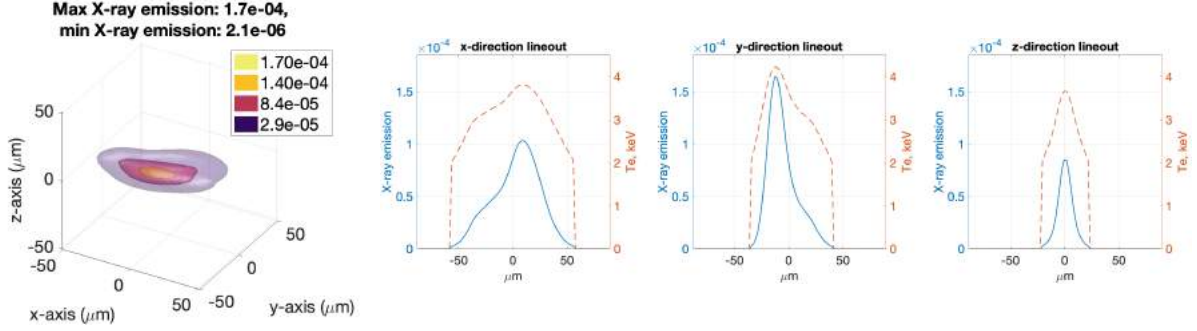


FIGURE 3.20. Detected x-ray emission from model A in channel 1 (left) and its central lineouts (right)

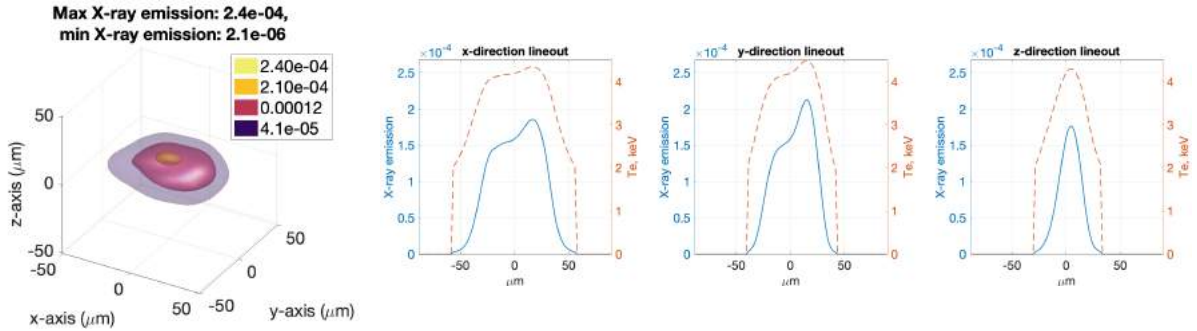


FIGURE 3.21. Detected x-ray emission from model B in channel 1 (left) and its central lineouts (right)

azimuthal angle as in the physics convention. There are three different LOS where x-ray diagnostics are commonly fielded in experiments:

- (1) $(0^\circ, 0^\circ)$ known as PDIM ³,
- (2) $(90^\circ, 89^\circ)$ known as ARIANE ⁴,
- (3) and $(90^\circ, 315^\circ)$.

For the reconstruction using 2 LOS only, we will use $(0^\circ, 0^\circ)$ and $(90^\circ, 89^\circ)$. The LOS $(90^\circ, 78^\circ)$, which is different than PDIM, ARIANE, and $(90^\circ, 315^\circ)$, used in the experimental data N181007 and N190730 will be introduced in the subsequent subsections.

In figure (3.22) we illustrate these three LOS inside the NIF target chamber (left) and the three LOS with the synthetic 3D hotspot x-ray emission. In figures (3.27) and (3.24) we show the 2D x-ray projections of models A and B along these three different LOS.

³Polar diagnostic instrument manipulator, refer to [Labb] for details on its construction

⁴Active Readout in a Neutron Environment, refer to [AFS⁺¹²], [SAB⁺¹¹] for details on its experimental setup

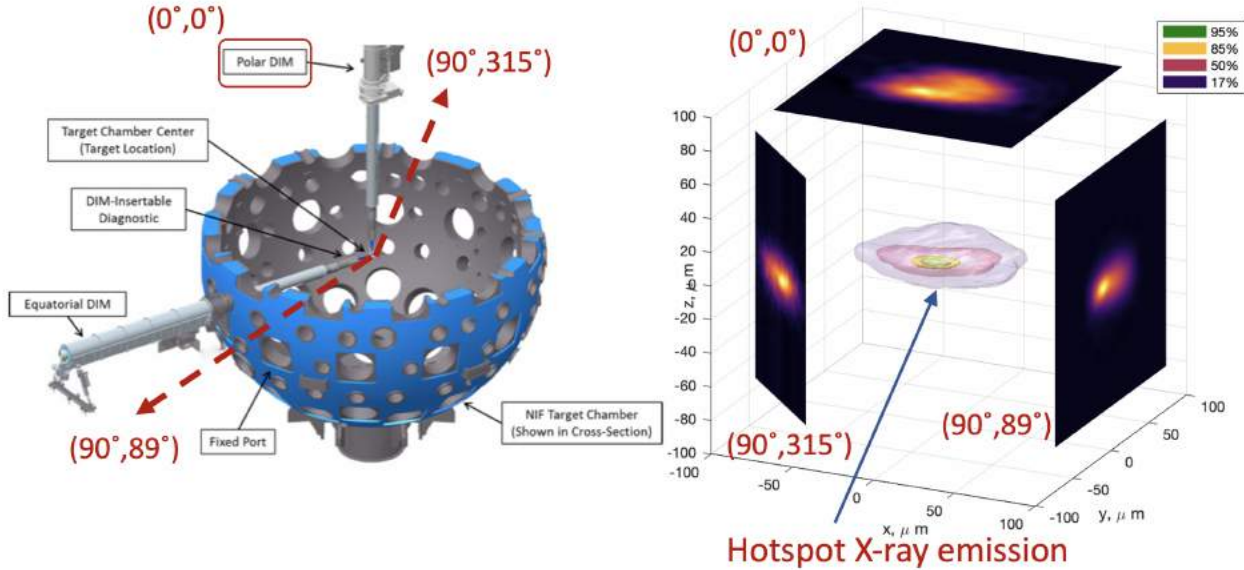


FIGURE 3.22. PDIM, ARIANE, and $(90^\circ, 315^\circ)$ inside target chamber (left) and with the 3D hotspot x-ray emission (right)

Source: target chamber figure (left) is taken from [TMA⁺17]

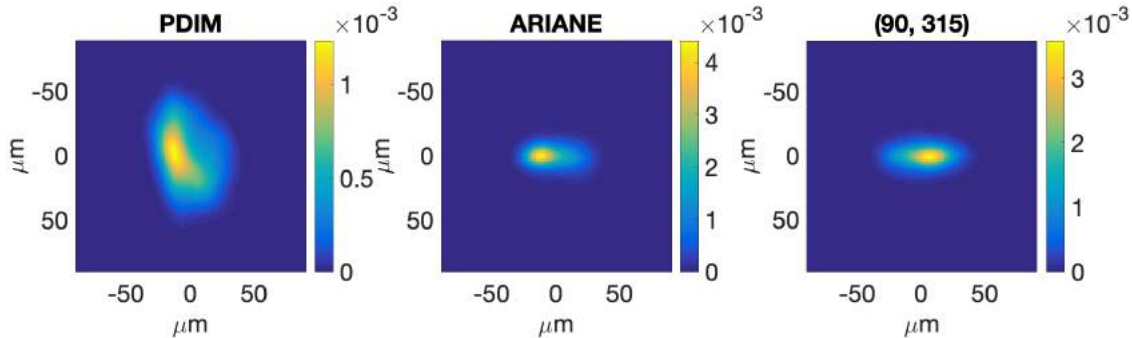


FIGURE 3.23. 2D x-ray projections of model A along PDIM, ARIANE, and $(90^\circ, 315^\circ)$ in channel 1

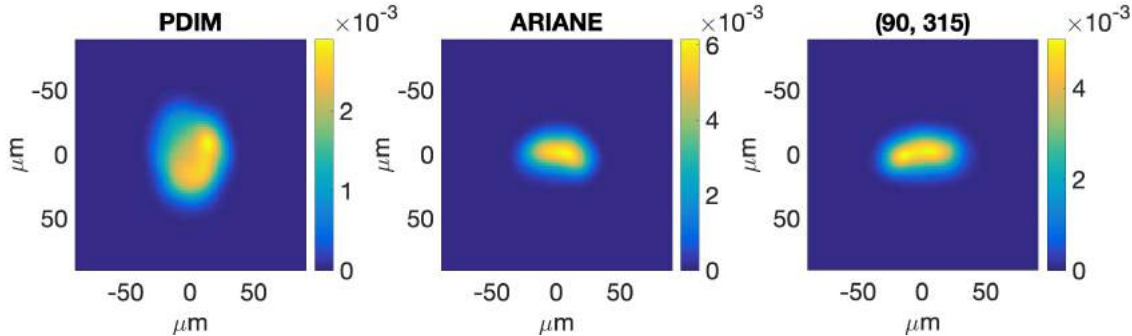


FIGURE 3.24. 2D x-ray projections of model B along PDIM, ARIANE, and $(90^\circ, 315^\circ)$ in channel 1

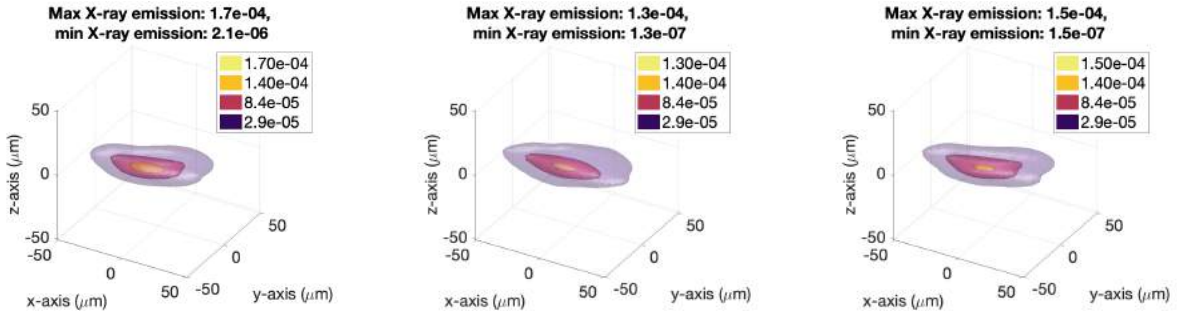


FIGURE 3.25. Synthetic x-ray model A (left) and 3D reconstructions using 2 LOS (middle) and 3 LOS (right)

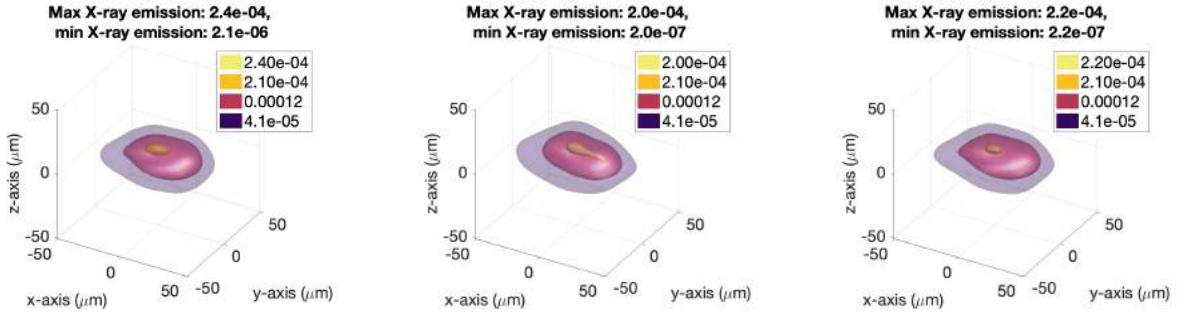


FIGURE 3.26. Synthetic x-ray model B (left) and 3D reconstructions using 2 LOS (middle) and 3 LOS (right)

3.3.2. Reconstructed 3D x-ray emission distributions in synthetic data study and error analysis. We show the contour plots of the reconstructed 3D x-ray emission distributions obtained from our ART algorithm using 2 LOS — PDIM and ARIANE versus 3 LOS — PDIM, ARIANE, and $(90^\circ, 315^\circ)$). *In comparison to using 2 LOS, the reconstruction using 3 LOS has a shape more similar to the original model and the reconstructed maximal value is also closer to the original x-ray maximal emission.* See figures (3.25) for model A and figures (3.26) for model B.

In order to check if the 3D x-ray reconstruction is consistent with the input images, we generate 2D projections from our reconstruction along the same LOS as the input projections to the ART algorithm. In both cases of using 2 LOS and 3 LOS, the reconstructed 2D projections look almost identical to the original input x-ray images. This is verified by the relative errors computed per pixel *which are almost zero everywhere*, see figures (3.27) and (3.28).

More importantly, we compare the central lineouts of the reconstructions using 2 LOS versus 3 LOS with the original. see figures (3.29) and (3.30) for model A and figures (3.31) and (3.32) for model B. On one hand, the reconstruction using 2 LOS has lineouts that are similar in shape to the synthetic models but there are discrepancies in the lineouts of the reconstructions. The relative

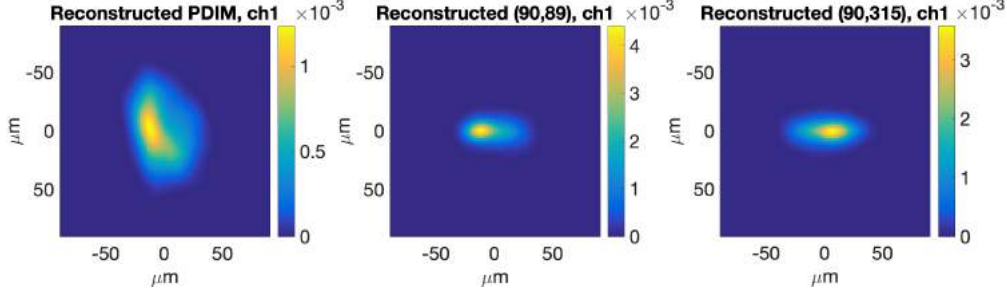


FIGURE 3.27. Consistency of 3D reconstruction (model A in channel 1) — reconstructed 2D projections along the same LOS as in input images

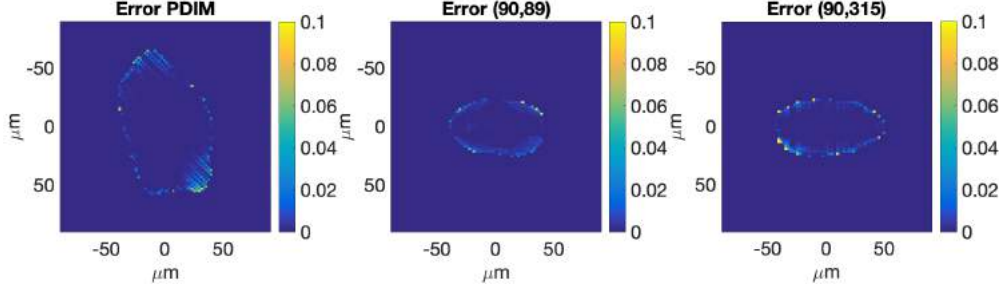


FIGURE 3.28. Relative errors of reconstructed 2D projections (model A in channel 1) are almost zero, colorbar from 0% to 10%

errors are roughly 20% or more in the center of the hotspot. On the other hand, the reconstruction using 3 LOS has lineouts that look almost identical to the synthetic models. The relative errors can be improved to below than 10% in the center of the hotspot. *This shows significant improvement in the 3D x-ray reconstruction from using 2 LOS to using 3 LOS.*

Finally, note that in the reconstructions of both models A and B using 2 or 3 LOS, *the relative errors are similar in both energy channels*. This observation will become very helpful in our 3D T_e measurement in the subsequent sections.

⁵In the first row, the two dash lines are the lineouts from the x-ray reconstructions in both channels whereas the solid lines are from the original synthetic model. In the second row, the two lines are relative errors.

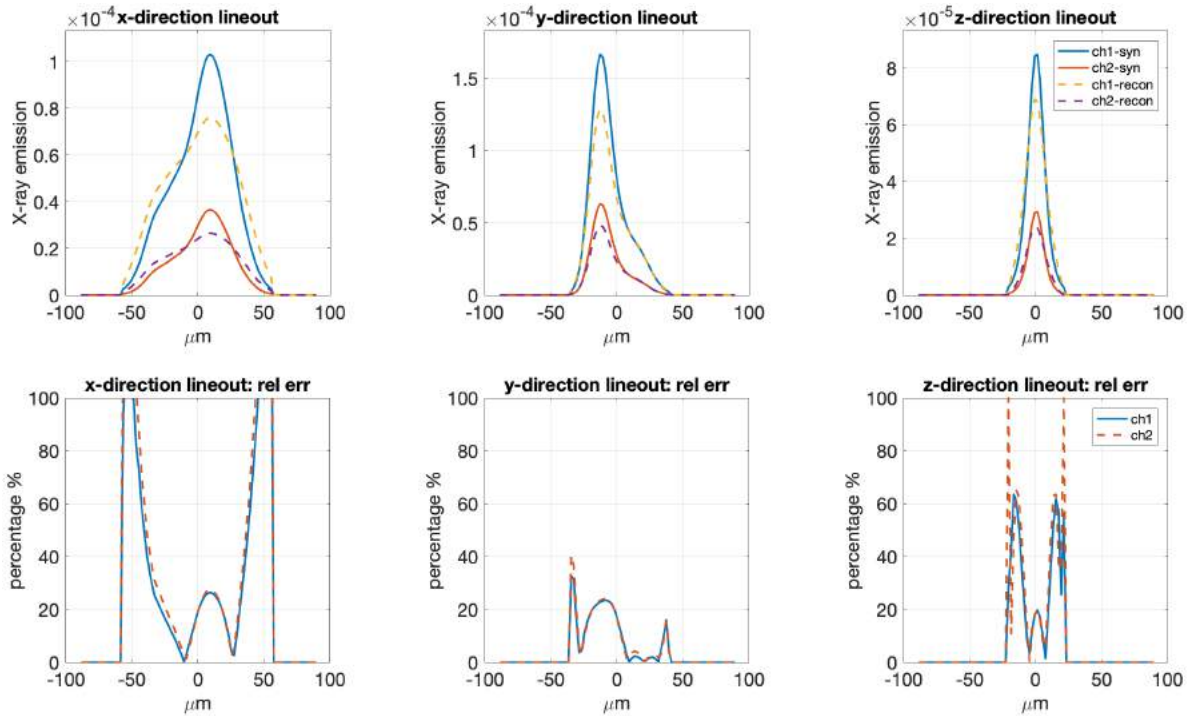


FIGURE 3.29. Central lineouts of 3D x-ray reconstruction using 2 LOS (model A) in both channels 1 and 2 and their relative errors.⁵

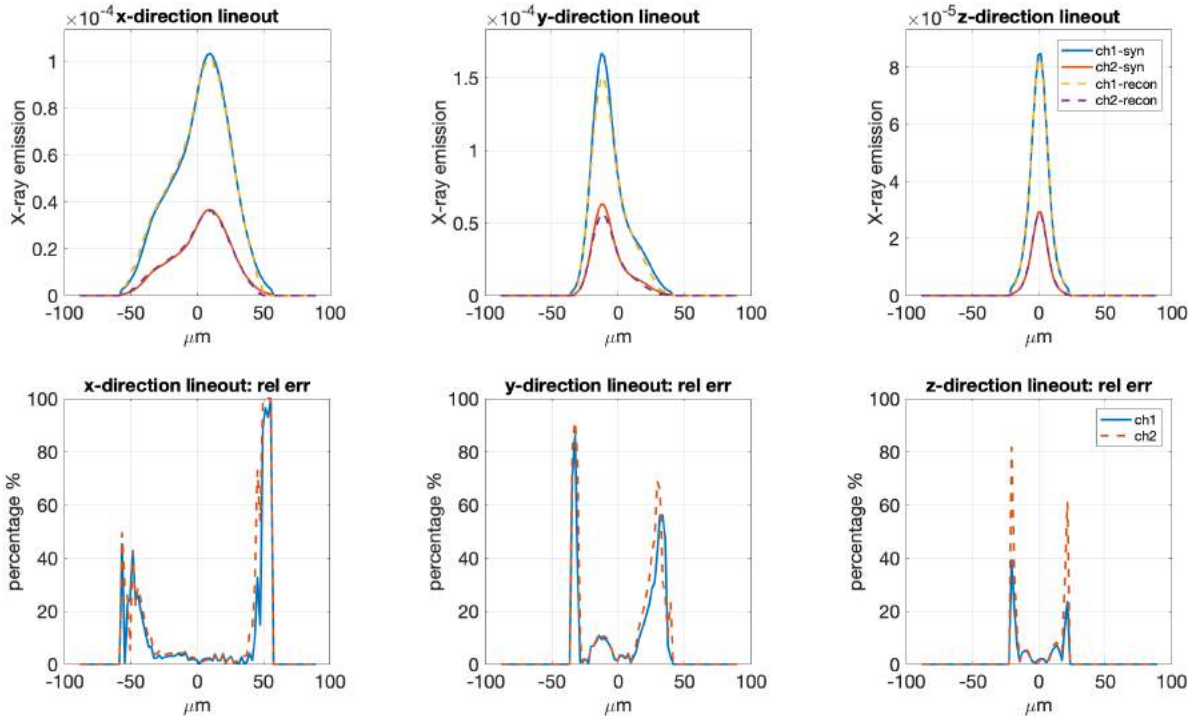


FIGURE 3.30. Central lineouts of 3D x-ray reconstruction using 3 LOS (model A) in both channels 1 and 2 and their relative errors.⁵

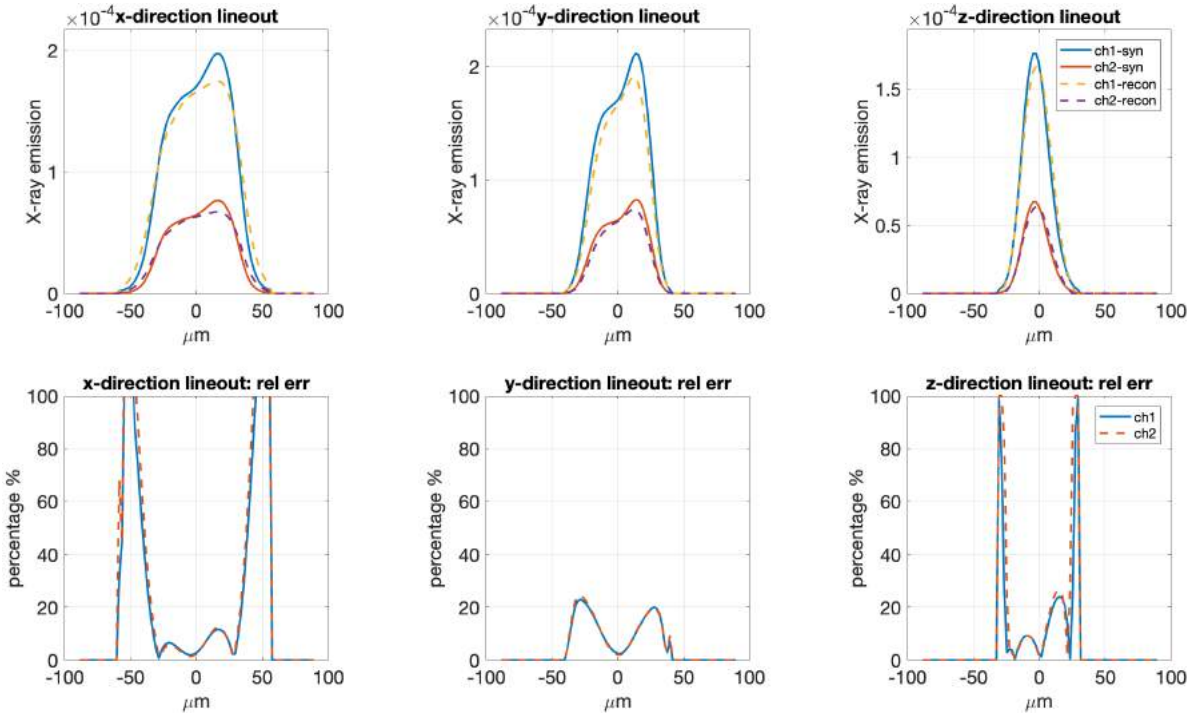


FIGURE 3.31. Central lineouts of 3D x-ray reconstruction using 2 LOS (model A) in both channels 1 and 2 and their relative errors⁵

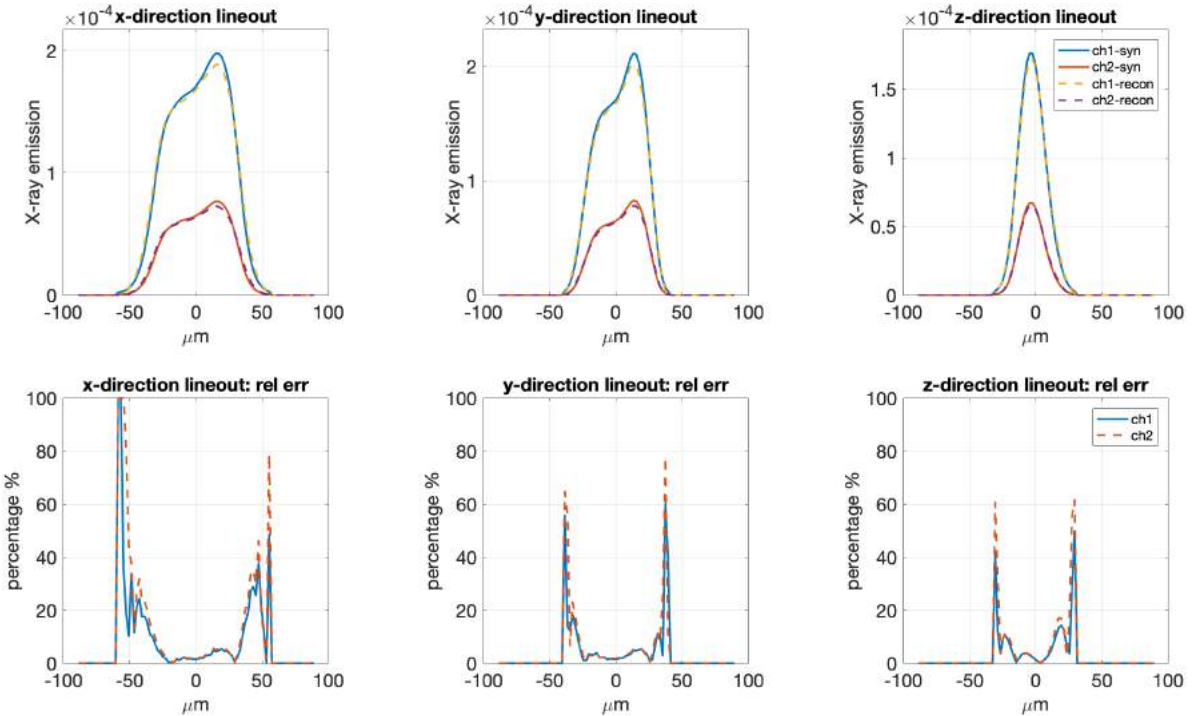


FIGURE 3.32. Central lineouts of 3D x-ray reconstruction using 3 LOS (model A) in both channels 1 and 2 and their relative errors⁵

3.3.3. X-ray reconstructions using experimental data N190602 and N190530. In this section, we apply our ART algorithm to reconstruct 3D x-ray distributions using the experimental data from ICF experiments N190602 and N190530 at NIF. In both experiments, we only have 2 LOS — PDIM and ARIANE, which share a similar energy channel. We list their filtration materials in a table and plot their system response, see figure (3.38). Note that the amount of titanium in both channels are almost the same whereas the channel at ARIANE has extra amount of gold and diamond which are the materials from the hohlraum's view window. Here we choose an experimentally estimated optical depth $\tau(11\text{keV}) = 2$, evaluated at a photon energy of 11 keV. Figures (3.34) and (3.35) shows the experimental penumbral x-ray images taken at PDIM and ARIANE in N190602 and N190530 respectively.

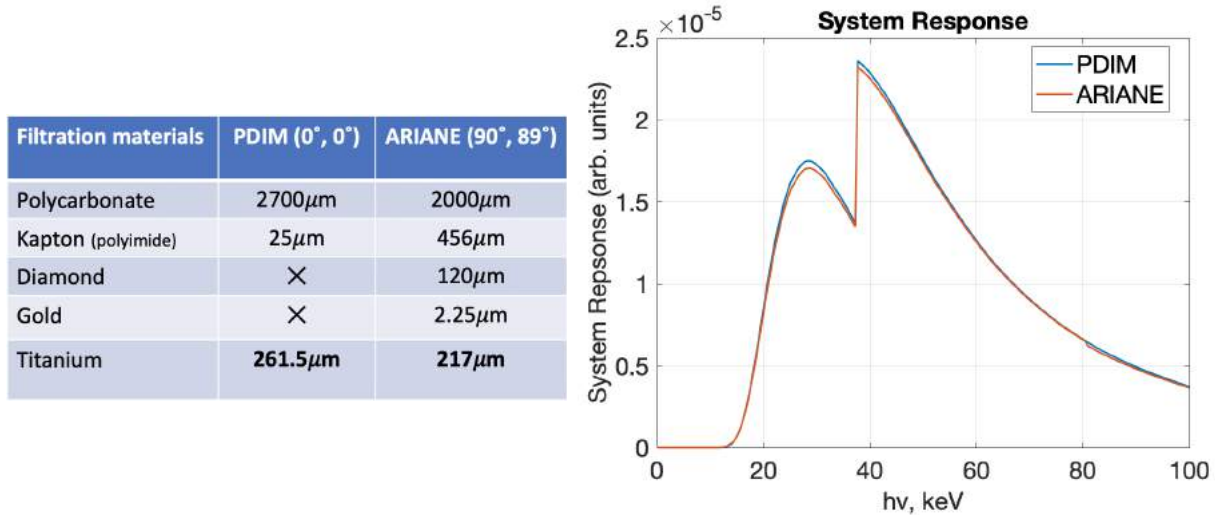


FIGURE 3.33. Filtration materials at PDIM and ARIANE in N190602 and N190530 (left) and system response (right)

However, in contrast to the previous synthetic data study, we need to compute the integrated x-ray emission values of the input images along the *common integrated profile (CIP)*, or known as the *common line of sight (CLOS)*, which is basically a line to which both the PDIM and ARIANE are adjacent, see figure (3.36). The integrated x-ray emission values can be easily computed by summing up the x-ray values per pixel of the input image onto the CIP. *We observe a discrepancy between experimental images from ARIANE and PDIM on the CIP.* This discrepancy can be attributed to a combination of the following three different factors:

- (1) the neutron background noise on the image plates at both ARIANE and PDIM

- (2) harder filtration at ARIANE than at PDIM due to the presence of gold and diamond
- (3) uneven shell opacity at ARIANE and PDIM

This also explains the absence of such discrepancy in the synthetic data study since we did not model noise or opacity and we keep two energy channel filtrations the same at both ARIANE and PDIM. Using one of our examples of 2D Sudoku puzzle illustrated in figure (3.8), we note that the sum of the horizontal projection values $3 + 7 = 10$ is equal to that of the vertical projection values $4 + 6 = 10$. This suggests that *our constraints in the linear system are consistent*, which in turn is crucial to the convergence of the ART algorithm since this condition implies that all hyperplanes intersect at one solution set (recall figures 3.9 and 3.13). Therefore, we need to come up with a method to modify the input PDIM and ARIANE images such that the integrated x-ray emissions agree along the CIP. This can also be seen as a scaling procedure of the input image to ensure that both images contain the same amount of energy.

The main difficulty in this image modification process is to *avoid compromising the underlying hotspot structure captured in the x-ray image*. Also, we want our method to be widely applicable on as many x-ray images as possible, independent of the hotspot geometry. The solution we suggest is to *apply a 2D ART reconstruction algorithm on the PDIM image with the line integrated profile from the ARIANE image*, see figure (3.37). In algorithm (4), We describe our method in details as follows:

- I_{PDIM} is the original experimental PDIM image
- I_{equat} is an equatorial image , e.g. ARIANE or any LOS $(90^\circ, \phi)$ with $0 \leq \phi \leq 2\pi$
- A is the projection matrix for PDIM image towards its CIP with the equatorial image
- ϵ is our tolerance for the discrepancy in CIP of the PDIM and the equatorial image
- \tilde{I}_{PDIM} is the scaled PDIM image, which has the same CIP as the equatorial image
- $x^{(n)}$ is the vector in the n -th iteration.

In this procedure, we use the original PDIM image as an initial guess to the 2D ART reconstruction and we reconstruct a modified PDIM image that matches with the CIP of the equatorial image (in this case, ARIANE).

Note that not only do the PDIM and ARIANE agree perfectly on the CIP after the 2D ART is applied, the hotspot shape in the image is preserved and not distorted. This is de facto a 2D reconstruction with 1 LOS, i.e. integrated x-ray emission at ARIANE.

Algorithm 4 2D ART algorithm applied on PDIM image

Input: I_{PDIM} , I_{equat} , A , and ϵ

Output: \tilde{I}_{PDIM}

- 1: **Initialize:** use I_{PDIM} as an initial guess $x^{(0)}$ and form vector b from image I_{equat} .
 - 2: **while** I_{PDIM} does not match with I_{equat} on CIP , i.e. $\|Ax^{(n+1)} - b\| > \epsilon$ **do**
 - 3: Perform Cimmino iteration on $x^{(n)}$ using A and b :

$$x^{(n+1)} \leftarrow \text{CIMMINO}(x^{(n)}, A, b)$$
 - 4: Generate scaled PDIM image \tilde{I}_{PDIM} from $x^{(n+1)}$
-

Moreover, there is a reason why we scale the PDIM image according to the ARIANE image but not vice versa, that is, *the ARIANE image generally has a much higher signal-to-noise ratio (SNR) than the PDIM image*. In order to explain this, first, we introduce the formula to compute the SNR in the x-ray penumbral images [BCP⁺16]:

$$(3.3) \quad \text{SNR} \approx \frac{S}{\sqrt{S + \left(\frac{1\text{MeV}}{E_{\text{x-ray}}}\right)^2 B}}$$

where S is the signal level, B is the background level, and the $E_{\text{x-ray}}$ is the photon energy measured in MeV.

In the NIF target chamber, the ARIANE image detector is positioned at a standoff distance of 6 meters versus PDIM at 1 meter. Therefore, the neutron background noise B on the image plate at ARIANE goes down. At the same time, more penumbral images are available at ARIANE at each energy channel. By averaging more images, the background noise in the image can further be reduced. As a result of these two factors reducing B in the formula (3.3), the SNR in the ARIANE image is higher compared to the PDIM image.

Figure (3.38) shows the contour plots of 95%, 85%, 50%, and 17% (with respect to the maximum x-ray emission) of the x-ray reconstructions for N190602 and N190530. As for the consistency of the 3D x-ray reconstructions to the input images, we show the reconstructed 2D projections along PDIM and ARIANE as well as their relative errors in figure (3.39) for N190602 and in figure (3.42) for N190530 respectively. The relative errors are almost zero in the hotspot region. This confirms that our reconstructions are consistent to the input images. Also, we show the top and side views

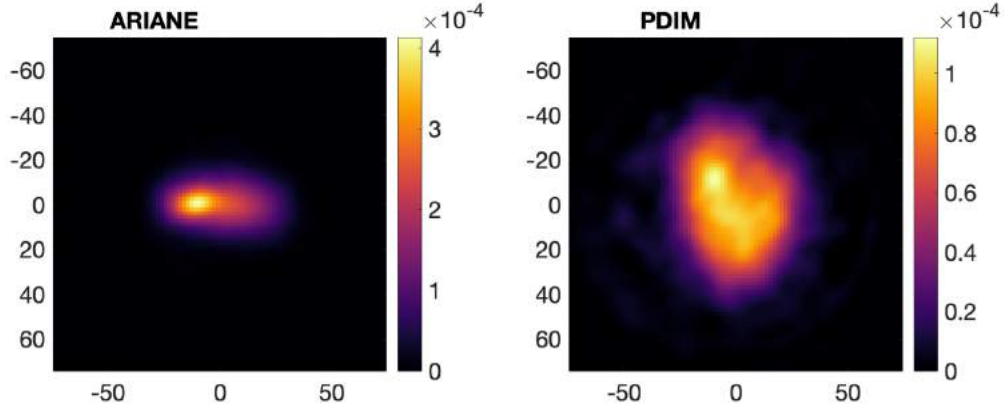


FIGURE 3.34. N190602 experimental x-ray images at PDIM and ARIANE with resolution of 8 microns

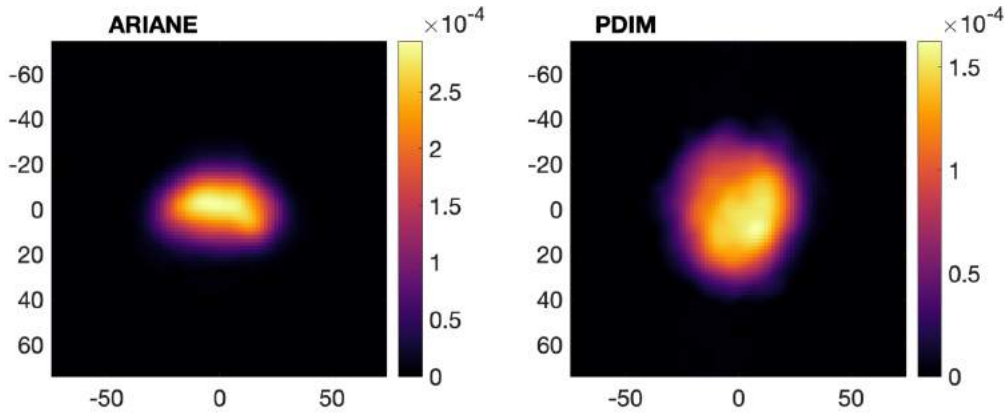


FIGURE 3.35. N190530 experimental x-ray images at PDIM and ARIANE with resolution of 8 microns

of the reconstructions together with their central lineouts in figures (3.40), (3.41) for N190602 and in figures (3.43), (3.44) for N190530 respectively. Hotspots in both reconstructions are oblate in shape. Their top and side views show a very similar shape of the hotspot in the input x-ray images.

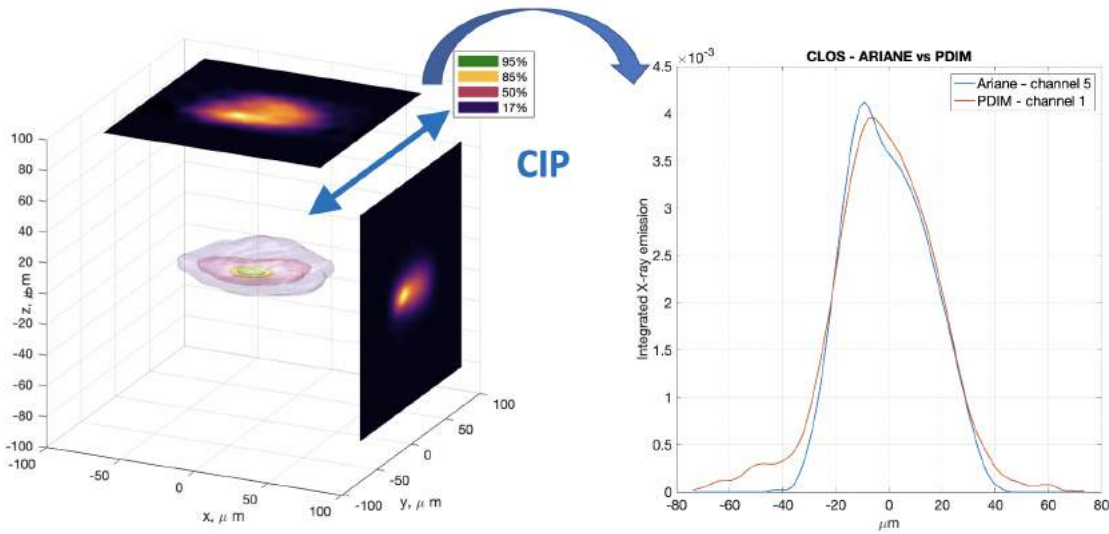


FIGURE 3.36. Discrepancy in the integrated x-ray emissions of PDIM and ARIANE on the Common Integrated Profile (CIP)

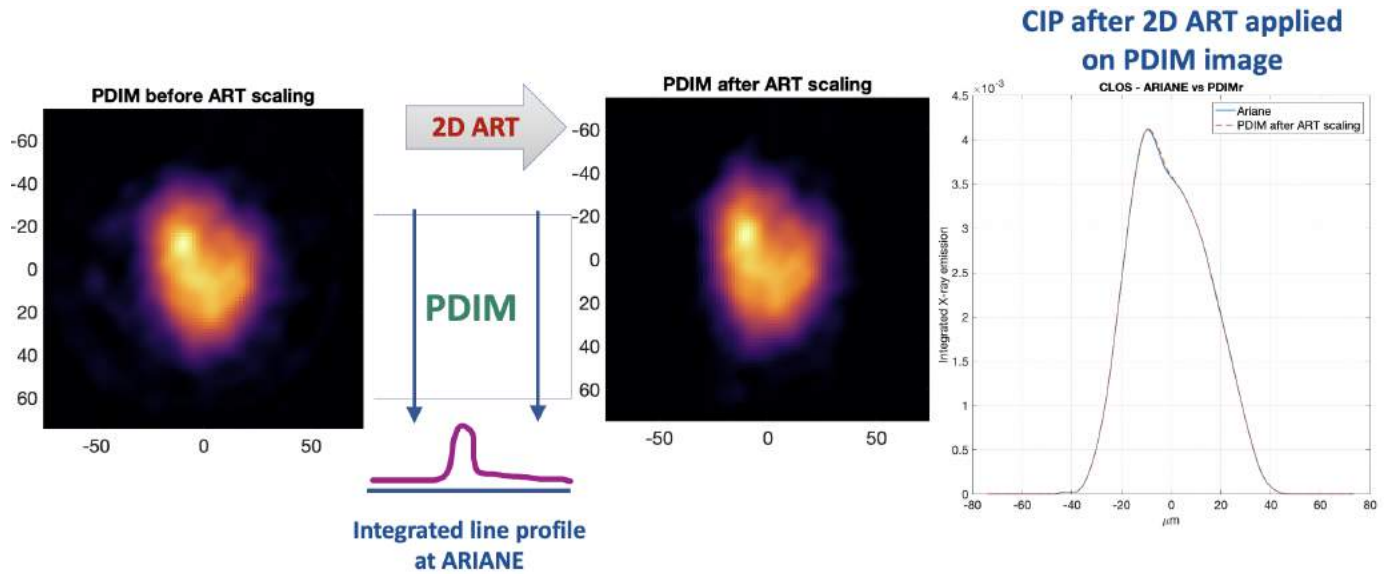


FIGURE 3.37. The integrated x-ray emissions of PDIM and ARIANE on the Common Integrated Profile (CIP) are the same after the 2D ART algorithm is applied on the PDIM image

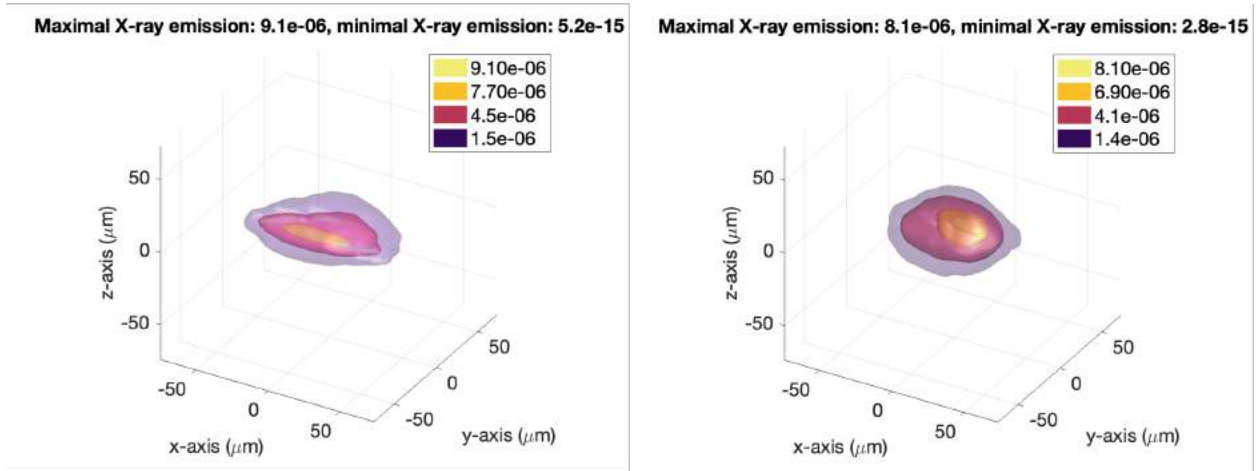


FIGURE 3.38. X-ray reconstructions for N190602 (left) and N190530 (right)

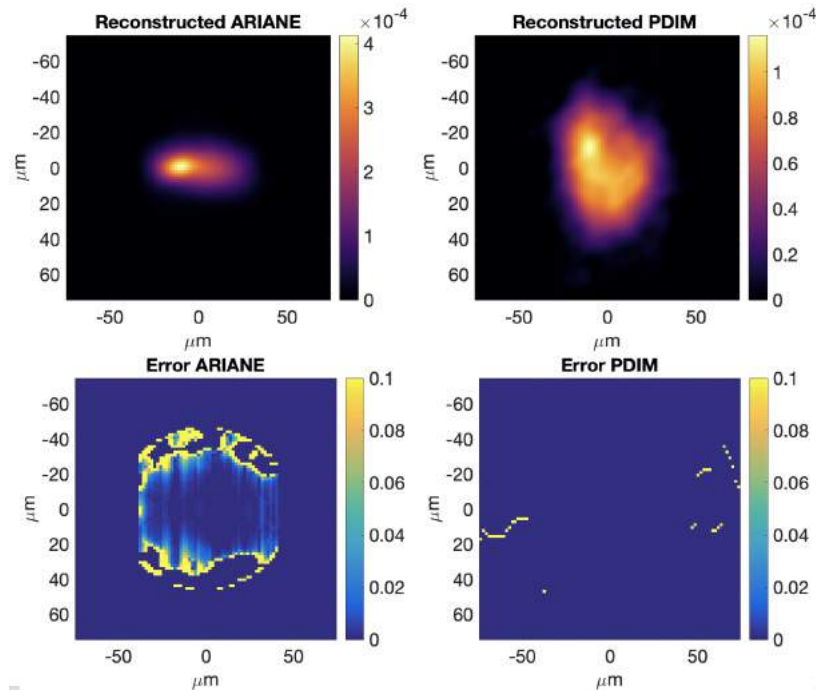


FIGURE 3.39. N190602 reconstructed ARIANE and PDIM projections (top row) and relative errors compared to the input images (bottom row)

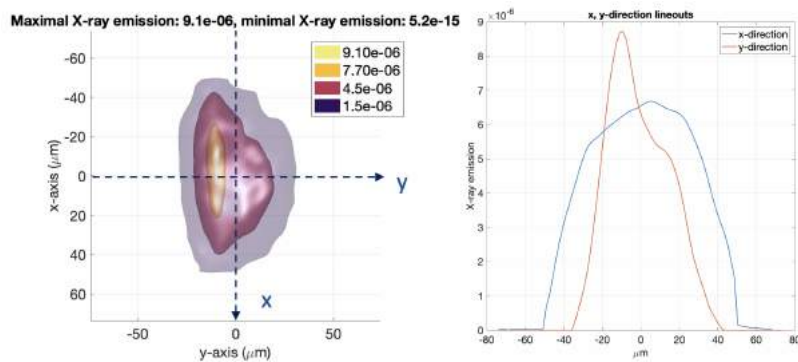


FIGURE 3.40. N190602 top view of reconstruction and x,y-lineouts

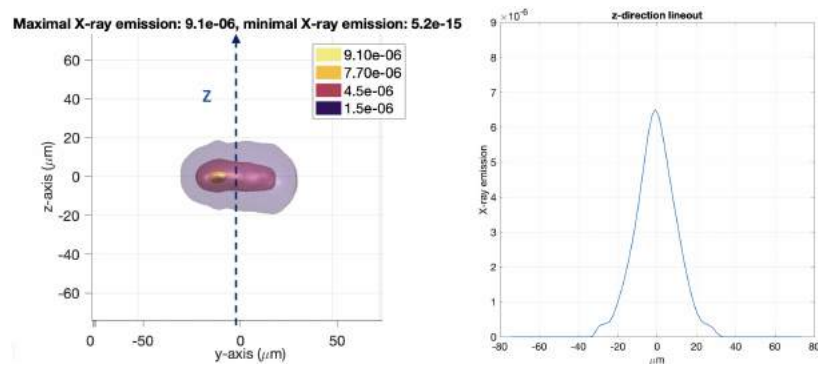


FIGURE 3.41. N190602 side view of reconstruction and z-lineout

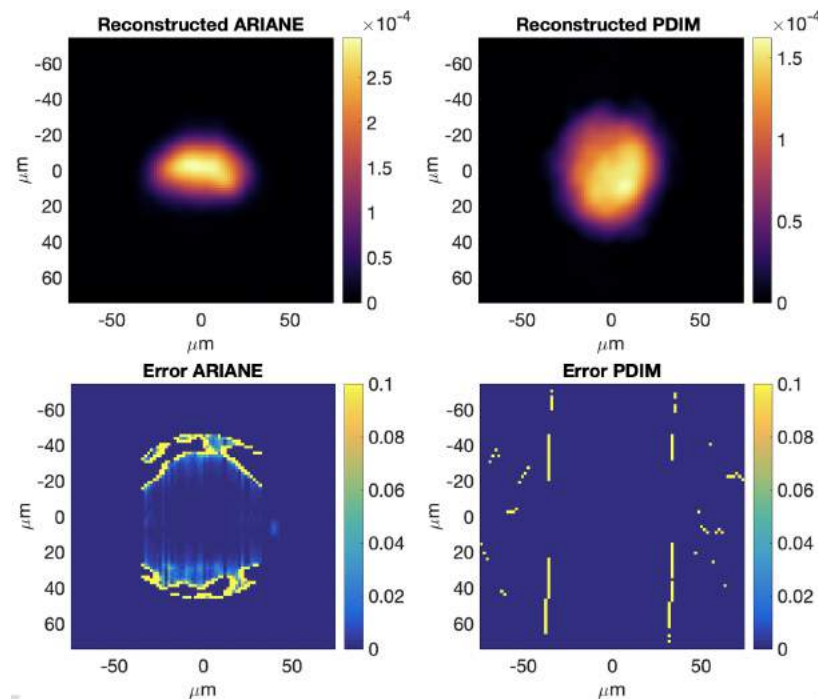


FIGURE 3.42. N190530 reconstructed ARIANE and PDIM projections (top row) and relative errors compared to the input images (bottom row)

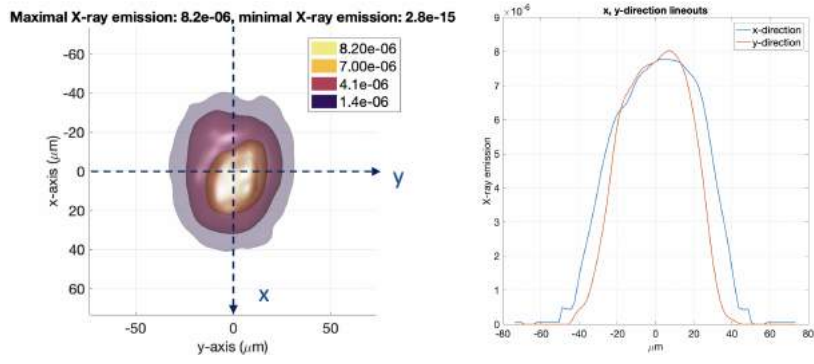


FIGURE 3.43. N190530 top view of reconstruction and x,y-lineouts

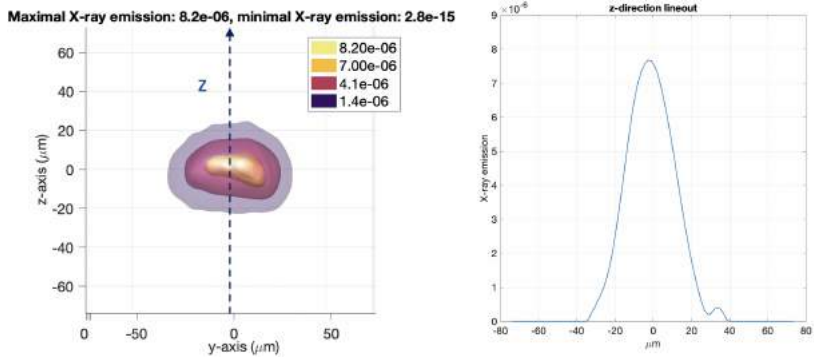


FIGURE 3.44. N190530 side view of reconstruction and z-lineout

3.3.4. X-ray reconstructions using experimental data N190730 and N181007. In this section, we apply our ART algorithm to reconstruct 3D x-ray distributions using the experimental data from ICF experiments N190730 and N181007 at NIF. In both experiments, we have two LOS, namely PDIM at the pole and $(90^\circ, 78^\circ)$ on the equator, which is a different LOS than before. There are two different energy channels (I and II) at these two LOS with much thicker titanium than before. We list their filtration materials in a table and plot their system response, see figure (3.45). Since there are much more titanium in the filters and hence both channels are much stronger, we can assume that the ablator becomes optically thin, i.e. the optical depth τ at a photon energy of 11 keV is equal to zero. Figures (3.46) and (3.47) shows the experimental penumbral x-ray images taken at PDIM and $(90^\circ, 78^\circ)$ in N190730 and N181007 respectively.

Note that the the x-ray images from channel I have higher x-ray emission values than that in channel II because channel I is a softer channel with less titanium and hence it allows more x-ray energy to pass through, as shown in its system response. More importantly, the N190730 images suggest a *globular shape* hotspot whereas the N181007 images suggest a *toroidal shape* hotspot.

Filtration materials	Channel I	Channel II
Polycarbonate	$2500\mu\text{m}$	$2500\mu\text{m}$
Kapton (polyimide)	$25\mu\text{m}$	$25\mu\text{m}$
Gold	$2.25\mu\text{m}$	$2.25\mu\text{m}$
Titanium	$261.5\mu\text{m}$	$525\mu\text{m}$

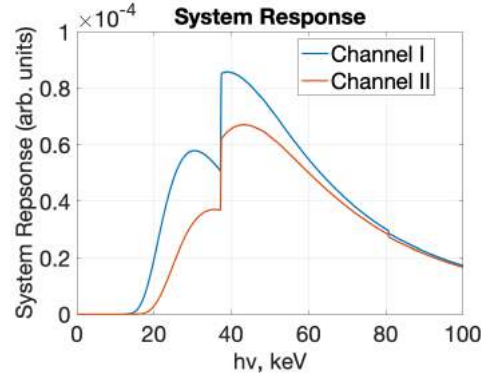


FIGURE 3.45. Filtration materials at $(90^\circ, 78^\circ)$ in N190730 and N181007 (left) and system response (right)

In both N190730 and N181007, we apply the 2D ART reconstruction algorithm on the PDIM image to ensure that the PDIM and $(90^\circ, 78^\circ)$ images agree with each other on the CIP. We show both the CIP and the PDIM image before and after the 2D ART is applied, see figures (3.48) and (3.49) for N190730 and figures (3.50) and (3.51) for N181007. The CIP of PDIM and $(90^\circ, 78^\circ)$ in the original input x-ray images in N190730 match pretty well, even before the 2D ART procedure. In contrast, there are noticeable discrepancies in CIP of PDIM and $(90^\circ, 78^\circ)$ in the original input x-ray images in N181007, as you can see by comparing the top and the bottom rows in figure

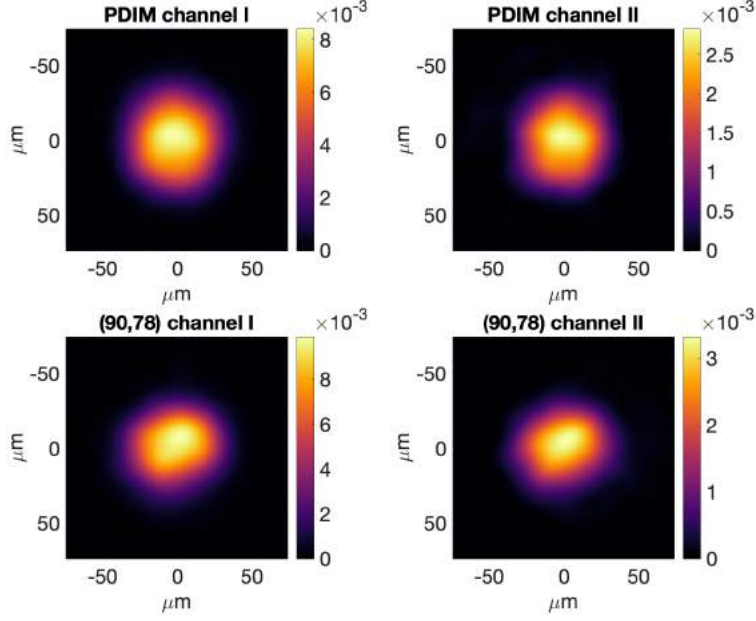


FIGURE 3.46. N190730 experimental x-ray images at PDIM and $(90^\circ, 78^\circ)$ with resolution of 14 microns, channel I in left column and channel II in right column

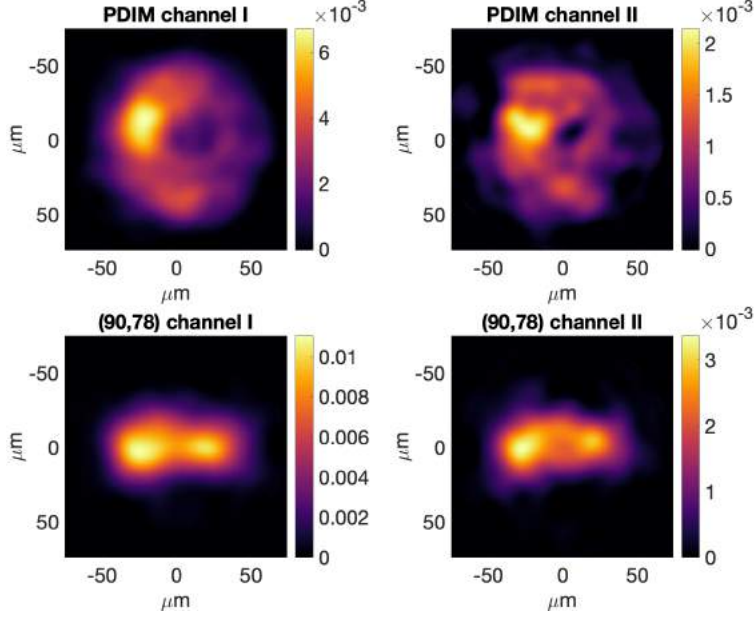


FIGURE 3.47. N181007 experimental x-ray images at PDIM and $(90^\circ, 78^\circ)$ with resolution of 14 microns, channel I in left column and channel II in right column

(3.51) that *without comprising the hotspot shape in the PDIM image, the 2D ART reconstruction algorithm matches the PDIM to the $(90^\circ, 78^\circ)$ image on the CIP.*

Figures (3.52) and (3.54) shows the contour plots of 95%, 85%, 50%, and 17% (with respect to the maximum x-ray emission) of the x-ray reconstructions for N190730 and N181007. Despite

some noise generated in the 3D ART algorithm on the periphery, the 3D x-ray reconstructions of N190730 and N181007 clearly indicate a globular and a toroidal hotspot x-ray emissions respectively. Moreover, figures (3.53) and (3.55) show the central lineouts of the x-ray reconstructions of N190730 and N181007 respectively. The central lineouts in two different channels have very similar shapes despite the difference in the absolute x-ray emission values.

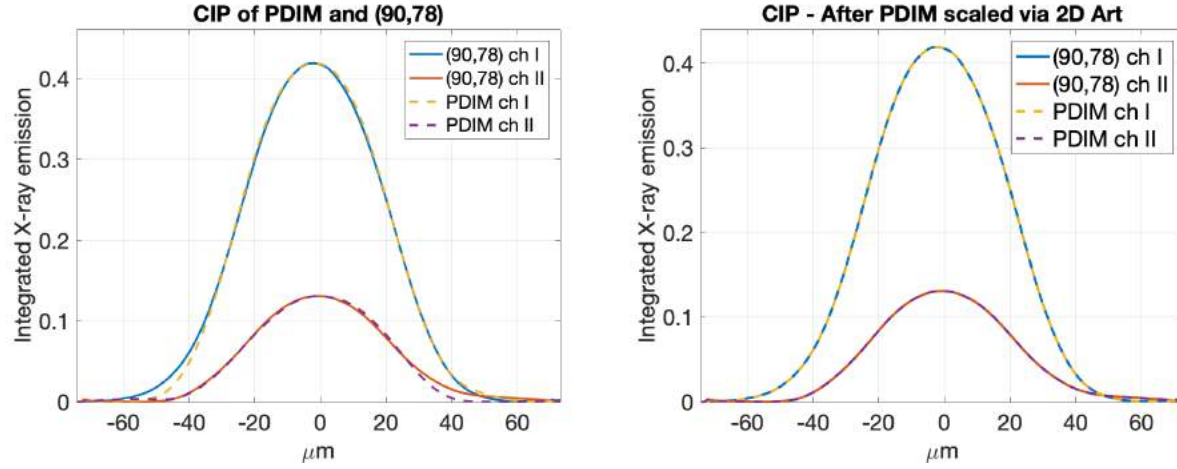


FIGURE 3.48. N190730 Common Integrated Profile (CIP) of PDIM and $(90^\circ, 78^\circ)$ images before (left) and after (right) the 2D ART reconstruction

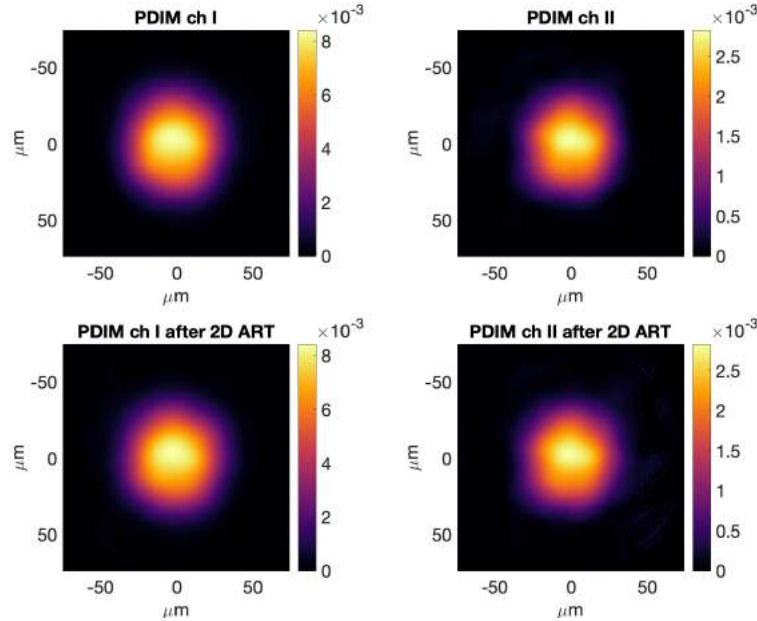


FIGURE 3.49. N190730 PDIM images before (top row) and after (bottom row) 2D ART in channels I and II; no significant changes in hotspot

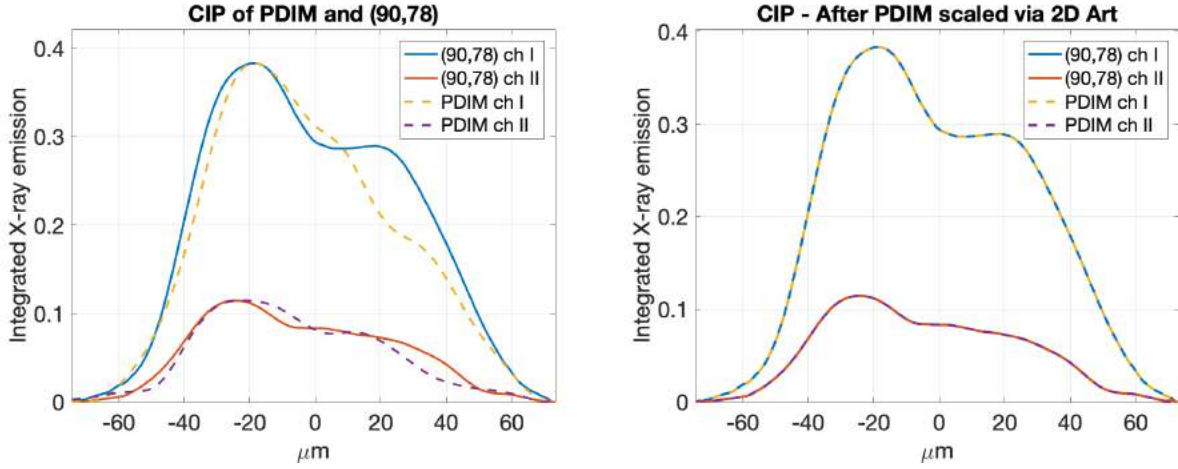


FIGURE 3.50. N181007 Common Integrated Profile (CIP) of PDIM and $(90^\circ, 78^\circ)$ images before (left) and after (right) the 2D ART reconstruction

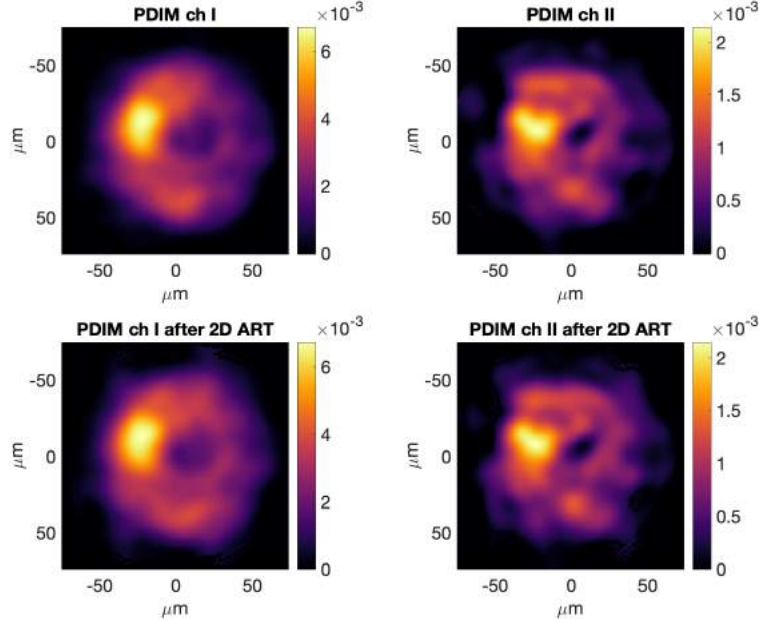


FIGURE 3.51. N181007 PDIM images before (top row) and after (bottom row) 2D ART in channels I and II; no significant changes in hotspot

As for the consistency of the 3D x-ray reconstructions to the input images, we show the reconstructed 2D projections along PDIM and $(90^\circ, 78^\circ)$ as well as their relative errors in figure (3.56) for N190730 and in figure (3.57) for N181007 respectively. The relative errors are in general less than 10% in the hotspot region. This confirms that our reconstructions are consistent to the input images.

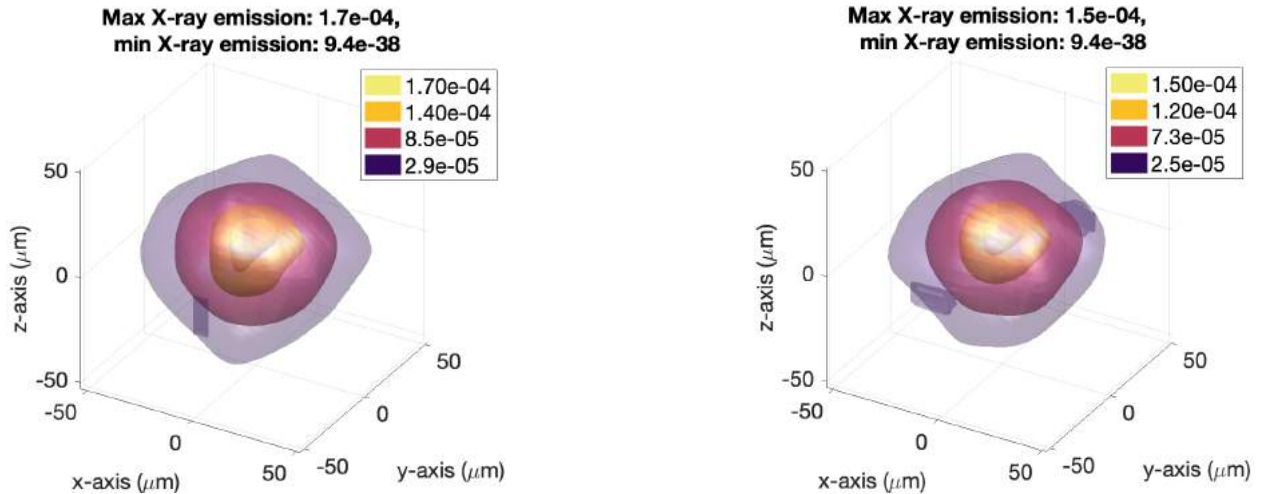


FIGURE 3.52. N190730 x-ray reconstructions in channels I (left) and II (right)

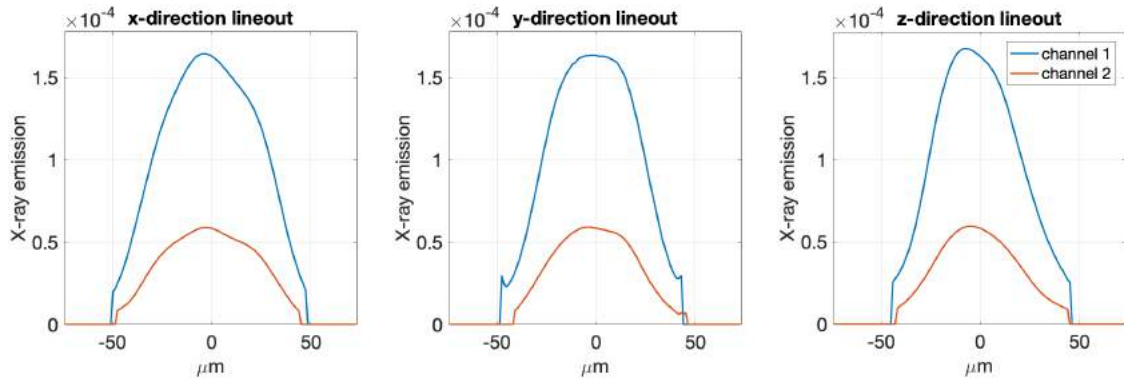


FIGURE 3.53. N190730 lineouts of x-ray reconstruction in channels I and II

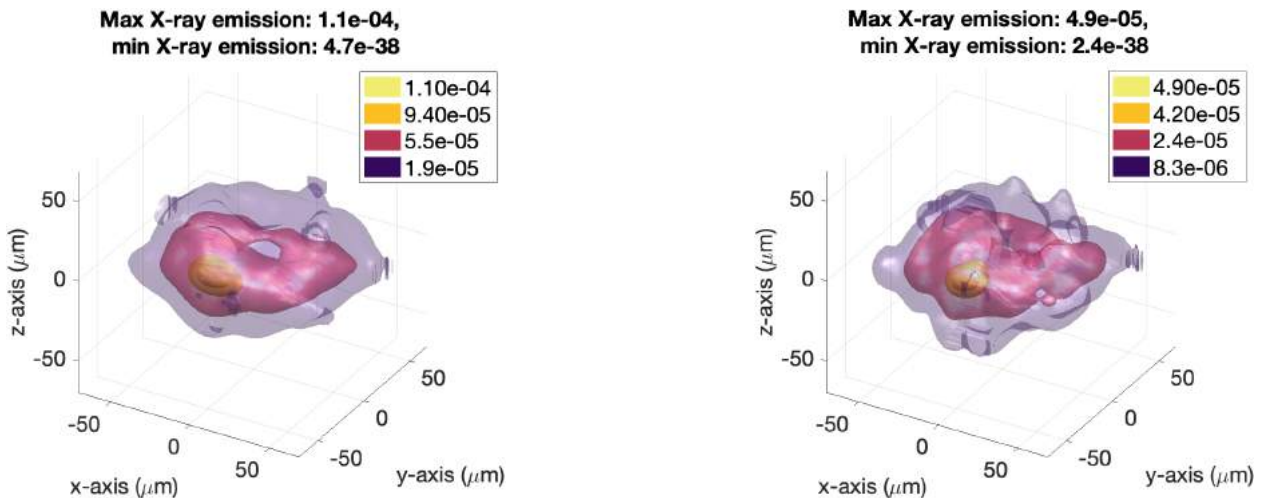


FIGURE 3.54. N181007 x-ray reconstructions in channels I (left) and II (right)

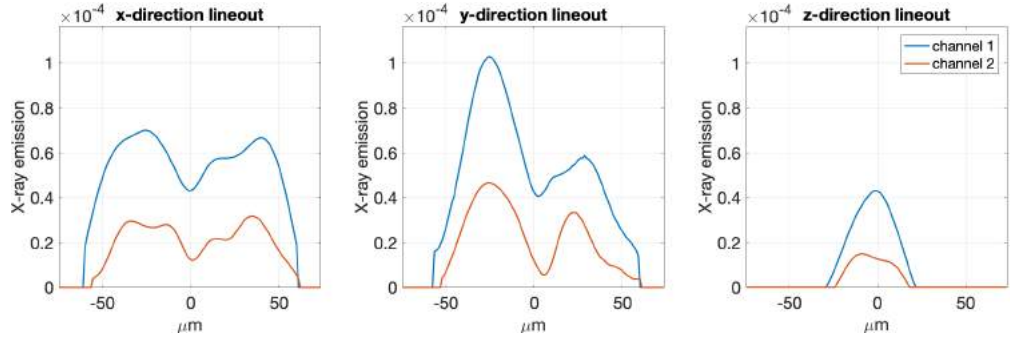


FIGURE 3.55. N181007 lineouts of x-ray reconstruction in channels I and II

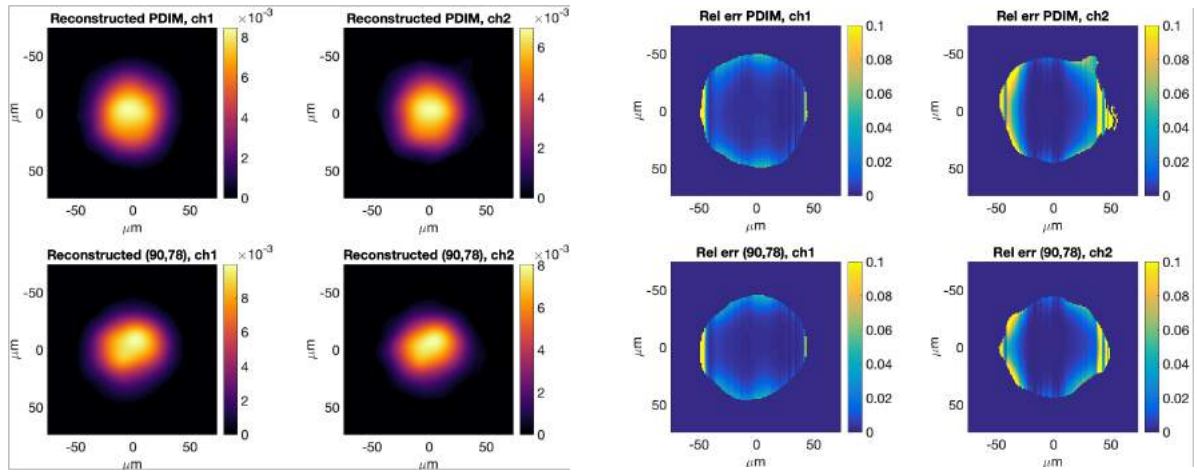


FIGURE 3.56. N190730 — reconstructed projections of PDIM and $(90^\circ, 78^\circ)$ (left) and their relative errors from 0 to 10% compared to the input images of the reconstruction (right)

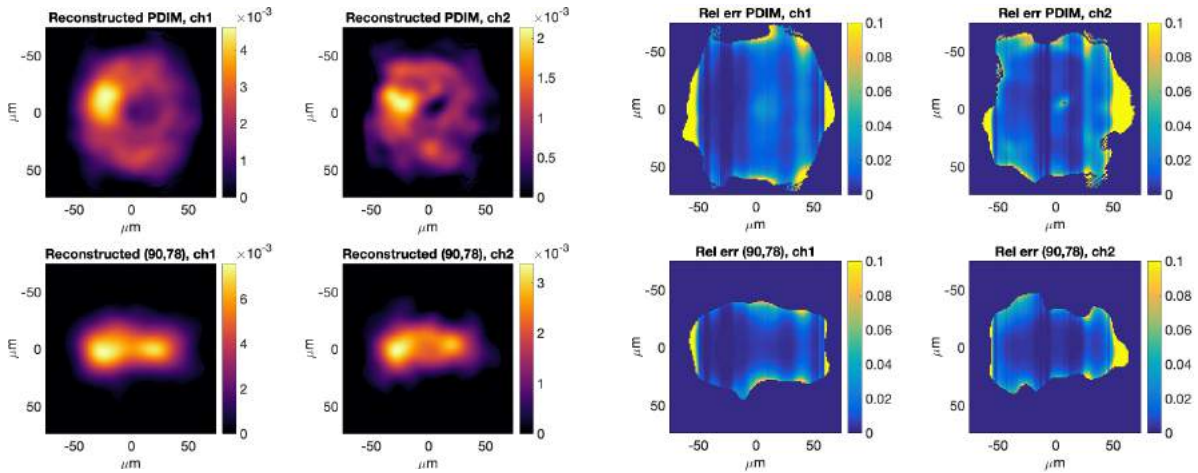


FIGURE 3.57. N181007 — reconstructed projections of PDIM and $(90^\circ, 78^\circ)$ (left) and their relative errors from 0 to 10% compared to the input images of the reconstruction (right)

3.4. 3D electron temperature measurement of nuclear fusion hotspot using 3D X-ray reconstructions

In this section, we first outline our method of inferring the electron temperature (T_e) measurement from the ratio of the 3D x-ray emission distributions in different energy channels. Then we present results from our synthetic data study of T_e measurement using two versus three lines-of-sight. Some of synthetic T_e models were already introduced in the previous section. Here is the procedure in our synthetic data study

- (1) We start with a synthetic 3D T_e distribution. We reconstruct the 3D x-ray emission distributions using two (or three) lines-of-sight (LOS) in different energy channels (see procedure in the previous section).
- (2) We infer the T_e from the ratio of these 3D x-ray emission distributions voxel by voxel and generate our 3D T_e measurement.
- (3) We use different metrics to compare our 3D T_e measurement with the original T_e distribution model.

Finally we apply our method on four different shots at NIF using the experimental data from N170821, N170827, N181007, and N190730. We already showed the x-ray reconstructions from the shots N181007 and N190730 in the previous section.

3.4.1. T_e measurement from the ratio of x-ray emissions in different energy channels. To begin with, we recall the formula (3.2) for computing the detected hotspot x-ray emission which is dependent on a T_e . Given detected x-ray emissions $\tilde{\epsilon}_1$ and $\tilde{\epsilon}_2$ in two different energy channels, we can write their ratio as a function of T_e :

$$(3.4) \quad f(T_e) := \frac{\tilde{\epsilon}_1(T_e)}{\tilde{\epsilon}_2(T_e)} = \frac{\int \epsilon(T_e, h\nu) \cdot s_1(h\nu) d(h\nu)}{\int \epsilon(T_e, h\nu) \cdot s_2(h\nu) d(h\nu)}$$

where s_1 and s_2 are the system responses of channels 1 and 2 respectively.

Recall that we use in our synthetic data study T_e models A and B in figure (3.58) together with two different energy channels shown earlier in figures (3.18) and (3.19). We plot here in figure (3.59) the detected x-ray emissions over a range of T_e up to 10keV and their ratio as a function of T_e . We illustrate in figure (3.60) how we measure the hotspot T_e by computing the ratio of the x-ray emissions voxel by voxel in our 3D reconstructions from the previous section.

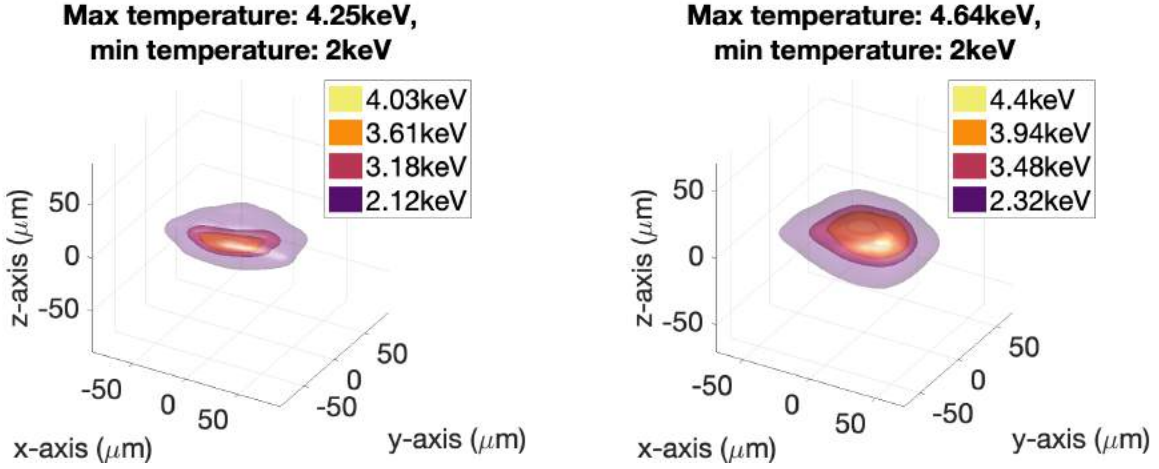


FIGURE 3.58. T_e models A (left) and B (right)

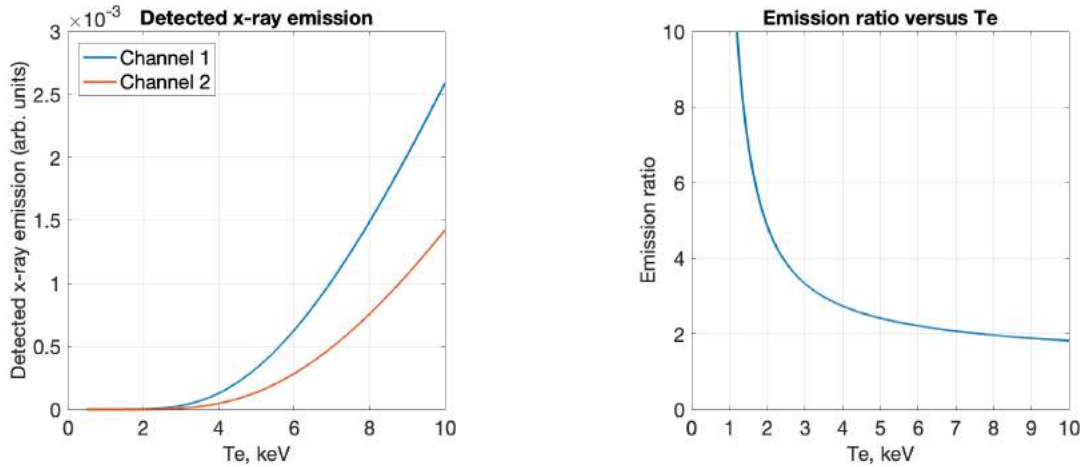


FIGURE 3.59. Detected emission in two different energy channels (left) and their ratio (right) over $T_e \in [0.5\text{keV}, 10\text{keV}]$

3.4.2. 3D T_e measurement in synthetic data study and error analysis. In practice, there is much noise towards the periphery of the 3D x-ray reconstructions generated in the ART reconstruction process. We also observe this along the central lineouts of the x-ray reconstructions in figures from (3.29) to (3.32) in the previous section as the relative errors escape to infinity at the boundary, in both cases using two or three LOS. We show in figures (3.61) and (3.62) the contour plots of 95%, 85%, 75%, and 50% (with respect to the maximum T_e) of the 3D T_e measurement of models A and B, which are computed directly from the ratio of the two x-ray reconstructions in channels 1 and 2. The peripheral regions have significant amount of noise.

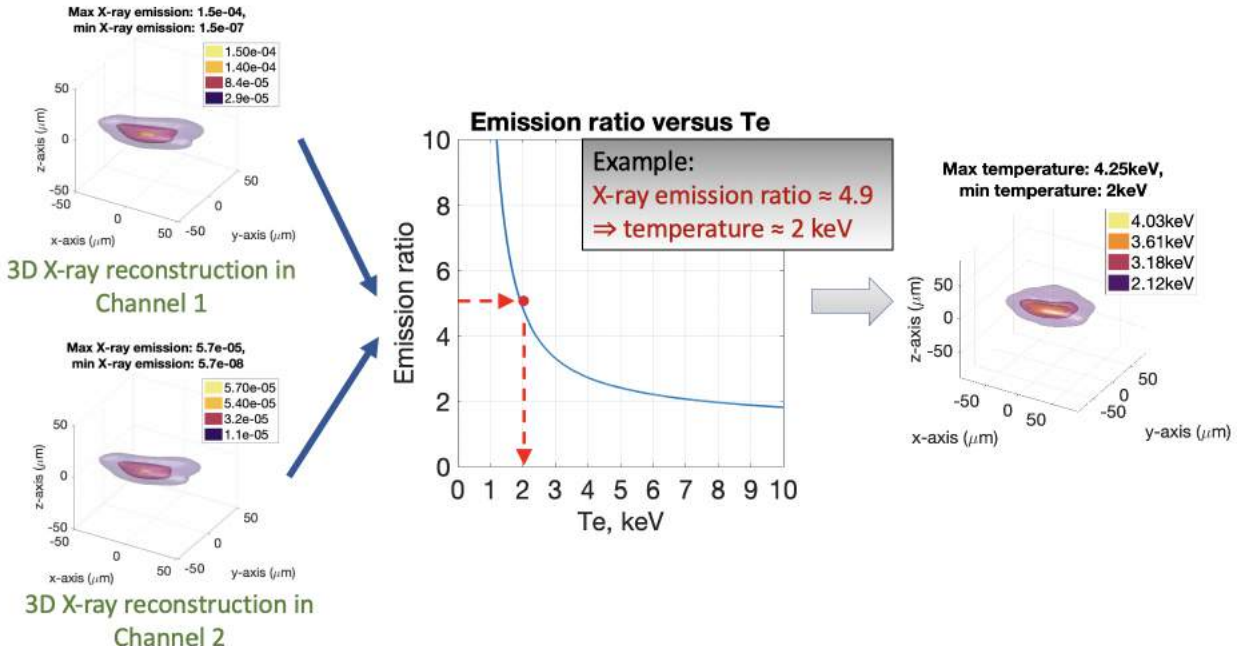


FIGURE 3.60. We infer T_e from the ratio of x-ray emission from reconstructions in two different energy channels

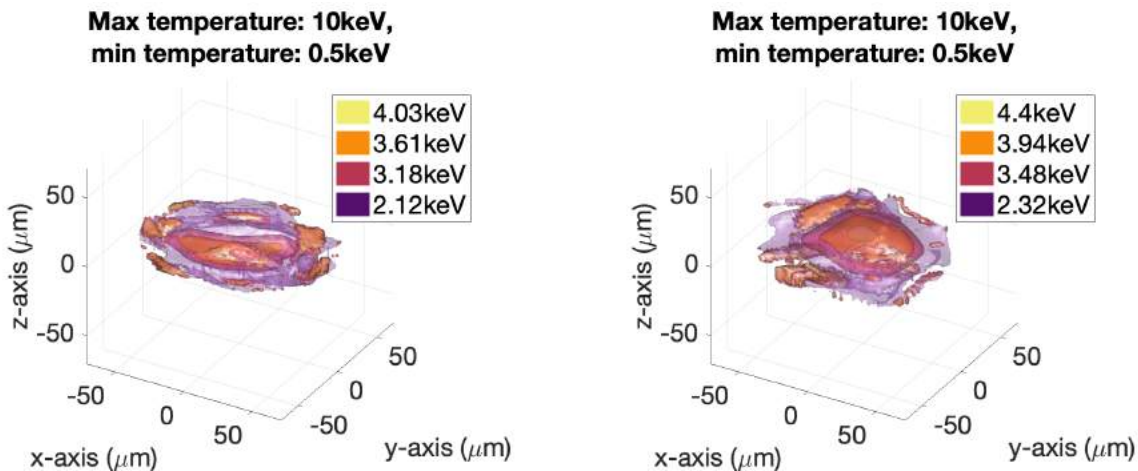


FIGURE 3.61. 3D T_e measurement of model A

FIGURE 3.62. 3D T_e measurement of model B

Our solution to overcome this noise is to blur the T_e measurement via convoluting with a 3-D Gaussian distribution with a standard deviation $\sigma = 4$ micron. In order to ensure fair comparison with our model, we blur the original T_e model using the same 3-D Gaussian smoothing kernel. Note that *in the typical experimental data this does not degrade the inherent spatial resolution, i.e. usually 8 to 14 microns per resolution element, significantly.*

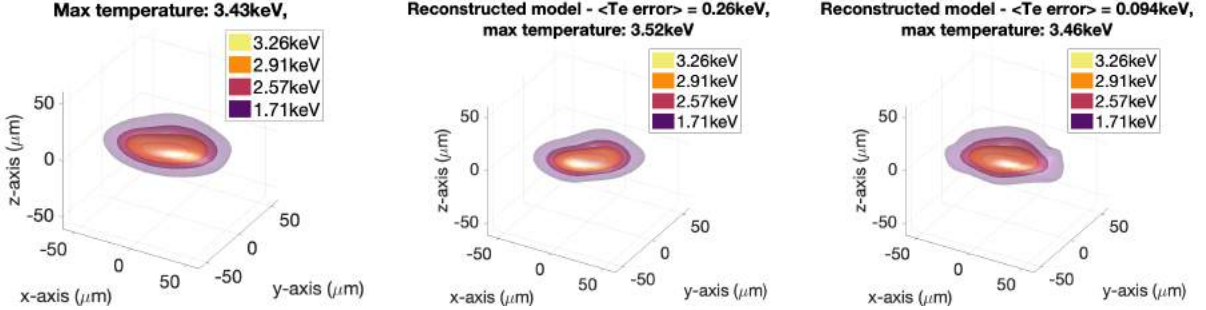


FIGURE 3.63. Synthetic T_e model A (left) and 3D T_e measurement using 2 LOS (middle) and 3 LOS (right); all three are blurred with $\sigma = 4$

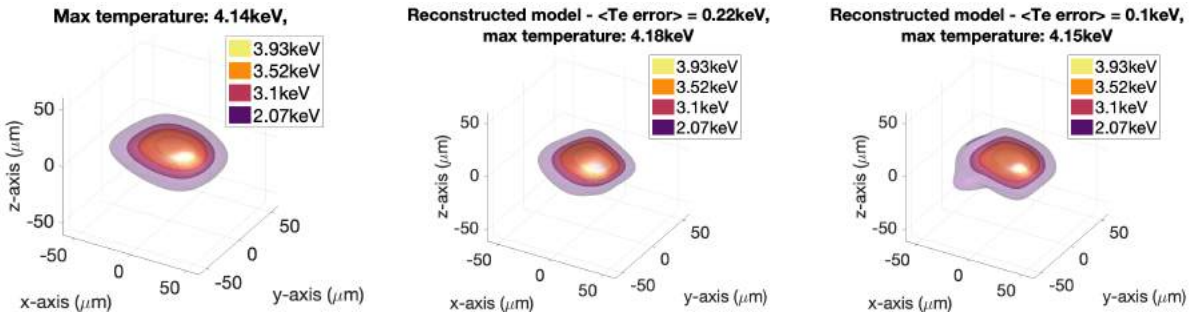


FIGURE 3.64. Synthetic T_e model B (left) and 3D T_e measurement using 2 LOS (middle) and 3 LOS (right); all three are blurred with $\sigma = 4$

We show both the synthetic T_e model and its measurements, using 2 LOS versus 3 LOS in the x-ray reconstructions, with the same degree of blurring in figure (3.63) for model A and figure (3.64) for model B. It is no longer meaningful to compare the minimum T_e value since the blurring can result in arbitrarily small values in the hotspot periphery. We also plot the central lineouts of the T_e measurement using 2 LOS versus 3 LOS in figures (3.65) and (3.66).

Although the 3D T_e measurement using 3 LOS in the x-ray reconstructions has a maximum T_e that is closer to the original maximum T_e , the shape of its outer contour (in this case the 50% contour) no longer resembles that in the original model. But if we take a closer look at the T_e central lineouts, the T_e measurement using 3 LOS generally has higher accuracy (lower relative error) in the central part of the hotspot, for example look at the relative errors of the x, z -direction lineouts of the hotspot in figures (3.65) and (3.66). More accurately, towards the boundary of the hotspot at roughly $[-50, -40]$ microns and $[40, 50]$ microns, using two 2 LOS can have relative errors as large as 40% or more whereas that using 3 LOS are below 20% and in general around 10%.

Furthermore, we computed the *weighted absolute T_e error* $\langle Te_{\text{err}} \rangle$, in keV, to quantify the quality of our T_e measurements. The definition is simply the sum of absolute T_e error from all voxels weighted by the corresponding synthetic x-ray values:

Given the synthetic 3D T_e distribution values $(t_1, t_2, \dots, t_{d^3})$ in keV, where the dimension in each direction is d . Also, given the synthetic x-ray values $(x_1, x_2, \dots, x_{d^3})$ and the reconstructed synthetic 3D T_e distribution values $(\tilde{t}_1, \tilde{t}_2, \dots, \tilde{t}_{d^3})$ in keV, we compute

$$\langle Te_{\text{err}} \rangle := \frac{\sum_1^{d^3} |t_i - \tilde{t}_i| \cdot x_i}{\sum_1^{d^3} x_i}$$

The $\langle Te_{\text{err}} \rangle$ are listed in the titles of the 3D T_e measurements using 2 and 3 LOS in figures (3.63) and (3.64). We can see the weighted absolute T_e error in the T_e measurements using 3LOS is generally lower than that using 2 LOS, 0.094keV versus 0.26keV in model A and 0.1 keV versus 0.22keV in model B.

So, in terms of the central lineouts and the weighted absolute T_e error, we can see a significant improvement in the accuracy of our 3D T_e measurement in both models A and B from using 2 LOS to 3 LOS.

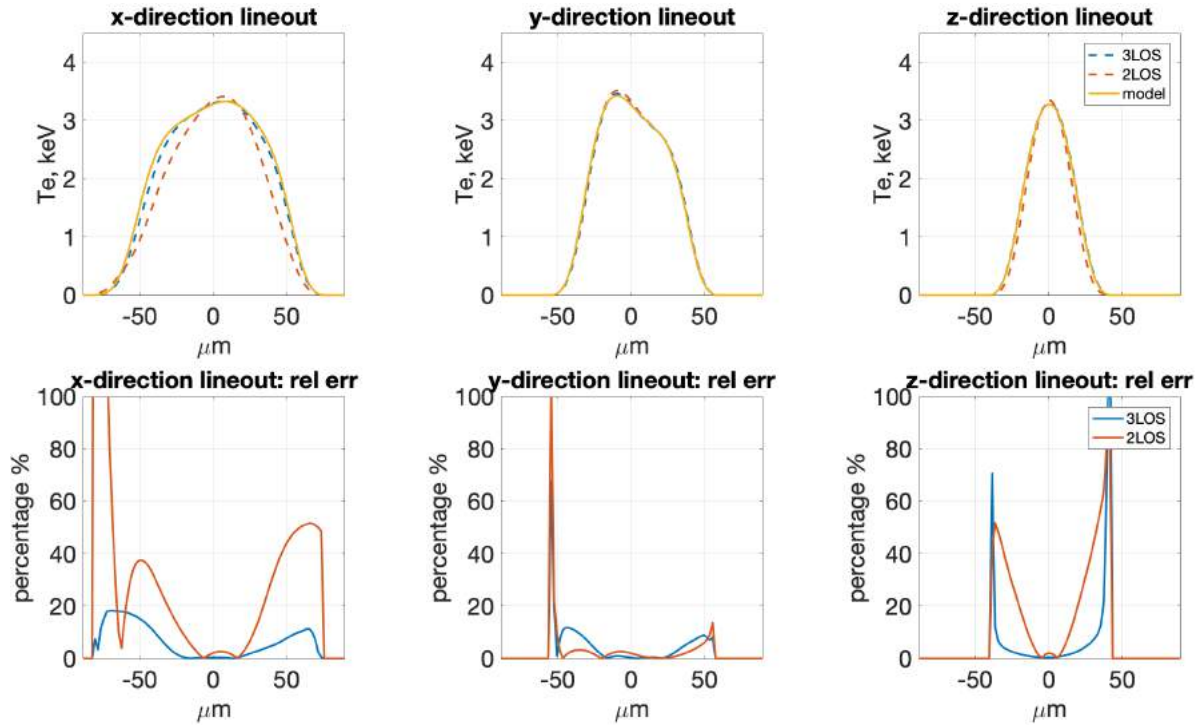


FIGURE 3.65. Comparison of central lineouts of 3D T_e measurement using 2 LOS versus 3LOS (model A)

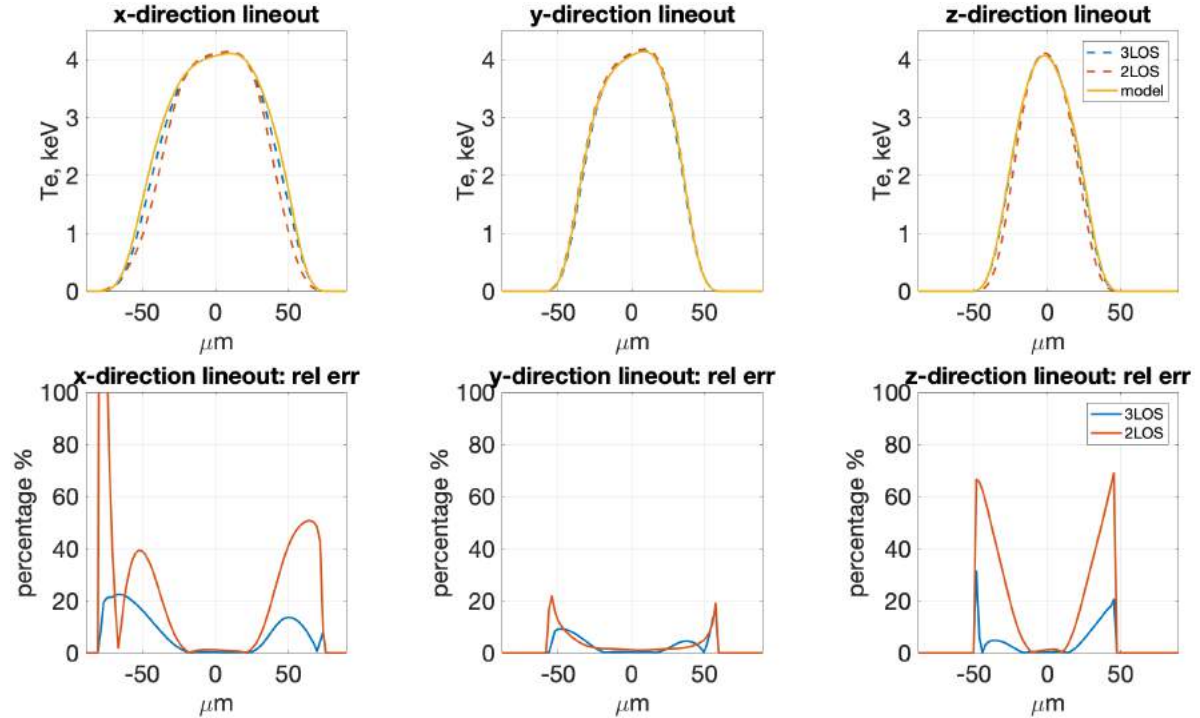


FIGURE 3.66. Comparison of central lineouts of 3D T_e measurement using 2 LOS versus 3LOS (model B)

3.4.3. T_e measurement on more T_e models in synthetic data and error analysis. We further test our 3D T_e measurement method on a collection of synthetic T_e distribution models with various shapes and geometries. We select six of them, which have distinct shapes, to present their results here. We begin by displaying and describing all the six T_e models. T_e models 1 to 3 have complex hotspot shape that can be described as an elongated ellipsoidal hotspot (models 1 and 3) and as a superposed ellipsoidal hotspots (model 2), whereas T_e models 4 to 6 have toroidal hotspot shapes.

For the 3D x-ray reconstructions of these models, we use the exact same two energy channels as in the synthetic data study of models A and B, listed in figure (3.18), assuming an optical depth $\tau(11\text{keV}) = 1$ evaluated at a photon energy of 11 keV. The 2 LOS used are $(0^\circ, 0^\circ)$ and $(90^\circ, 89^\circ)$ while the additional LOS used in the 3 LOS is $(90^\circ, 315^\circ)$.

For each model, we present contour plots of our 3D T_e measurements using 2 LOS versus 3 LOS and the plots of central lineouts together with the relative errors of these measurements. Moreover, both synthetic and the reconstructed T_e distributions presented here are blurred using a Gaussian smoothing kernel with the same standard deviation to eliminate the noise and at the same time to ensure a fair comparison.

All the synthetic T_e models and their 3D T_e measurements using 2 LOS versus 3 LOS are shown in the appendix (B).

3.4.4. 3D T_e measurement using experimental data N190730, N181007, N170827, and N170821. In this section, we infer the 3D electron temperature distributions using the experimental data from ICF experiments N190730, N181007, N170827, and N170821 at NIF.

For the experiments N190730 and N181007, we described their experimental setup, presented the x-ray images, and their corresponding 3D x-ray reconstructions in the previous section. *The 2 LOS, namely PDIM and (90°, 78°), and the filtration materials of the two x-ray energy channels used for the N170827 and N170821 are exactly the same as that in N190730 and N181007*, as shown in the figure (3.45). We plot below in figure (3.67) the corresponding detected x-ray emissions over a range of T_e up to 10keV and their ratio as a function of T_e .

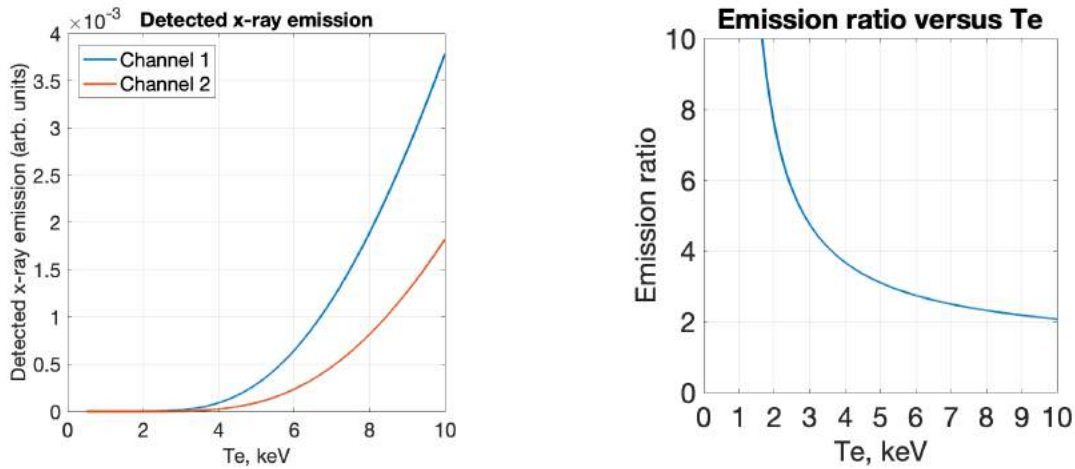


FIGURE 3.67. Detected emission in two experimental x-ray energy channels (left) and their ratio (right) over $T_e \in [0.5\text{keV}, 10\text{keV}]$

N190730 — 3D T_e measurement

We present the 3D T_e measurement by computing the ratio of the x-ray emissions in the reconstructions shown in figure (3.52). We show a contour plot of 95%, 85%, 75%, and 50% (with respect to the maximum T_e , marked as a black dot) of the 3D Te measurement in figure (3.68). Also, we plot their central lineouts at $0\mu\text{m}$ in x, y, z -directions in figure (3.69) together with three orthogonal lineouts through the maximum T_e in figure (3.70). The blue colored segments of the lineouts are located in the central part of the hotspot.

N190730 - max temperature: 5.5keV

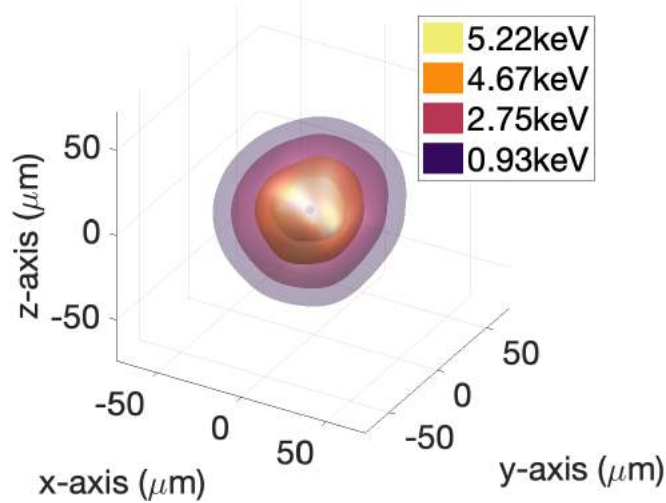


FIGURE 3.68. N190730 — 3D T_e measurement

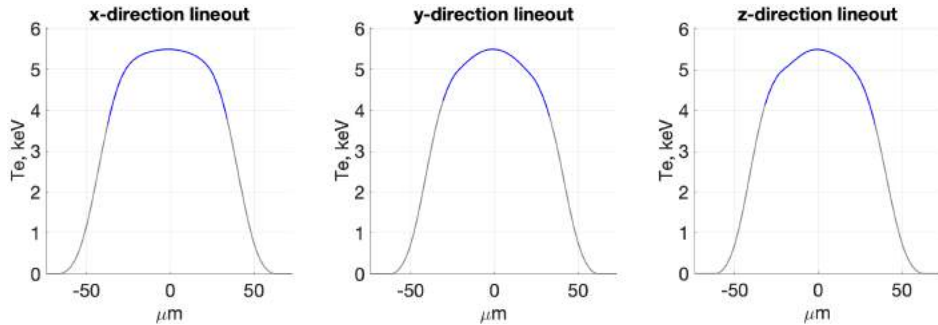


FIGURE 3.69. N190730 central lineouts of 3D T_e measurement

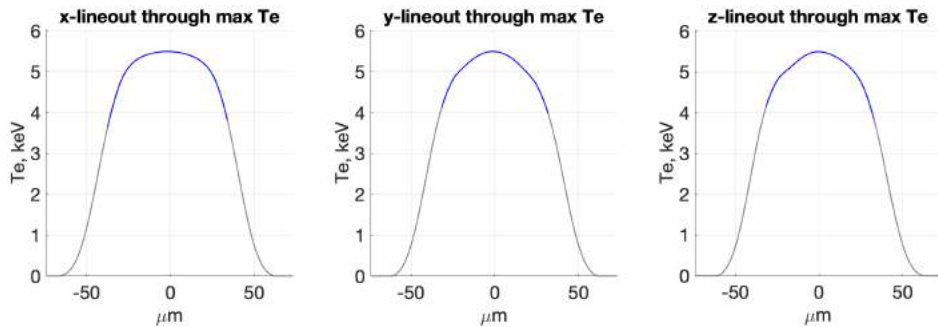


FIGURE 3.70. N190730 lineouts through maximum T_e

N181007 — 3D T_e measurement

Similar to the shot N190730, we present the 3D T_e measurement by using the x-ray emission reconstructions in figure (3.54), a T_e contour plot in figure (3.71), a plot of central lineouts in figure

(3.72), and a plot of lineouts through the maximum T_e in figure (3.73). Our T_e measurement clearly indicates a toroidal shape hotspot.

N181007 - max temperature: 7.03keV

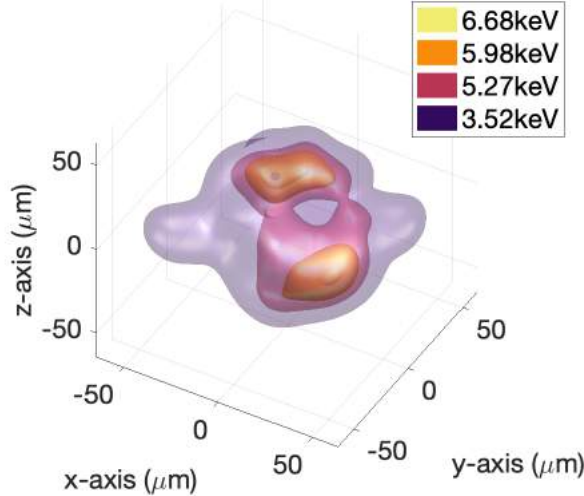


FIGURE 3.71. N181007 — 3D T_e measurement

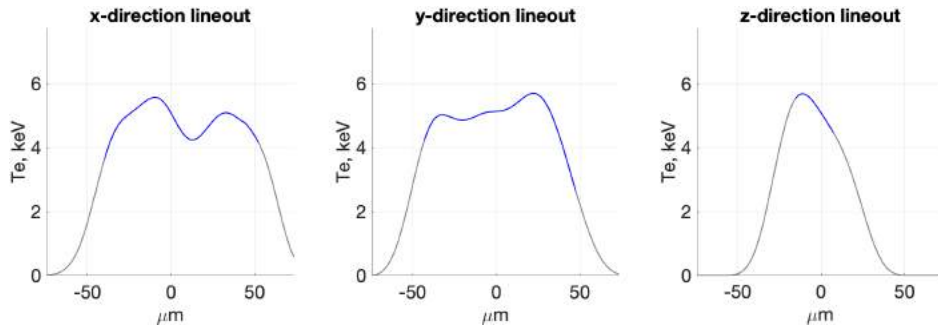


FIGURE 3.72. N181007 central lineouts of 3D T_e measurement

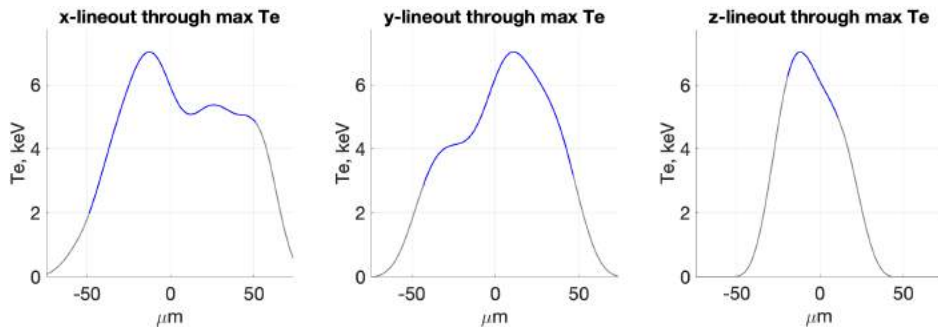


FIGURE 3.73. N181007 lineouts through maximum T_e

N170827 — 3D T_e measurement

Here we show the experimental x-ray images, the 3D x-ray reconstructions, and their central line-outs.

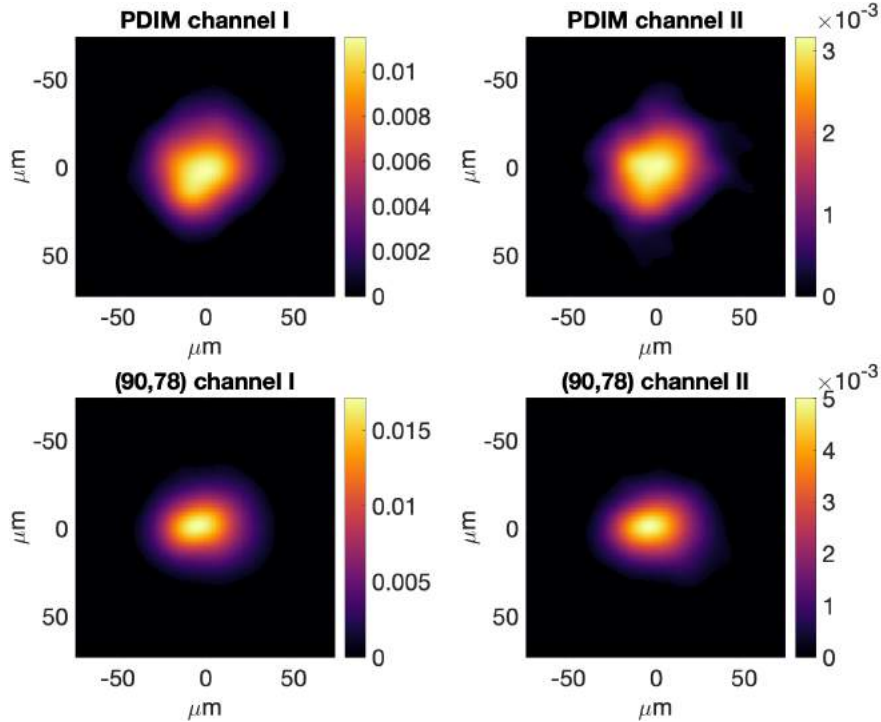


FIGURE 3.74. N170827 experimental x-ray images at PDIM and $(90^\circ, 78^\circ)$ with resolution of 14 microns, channel I in left column and channel II in right column

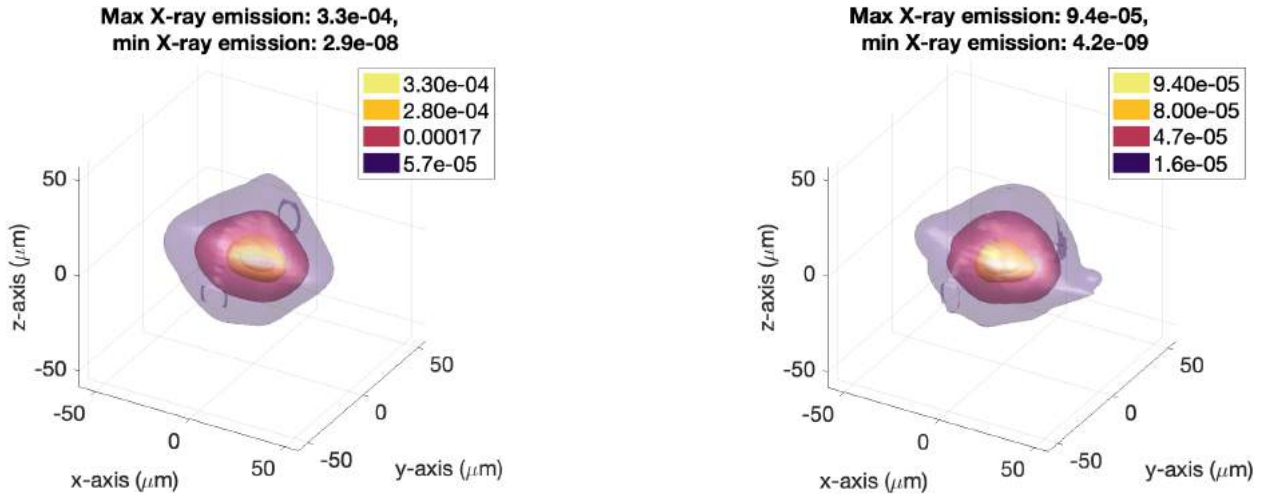


FIGURE 3.75. N170827 x-ray reconstructions in channels I (left) and II (right)

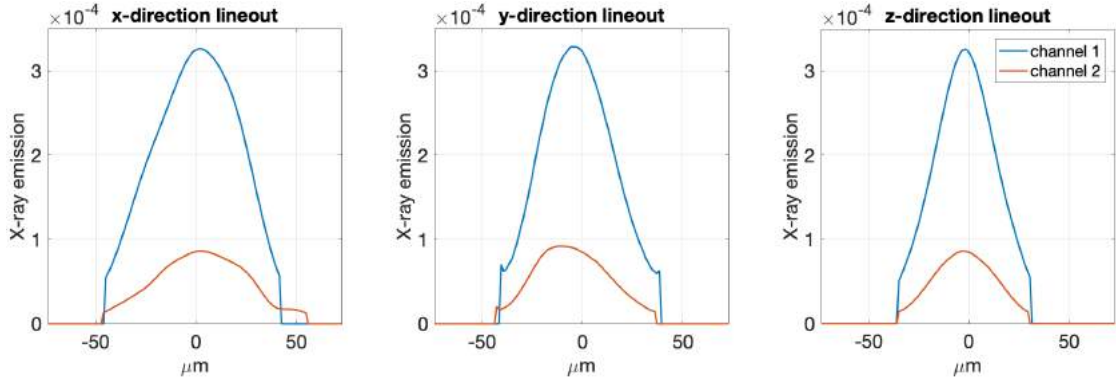


FIGURE 3.76. N170827 lineouts of x-ray reconstruction in channels I and II

Our 3D x-ray reconstructions are consistent to the input images. Here we show the reconstructed 2D projections and their relative errors.

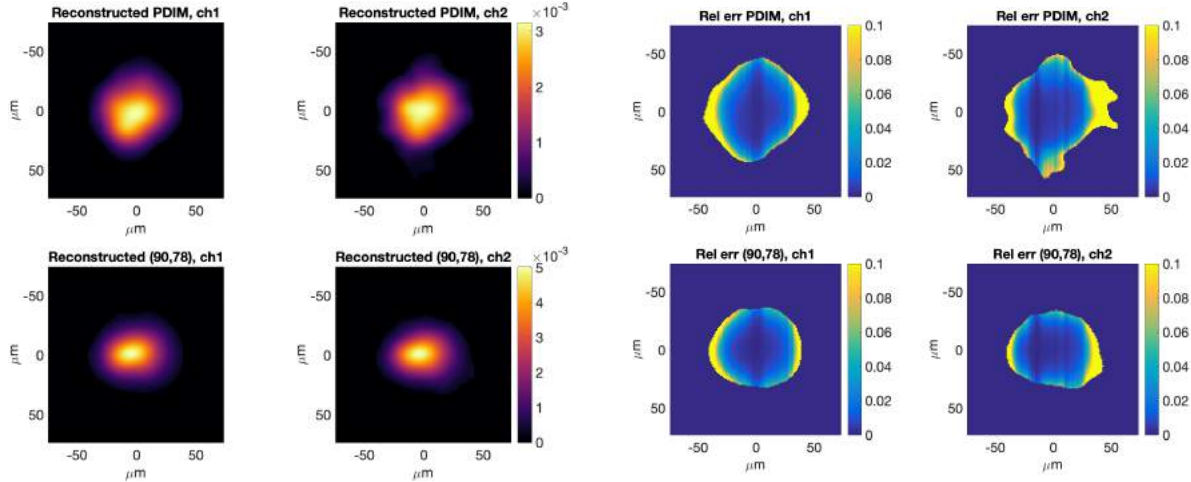


FIGURE 3.77. N170827 — reconstructed projections of PDIM and $(90^\circ, 78^\circ)$ (left) and their relative errors from 0 to 10% compared to the input images of the reconstruction (right)

Finally we present the 3D T_e measurement, a T_e contour plot, a plot of central lineouts, and a plot of lineouts through the maximum T_e .

N170827 - max temperature: 5.8keV

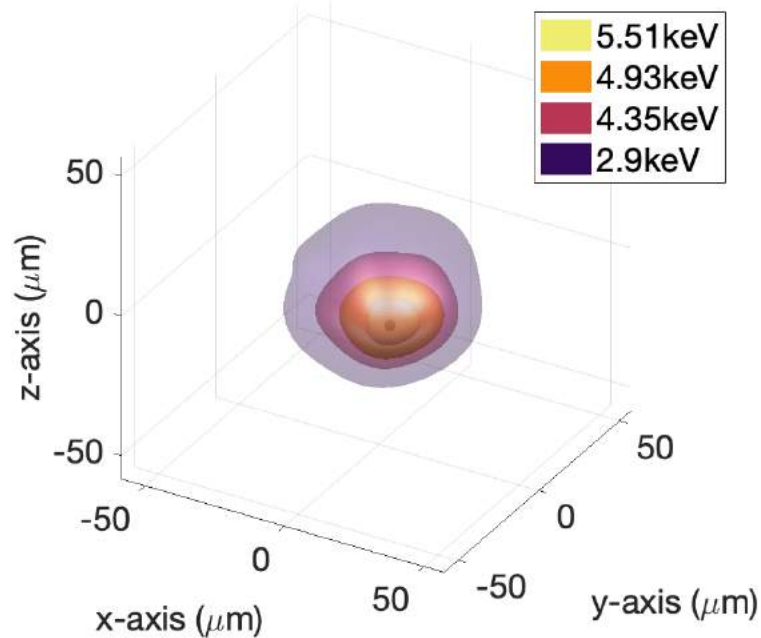


FIGURE 3.78. N170827 — 3D T_e measurement

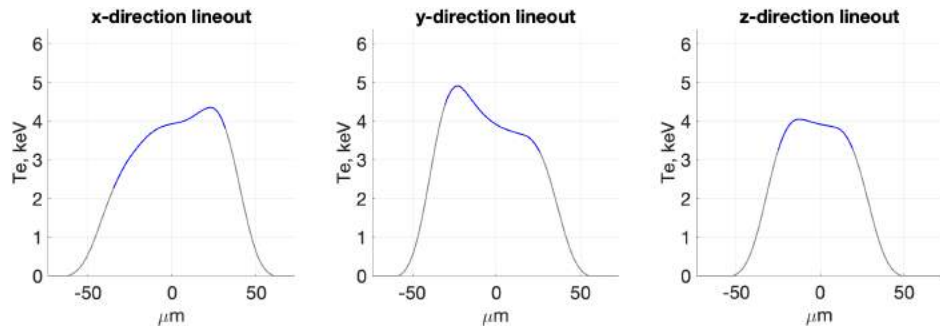


FIGURE 3.79. N170827 central lineouts of 3D T_e measurement

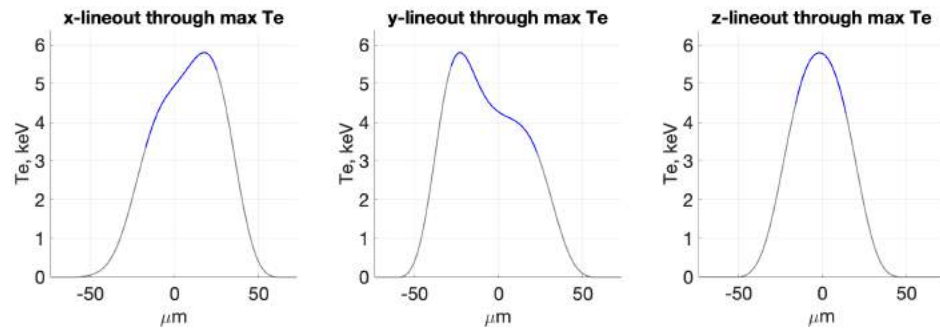


FIGURE 3.80. N170827 lineouts through maximum T_e

N170821 — 3D T_e measurement

Here we show the experimental x-ray images, the 3D x-ray reconstructions, and their central line-outs.

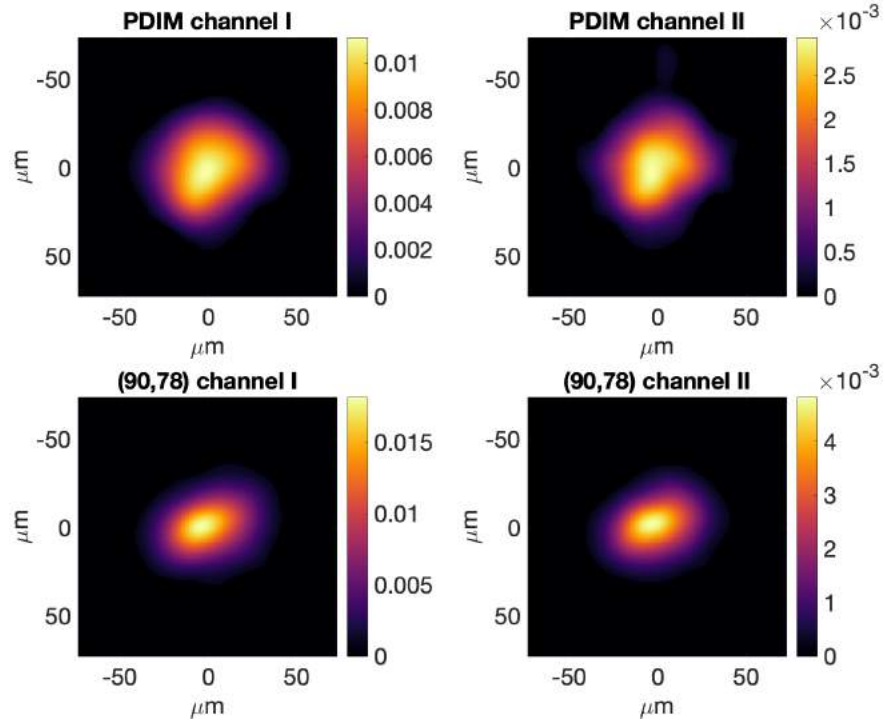


FIGURE 3.81. N170821 experimental x-ray images at PDIM and $(90^\circ, 78^\circ)$ with resolution of 14 microns, channel I in left column and channel II in right column

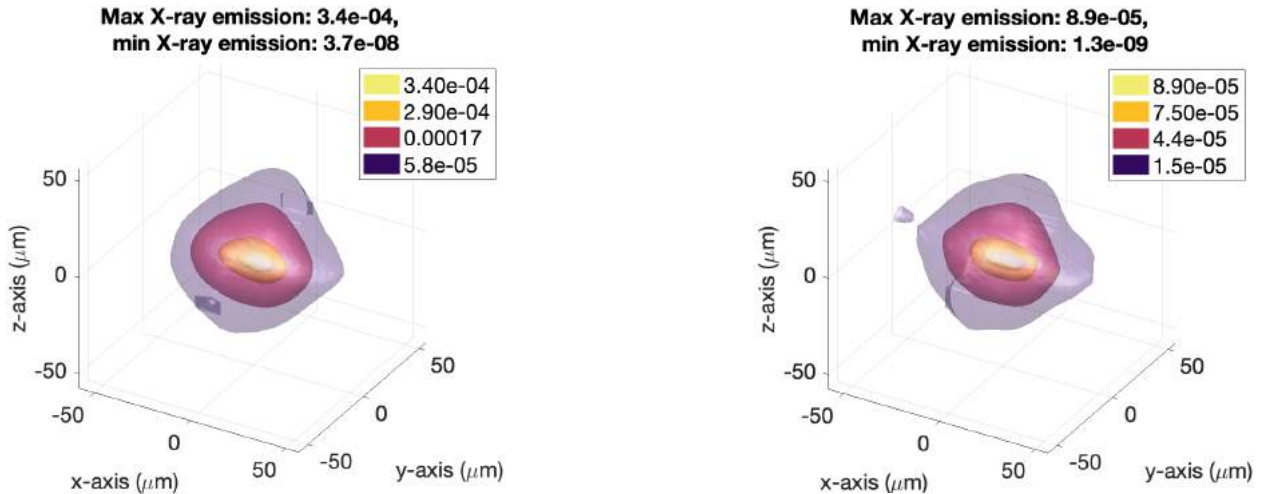


FIGURE 3.82. N170821 x-ray reconstructions in channels I (left) and II (right)

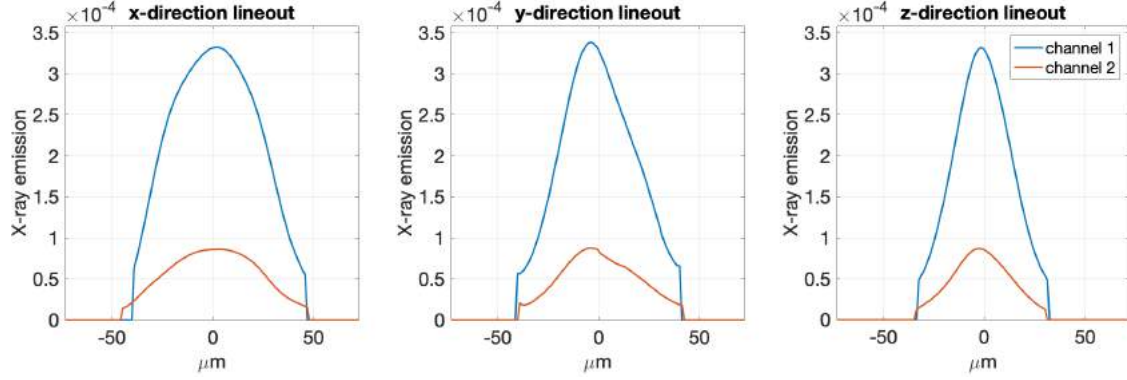


FIGURE 3.83. N170821 lineouts of x-ray reconstruction in channels I and II

Our 3D x-ray reconstructions are consistent to the input images. Here we show the reconstructed 2D projections and their relative errors.

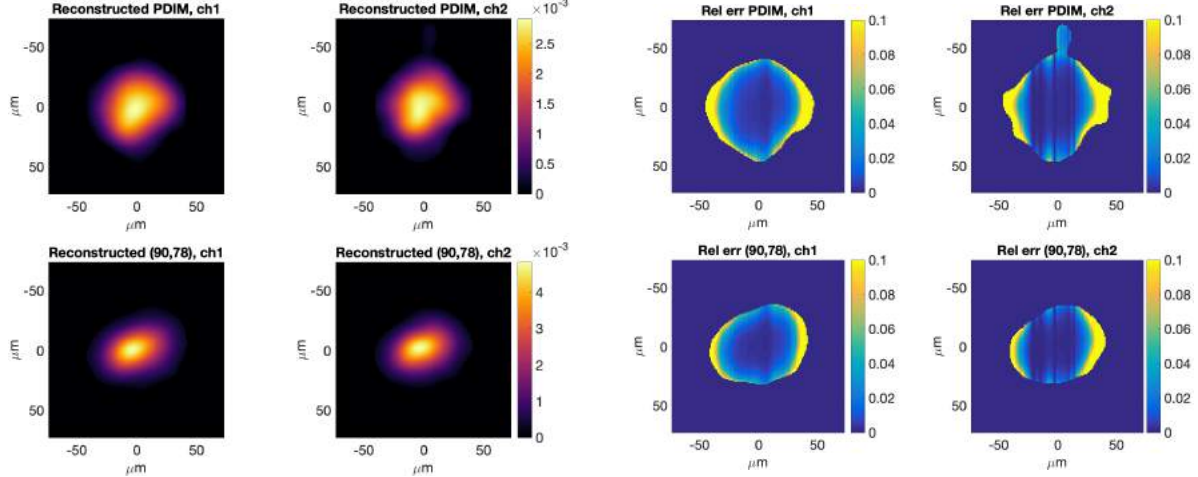


FIGURE 3.84. N170821 — reconstructed projections of PDIM and $(90^\circ, 78^\circ)$ (left) and their relative errors from 0 to 10% compared to the input images of the reconstruction (right)

Finally we present the 3D T_e measurement, a T_e contour plot, a plot of central lineouts, and a plot of lineouts through the maximum T_e .

N170821 - max temperature: 4.15keV

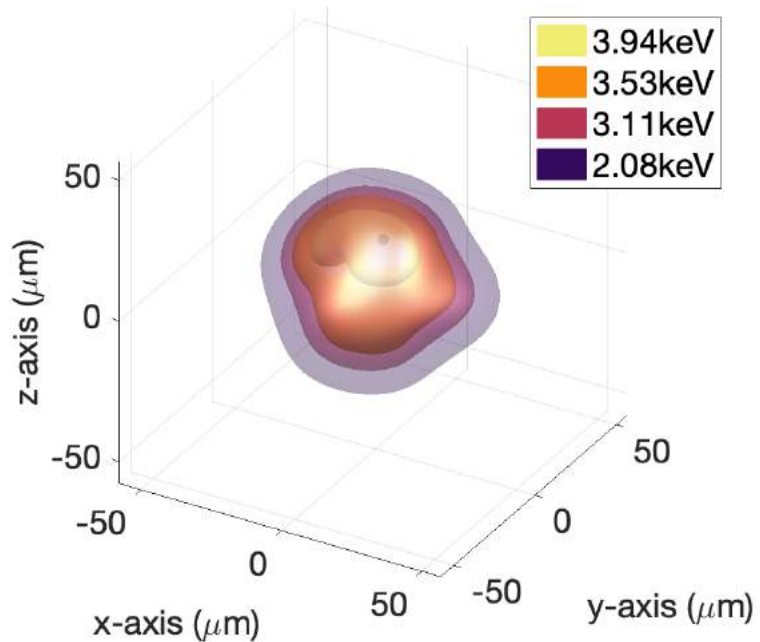


FIGURE 3.85. N170821 — 3D T_e measurement

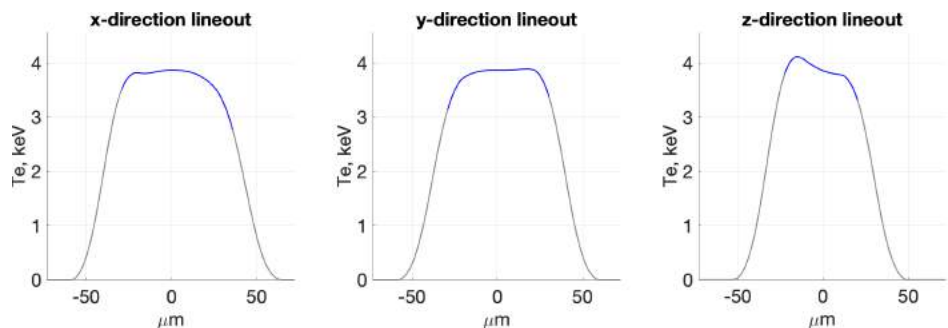


FIGURE 3.86. N170821 central lineouts of 3D T_e measurement

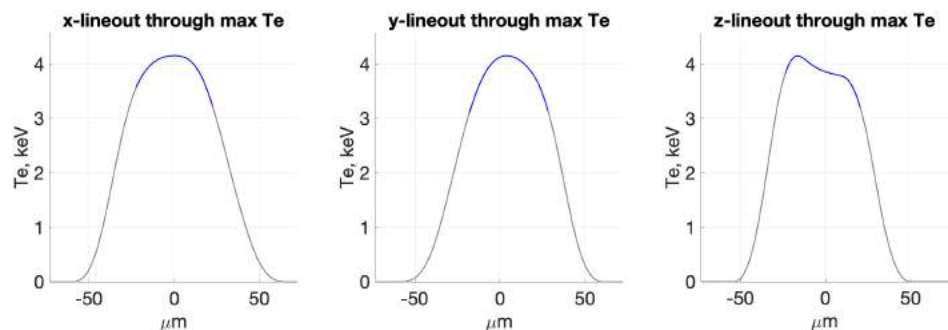


FIGURE 3.87. N170821 lineouts through maximum T_e

APPENDIX A

Mathematical derivation for formulas in chapter 1

Derivation of formula (1.6)

Given a planar triangle T with vertices $v_i = (x_i, y_i)$ for $i = 1, 2, 3$, the area of T is given by

$$A_T = \frac{1}{2} \det \begin{pmatrix} x_2 - x_1 & y_2 - y_1 \\ x_3 - x_1 & y_3 - y_1 \end{pmatrix}$$

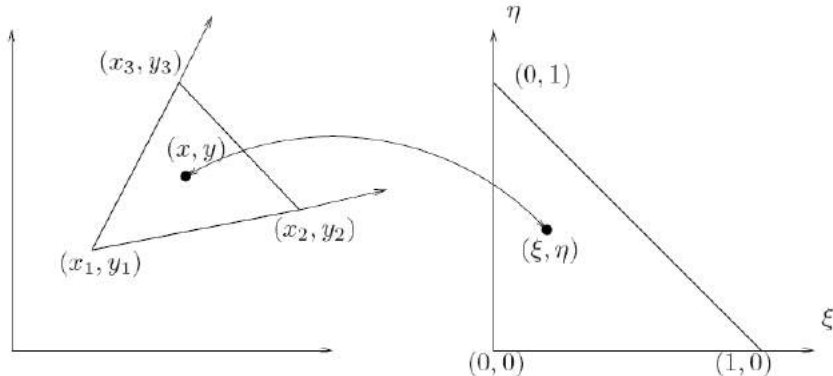


FIGURE A.1. Change of variable from (x, y) to (ξ, η)

We use the change of variable from (x, y) to (ξ, η) , see figure (A.1), and map the triangle T to triangle C with its vertices being $(0, 0)$, $(1, 0)$, $(0, 1)$. The map can be expressed as

$$\begin{pmatrix} x \\ y \end{pmatrix} = \begin{pmatrix} x_1 \\ y_1 \end{pmatrix} (1 - \xi - \eta) + \begin{pmatrix} x_2 \\ y_2 \end{pmatrix} \xi + \begin{pmatrix} x_3 \\ y_3 \end{pmatrix} \eta$$

We compute the corresponding Jacobian:

$$J = \frac{\partial(x, y)}{\partial(\xi, \eta)} = \begin{pmatrix} x_\xi & x_\eta \\ y_\xi & y_\eta \end{pmatrix} = \begin{pmatrix} x_2 - x_1 & y_2 - y_1 \\ x_3 - x_1 & y_3 - y_1 \end{pmatrix}$$

Therefore, the area of T is

$$A_T = \int_T dx dy = \int_C |J| d\xi d\eta = \frac{\det(J)}{2}$$

We define hat basis B_1 and B_2 which are supported at vertices v_1 and v_2 , with $B_i: T \rightarrow [0, 1]$ as defined in (1.5). Using the linear transformation shown above, we can write down the corresponding transformed hat basis \tilde{B}_1 and \tilde{B}_2 , with $B_i: C \rightarrow [0, 1]$. So we have $\tilde{B}_1(\xi, \eta) = 1 - \xi - \eta$, $\tilde{B}_2(\xi, \eta) = \xi$ and hence

$$\int_T B_1 B_2 d(x, y) = |J| \int_K \tilde{B}_1 \tilde{B}_2 d(\xi, \eta) = 2A_T \int_K \xi - \xi^2 - \xi\eta d\xi d\eta.$$

We compute the integration

$$\int_0^1 \int_0^{1-\xi} \xi - \xi^2 - \xi\eta d\eta d\xi = \int_0^1 (\xi - \xi^2)(1 - \xi) - \xi \frac{(1 - \xi)^2}{2} d\xi = \int_0^1 \frac{\xi}{2} - \xi^2 + \frac{\xi^3}{2} d\xi = \frac{1}{4} - \frac{1}{3} + \frac{1}{8} = \frac{1}{24}.$$

Therefore,

$$\int_T B_1 B_2 d(x, y) = \frac{A_T}{12}$$

As we can see in figure (1.15), the two adjacent triangles T_{ij}^1, T_{ij}^2 share an edge $e_{ij} = (v_i, v_j)$, and we have two hat basis functions B_i and B_j that are supported at v_i and v_j respectively.

In order to compute the entries of the mass matrix D , for $i \sim j$,

$$D_{ij} := \left(\int_{T_{ij}^1} + \int_{T_{ij}^2} \right) B_i B_j dA = \frac{1}{12} (A_{T_{ij}^1} + A_{T_{ij}^2}).$$

In the case of $i = j$, by considering the volume bound by the hat basis function, i.e. $\int_T B_1 B_1 d(x, y) = \int_T B_2 B_2 d(x, y)$. We have

$$\int_T B_1 B_1 d(x, y) = |J| \int_0^1 \int_0^{1-\xi} \xi^2 d\eta d\xi = \int_0^1 \xi^2 (1 - \xi) d\xi = \frac{|J|}{3} - \frac{|J|}{4} = \frac{A_T}{6}$$

Therefore, as we can see in figure (A.2), we sum over the *one-ring* region of vertex v_i which are all triangles adjacent to vertex v_i

$$D_{ii} = \sum_{k \sim i} \int_{T_{ik}} B_i B_i dA = \sum_{k \sim i} \frac{2 \cdot A_{T_{ik}}}{12} = \frac{1}{12} \sum_{k \sim i} (A_{T_{ik}^1} + A_{T_{ik}^2}) = \sum_{k \sim i} D_{ik}.$$

Finally, if $i \neq j$ and v_i is not adjacent to v_j , the two hat basis functions B_i and B_j do not have common intersection. Therefore

$$D_{ij} = \int_T B_i B_j dA = 0$$

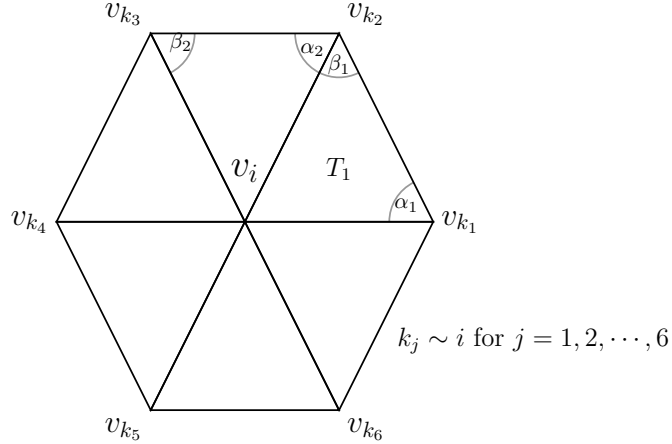


FIGURE A.2. Triangles T_{ik} adjacent to vertex v_i , i.e. $k \sim i$

Derivation of formula (1.7)

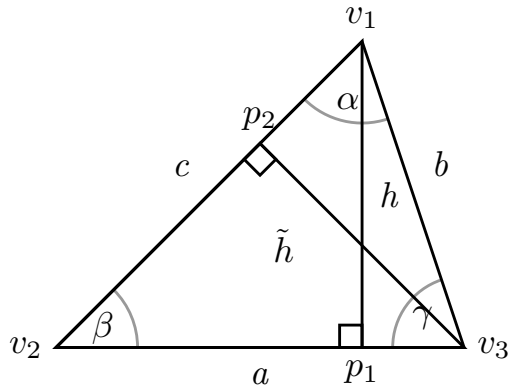


FIGURE A.3. Triangle T

Given a triangle T as shown in figure (A.3), we define a height h as the length of a perpendicular line from vertex v_1 to the side a . Then the aspect ratio is $\frac{a}{h}$ and

$$\frac{a}{h} = \cot(\beta) + \cot(\gamma)$$

Now we construct a hat (*piecewise linear*) function $f := \mathbb{R}^2 \rightarrow \mathbb{R}$ such that f is piecewise linear and $f(v_1) = 1$ and $f(v_2) = 0 = f(v_3)$. We define the hat function using

$$f(x, y) := f(x_0, y_0) + \nabla f|_{(x_0, y_0)} \cdot (x - x_0, y - y_0).$$

It follows directly from the definition that

$$\nabla f \cdot (v_1 - v_3) = 1, \quad \nabla f \cdot (v_1 - v_2) = 1.$$

Let $f(x, y) = k_1 x + k_2 y + k_3 \Rightarrow \nabla f = (k_1, k_2, 0)$, so ∇f is a constant vector lying within the plane containing the triangle. Hence we have

$$\nabla f \cdot n = 0$$

The level set of f is a set of straight lines parallel to the edge e_{23} . Since ∇f is perpendicular to the level set, hence

$$\nabla f \cdot (v_2 - v_3) = 0.$$

Moreover, we let e_{ij} denote the vector from vertex v_i to v_j and e_{ij}^\perp denote the vector e_{ij} by 90° counter-clockwise. So

$$\nabla f \parallel e_{23}^\perp$$

Also,

$$1 = \nabla f \cdot (v_1 - v_3) = \|\nabla f\| b \cos(\frac{\pi}{2} - \gamma) \Rightarrow \|\nabla f\| = \frac{1}{b \sin \gamma} = \frac{1}{h},$$

which is exactly the linear growth rate of f from 0 to 1 within h .

Combining $\nabla f \parallel e_{23}^\perp$, $\|\nabla f\| = \frac{1}{h}$, and the area $A = \frac{1}{2}ah$, we have

$$\nabla f = \frac{e_{23}^\perp}{2A}.$$

Therefore,

$$\int_T \langle \nabla f, \nabla f \rangle d(x, y) = A \|\nabla f\|^2 = \frac{A}{h^2} = \frac{a}{2h} = \frac{1}{2} (\cot(\beta) + \cot(\gamma))$$

A key observation is that *there is no variable of length involved in our above derivation*. So $\int_T \langle \nabla f, \nabla f \rangle d(x, y)$ is **conformal invariant**, i.e. it remains unchanged under uniform scaling of the triangles.

Now for two different hat functions f_1, f_2 defined by $f_1(v_1) = 1, f_2(v_2) = 1$ and with zero otherwise. We compute

$$\int_T \langle \nabla f_1, \nabla f_2 \rangle d(x, y) = A \langle \nabla f_1, \nabla f_2 \rangle = \frac{\langle e_{23}^\perp, e_{13}^\perp \rangle}{4A} = \frac{a \cdot b \cdot \cos(\pi - \gamma)}{4A} = -\frac{a \cdot b \cdot \cos\gamma}{2c\tilde{h}}.$$

As we see in figure (A.3), we have $a = \frac{\tilde{h}}{\sin\beta}$ and $b = \frac{\tilde{h}}{\sin\alpha}$,

$$\int_T \langle \nabla f_1, \nabla f_2 \rangle d(x, y) = -\frac{\left(\frac{\tilde{h}}{\sin\beta}\right) \cdot \left(\frac{\tilde{h}}{\sin\alpha}\right) \cdot \cos\gamma}{2c\tilde{h}} = -\frac{\tilde{h}\cos\gamma}{2(\tilde{h}\cot\alpha + \tilde{h}\cot\beta)\sin\alpha\sin\beta} = -\frac{\cos\gamma}{2(\cos\alpha\sin\beta + \sin\alpha\cos\beta)}$$

We use trigonometric formula to further simplify the expression

$$\int_T \langle \nabla f_1, \nabla f_2 \rangle d(x, y) = -\frac{\cos\gamma}{2(\sin(\alpha + \beta))} = -\frac{\cos\gamma}{2\sin(\pi - \gamma)} = -\frac{\cos\gamma}{2\sin(\gamma)}$$

Finally we arrive at the expression

$$\int_T \langle \nabla f_1, \nabla f_2 \rangle d(x, y) = -\frac{1}{2}\cot(\gamma)$$

In order to compute the entries of the stiffness matrix L , for $i \sim j$:

Given two adjacent triangles T_{ij}^1, T_{ij}^2 with the corresponding hat basis functions B_i, B_j , see figure (1.15), we have

$$L_{ij} = \int_{(T_{ij}^1 \cup T_{ij}^2)} \nabla B_i \cdot \nabla B_j dA = -\frac{1}{2} (\cot(\beta_{ij}^1) + \cot(\beta_{ij}^2))$$

For $i = j$, we use α_k, β_k as labelled in the figure (A.2),

$$L_{ii} = \int \nabla B_i \cdot \nabla B_i dA = \frac{1}{2} \sum_{k \sim i} (\cot(\alpha_k) + \cot(\beta_k)) = \sum_{k \sim i} \left(\frac{\cot(\alpha_k) + \cot(\beta_{k+1})}{2} \right)$$

Therefore,

$$L_{ii} = - \sum_{k \sim i} L_{ik}$$

Finally, if $i \neq j$ and v_i is not adjacent to v_j , the two hat basis functions B_i and B_j do not have common intersection. Therefore

$$L_{ij} = \nabla B_i \cdot \nabla B_j dA = 0$$

Notice that *both mass matrix D and stiffness matrix L are symmetric and their diagonal entry in each row is equal to the sum of the off-diagonal entries, i.e. matrix $M := [m_{ij}]$ with $\forall i |m_{ii}| = \sum_{j \neq i} |m_{ij}|$.*

Existence of linear map $\Lambda: T\Phi_0 \mapsto T\Phi_1$

We want to prove the existence of the linear map Λ which maps orthogonal vectors $\partial_{v_1}, \partial_{v_2} \in T\Phi_0(p)$ with $\partial_{v_1} \perp \partial_{v_2}$ to the two orthogonal vectors, $\partial_{w_1}, \partial_{w_2} \in T\Phi_1(p)$ with $\partial_{w_1} \perp \partial_{w_2}$

PROOF. Without loss of generality, assume that a linear map Λ_0 maps the two orthogonal vectors $\partial_{v_1}, \partial_{v_2}$ to two vectors $\partial_{w_1}, \partial_{w_2}$ with an acute angle between them, says $0 < \alpha < \frac{\pi}{2}$, as shown in figure (A.4).

If we now rotate the vector ∂_{v_1} to the position of ∂_{v_2} , then ∂_{v_2} moves $-\partial_{v_1}$. Since the map is linear, ∂_{w_1} moves to ∂_{w_2} and ∂_{w_2} to $-\partial_{w_1}$. Therefore, we obtain a new linear map Λ_1 that maps $\partial_{v_1}, \partial_{v_2}$ to two vectors $\partial_{w_1}, \partial_{w_2}$ and the angle between $\partial_{w_1}, \partial_{w_2}$ is $\pi - \alpha$, which is larger than $\frac{\pi}{2}$.

So by the intermediate value theorem, there exists a linear map (“an intermediate step between Λ_0 and Λ_1 ”) such that the orthogonal vectors $\partial_{v_1}, \partial_{v_2}$ are mapped to two orthogonal vector $\partial_{w_1}, \partial_{w_2}$.

This proves the existence of the linear map Λ .

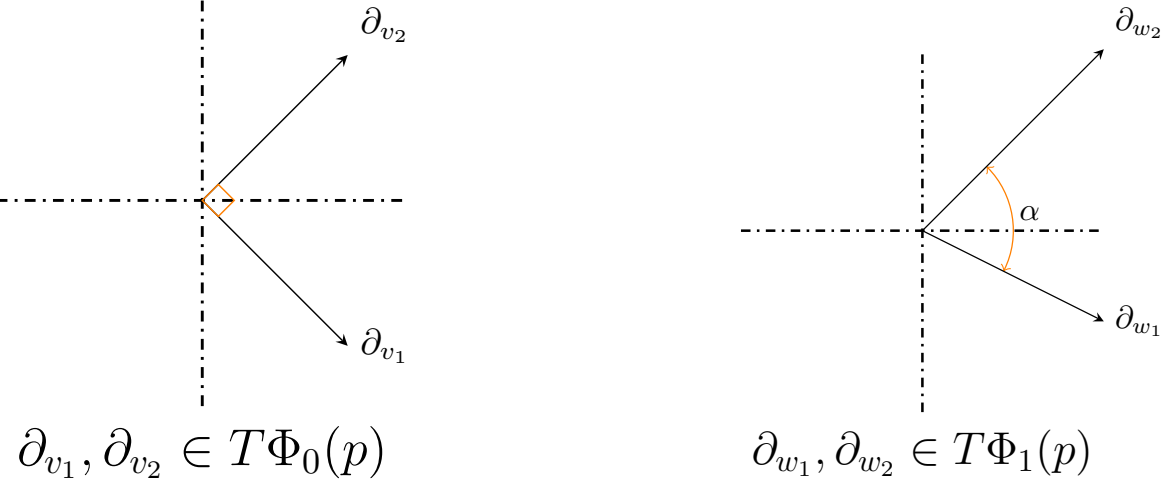


FIGURE A.4. Tangent plane of Φ_0 (left) and Φ_1 (right)

APPENDIX B

Synthetic models and their 3D electron temperature measurement

Synthetic T_e model 1 and its 3D T_e measurement



FIGURE B.1. Synthetic T_e model 1 at (30°, 30°) (left) and (210°, 30°) (right)

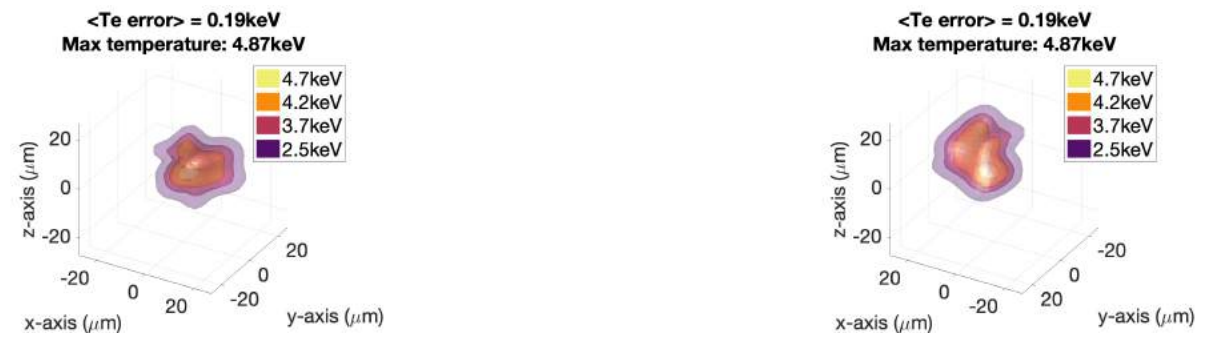


FIGURE B.2. 3D T_e measurement using 2 LOS at (30°, 30°) (left) and (210°, 30°) (right)



FIGURE B.3. 3D T_e measurement using 3 LOS at (30°, 30°) (left) and (210°, 30°) (right)

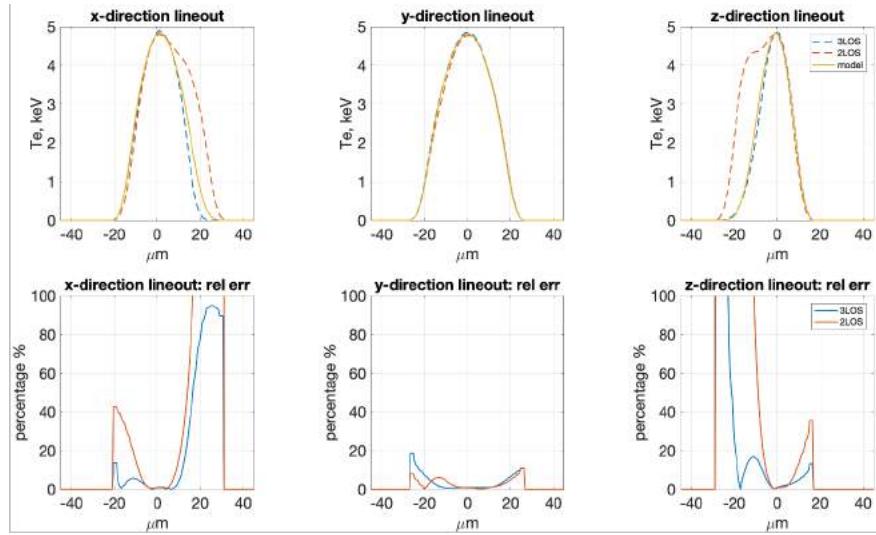


FIGURE B.4. Comparison of central lineouts of 3D T_e measurement using 2 LOS versus 3 LOS (model 1)

Synthetic T_e models 2 and its 3D T_e measurements



FIGURE B.5. Synthetic T_e model 2 at (30°, 30°) (left) and (210°, 30°) (right)



FIGURE B.6. 3D T_e measurement using 2 LOS at (30°, 30°) (left) and (210°, 30°) (right)



FIGURE B.7. 3D T_e measurement using 3 LOS at $(30^\circ, 30^\circ)$ (left) and $(210^\circ, 30^\circ)$ (right)

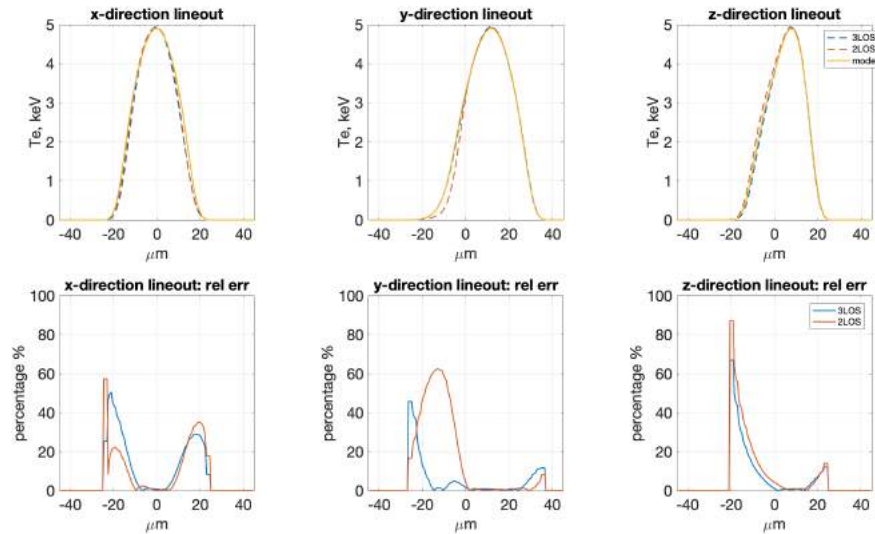


FIGURE B.8. Comparison of central lineouts of 3D T_e measurement using 2 LOS versus 3 LOS (model 2)

Synthetic T_e models 3 and its 3D T_e measurements



FIGURE B.9. Synthetic T_e model 3 at at $(30^\circ, 30^\circ)$ (left) and $(210^\circ, 30^\circ)$ (right)



FIGURE B.10. 3D T_e measurement using 2 LOS at $(30^\circ, 30^\circ)$ (left) and $(210^\circ, 30^\circ)$ (right)



FIGURE B.11. 3D T_e measurement using 3 LOS at $(30^\circ, 30^\circ)$ (left) and $(210^\circ, 30^\circ)$ (right)

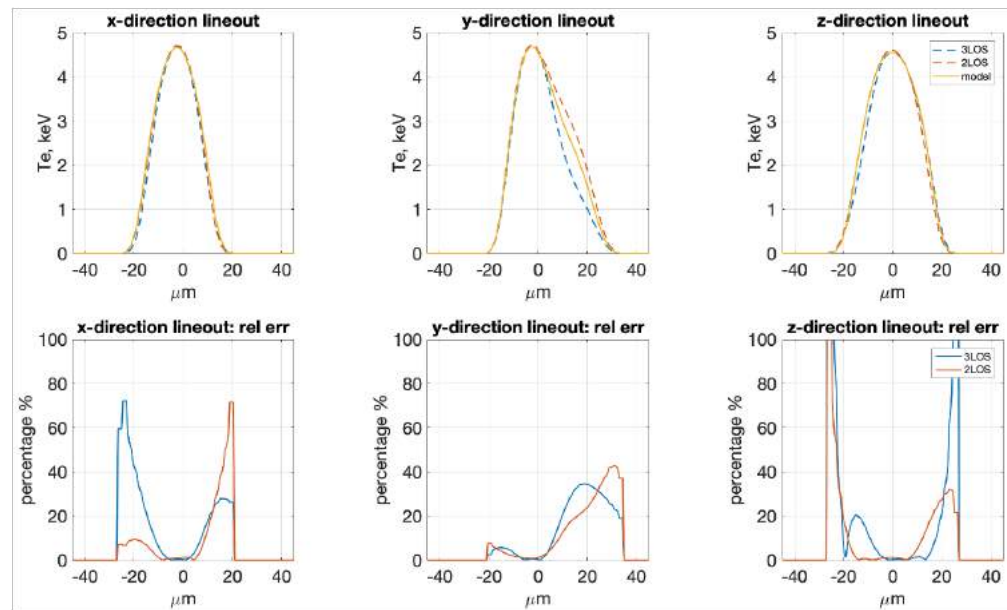


FIGURE B.12. Comparison of central lineouts of 3D T_e measurement using 2 LOS versus 3 LOS (model 3)

Synthetic T_e models 4 and its 3D T_e measurements

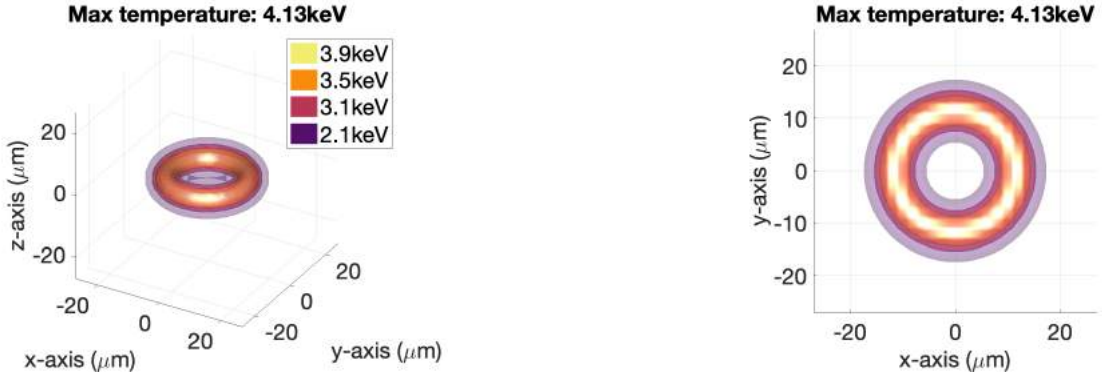


FIGURE B.13. Synthetic T_e model 4 at $(30^\circ, 30^\circ)$ (left) and $(0^\circ, 0^\circ)$ (right)



FIGURE B.14. 3D T_e measurement using 2 LOS at $(30^\circ, 30^\circ)$ (left) and $(0^\circ, 0^\circ)$ (right)



FIGURE B.15. 3D T_e measurement using 3 LOS at $(30^\circ, 30^\circ)$ (left) and $(0^\circ, 0^\circ)$ (right)

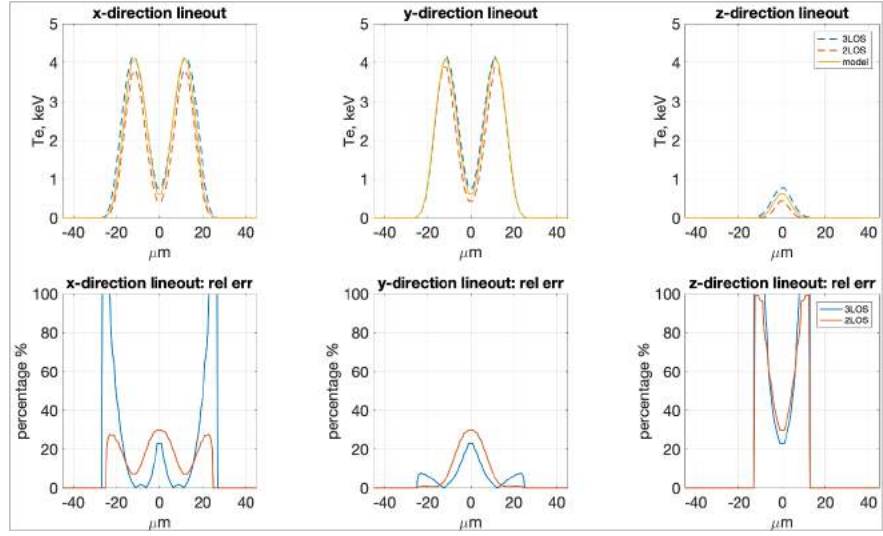


FIGURE B.16. Comparison of central lineouts of 3D T_e measurement using 2 LOS versus 3 LOS (model 4)

Synthetic T_e models 5 and its 3D T_e measurements



FIGURE B.17. Synthetic T_e model 5 at (30°, 30°) (left) and (0°, 0°) (right)



FIGURE B.18. 3D T_e measurement using 2 LOS at (30°, 30°) (left) and (0°, 0°) (right)



FIGURE B.19. 3D T_e measurement using 3 LOS at $(30^\circ, 30^\circ)$ (left) and $(0^\circ, 0^\circ)$ (right)

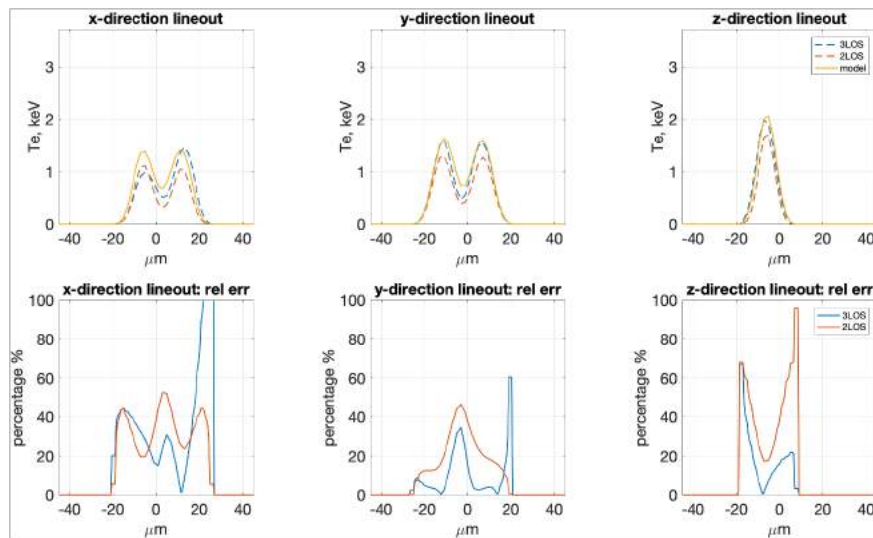


FIGURE B.20. Comparison of central lineouts of 3D T_e measurement using 2 LOS versus 3 LOS (model 5)

Synthetic T_e models 6 and its 3D T_e measurements



FIGURE B.21. Synthetic T_e model 6 at at $(30^\circ, 30^\circ)$ (left) and $(210^\circ, 30^\circ)$ (right)



FIGURE B.22. 3D T_e measurement using 2 LOS at $(30^\circ, 30^\circ)$ (left) and $(210^\circ, 30^\circ)$ (right)



FIGURE B.23. 3D T_e measurement using 3 LOS at $(30^\circ, 30^\circ)$ (left) and $(210^\circ, 30^\circ)$ (right)

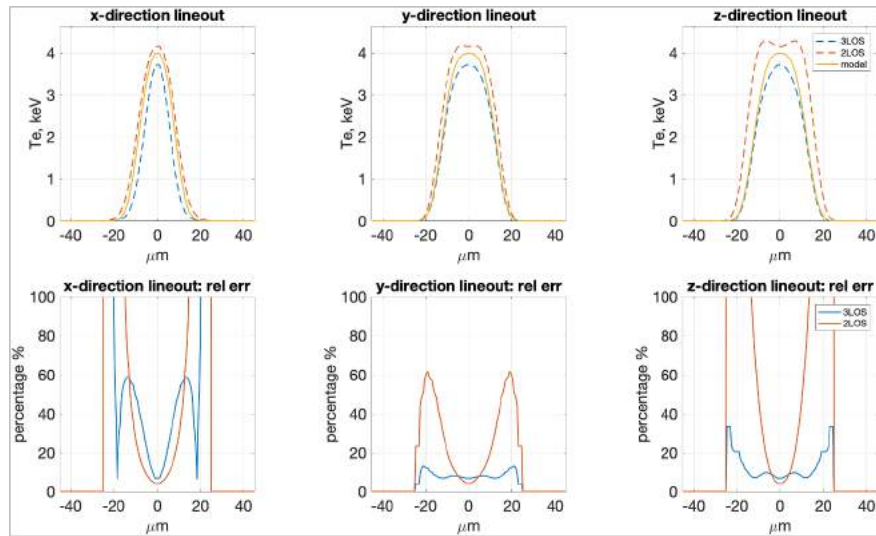


FIGURE B.24. Comparison of central lineouts of 3D T_e measurement using 2 LOS versus 3 LOS (model 6)

⁰ The view angle (θ, ϕ) is defined in which $0 \leq \theta \leq 2\pi$ is the azimuth angle and $-\pi \leq \phi \leq \pi$ is the elevation angle.

Bibliography

- [AB11] B. Andrews and P. Bryan, *Curvature bound for curve shortening flow via distance comparison and a direct proof of grayson’s theorem*, Journal für die reine und angewandte Mathematik **2011** (2011), no. 653, 179 – 187.
- [AFS⁺12] J. Ayers, B. Felker, V. Smalyuk, N. Izumi, K. Piston, J. Holder, G. Power, F. Allen, N. Simanovska, P. Bell, D. Bradley, and Z. Lamb, *Design and implementation of high magnification framing camera for NIF “ARIANE Light”*, Target Diagnostics Physics and Engineering for Inertial Confinement Fusion (P. Bell and G. P. Grim, eds.), vol. 8505, International Society for Optics and Photonics, SPIE, 2012, pp. 133 – 144.
- [AKL17] N. Aigerman, S. Z. Kovalevsky, and Y. Lipman, *Spherical orbifold tutte embeddings*, ACM Trans. Graph. **36** (2017), no. 4.
- [AL15] N. Aigerman and Y. Lipman, *Orbifold tutte embeddings*, ACM Trans. Graph. **34** (2015), no. 6.
- [AL16] ———, *Hyperbolic orbifold tutte embeddings*, ACM Trans. Graph. **35** (2016), no. 6.
- [BASA⁺17] B. Bachmann, H. Abu-Shawareb, N. Alexander, J. Ayers, C. G. Bailey, P. Bell, L. R. Benedetti, D. Bradley, G. Collins, L. Divol, T. Döppner, S. Felker, J. Field, A. Forsman, J. D. Galbraith, C. M. Hardy, T. Hilsabeck, N. Izumi, C. Jarrot, J. Kilkenny, S. Kramer, O. L. Landen, T. Ma, A. MacPhee, N. Masters, S. R. Nagel, A. Pak, P. Patel, L. A. Pickworth, J. E. Ralph, C. Reed, J. R. Rygg, and D. B. Thorn, *X-ray penumbral imaging diagnostic developments at the National Ignition Facility*, Target Diagnostics Physics and Engineering for Inertial Confinement Fusion VI (J. A. Koch and G. P. Grim, eds.), vol. 10390, International Society for Optics and Photonics, SPIE, 2017, pp. 27 – 37.
- [BBC⁺97] T. Boehly, D. Brown, R. Craxton, R. Keck, J. Knauer, J. Kelly, T. Kessler, S. Kumpan, S. Loucks, S. Letzring, F. Marshall, R. McCrory, S. Morse, W. Seka, J. Soures, and C. Verdon, *Initial performance results of the omega laser system*, Optics Communications **133** (1997), no. 1, 495 – 506.
- [BBM14] M. Bauer, M. Bruveris, and P. W. Michor, *Overview of the geometries of shape spaces and diffeomorphism groups*, Journal of Mathematical Imaging and Vision **50** (2014), no. 1, 60–97.
- [BCK18] A. Baden, K. Crane, and M. Kazhdan, *Möbius registration*, Computer Graphics Forum **37** (2018), no. 5, 211–220, <https://onlinelibrary.wiley.com/doi/pdf/10.1111/cgf.13503>.
- [BCP⁺16] B. Bachmann, R. Chow, N. E. Palmer, M. Hoover, E. Huffman, J. J. Lee, E. Romano, C. Kumar, R. D. Hulbert, F. Albert, E. L. Dewald, L. Divol, M. Hohenberger, O. L. Landen, A. Warrick, and T. Döppner, *Improved hard x-ray (50-80 kev) imaging of hohlraum implosion experiments at the national ignition*

- facility*, Target Diagnostics Physics and Engineering for Inertial Confinement Fusion V (J. A. Koch and G. P. Grim, eds.), vol. 9966, International Society for Optics and Photonics, SPIE, 2016, pp. 20 – 33.
- [BE79] Å. Björck and T. Elfving, *Accelerated projection methods for computing pseudoinverse solutions of systems of linear equations*, BIT Numerical Mathematics **19** (1979), no. 2, 145–163.
- [Ber72] L. Bers, *Uniformization, Moduli, and Kleinian Groups†*, Bulletin of the London Mathematical Society **4** (1972), no. 3, 257–300, <https://academic.oup.com/blms/article-pdf/4/3/257/839734/4-3-257.pdf>.
- [Ber11] D. P. Bertsekas, *Incremental proximal methods for large scale convex optimization*, Mathematical Programming **129** (2011), no. 2, 163.
- [BHF⁺16] B. Bachmann, T. Hilsabeck, J. Field, N. Masters, C. Reed, T. Pardini, J. R. Rygg, N. Alexander, L. R. Benedetti, T. Döppner, A. Forsman, N. Izumi, S. LePape, T. Ma, A. G. MacPhee, S. Nagel, P. Patel, B. Spears, and O. L. Landen, *Resolving hot spot microstructure using x-ray penumbral imaging (invited)*, Review of Scientific Instruments **87** (2016), no. 11, 11E201, <https://aip.scitation.org/doi/10.1063/1.4959161>.
- [Bla09] S. Blatt, *A singular example for the willmore flow*, Analysis **29** (2009), no. 4, 407 – 430.
- [BPS15] A. I. Bobenko, U. Pinkall, and B. A. Springborn, *Discrete conformal maps and ideal hyperbolic polyhedra*, Geom. Topol. **19** (2015), no. 4, 2155–2215.
- [Bra92] K. A. Brakke, *The surface evolver*, Experimental Mathematics **1** (1992), 141–165.
- [BS04] A. Bobenko and B. Springborn, *Variational principles for circle patterns and koebe’s theorem*, Transactions of the American Mathematical Society **356** (2004).
- [Büc08] U. Bücking, *Approximation of conformal mappings by circle patterns*, Geometriae Dedicata **137** (2008), no. 1, 163–197.
- [Buz08] T. Buzug, *Computed tomography : From photon statistics to modern cone-beam ct*, 01 2008.
- [Bü16] U. Bücking, *Approximation of conformal mappings using conformally equivalent triangular lattices*, pp. 133–149, 08 2016.
- [Bü17] ———, *c^∞ -convergence of conformal mappings on triangular lattices*, Results in Mathematics **73** (2017).
- [CDD⁺04] U. Clarenz, U. Diewald, G. Dziuk, M. Rumpf, and R. Rusu, *A finite element method for surface restoration with smooth boundary conditions*, Computer Aided Geometric Design **21** (2004), no. 5, 427 – 445.
- [CDR00] U. Clarenz, U. Diewald, and M. Rumpf, *Anisotropic geometric diffusion in surface processing*, Proceedings of the Conference on Visualization ’00 (Washington, DC, USA), VIS ’00, IEEE Computer Society Press, 2000, p. 397–405.
- [CDS12] S.-W. Cheng, T. K. Dey, and J. Shewchuk, *Delaunay mesh generation*, 1st ed., Chapman & Hall/CRC, 2012.
- [CL03] B. Chow and F. Luo, *Combinatorial ricci flows on surfaces*, J. Differential Geom. **63** (2003), no. 1, 97–129.
- [CMM91] V. Cervera, F. Mascaró, and P. Michor, *The action of the diffeomorphism group on the space of immersions*, Differential Geometry and its Applications **1** (1991), 391–401.

- [CMP15] T. Colding, W. Minicozzi, and E. Pedersen, *Mean curvature flow*, Bulletin of the American Mathematical Society **52** (2015), 1.
- [CPS11] K. Crane, U. Pinkall, and P. Schröder, *Spin transformations of discrete surfaces*, ACM Trans. Graph. **30** (2011), no. 4.
- [CPS13] ———, *Robust fairing via conformal curvature flow*, ACM Trans. Graph. **32** (2013), no. 4.
- [CS03] C. R. Collins and K. Stephenson, *A circle packing algorithm*, Computational Geometry **25** (2003), no. 3, 233 – 256.
- [CW17] K. Crane and M. Wardetzky, *A glimpse into discrete differential geometry*, Notices of the American Mathematical Society **64** (2017), no. 10.
- [Deu85] F. Deutsch, *Rate of convergence of the method of alternating projections*, pp. 96–107, Birkhäuser Basel, Basel, 1985.
- [DH97] F. Deutsch and H. Hundal, *The rate of convergence for the method of alternating projections, ii*, Journal of Mathematical Analysis and Applications **205** (1997), no. 2, 381 – 405.
- [DMSB99] M. Desbrun, M. Meyer, P. Schröder, and A. H. Barr, *Implicit fairing of irregular meshes using diffusion and curvature flow*, Proceedings of the 26th Annual Conference on Computer Graphics and Interactive Techniques (USA), SIGGRAPH '99, ACM Press/Addison-Wesley Publishing Co., 1999, p. 317–324.
- [DSL19] N. Dym, R. Slutsky, and Y. Lipman, *Linear variational principle for riemann mappings and discrete conformality*, Proceedings of the National Academy of Sciences **116** (2019), no. 3, 732–737, <https://www.pnas.org/content/116/3/732.full.pdf>.
- [Dur04] P. Duren, *Harmonic mappings in the plane*, Cambridge Tracts in Mathematics, Cambridge University Press, 2004.
- [EL95] J. EELLS and L. LEMAIRE, *A report on harmonic maps*, pp. 1–68, 1995, https://www.worldscientific.com/doi/pdf/10.1142/9789812832030_0001.
- [Flo03a] M. S. Floater, *Mean value coordinates*, Computer Aided Geometric Design **20** (2003), no. 1, 19 – 27.
- [Flo03b] ———, *One-to-one piecewise linear mappings over triangulations*, Mathematics of Computation **72** (2003), no. 242, 685–696.
- [Gag83] M. E. Gage, *An isoperimetric inequality with applications to curve shortening*, Duke Math. J. **50** (1983), no. 4, 1225–1229.
- [Gag84] ———, *Curve shortening makes convex curves circular*, Inventiones mathematicae **76** (1984), no. 2, 357–364.
- [Gal05] A. Galántai, *On the rate of convergence of the alternating projection method in finite dimensional spaces*, Journal of Mathematical Analysis and Applications **310** (2005), no. 1, 30 – 44.
- [GBH70] R. Gordon, R. Bender, and G. T. Herman, *Algebraic reconstruction techniques (art) for three-dimensional electron microscopy and x-ray photography*, Journal of Theoretical Biology **29** (1970), no. 3, 471 – 481.
- [GGS03] C. Gotsman, X. Gu, and A. Sheffer, *Fundamentals of spherical parameterization for 3d meshes*, ACM Trans. Graph. **22** (2003), no. 3, 358–363.

- [GH86] M. E. Gage and R. S. Hamilton, *The heat equation shrinking convex plane curves*, J. Differential Geom. **23** (1986), no. 1, 69–96.
- [GLSW18] X. D. Gu, F. Luo, J. Sun, and T. Wu, *A discrete uniformization theorem for polyhedral surfaces*, J. Differential Geom. **109** (2018), no. 2, 223–256.
- [GLW19] X. D. Gu, F. Luo, and T. Wu, *Convergence of discrete conformal geometry and computation of uniformization maps*, Asian Journal of Mathematics **23** (2019), no. 1, 21–34 (English (US)).
- [Gor18] D. Gordon, *The cimmino-kaczmarz equivalence and related results*, (2018), 253–270.
- [Gra87] M. A. Grayson, *The heat equation shrinks embedded plane curves to round points*, J. Differential Geom. **26** (1987), no. 2, 285–314.
- [Gra89] ———, *A short note on the evolution of a surface by its mean curvature*, Duke Math. J. **58** (1989), no. 3, 555–558.
- [Hat00] A. Hatcher, *Algebraic topology*, Cambridge Univ. Press, Cambridge, 2000.
- [HCC⁺14] O. A. Hurricane, D. A. Callahan, D. T. Casey, P. M. Celliers, C. Cerjan, E. L. Dewald, T. R. Dittrich, T. Döppner, D. E. Hinkel, L. F. B. Hopkins, J. L. Kline, S. Le Pape, T. Ma, A. G. MacPhee, J. L. Milovich, A. Pak, H. S. Park, P. K. Patel, B. A. Remington, J. D. Salmonson, P. T. Springer, and R. Tommasini, *Fuel gain exceeding unity in an inertially confined fusion implosion*, Nature **506** (2014), no. 7488, 343–348.
- [HCC⁺16] O. A. Hurricane, D. A. Callahan, D. T. Casey, E. L. Dewald, T. R. Dittrich, T. Döppner, S. Haan, D. E. Hinkel, L. F. Berzak Hopkins, O. Jones, A. L. Kratcher, S. Le Pape, T. Ma, A. G. MacPhee, J. L. Milovich, J. Moody, A. Pak, H. S. Park, P. K. Patel, J. E. Ralph, H. F. Robey, J. S. Ross, J. D. Salmonson, B. K. Spears, P. T. Springer, R. Tommasini, F. Albert, L. R. Benedetti, R. Bionta, E. Bond, D. K. Bradley, J. Caggiano, P. M. Celliers, C. Cerjan, J. A. Church, R. Dylla-Spears, D. Edgell, M. J. Edwards, D. Fittinghoff, M. A. Barrios Garcia, A. Hamza, R. Hatarik, H. Herrmann, M. Hohenberger, D. Hoover, J. L. Kline, G. Kyrala, B. Kozioziemski, G. Grim, J. E. Field, J. Frenje, N. Izumi, M. Gatu Johnson, S. F. Khan, J. Knauer, T. Kohut, O. Landen, F. Merrill, P. Michel, A. Moore, S. R. Nagel, A. Nikroo, T. Parham, R. R. Rygg, D. Sayre, M. Schneider, D. Shaughnessy, D. Strozzi, R. P. J. Town, D. Turnbull, P. Volegov, A. Wan, K. Widmann, C. Wilde, and C. Yeamans, *Inertially confined fusion plasmas dominated by alpha-particle self-heating*, Nature Physics **12** (2016), no. 8, 800—806.
- [Her09] G. T. Herman, *Fundamentals of computerized tomography: Image reconstruction from projections*, 2nd ed., Springer Publishing Company, Incorporated, 2009.
- [HJ18] P. C. Hansen and J. S. Jørgensen, *Air tools ii: algebraic iterative reconstruction methods, improved implementation*, Numerical Algorithms **79** (2018), no. 1, 107–137.
- [HK14] J. Hass and P. Koehl, *How round is a protein? exploring protein structures for globularity using conformal mapping*, Frontiers in Molecular Biosciences **1** (2014), 26.
- [HK15] ———, *Landmark-free geometric methods in biological shape analysis*, Journal of The Royal Society Interface **12** (2015).

- [HK17] ———, *Comparing shapes of genus-zero surfaces*, Journal of Applied and Computational Topology **1** (2017), no. 1, 57–87.
- [HS93] Z.-X. He and O. Schramm, *Fixed points, koebe uniformization and circle packings*, Annals of Mathematics **137** (1993), no. 2, 369–406.
- [HS96] Z.-X. He and O. Schramm, *On the convergence of circle packings to the riemann map*, Inventiones mathematicae **125** (1996), 285–305.
- [HS98] ———, *The c^∞ -convergence of hexagonal disk packings to the riemann map*, Acta Mathematica **180** (1998), 219–245.
- [Hui84] G. Huisken, *Flow by mean curvature of convex surfaces into spheres*, J. Differential Geom. **20** (1984), no. 1, 237–266.
- [JBM⁺18] L. C. Jarrott, B. Bachmann, T. Ma, L. R. Benedetti, F. E. Field, E. P. Hartouni, R. Hatarik, N. Izumi, S. F. Khan, O. L. Landen, S. R. Nagel, R. Nora, A. Pak, J. L. Peterson, M. B. Schneider, P. T. Springer, and P. K. Patel, *Thermal temperature measurements of inertial fusion implosions*, Phys. Rev. Lett. **121** (2018), 085001.
- [JKLG08] M. Jin, J. Kim, F. Luo, and X. Gu, *Discrete surface ricci flow*, IEEE Trans Vis Comput Graph **14** (2008), no. 5, 1030–1043.
- [Kac] S. Kaczmarz, *1379 angenäherte auflösung von systemen linearer gleichungen*, Bull. Int. Acad. Pol. Sci. Lett. Class. Sci. Math. Nat, 355–7.
- [KH14] P. Koehl and J. Hass, *Automatic alignment of genus-zero surfaces*, IEEE Transactions on Pattern Analysis and Machine Intelligence **36** (2014), no. 3, 466–478.
- [KM97] A. Kriegl and P. Michor, *The convenient setting of global analysis*, Mathematical Surveys and Monographs **53** (1997).
- [KSBC12] M. Kazhdan, J. Solomon, and M. Ben-Chen, *Can mean-curvature flow be modified to be non-singular?*, Comput. Graph. Forum **31** (2012), no. 5, 1745–1754.
- [KSS06] L. Kharevych, B. Springborn, and P. Schröder, *Discrete conformal mappings via circle patterns*, ACM Trans. Graph. **25** (2006), no. 2, 412–438.
- [Laba] L. L. N. Laboratory, *Nif diagnostics*, <https://lasers.llnl.gov/for-users/experimental-capabilities/diagnostics>.
- [Labb] ———, *Nif diagnostics instrument manipulator*, <https://nifuserguide.llnl.gov/home/5-target-area/53-diagnostic-instrument-manipulator>.
- [LAB⁺04] J. D. Lindl, P. Amendt, R. L. Berger, S. G. Glendinning, S. H. Glenzer, S. W. Haan, R. L. Kauffman, O. L. Landen, and L. J. Suter, *The physics basis for ignition using indirect-drive targets on the national ignition facility*, Physics of Plasmas **11** (2004), no. 2, 339–491, <https://doi.org/10.1063/1.1578638>.
- [Lei02] G. Leibon, *Characterizing the delaunay decompositions of compact hyperbolic surfaces*, Geom. Topol. **6** (2002), no. 1, 361–391.

- [Luo04] F. Luo, *Combinatorial Yamabe flow on surfaces*, Communications in Contemporary Mathematics **06** (2004), no. 05, 765–780.
- [Luo19] Y. Luo, *Comparing shapes of high genus surfaces*, <https://arxiv.org/abs/1910.02215> (2019).
- [MBB⁺12] F. E. Merrill, D. Bower, R. Buckles, D. D. Clark, C. R. Danly, O. B. Drury, J. M. Dzenitis, V. E. Fatherley, D. N. Fittinghoff, R. Gallegos, G. P. Grim, N. Guler, E. N. Loomis, S. Lutz, R. M. Malone, D. D. Martinson, D. Mares, D. J. Morley, G. L. Morgan, J. A. Oertel, I. L. Tregillis, P. L. Volegov, P. B. Weiss, C. H. Wilde, and D. C. Wilson, *The neutron imaging diagnostic at nif (invited)*, Review of Scientific Instruments **83** (2012), no. 10, 10D317, <https://doi.org/10.1063/1.4739242>.
- [Mil65] J. Milnor, *Topology from the differentiable viewpoint*, University Press of Virginia, 1965.
- [Nat01] F. Natterer, *The mathematics of computerized tomography*, Society for Industrial and Applied Mathematics, 2001, <https://epubs.siam.org/doi/pdf/10.1137/1.9780898719284>.
- [Nes14] Y. Nesterov, *Introductory lectures on convex optimization: A basic course*, 1 ed., Springer Publishing Company, Incorporated, 2014.
- [NMF⁺12] T. Nagayama, R. C. Mancini, R. Florido, D. Mayes, R. Tommasini, J. A. Koch, J. A. Delettrez, S. P. Regan, and V. A. Smalyuk, *Investigation of a polychromatic tomography method for the extraction of the three-dimensional spatial structure of implosion core plasmas*, Physics of Plasmas **19** (2012), no. 8, 082705, <https://doi.org/10.1063/1.4743017>.
- [PP93] U. Pinkall and K. Polthier, *Computing discrete minimal surfaces and their conjugates*, Experimental Mathematics **2** (1993), no. 1, 15–36, <https://doi.org/10.1080/10586458.1993.10504266>.
- [Riv94] I. Rivin, *Euclidean structures on simplicial surfaces and hyperbolic volume*, Annals of Mathematics **139** (1994), no. 3, 553–580.
- [RS87] B. Rodin and D. Sullivan, *The convergence of circle packings to the riemann mapping*, J. Differential Geom. **26** (1987), no. 2, 349–360.
- [SAB⁺11] V. A. Smalyuk, J. Ayers, P. M. Bell, J.-L. Bourgade, D. K. Bradley, J. Celeste, C. Cerjan, S. Darbon, J. Emig, B. Felker, C. Hagmann, J. Holder, N. Izumi, J. D. Kilkenney, J. Moody, K. Piston, A. Rousseau, C. Sorce, and R. Tommasini, *X-ray imaging in an environment with high-neutron background on National Ignition Facility*, Penetrating Radiation Systems and Applications XII (G. P. Grim and R. C. Schirato, eds.), vol. 8144, International Society for Optics and Photonics, SPIE, 2011, pp. 157 – 162.
- [Sim01] G. Simonett, *The Willmore flow for near spheres*, Differential and Integral Equations **14** (2001), 2001.
- [SK00a] R. Schneider and L. Kobbelt, *Discrete fairing of curves and surfaces based on linear curvature distribution*, In Curve and Surface Design: Saint-Malo, University Press, 2000, pp. 371–380.
- [SK00b] R. Schneider and L. Kobbelt, *Generating fair meshes with g1 boundary conditions*, Proceedings of the Geometric Modeling and Processing 2000 (USA), GMP ’00, IEEE Computer Society, 2000, p. 251.
- [SSP08] B. Springborn, P. Schröder, and U. Pinkall, *Conformal equivalence of triangle meshes*, ACM SIGGRAPH 2008 Papers (New York, NY, USA), SIGGRAPH ’08, Association for Computing Machinery, 2008.

- [SV08] T. Strohmer and R. Vershynin, *A randomized kaczmarz algorithm with exponential convergence*, Journal of Fourier Analysis and Applications **15** (2008), no. 2, 262.
- [SWGL14] J. Sun, T. Wu, X. Gu, and F. Luo, *Discrete conformal deformation: Algorithm and experiments*, SIAM Journal on Imaging Sciences **8** (2014).
- [SY97] R. Schoen and S. T. Yau, *Lectures on harmonic maps*, 1997.
- [Tan71] K. Tanabe, *Projection method for solving a singular system of linear equations and its applications*, Numerische Mathematik **17** (1971), no. 3, 203–214.
- [TMA⁺17] D. B. Thorn, A. MacPhee, J. Ayers, J. Galbraith, C. M. Hardy, N. Izumi, D. K. Bradley, L. A. Pickworth, B. Bachmann, B. Kozioziemski, O. Landen, D. Clark, M. B. Schneider, K. W. Hill, M. Bitter, S. Nagel, P. M. Bell, S. Person, H. Y. Khater, C. Smith, and J. Kilkenny, *On the design of the NIF Continuum Spectrometer*, Target Diagnostics Physics and Engineering for Inertial Confinement Fusion VI (J. A. Koch and G. P. Grim, eds.), vol. 10390, International Society for Optics and Photonics, SPIE, 2017, pp. 22 – 41.
- [Tut63] W. T. Tutte, *How to draw a graph*, Proceedings of the London Mathematical Society **s3-13** (1963), no. 1, 743–767, <https://londmathsoc.onlinelibrary.wiley.com/doi/pdf/10.1112/plms/s3-13.1.743>.
- [VDF⁺14] P. Volegov, C. R. Danly, D. N. Fittinghoff, G. P. Grim, N. Guler, N. Izumi, T. Ma, F. E. Merrill, A. L. Warrick, C. H. Wilde, and D. C. Wilson, *Neutron source reconstruction from pinhole imaging at national ignition facility*, Review of Scientific Instruments **85** (2014), no. 2, 023508, <https://doi.org/10.1063/1.4865456>.
- [VDF⁺17] P. L. Volegov, C. R. Danly, D. Fittinghoff, V. Geppert-Kleinrath, G. Grim, F. E. Merrill, and C. H. Wilde, *Three-dimensional reconstruction of neutron, gamma-ray, and x-ray sources using spherical harmonic decomposition*, Journal of Applied Physics **122** (2017), no. 17, 175901, <https://doi.org/10.1063/1.4986652>.
- [VDM⁺15] P. L. Volegov, C. R. Danly, F. E. Merrill, R. Simpson, and C. H. Wilde, *On three-dimensional reconstruction of a neutron/x-ray source from very few two-dimensional projections*, Journal of Applied Physics **118** (2015), no. 20, 205903, <https://doi.org/10.1063/1.4936319>.
- [WBH⁺07] M. Wardetzky, M. Bergou, D. Harmon, D. Zorin, and E. Grinspun, *Discrete quadratic curvature energies*, Comput. Aided Geom. Des. **24** (2007), no. 8–9, 499–518.
- [Whi73] J. H. White, *A global invariant of conformal mappings in space*, Proceedings of the American Mathematical Society **38** (1973), no. 1, 162–164.
- [YB02] S. Yoshizawa and A. G. Belyaev, *Fair triangle mesh generation with discrete elastica*, Geometric Modeling and Processing. Theory and Applications. GMP 2002. Proceedings, 2002, pp. 119–123.
- [ZZG⁺15] M. Zhang, W. Zeng, R. Guo, F. Luo, and X. D. Gu, *Survey on discrete surface ricci flow*, Journal of Computer Science and Technology **30** (2015), no. 3, 598–613.